

Charge ordering in strongly correlated systems

Ivek, Tomislav

Doctoral thesis / Disertacija

2011

Degree Grantor / Ustanova koja je dodijelila akademski / stručni stupanj: **University of Zagreb, Faculty of Science / Sveučilište u Zagrebu, Prirodoslovno-matematički fakultet**

Permanent link / Trajna poveznica: <https://um.nsk.hr/um:nbn:hr:217:988646>

Rights / Prava: [In copyright](#)/[Zaštićeno autorskim pravom.](#)

Download date / Datum preuzimanja: **2025-02-26**



Repository / Repozitorij:

[Repository of the Faculty of Science - University of Zagreb](#)



University of Zagreb
Faculty of Science
Department of Physics

Tomislav Ivek

**CHARGE ORDERINGS
IN STRONGLY CORRELATED SYSTEMS**

A doctoral dissertation submitted to
the Department of Physics,
Faculty of Science, University of Zagreb,
for the academic degree of
Doctor of Natural Sciences (Physics)

Zagreb, 2011.

TEMELJNA DOKUMENTACIJSKA KARTICA

Sveučilište u Zagrebu
Prirodoslovno-matematički fakultet
Fizički odsjek

Doktorska disertacija

UREĐENJA NABOJA U JAKO KORELIRANIM SUSTAVIMA

TOMISLAV IVEK

Institut za fiziku, Zagreb

U fokusu ove doktorske disertacije nalaze se sustavi s jakim elektronskim korelacijama i reduciranom dimenzionalnošću: anorganski kvazi-1D lančasti spoj BaVS_3 s itinerantnim i lokaliziranim nabojima, kompozit kupratnih lanaca i ljestvica $(\text{La}, \text{Y}, \text{Sr}, \text{Ca})_{14}\text{Cu}_{24}\text{O}_{41}$, te kvazi-2D organski vodič $\alpha\text{-(BEDT-TTF)}_2\text{I}_3$ koji pokazuje tzv. uređenje naboja s horizontalnim prugama. Uzorci su karakterizirani optičkim metodama i mjerenjem električnog transporta: anizotropija istosmjerne vodljivosti, niskofrekventni dielektrični odziv te terahertzna i infracrvena spektroskopija. U fazi orbitalnog uređenja BaVS_3 nađeni su dokazi kolektivnih pobuđenja ispod faznog prijelaza iz metala u izolator sličnog Peierlsovom. Nadalje, u $(\text{La}, \text{Y})_y(\text{Sr}, \text{Ca})_{14-y}\text{Cu}_{24}\text{O}_{41}$ je na $y \approx 2$ pokazano postupno prebacivanje transporta naboja s jednodimenzionalnog preskakivanja duž lanaca na kvazi-dvodimenzionalno vođenje u ravninama ljestvica. Rezultati ukazuju na zanimljivu međuzavisnost stvaranja dugodosežnog uređenja u dva sustava: anti-feromagnetskog dimerskog uređenja na lancima, te vala gustoće naboja na ljestvicama. Na kraju, ispitan je i elektrodinamički odziv $\alpha\text{-(BEDT-TTF)}_2\text{I}_3$. U optičkim spektrima pronalazimo dokaze naglog dugodosežnog uređenja naboja. Kao najkonzistentniju sliku te uređene faze predlažemo zanimljiv pogled horizontalnih pruga kao kooperativnog vala gustoće veza i naboja feroelektrične prirode umjesto potpuno lokaliziranog Wignerovog kristala. (212 stranice, 112 slika, 1 tablica, 248 literaturnih navoda, jezik izvornika: engleski)

Rad je pohranjen u Središnjoj knjižnici za fiziku, PMF - Fizički odsjek, Bijenička c. 32, Zagreb.

Ključne riječi: uređenje naboja / val gustoće naboja / orbitalno uređenje / fazni prijelaz / jake korelacije / vodljivost / anizotropija / dielektrični odziv / infracrvena spektroskopija

Mentor: Dr. sc. Silvia Tomić, znanstveni savjetnik, Institut za fiziku

Ocjenjivači: Dr. sc. Amir Hamzić, red. prof., PMF
Dr. sc. Silvia Tomić, zn. savj., IF
Dr. sc. Slaven Barišić, red. prof., PMF
Prof. Martin Dressel, 1. Physikalisches Institut, Universität Stuttgart, Njemačka
Prof. László Forró, Ecole Polytechnique Fédérale de Lausanne, Švicarska

Rad prihvaćen 14. lipnja 2011.

BASIC DOCUMENTATION CARD

University of Zagreb
Faculty of Science
Department of Physics

Doctoral Thesis

CHARGE ORDERINGS IN STRONGLY CORRELATED SYSTEMS

TOMISLAV IVEK

Institute of Physics, Zagreb

At the focus of this thesis are systems with strong correlations and reduced dimensionality: the inorganic quasi-1D chain compound BaVS_3 with itinerant and localized charges, spin chain and ladder composite $(\text{La}, \text{Y}, \text{Sr}, \text{Ca})_{14}\text{Cu}_{24}\text{O}_{41}$, and the quasi-2D organic conductor $\alpha\text{-(BEDT-TTF)}_2\text{I}_3$ with the so-called horizontal stripe charge order. Samples have been characterized by transport and optical methods used in solid state and low-temperature physics: anisotropy of dc conductivity, nonlinear conductivity and low-frequency dielectric response as well as terahertz and infrared spectroscopy. In the orbitally ordered phase of BaVS_3 evidence is presented of collective excitations below the Peierls-like metal-insulator transition. Further, in $(\text{La}, \text{Y})_y(\text{Sr}, \text{Ca})_{14-y}\text{Cu}_{24}\text{O}_{41}$ a crossover in charge transport is demonstrated at $y \approx 2$ from a one-dimensional hopping along the chain subsystem to a quasi-two-dimensional charge conduction in the ladder planes. It is found that an interdependent formation of long-range orders takes place in the two subsystems: an antiferromagnetic dimer order in chains and a charge-density wave in ladders. Lastly, electrodynamic response in the organic conductor $\alpha\text{-(BEDT-TTF)}_2\text{I}_3$ has been investigated. Optical spectra show a sudden appearance of long-range charge order below the phase transition. Rather than a fully localized Wigner crystal, our results favor an interesting interpretation of horizontal stripes as a cooperative bond-charge density wave with a ferroelectric-like nature.

(212 pages, 112 figures, 1 table, 248 references)

Thesis deposited in The Central Library for Physics, Faculty of Science - Department of Physics, Bijenička c. 32, Zagreb.

Keywords: charge ordering / charge-density wave / orbital ordering / phase transition / strong correlations / conductivity / anisotropy / dielectric response / infrared spectroscopy

Supervisor: Silvia Tomić, Senior Scientist, Institute of Physics

Reviewers: Prof. Amir Hamzić, PMF
Dr. Silvia Tomić, IF
Prof. Slaven Barišić, PMF
Prof. Martin Dressel, 1. Physikalisches Institut, Universität Stuttgart, Germany
Prof. László Forró, Ecole Polytechnique Fédérale de Lausanne, Switzerland

Thesis accepted on June 14th 2011.

This dissertation has been conducted at the *Group for Dielectric Spectroscopy and Magnetotransport Properties* at the Institut za fiziku, Zagrebu, under the supervision of Silvia Tomić, as part of the Doctoral studies at the Department of Physics, Faculty of Science in Zagreb.

I am most grateful to my supervisor and mentor dr. Silvia Tomić, for showing me into this exciting field of research, her positive outlook and all the patience through the years. I also thank dr. Tomislav Vuletić, dr. Bojana Hamzić and dr. Sanja Dolanski-Babić for introducing me to the laboratories, our long talks and laughs.

I particularly appreciate the opportunity to broaden my perspectives during the visit to the group of prof. M. Dressel at the Universität Stuttgart. I extend my gratitude and thanks to dr. Martin Dressel and his group, especially Conrad Clauss, dr. Boris Gorshunov and dr. Natalia Drichko for our productive collaboration and making me feel welcome. Here I also thank prof. László Forró and dr. Ana Akrap for the opportunity to work and publish together.

For the understanding and assistance in the final preparation stages of my thesis I use this opportunity to thank prof. Amir Hamzić and prof. Slaven Barišić.

During the several years' worth of experimental research there have been many instances, too difficult to number, where advice, criticism or just a helping hand has proven to be invaluable. I am indebted to all my colleagues and personell at the Institut za fiziku in Zagreb for their support.

To my friends at work and off work: Damir, Juraj, Zlatko, Nino, Mile, Ivan, Ivan again, J, Nikica, Matija, Karla, Marko, Grgo, Vrc, Sanja, Zif, Taja, Daniela, Filip - thank you for accepting me with all my quirks. Keep hitting me on the head when you see I need it.

Most importantly, I thank my family: granny Katarina, parents Mira and Zlatko, brother Ivan, sister Ana. I love you.

Contents

1	Introduction	1
1.1	Orbital ordering in the quasi-1D chain compound BaVS_3	6
1.1.1	Properties and phase transitions	6
1.1.2	Band structure	11
1.1.3	Open questions	14
1.2	From underdoped to fully doped cuprate composites $(\text{La,Y,Sr,Ca})_{14}\text{Cu}_{24}\text{O}_{41}$	16
1.2.1	Structure and electronic properties	17
1.2.2	Phase diagrams with respect to hole doping	22
1.2.3	Open questions	27
1.3	Charge ordering in the quasi-2D organic conductor $\alpha\text{-(BEDT-TTF)}_2\text{I}_3$	29
1.3.1	2D $(\text{BEDT-TTF})_2X$ charge-transfer salts	29
1.3.2	Crystallographic structure of $\alpha\text{-(BEDT-TTF)}_2\text{I}_3$	35
1.3.3	Electronic properties and charge ordering in $\alpha\text{-(BEDT-TTF)}_2\text{I}_3$	35
1.3.4	Open questions	42
2	Overview of theory	43
2.1	Standard charge-density waves: The Peierls transition	43
2.1.1	Charge-density wave sliding motion	47
2.1.2	Phason response	48
2.2	Strongly interacting electrons in 1D	51
2.2.1	Extended Hubbard model in 1D	52
2.2.2	Cuprates - the strong coupling limit	55
2.2.3	More than one orbital per site	59
2.3	Charge order on a 2D anisotropic triangular lattice	62
2.3.1	Identifying the charge pattern of ground state	63
2.3.2	Excitations in a charge-ordered phase with horizontal stripes	67
3	Experimental techniques	71
3.1	DC conductivity	71
3.2	Dielectric spectroscopy	72
3.3	THz spectroscopy	75
3.4	Infrared spectroscopy	77
3.5	Sample preparation and protocols	78
3.5.1	BaVS_3	79
3.5.2	$(\text{La,Y,Sr,Ca})_{14}\text{Cu}_{24}\text{O}_{41}$	80

3.5.3	α -(BEDT-TTF) ₂ I ₃	81
4	Evidence of orbital ordering in BaVS₃	83
4.1	Transport and dielectric response	83
4.2	Discussion	88
5	(La,Y,Sr,Ca)₁₄Cu₂₄O₄₁ - crossover of electrical transport from chains to ladders	93
5.1	Anisotropy of dc transport	93
5.2	Frequency-dependent conductivity and dielectric function	99
5.3	Discussion	104
6	Collective excitations in the charge-ordered α-(BEDT-TTF)₂I₃	107
6.1	Optics	107
6.2	DC transport	113
6.3	Dielectric response	115
6.4	Discussion	120
7	Concluding remarks	129
8	Sažetak	133
8.1	Dokazi orbitalnog uređenja u BaVS ₃	134
8.1.1	Uvod	134
8.1.2	Eksperimentalne metode i uzorci	136
8.1.3	Rezultati i diskusija	137
8.2	Prebacivanje mehanizma transporta s kupratnih lanaca na ljestvice u (La,Y,Sr,Ca) ₁₄ Cu ₂₄ O ₄₁	142
8.2.1	Eksperimentalne metode i uzorci	144
8.2.2	Rezultati i analiza	145
8.2.3	Diskusija	155
8.3	Uređenje naboja u α -(BEDT-TTF) ₂ I ₃	157
8.3.1	Uvod	157
8.3.2	Eksperimentalne metode i uzorci	160
8.3.3	Rezultati i analiza	161
8.3.4	Diskusija	175
8.4	Zaključak	179
A	Dielectric spectroscopy: contact verification	181
A.1	BaVS ₃	184
A.2	α -(BEDT-TTF) ₂ I ₃	190
A.3	(La,Y,Sr,Ca) ₁₄ Cu ₂₄ O ₄₁	193

Chapter 1

Introduction

Historically, simple metals such as copper have been among the most ubiquitously used materials. Their properties are generally accounted for by a simple physical picture where electrons wander freely through the crystal lattice of the metal, one electron effectively independent from another. There are materials however where one cannot ignore the electrostatic interaction between electrons and the quantum-statistical effects of exchange on their motion. The study of these *strongly-correlated electron systems* has occupied the center of attention in modern physics of condensed matter: in the presence of strong interactions electrons cannot just be thought of as particles embedded in a static mean field created by other electrons. Hence, such systems urge theoretical advances in the difficult problem of electron correlations. At the same time, they are also an involved experimental challenge due to the requirement of extreme conditions: low temperatures, high pressures and magnetic fields are often needed to induce novel electronic states.

Because of the often delicate relationship between the electronic and structural degrees of freedom, it is possible to alter their electronic properties by changes in their chemistry, e.g., through partial ionic substitutions. In this way one can prepare model experimental systems for examination of various broken-symmetry phases, testing the fundamental properties of Fermi, Luttinger liquids etc., or even design system with novel electronic phases as their ground states. Among the inorganic materials strong correlations notably appear in systems with open d and f electron shells. These orbitals are spatially confined close to the atomic nuclei. Hence, the bands they form are very narrow which makes the Coulomb repulsion between electrons an important influence on their motion. Various broken-symmetry ground states emerge in such systems thanks to the interactions between the spin, charge, orbital and lattice degrees of freedom. Prominent

examples of such materials include cuprates BSSCO, YBCO as well as various layered iron pnictides which feature the high-temperature superconductivity (SC), or the oxide V_2O_3 with long-range patterns of orbital occupancies, the so-called orbital ordering.

Another class of materials which also exhibits strong correlation effects is the growing list of molecular solids, i.e., crystallized salts of organic molecules with conductive bands formed by highly anisotropic molecular orbitals. Why consider molecular salts instead of materials composed of only one molecular species? Single molecules have closed shells. Therefore, materials crystallized of a single species of molecules are usually band insulators. Combining different kinds of molecules and ions turns out to be a successful strategy to make their crystallized salts conductive due to the effects of charge transfer from one ion species into another's electron bands. Early molecular conductors consisted of 1:1 compositions between two kinds of molecules A and B , the so-called " AB compounds". Later 2:1 systems, the " A_2B compounds", were found to realize conductivity more easily, and on top of that provide a rich selection of novel physical phenomena. Due to their low Fermi energy, small carrier concentrations and high structural and electronic anisotropy, many surprising physical effects have first been observed, or observed more clearly, in crystals of organic salts, which has ensured them a place among model systems for physics of reduced dimensions: Peierls transitions in TMTTF, TMTSF or TTF-TCNQ salts, charge- and spin-density waves (CDW, SDW), Luttinger liquid ground states, superconductivity, ferroelectricity, Mott insulator phase, and recently charge order (CO) in one- and two-dimensional organic solids.

Exotic ordered phases, insulating or metallic, are often found near superconductivity in the respective phase diagrams. [1, 2, 3] It cannot be denied that a great number of studies on exotic insulating phases (if not most) have been offshoots of the search for the much-coveted room-temperature superconductor. A standard assumption is that they compete with superconductivity for the same phase space; other insights indicate that broken-symmetry ordered phases might play an important role in stabilizing superconductivity. Be as it may, our understanding of their relationships is mostly still lacking, which brings us to **the prime drive behind the experimental work presented in this thesis: to probe some of the exotic insulating broken-symmetry phases by means of their response to electric fields.** This experimental survey tackles three strongly-correlated electron systems, all with reduced dimensionality and quite different insulating ground states:

- the quasi-one-dimensional (1D) perovskite sulfide $BaVS_3$,
- composite quasi-1D cuprates $(La, Y)_y(Sr, Ca)_{14-y}Cu_{24}O_{41}$ ($0 \leq y \leq 5.2$), and

-
- the quasi-two-dimensional (2D) organic α -(BEDT-TTF)₂I₃.

Starting with the lowest dimensionality, BaVS₃ is a quasi-1D system which presents a whole set of interwoven and correlation-driven phenomena. The physics of its electrons is governed by their distribution between one delocalized, wide vanadium band with a strong one-dimensional character, and two narrow bands which represent practically localized states. [4, 5] The exact electron distribution between them seems to be highly sensitive and dependent on the lattice coupling which allows for a whole series of phase transitions as BaVS₃ is cooled: a structural Jahn-Teller transition, then a metal-insulator phase transition at 69 K accompanied by tetramerization of vanadium chains, and a magnetic transition to an incommensurate antiferromagnetic-like ground state at 30 K. [6, 7, 8, 9] The nature of the metal-to-insulator and magnetic phase transitions is still open for discussion, however some of their unusual structural characteristics point to the development of an orbital ordering, i.e., a long-range pattern of orbital occupancies. [10, 9] The here-presented dielectric spectroscopy study hopes to elucidate this issue by presenting evidence of low-lying collective excitations in the orbitally-ordered phase of BaVS₃.

Exhaustive literature on the second system, the composite (La,Y,Sr,Ca)₁₄Cu₂₄O₄₁ built of layers of cuprate chains and ladders, was originally incited by the discovery of superconductivity in the ladder subsystem of Sr_{0.4}Ca_{13.6}Cu₂₄O₄₁ as the first superconducting copper oxide with a non-square lattice. [11] The parent material Sr₁₄Cu₂₄O₄₁ is an insulator best-known for its charge-density wave in the ladders. Isovalent substitution of Sr with Ca atoms suppresses the charge-density wave phase [12, 13] and at high enough Ca content introduces the abovementioned superconductivity as the ground state. The concentration of self-doped holes and their relative number on ladders and chains fully determines the electronic ground states and the dynamics of both spin and charge – and again we encounter the concept of distribution of charge carriers between different subsystems. In the fully-doped materials Sr_{14-x}Ca_xCu₂₄O₄₁ there is a total of $n_h = 6$ holes per formula unit, out of which at room temperature 1 is situated on ladders and 5 on the chains. [14] There ladders are the dominant two-dimensional transport channel of insulating characteristics which eventually approaches a charge-density wave transition due to electron-electron interactions. [16, 17]. Holes on chains have a negligible contribution to transport, namely they are localized in a spin-dimer- and charge order. [18, 19, 20, 21] On the other hand, the far-underdoped materials (La,Y)_y-(Sr,Ca)_{14-y}Cu₂₄O₄₁, $y \leq 3$, ($n_h = 6 - y$) display no sign of a charge-density wave in the ladders, and seem to have all the remaining holes present on chains where the charge

order is replaced by a disordered insulating phase. [22] Transport studies point to a crossover or perhaps a phase transition as the composition approaches full hole doping at $y = 0$ ($n_h = 6$). One of the goals of this thesis was to explore the low- y part of the phase diagram in $(\text{La,Y,Sr,Ca})_{14}\text{Cu}_{24}\text{O}_{41}$, among other things to learn at which point do the holes populate ladders and form their charge-density wave.

The third and final system under study is the organic conductor α -(BEDT-TTF) $_2$ I $_3$ where BEDT-TTF stands for a mouthful of bis(ethylenedithiolo)tetrathiofulvalene. It is a layered material of alternating anion (I $_3$) and donor (BEDT-TTF) planes in the crystal. The appreciable overlap between neighboring molecular orbitals results in a semimetallic character of BEDT-TTF planes at room temperature, with electron and hole pockets at the Fermi surface. [23] There is a (MI) metal-insulator transition at 136 K where conductivity drops drastically and a temperature-dependent charge and spin gap opens. [24] In the low-temperature phase the NMR and synchrotron x-ray diffraction measurements show the existence of a long-range charge ordering in the BEDT-TTF molecular planes. Interestingly, fluctuations of said charge order are noticed all the way up to room temperature. [25, 26, 27] Below the metal-insulator transition a rather large charge disproportionation appears at the four non-equivalent BEDT-TTF molecules per unit cell, approximately $A = 0.82(9)$, $A' = 0.29(9)$, $B = 0.73(9)$ and $C = 0.26(9)$. [25, 26, 27, 28, 29] At the beginning of this study the up-to-date literature did not clarify whether the charge order in α -(BEDT-TTF) $_2$ I $_3$ was a Wigner-type ordering with localized charges, or maybe more akin to a delocalized density-wave-like picture. As was the case of BaVS $_3$, there was no information or theoretical predictions on the electrodynamic observables related to low-lying excitations above the ground state. The work presented here will show the abrupt onset of charge disproportionation evident in infrared spectra, as well as point out some revealing similarities between the dielectric response of this two-dimensional charge order and standard one-dimensional charge-density waves.

In line with the main topic of this work, the employed experimental methods concentrate on the response of charges in the presence of an applied electric field, or in short measuring electrical conductivity in different regimes, of various samples along different crystal axes. The focus is mostly on low-frequency methods – the standard dc resistance measurements and low-frequency dielectric spectroscopy which together provide rich information about capacitive properties in the Hz – MHz range of frequencies. These results are complemented by measurements at higher frequencies using THz and infrared spectroscopy in the group of prof. M. Dressel at the University of Stuttgart,

Germany.

With a clear and concise presentation in mind, the text is divided in four parts. In this, the first chapter, an overview is offered on known physical properties of BaVS_3 , $(\text{La,Y,Sr,Ca})_{14}\text{Cu}_{24}\text{O}_{41}$ and $\alpha\text{-(BEDT-TTF)}_2\text{I}_3$. The second chapter goes through basic theoretical concepts regarding ground states and excitations in strongly correlated systems with reduced dimensionality. The third chapter introduces experimental methods and setups employed in probing the charge response, which covers spectroscopic methods in the optical, terahertz and radio range as well as dc transport. Finally, in the fourth part we discuss the experimental results and their ramifications.

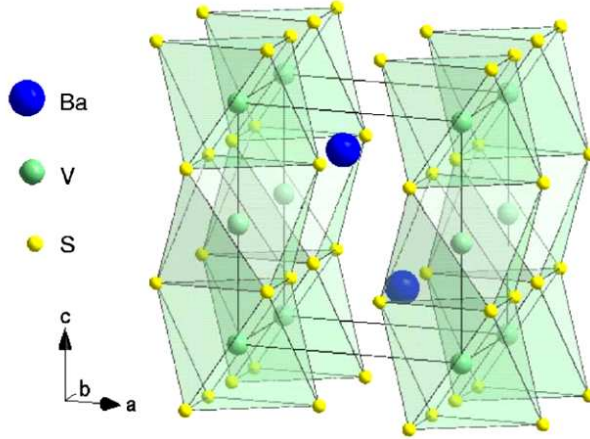


Figure 1.1 – Hexagonal perovskite structure of BaVS_3 .

1.1 Orbital ordering in the quasi-1D chain compound BaVS_3

BaVS_3 is a perovskite sulfide material first synthesized back in 1968, with the crystal structure deduced shortly after. [30, 6] It consists of parallel, linear chains of vanadium atoms encased in face-sharing sulfur octahedra which are separated by barium ions. The arrangement of atoms suggests a clear-cut quasi-1D system, but its physics is surprisingly rich and intricate – e.g., already a cursory look at the room temperature transport anisotropy ratio, $\sigma_c/\sigma_a = 3$, reveals a value which is atypically low for a one-dimensional system. The vanadium electrons are distributed among three overlapping bands and highly sensitive to the local ligand environment. This results in a series of phase transitions at ambient pressure with significant effect on the structure, transport and magnetic properties of BaVS_3 . The complex interplay between the lattice, orbital and spin degrees of freedom in BaVS_3 is still not completely understood.

1.1.1 Properties and phase transitions

At room temperature BaVS_3 crystallizes in a $P6_3/mmc$ hexagonal close-packed arrangement of linear chains along the c -axis, shown in Fig. 1.1, which consist of face-sharing VS_6 octahedra separated by Ba atoms. There are two formula units per cell. The VS_6 octahedra stacking along the c -axis give rise to strongly anisotropic V–V interatomic distances. In the direction of chains the V–V separation is only $\approx 2.8 \text{ \AA}$, quite close to the distance in pure metallic BCC vanadium. In the ab plane the neighboring vanadium atoms are further apart at 6.7 \AA . A simple stoichiometric consideration gives

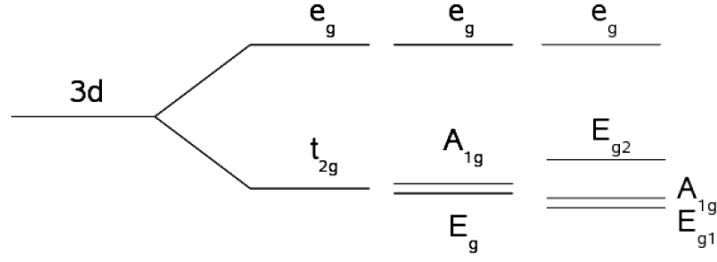


Figure 1.2 – Sequence of V3d orbital splitting, from left to right: loss of spherical symmetry, cubic symmetry crystal field separation, trigonal $A_{1g} - E_g$ splitting in the hexagonal phase, E_g splitting in the orthorhombic phase.

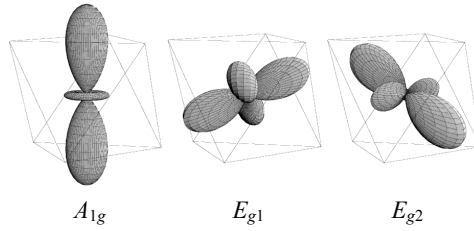


Figure 1.3 – The vanadium A_{1g} orbital (left) has a good direct overlap with the first neighbor. On the other hand, the E_g doublet (middle, right) points out of the chain from vanadium towards the sulfur atoms.

the nominal vanadium oxidation state of V^{4+} with a $3d^1$ configuration. The six sulfur atoms around each V-site act as an octahedral crystal field which lift the fivefold degeneracy of vanadium 3d atomic orbitals. The splitting of V $3d(t_{2g})$ orbitals is schematically shown in Fig. 1.2. [7] The V^{4+} $3d^1 - t_{2g}$ electron is shared between one broad, highly anisotropic quasi-1D d_{z^2} (A_{1g}) band and two quasi-degenerate isotropic narrow bands associated with the $e(t_{2g})$ (E_g) doublet (see Fig. 1.3). [4, 5] The d_{z^2} band is formed by direct overlap along the c -axis between vanadium d_{z^2} orbitals and is responsible for metallic properties near room temperature. On the other hand, the two narrow bands are formed via V-S-S-V bonds, describing what are essentially localized electrons.

Through cooling at ambient pressure BaVS₃ undergoes a sequence of three second-order phase transitions. The first transition, discovered shortly after first successful synthesis of the material, [6] is a Jahn-Teller type zig-zag deformation of the vanadium chains at $T_S = 240$ K. As confirmed by latter x-ray and neutron diffraction studies, [31, 4, 32, 33] crystal symmetry is reduced from hexagonal to orthorhombic with space group changing from $P6_3mmc$ to $Cmc2_1$. Charge transport remains metallic with only a slight change in slope of resistivity *vs.* temperature (see Fig. 1.4). [7] The reduction of crystal symmetry in the orthorhombic phase removes the degeneration between the two $e(t_{2g})$ orbitals. Magnetic susceptibility remains that of a Curie-Weiss paramagnet

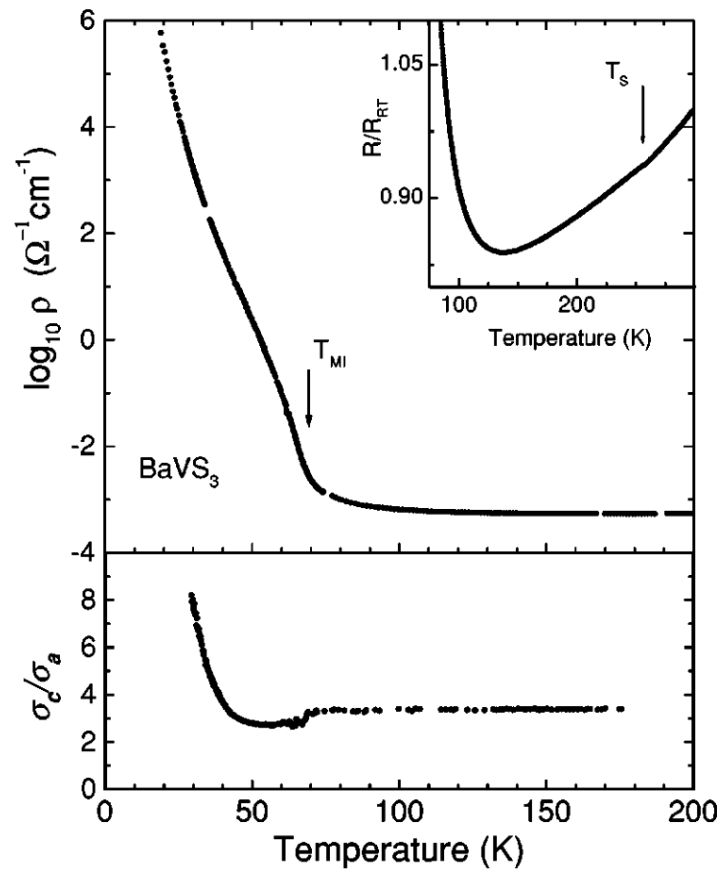


Figure 1.4 – Temperature dependence of the resistivity $\rho_c(T)$ and the conductivity anisotropy σ_c/σ_a in BaVS₃. The arrows indicate T_{S} and T_{MI} (see text). From Mihaly *et al.* [7]

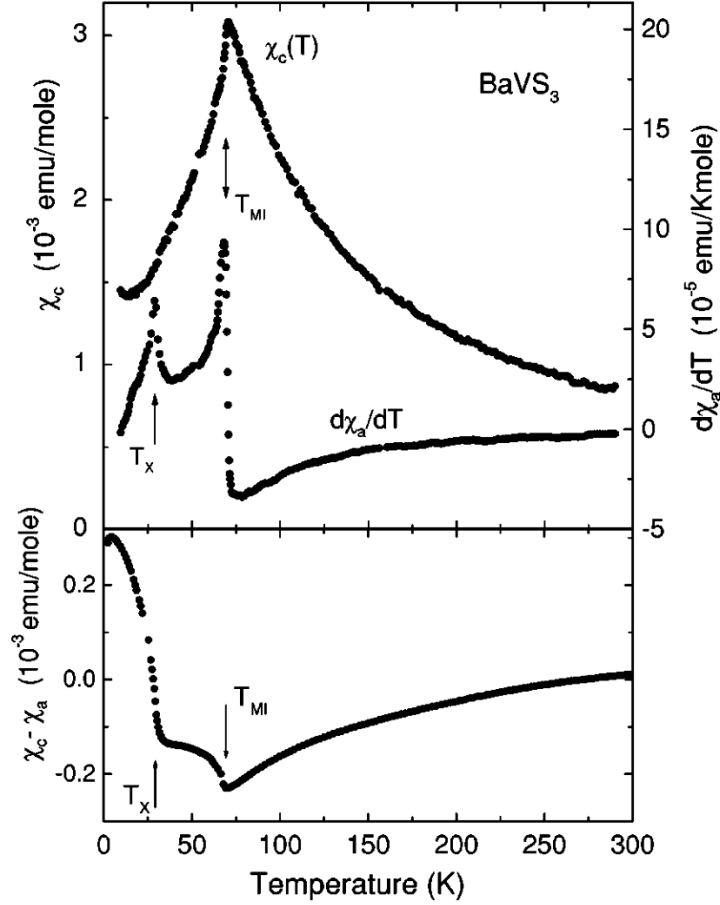


Figure 1.5 – Temperature dependence of the c -axis magnetic susceptibility χ_c , the derivative of the a -axis susceptibility $d\chi_a/dT$, and the susceptibility anisotropy, $\chi_c - \chi_a$. From Mihaly *et al.* [7]

through this structural transition (see Fig. 1.5).

Next, the system undergoes a metal-insulator transition at $T_{MI} \approx 69$ K: the resistivity increases steeply [4] due to the opening of charge gap of about 40 meV. [7, 34] A spin gap of 10–20 meV has been reported in the insulating phase by NMR/NQR and magnetic susceptibility measurements. [10, 35] The structure also changes to monoclinic symmetry and the space group is further reduced to Im . [36] Due to the deformation of sulfur octahedra the vanadium chains undergo a tetramerization, i.e., the unit cell is doubled in periodicity along the c -axis, which was originally interpreted as the only order parameter of the MI transition. Underlining the relevance of the structural transition, diffuse x-ray scattering experiments [8] clearly show a formation of a superstructure at the wave vector corresponding to $2k_F$ of the wide A_{1g} electron band as well as strong precursory fluctuations up to 170 K. Both observations by themselves are telltale signs of a Peierls-like 1D instability in an electron gas. However, also present are features

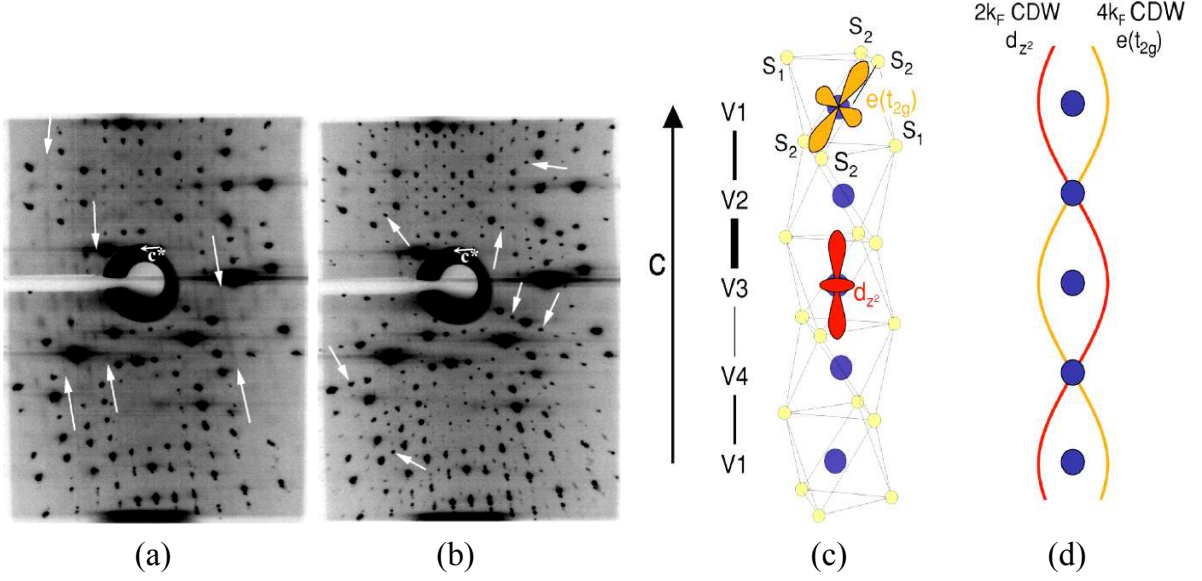


Figure 1.6 – (a) X-ray diffraction pattern of BaVS₃ at 80 K showing pretransitional diffuse lines perpendicular to the c^* and (b) 25 K satellites at the wave vector $2k_F = 0.5c^*$. From Fagot *et al.* [8] (c) A possible ordering of d_{z^2} and $e(t_{2g})$ orbitals along the V-S chain. (d) Two out-of-phase d_{z^2} and $e(t_{2g})$ CDWs explain the absence of the charge density modulation and suggests an orbital ordering. From Fagot *et al.* [9]

not expected of a Peierls CDW. Most surprisingly, vanadium K-edge resonant x-ray scattering demonstrated only a minuscule charge disproportionation on V-sites in the low-temperature phase, not larger than $0.01e$. [9] Further, a second harmonic is present in the superstructure with a clear $4k_F(A_{1g})$ diffraction maximum, without a corresponding precursor. Last, magnetic susceptibility does not follow the typical Pauli behavior of a 1D electron gas, yet around room temperature it corresponds to a Curie-Weiss law with the effective magnetic moment of approximately half a localized spin per vanadium site. These three unusual observations suggest that only half the vanadium d -electrons are delocalized and form the CDW as per standard Peierls picture, while the other half is localized and accounted for in the magnetic response. The apparent need for a secondary order parameter was addressed by a very intriguing interpretation involving the stabilization of two superimposed out-of-phase charge-density waves: a $2k_F$ CDW formed by A_{1g} electrons, and a $4k_F$ CDW of localized E_g electrons (see Fig. 1.6). [9] The resulting ground state, with its negligible charge disproportionation, can be thought of as an *orbital ordering*, i.e., a modulated occupancy of d_{z^2} and $e(t_{2g})$ electrons. This unusual arrangement is indeed supported by earlier low-temperature ^{51}V NMR measurements that found large and asymmetric electrical field gradients at V-sites. [10] Upon applying hydrostatic pressure to BaVS₃ an increase of the MI phase transition temper-

ature is expected due to the increase of orbital overlap which reduces the density of states at Fermi level. Contrary, as the pressure is increased the MI transition is linearly suppressed towards lower temperatures, the reason being a significant increase of inter-chain coupling which leads to imperfect nesting. [37,38,39] The phase transition is fully suppressed at the critical pressure of ≈ 2 GPa, at which BaVS₃ is an anisotropic metal at all temperatures.

The third phase transition [40] concerns the establishing of a magnetic structure below $T_\chi = 30$ K. Neutron diffraction experiments on powder samples infer an antiferromagnetic ordering with an incommensurate wave vector (0.226,0.226,0) indexed in the hexagonal lattice. [41] As shown by Fig. 1.5 it seems the system starts to order magnetically at 30 K which is seen as a peak in the temperature derivative of a -axis susceptibility $d\chi_a/dT$, and as a break in the anisotropy $\chi_c - \chi_a$ at $T_\chi = 30$ K. [7] ⁵¹V NQR measurements found a huge asymmetric electrical-field gradient at T_χ which suggests an orbital ordering in the spin-ordered state. [10]

1.1.2 Band structure

The key to physics of BaVS₃ lies in understanding the distribution of vanadium electrons between the wide A_{1g} and narrow E_g orbitals. Theoretical development has accompanied hand-in-hand the growing experimental knowledge on BaVS₃. An early explanation of the MI transition by Massenet *et al.* [42] suggested a gradual transfer of electrons from localized magnetic states to a non-magnetic band separated by a small gap which would take BaVS₃ from a paramagnetic metal to a diamagnetic insulator. This picture was soon proven too simplistic by the discovery of magnetic ordering transition at T_χ . What followed were *ab initio* local-density approximation (LDA) calculations by Mattheiss which pointed at two different types of electron bands crossing the Fermi level: two narrow E_g bands, and a A_{1g} -like band along the c^* direction. [5] However, LDA tended to predict an almost completely filled A_{1g} band. Subsequent work by Whangbo *et al.* avoided the drawbacks of LDA by using both tight-binding calculations as well as *ab-initio* density functional theory with generalized gradient approximation (DFT GGA). [43] They take into account the short intrachain S-S orbital overlap to explain the rather isotropic bulk conductivity of BaVS₃. Independent DFT calculations with the Hubbard term U (LDA+U) predicted a charge gap of 150 meV below the MI transition. [44] Both LDA calculations revealed a magnetic anisotropy with intrachain ferromagnetic ($J_c = 10$ – 20 meV) and interchain antiferromagnetic coupling ($J_{ab} \sim 1$ meV). [43,44]

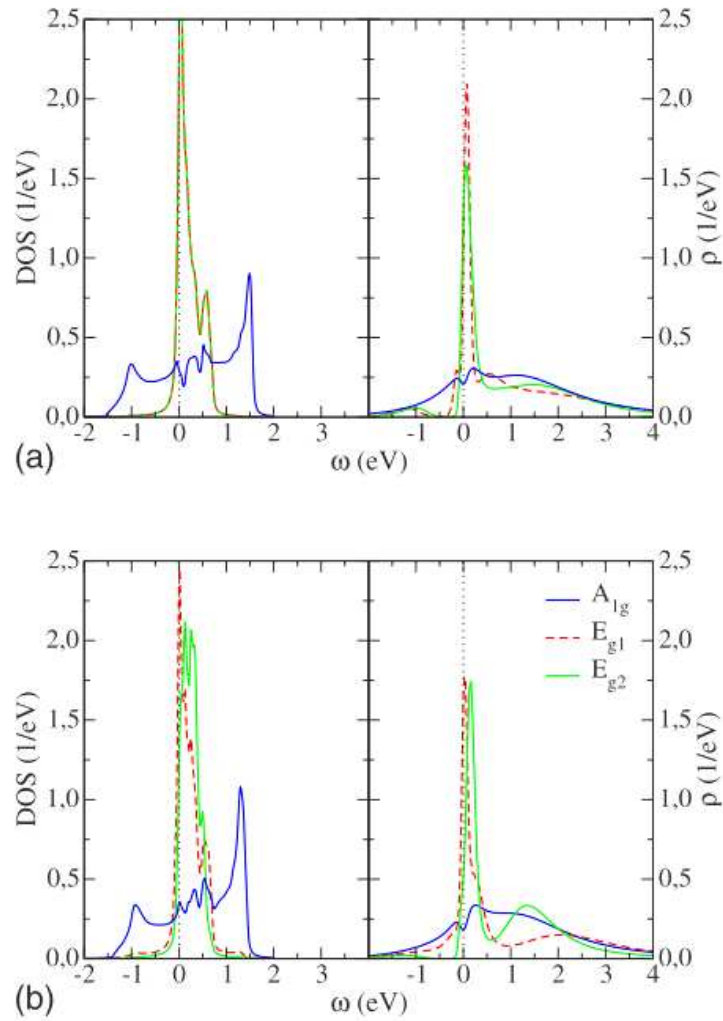


Figure 1.7 – t_{2g} manifold of the (a) hexagonal metallic phase and (b) orthorhombic metallic phase. LDA DOS is shown on the left and the DMFT spectral functions on the right side of each figure (see text). From Lechermann *et al.* [45]

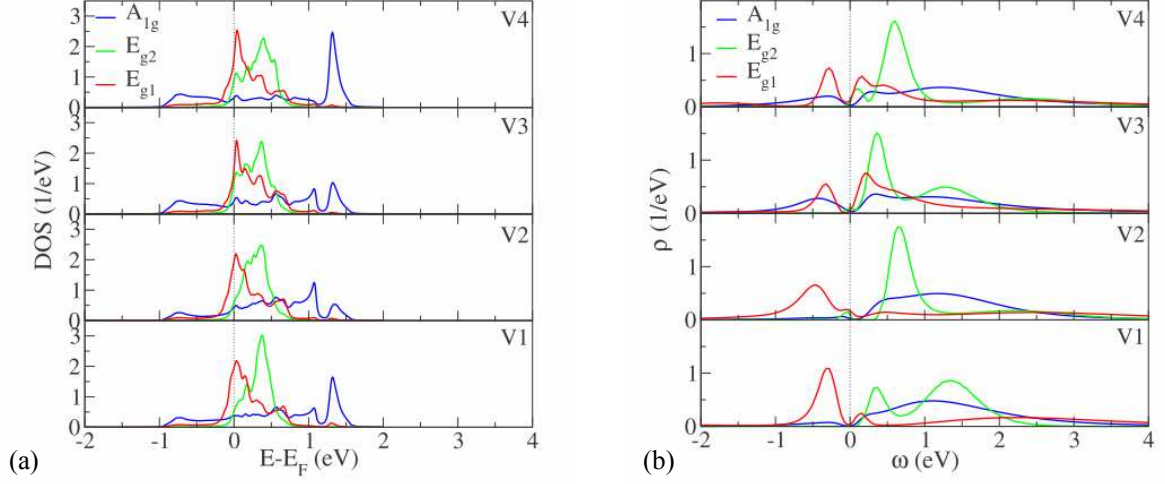


Figure 1.8 – t_{2g} manifold in the monoclinic insulating phase: (a) LDA DOS and (b) DMFT spectral functions (see text). From Lechermann *et al.* [45]

Calculations based on dynamical mean-field theory (DMFT) were needed to show that charge correlation and exchange effects can bring about an equal orbital occupancy in both the wide A_{1g} band and E_g bands. [46] At room temperature the equivalent E_{g1} and E_{g2} orbitals each carry 25% of electrons. Transition into the orthorhombic metal phase at T_S breaks the symmetry between the two orbitals. There the E_{g1} states hybridize with A_{1g} which increases the E_{g1} filling to almost 0.5. The E_{g2} band remains almost empty: [45] namely, the DMFT shifts its maximum in density of states by about 70 meV above the E_{g1} 's (see Fig. 1.7). Entering the monoclinic paramagnetic insulator phase at T_{MI} tetramerizes the V-sites along the chains. This is clearly seen by their distinct DMFT spectral functions (Fig. 1.8 which predict that V1 and V2 sites on one hand, V3 and V4 on the other, have similar orbital occupancies. In such an orbital ordering two first-neighbor sites with preferential E_{g1} occupancy would form a singlet along the V chain, [47] which could in principle facilitate the magnetic phase transition at T_X . However, this exact orbital ordering is at odds with neutron inelastic scattering which report an antiferromagnetic order in the ab plane, and it also does not match the ordering suggested by the resonant x-ray diffraction measurements, as shown by Fig. 1.6(d). [9] Also of note are the finite-size cluster calculations by Tanaka *et al.* based on a 1D two-band Hubbard model. [48] He proposes that the MI transition is governed by strong electron-lattice coupling where the monoclinic lattice distortion of the insulating phase induces a large periodic disproportionation in the two modeled bands. An orbital density wave as observed by resonant diffraction measurements [9] would be the primary order parameter, with a small accompanying component of CDW.

As complicated scenarios for the MI transition arise, it is obviously important to have a clear experimental picture of the band structure. Angle-resolved photoemission (ARPES) measurements on BaVS₃ have been performed by Mitrovic *et al.* at both sides of the metal-insulator transition, between T_χ and T_S . [49] The employed photon energy of 50 eV targets the photoionization cross-section of vanadium. As reported by authors, essentially the same intensity map is obtained in the whole 40 – 150 K temperature range (see Fig. 1.9), save for the usual temperature broadening and the leading edge shift close to Fermi level. In the low-energy part of the spectrum, below 1 eV, an approximately 5 eV wide quasi-1D band is detected and ascribed to the A_{1g} electrons, as well as a seemingly flat band just under the Fermi level associated with the E_g electrons. In the metallic phase the spectra are pseudogapped without an obvious Fermi-level crossing for any of the bands. The lack of a clear Fermi edge in the metallic phase is interpreted as a consequence of significant coupling of quasiparticles to collective excitations which then diminishes spectral weight from the quasiparticle peak in BaVS₃. [49, 50] The remaining reduced spectral weight near Fermi level seems to shift significantly below 90 K indicating an opening of the charge gap of about 60–70 meV. Even though the exact ratio of A_{1g} and E_g electrons could not be determined, the ARPES data point toward their concentrations both being significant and close in number, $n(A_{1g}) \approx n(E)$. [47] Interestingly, based on ARPES data it appears that the A_{1g} band by itself does not satisfy the nesting condition and therefore cannot drive the Peierls-like density-wave transition on its own. Rather, the charge gap opens over the whole Fermi surface and involves the wide as well as the narrow electron bands. This scenario cannot be fully reconciled with the x-ray diffraction experiments, however it is obvious that a complete description of the MI transition must include both bands.

1.1.3 Open questions

The two metallic phases of BaVS₃, a non-standard quasi-1D system with three vanadium orbitals crossing the Fermi level, seem to be well understood. However, the exact mechanism which brings about an almost equal occupancies of A_{1g} and E_{g1} electrons is still open for discussion. In the low-temperature paramagnetic insulating phase a superstructure is observed with the $2k_F$ wave vector corresponding to a quarter-filled A_{1g} band, [8] while the DMFT calculations disagree and favor this band's depletion. [45] Filling of the wide and narrow vanadium bands is inextricably linked with the question of orbital ordering which accompanies the Peierls-like density wave transition. At the beginning of this work the orbital ordering was only invoked as an indirect ex-

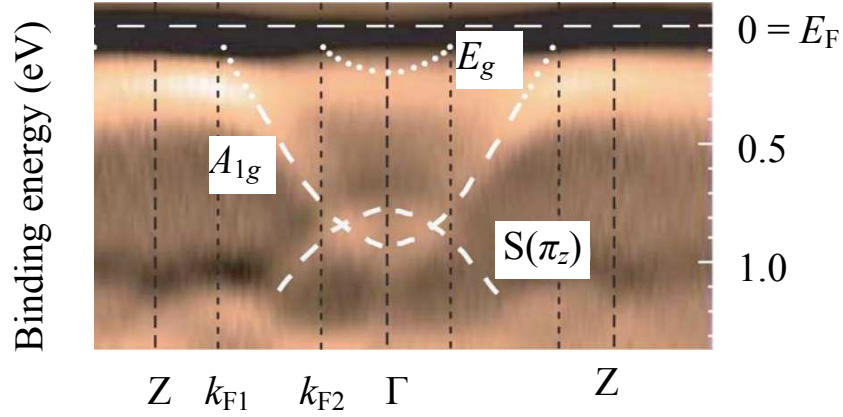


Figure 1.9 – Detail from the ARPES intensity map of BaVS₃ at 150 K with momenta parallel to vanadium chains. k_{F1} and k_{F2} are Fermi wave vectors associated respectively with the wide A_{1g} and narrow E_g bands. After Mitrovic *et al.* [49]

planation for the observed effects rather than being demonstrated by a discriminatory experiment. Also, the antiferromagnetic ground state below T_χ was still to be fully understood. Neither theory nor experiment have addressed the properties of low-energy collective excitations in the orbitally ordered phase. Hoping to learn more about the nature of this non-standard quasi-1D system, we thought it worthwhile to explore the dielectric response in BaVS₃.

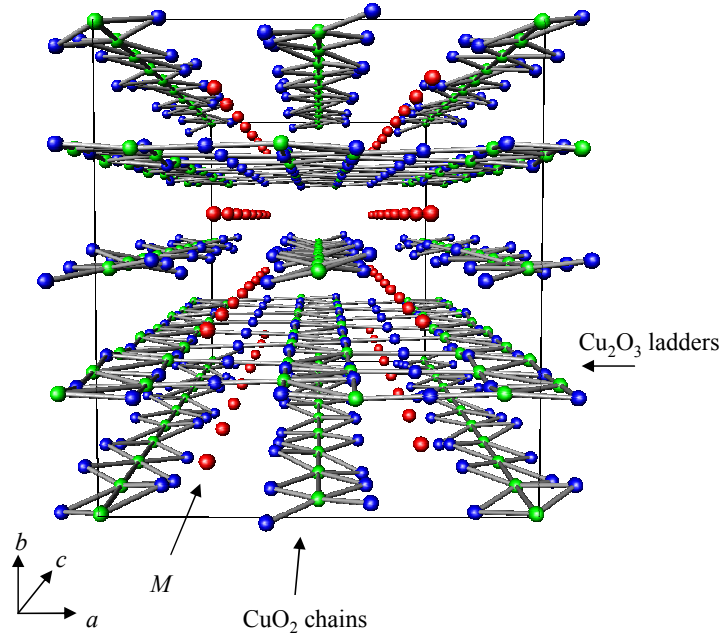


Figure 1.10 – The $(\text{La}, \text{Y}, \text{Sr}, \text{Ca})_{14}\text{Cu}_{24}\text{O}_{41}$ approximate super-structure cell consisting of four formula units, viewed along the c -axis. The CuO_2 chain layers, strings of $M = \text{La}, \text{Y}, \text{Sr}, \text{Ca}$ atoms, and Cu_2O_3 ladder layers are placed in the crystallographic ac plane aligned along the c -direction and stack in an alternating manner in the b -direction. The composition of $\text{La}, \text{Y}, \text{Sr}, \text{Ca}$ strings dictates the superstructural cell parameter in b -direction and the degree of intrinsic disorder (see text).

1.2 From underdoped to fully doped cuprate composites $(\text{La}, \text{Y}, \text{Sr}, \text{Ca})_{14}\text{Cu}_{24}\text{O}_{41}$

Soon after the historical discovery of high- T_c superconductivity in perovskite-like BaLaCuO cuprates [51] the interest spurred synthesis of many a novel structure, among them also the composite quasi-1D cuprates of the general formula $(\text{La}, \text{Y}, \text{Sr}, \text{Ca})_{14}\text{Cu}_{24}\text{O}_{41}$. This particular family consists of alternating layers of cuprate chains and two-legged ladders, each with a different arrangement of spin and charge. The first successful synthesis of single crystals was independently announced in 1988 by Siegrist *et al.* and McCarron *et al.* [52, 53] This by itself would not be as noticed without theoretical work by Dagotto *et al.* [54] who proposed a possible mechanism of superconducting pairing in the planes of doped two-legged ladders. Other theoretical investigations of doped even-legged ladders predicted their ground state would be a superconductivity similar to the two-dimensional high- T_c cuprate planes, or, alternatively, a charge-density wave phase. [55, 56] Experiments on a simpler material built exclusively of cuprate ladders, the SrCu_2O_3 , failed to detect a collective ground state. [57]

The next family of systems to be thoroughly investigated were the $(\text{La}, \text{Y}, \text{Sr}, \text{Ca})_{14}\text{Cu}_{24}\text{O}_{41}$ composite materials: indeed a superconducting phase has been identified in $\text{Sr}_{0.4}\text{Ca}_{13.6}\text{Cu}_{24}\text{O}_{41}$ under pressure, [11] propelling the whole family as a very inviting subject for study. The structure of these materials comprises two weakly-coupled incommensurate subsystems, the alternating planes of CuO_2 chains and Cu_2O_3 two-legged ladders. Layers of (Sr, Ca, La, Y) atoms between them are coordinated to the ladders. [52, 53] As a contrast to the extrinsically-doped planar superconducting cuprates, this composite system is self-doped in the sense that the ladders contain holes transferred from chains. The appearance of collective ground states in ladders and chains is inextricably linked with the distribution of holes between the two subsystems. Fully doped $\text{Sr}_{14-x}\text{Ca}_x\text{Cu}_{24}\text{O}_{41}$ variants show an interesting ladder phase diagram with a superconducting ground state on one end, $10 \leq x \leq 13.6$, and a charge-density wave on the other, $0 \leq x \leq 9$. [11, 12, 16, 2] Concomitantly, the subsystem of chains features a charge ordering with holes which facilitate an antiferromagnetic dimer order. [19, 21] Holes can be removed from the system by a substituting (Sr, Ca) atoms with (La, Y) elements, each bringing in an extra electron which makes the material underdoped. On the far-underdoped side the remaining few holes of $\text{La}_3\text{Sr}_3\text{Ca}_8\text{Cu}_{24}\text{O}_{41}$ and $\text{La}_{5.2}\text{Ca}_{8.8}\text{Cu}_{24}\text{O}_{41}$ materials seem to reside exclusively in the chain subsystem as a sort of “charged spinless defects”, Zhang-Rice singlets, in the chains of ferromagnetically coupled spins, with the charge-density wave phase completely absent in the ladders. [22, 58].

1.2.1 Structure and electronic properties

Fig. 1.10 shows the structure of the composite materials $(\text{La}, \text{Y}, \text{Sr}, \text{Ca})_{14}\text{Cu}_{24}\text{O}_{41}$ which consists of two distinct substructures: CuO_2 chains and Cu_2O_3 two-leg ladders. [52, 53] Chains may be regarded as strings of edge-sharing CuO_4 squares. Legs of the two-leg ladders are zig-zag chains composed of edge-sharing CuO_4 squares rotated by 45° with respect to the squares in the CuO_2 chains; the zig-zag chains have mirror image symmetry and touch at the corners of CuO_4 squares, which represents the ladder legs. Neighboring ladders are offset by $c_L/2$. Fig. 1.11 clarifies the arrangement of chain and ladder layers. [53] Strings of M atoms ($M = \text{La}, \text{Y}, \text{Sr}, \text{Ca}$) are intercalated between these layers. Strictly speaking, these atoms are coordinated to the ladder layer and enter in the void opened between the zig-zag ladder legs. Thus, atomic M strings and the ladder layer constitute the ladder subsystem ($M_2\text{Cu}_2\text{O}_3$), while CuO_2 chains arranged in a parallel layer form the chain subsystem (CuO_2). Both of these two sublattices have orthorhombic symmetry. In the case of parent $\text{Sr}_{14}\text{Cu}_{24}\text{O}_{41}$, the

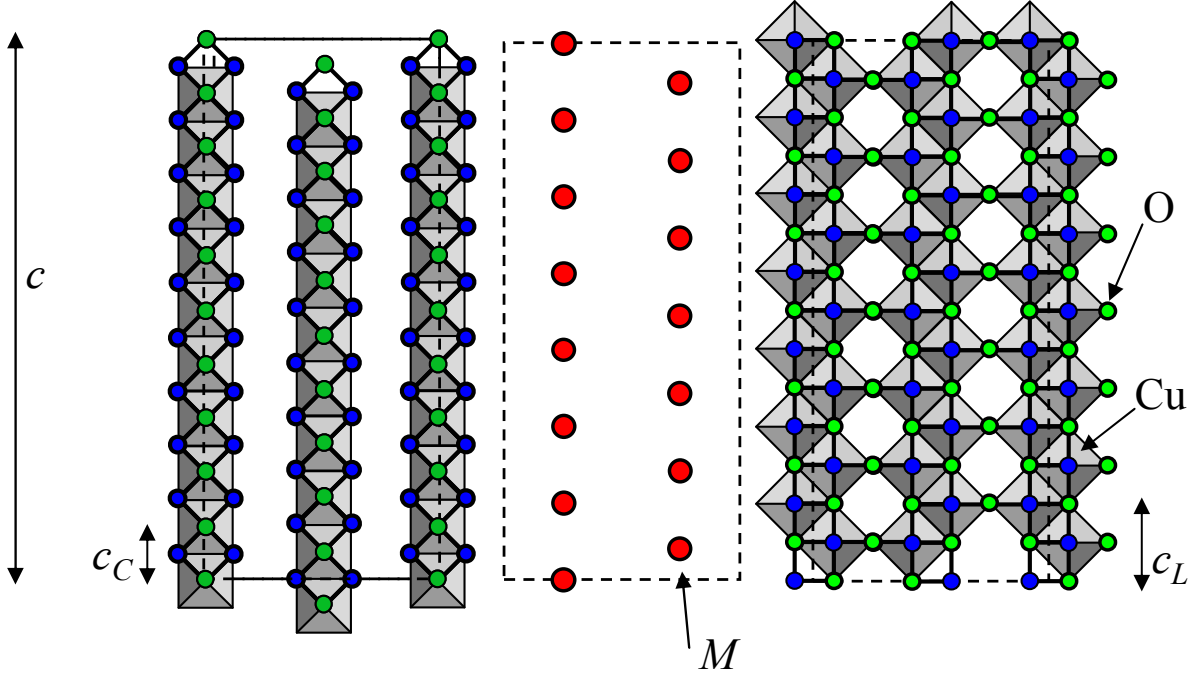


Figure 1.11 – CuO_2 chain layer (left), layer of strings of $M = \text{La}, \text{Y}, \text{Sr}, \text{Ca}$ atoms (middle) and Cu_2O_3 ladder layer (right). The periodicity of the chains and the ladders $\alpha = c_C/c_L = 1/\sqrt{2}$ is not commensurate, but close to $7/10$. After [53].

lattice parameters are: $a = 11.469 \text{ \AA}$, $b = 13.368 \text{ \AA}$; along the c -direction the ladder unit cell length is $c_L = 3.931 \text{ \AA}$ and for chains $c_C = 2.749 \text{ \AA}$. The unit cell with an unusually large volume of about 4000 \AA^3 has orthorhombic symmetry, but belongs to different space groups depending on the $(\text{La}, \text{Y}, \text{Sr}, \text{Ca})$ content. In (Sr, Ca) compounds with low Ca content the ladder sublattice has F-centered orthorhombic symmetry (i.e., face centered symmetry on all faces), while the chain sublattice has A-centered (i.e., face-centered symmetry only at the face corresponding to the bc plane) which changes to F-centered symmetry at high Ca content $x \geq 8$. [53] The a and c lattice parameters remain almost the same, but the b -axis parameter varies slightly with $(\text{La}, \text{Y}, \text{Sr}, \text{Ca})$ content. If the CuO_4 squares were ideal, there would always be an $\alpha = c_C/c_L = 1 : \sqrt{2}$ incommensurability between the chain and ladder subsystems, a ratio of the distance between two copper sites in the chains (side of a CuO_4 square) and the Cu sites in the ladders (diagonal of a CuO_4 square). The chemical formula taking this structural feature into account reads $(\text{Sr}_2\text{Cu}_2\text{O}_3)_\alpha(\text{CuO}_2)$ and modern literature has settled on $\alpha \approx 7/10$, meaning $\text{Sr}_{14}\text{Cu}_{24}\text{O}_{41}$. In the real quasi-one-dimensional cuprate materials the chains and ladders remain incommensurate. However, the distortions related to incommensurability lead to additional modulations of the crystallographic positions, i.e., each subsystem is weakly modulated to adjust to the other. These effects may be regarded

as an intrinsic source of disorder. [59, 60]

In the systems with isovalent Sr, Ca substitution the simple requirement of electric neutrality gives the average copper-ion valency of +2.25 instead of +2. Thus the $Sr_{14-x}Ca_xCu_{24}O_{41}$ are self-doped (intrinsically doped) with 0.25 holes/Cu ion, i.e., 6 holes/formula unit (f.u.). Non-isovalent substitution of Sr and Ca atoms with Y and La removes holes, each Y/La atom removing one hole, which means a $(La, Y, Sr, Ca)_{14}Cu_{24}O_{41}$ material has $n_h = 6 - y$ holes/f.u., making it effectively underdoped. It is useful to abstract away the separate treatment of $Cu3d_{x^2+y^2}$ and $O2p_x, O2p_y$ orbitals. For this purpose the Zhang-Rice model is proven to be the most instructive. [61] First devised to describe high-temperature superconducting cuprates, this description of holes on a cuprate lattice assumes they are placed primarily on oxygen sites, and that the Cu-O hybridization strongly binds a hole to the central copper ion of the Cu_4 square. Hence, a copper site is in an oxydation state of Cu^{3+} if a hole is bound to it, or Cu^{2+} when the hole is absent. The Cu^{2+} ion in a cuprate lattice can be thought of as a spin 1/2 of the unpaired $3d^9$ electron. The Cu^{3+} ion on the other hand can be regarded as a spin 0, the so-called Zhang-Rice singlet formed by the spin 1/2 hole with spin 1/2 of the unpaired $3d^9$ electron. The concept of a Zhang-Rice singlet is important and useful since it effectively implies a complementary arrangement of spin and charge in cuprate structures: on a CuO_4 square the presence of a hole means absence of spin, and vice versa.

Between the spins of the nearest-neighbor Cu^{2+} ions, superexchange interaction occurs either along the σ -bond configurations (for intraladder, intrachain and interladder couplings), or through a quasi-linear Cu-O-O-Cu path (for interchain coupling). In the latter case, the coupling is weakly antiferromagnetic due to a slight overlap of oxygen orbitals. [62] On the other hand, the strength and sign of the dominant coupling J , which occurs along the σ -bond configurations, considerably depends upon the angle between Cu-O bonds as per Goodenough-Kanamori-Anderson rules. [63, 64, 65] In the case of a 180° configuration, the strong antiferromagnetic coupling between two neighboring Cu^{2+} in $3d^9$ configuration with a single hole in the antibonding orbital is mediated via a single $O2p$ orbital. In a 90° configuration, the character of the superexchange interaction transforms into a much weaker ferromagnetic coupling due to the orthogonal orbitals coupled via Hund's rule. [66] In the ladder layers the interladder coupling is hence frustrated due to a triangular arrangement of Cu atoms between neighboring ladders, which are offset by $c_L/2$. The theoretical considerations of Gopalan *et al.* [67] indicated that even if a much larger interladder coupling is assumed (only an order of

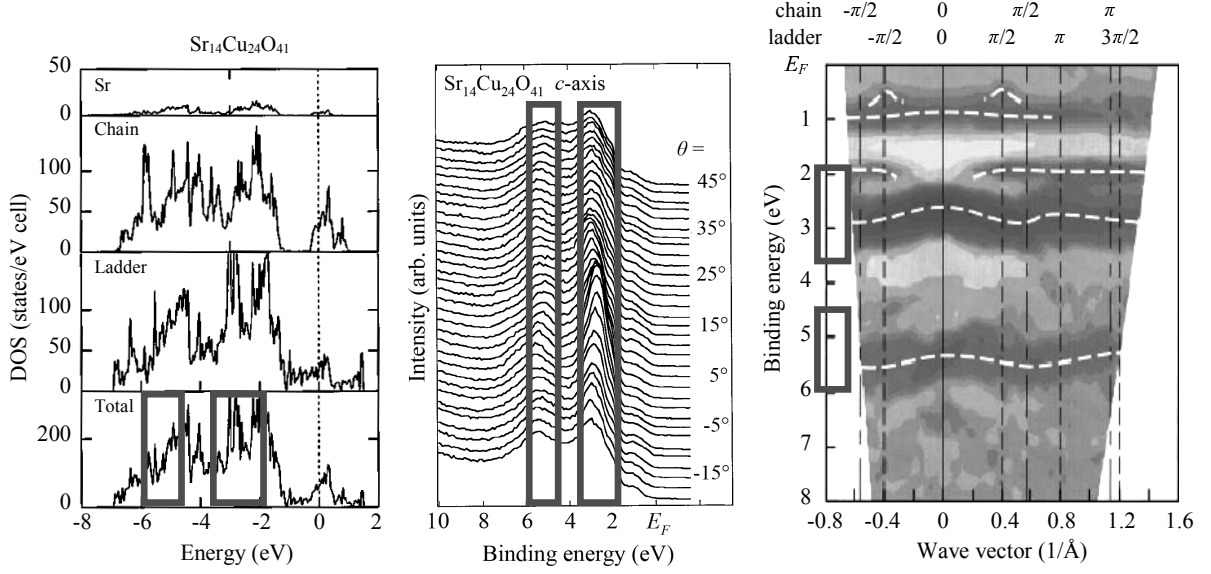


Figure 1.12 – Calculated (left panel) and measured (middle panel) valence band spectra for $Sr_{14}Cu_{24}O_{41}$ along the c -axis. The change of peak position with respect to the polar angle θ (middle panel) corresponds to the spectra in the reciprocal space (right panel). The dashed lines are guides to the eye, indicating energy dispersions. The boxes emphasize bands which appear both in the calculation and experiment. After Refs. [68, 69].

magnitude smaller than the coupling along ladder legs and rungs), the ladder layer may be considered as a system composed of almost isolated ladders due to the frustration itself.

The electronic structure of the parent compound $Sr_{14}Cu_{24}O_{41}$ was calculated within the local-density approximation. [68, 70] *Ab initio*, linear muffin-tin-orbital calculations were performed on a small cell containing one formula unit of $Sr_{14}Cu_{24}O_{41}$; the structural modulation due to chain-ladder incommensuration is ignored for simplicity. Quasi-one-dimensional bands originating from the ladder and chain subsystems are positioned near the Fermi level. The bands can be described by simple quasi-one-dimensional tight-binding dispersions with nearest neighbor and next-nearest neighbor hopping energies along and between the ladders or chains. The nearest neighbor interladder hopping energies are approximately 5–20% of the intraladder ones, which indicates the small but considerable transverse coupling. This calculation however does not consider electronic correlations, leading to a finite density of states (DOS) at the Fermi level and thus metallic properties which is obviously in contradiction with the experimentally observed insulating behavior for all $Sr_{14-x}Ca_xCu_{24}O_{41}$, $x < 11$. Still, the calculated density of states is in good agreement with the findings of an angle-resolved photoemission spectroscopy study on $Sr_{14}Cu_{24}O_{41}$. [69] There the two calculated peaks at 2-3 eV and

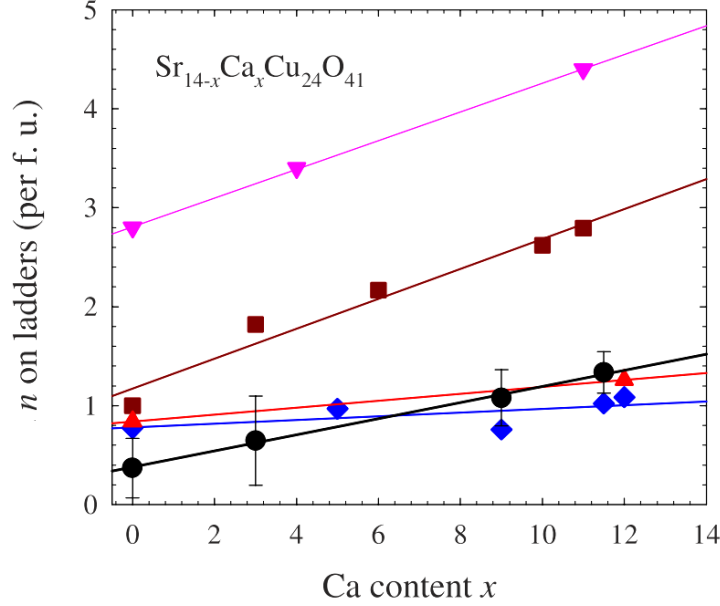


Figure 1.13 – The number of holes n per formula unit in the ladder subsystem *vs.* Ca content x in fully doped $Sr_{14-x}Ca_xCu_{24}O_{41}$ as determined by various experimental techniques: optical conductivity [72] (brown squares), NEXAFS [14] (blue diamonds), NMR [73] (red triangles), x-ray absorption [74] (pink triangles) and Hall effect measurements [75] (black circles). After Tafra *et al.* [75]

5 eV (see Fig. 1.12, left panel) are actually observed at 3 and 5.5 eV (Fig. 1.12, middle panel, and the corresponding spectra in the right panel). The band at 3 eV does not agree with periodicity of neither ladders nor chains and probably consists of more than two bands originating on both cuprate subsystems. The periodicity of the narrow band located at 5.5 eV agrees with that of chains. There is another band near the Fermi level with a very pronounced dispersion of about 0.5 eV most likely belonging to the ladders. [69, 71] The wide band is folded at $q_c = (\pm\pi/2c_L)(2n + 1)$, $n = 0, 1, 2, \dots$ without crossing the Fermi level, which implies an opened gap. Photoemission experiments situate the top of the wide ladder band at 0.4 eV below the Fermi level and also find it to be the closest band to E_F , which means that the holes are present in the ladders of parent material $Sr_{14}Cu_{24}O_{41}$. In other words, a certain fraction of 6 holes/f.u. in total is transferred from chains to ladders in a process of self-doping.

The question of hole distribution between chains and ladders is central to the physics of $(La, Y, Sr, Ca)_{14}Cu_{24}O_{41}$. A number of experiments attempted to pinpoint the exact hole distribution with regard to temperature and Ca content in fully doped systems. In the parent $Sr_{14}Cu_{24}O_{41}$ at room temperature there are most likely approximately five holes per formula unit residing on chains and approximately one hole in the ladders (refer to Fig. 1.13). Upon Ca substitution holes are transferred from chains to ladders, with

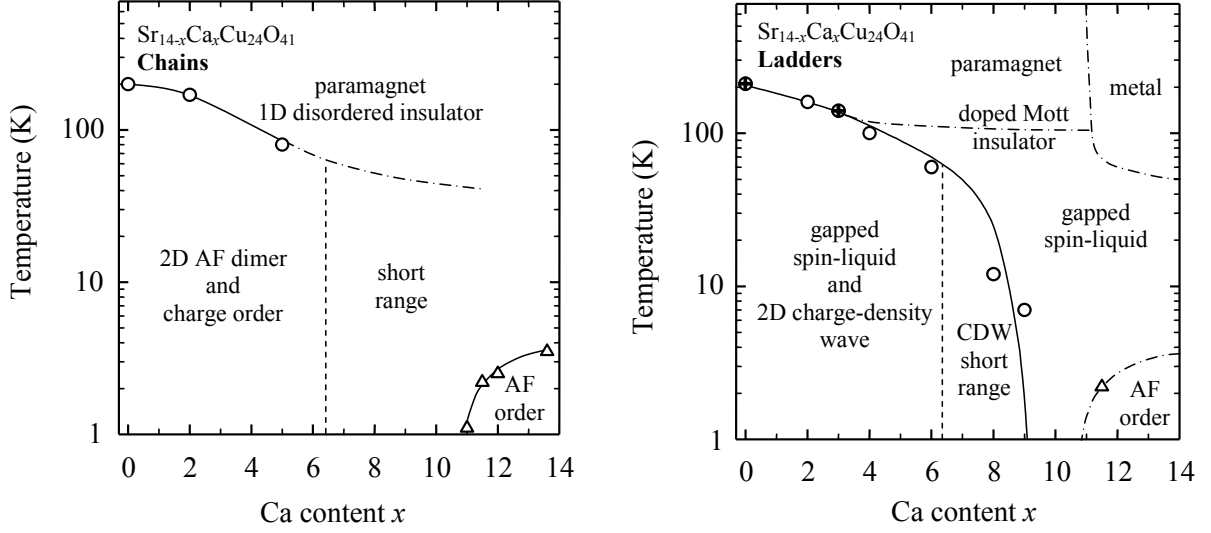


Figure 1.14 – Phase diagram of chains (left) and ladders (right) in the fully doped $Sr_{14-x}Ca_xCu_{24}O_{41}$ materials. From Vuletić *et al.* [2]

again different suggestions for redistribution when going from $x = 0$ to 12 (estimated range from approximately 0.4 to 2 holes/f.u.). [72, 14, 73, 74, 75] Going up in Ca content, at the $Sr_{2.5}Ca_{11.5}Cu_{24}O_{41}$ material the valence band becomes wider and touches the Fermi level at certain angles, which is in accord with the observed metallic behavior of this system. [71, 76]. The folding of the wide band is suppressed, indicating weaker electron correlations compared to $Sr_{14}Cu_{24}O_{41}$ and a transfer of holes from chains to ladders with increasing Ca content.

1.2.2 Phase diagrams with respect to hole doping

Fig. 1.14 shows qualitative phase diagrams of chains and ladders in the fully doped materials $Sr_{14-x}Ca_xCu_{24}O_{41}$. [2] **The high temperature phase of chains in the fully-doped materials** is that of a paramagnetic 1D disorder-driven insulator (see Fig. 1.14 left). Lowering the temperature establishes an antiferromagnetic dimer order with complementary charge order in the ac plane of chain layers. The number of holes in $Sr_{14-x}Ca_xCu_{24}O_{41}$ in the chains comes close to 6/f.u. so the antiferromagnetic dimer order develops at long length scales. The AF dimer/charge order of chains at low x can be visualised as in Fig. 1.15. However, noting that $Sr_{14-x}Ca_xCu_{24}O_{41}$ has approximately 5 spins and 5 holes per Cu site of chains, the actual situation is somewhat more complex due to irregularities in the pattern of holes: the chains are largely dimerized but there are also unpaired spins and short antiferromagnetic chains with odd and even numbers of spins. Substitution of Sr with Ca atoms destroys the long-range order, and an AF

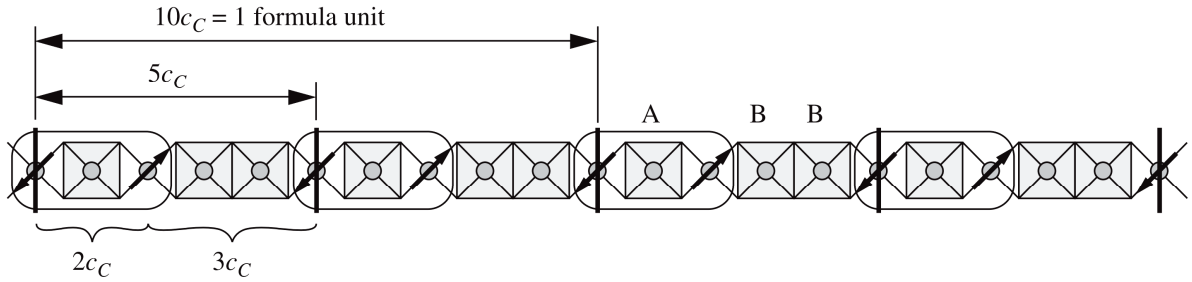


Figure 1.15 – Antiferromagnetic dimers (ovals) form in a cuprate chain with 6 holes and 4 spins per 10 Cu sites. This situation is similar to $Sr_{14-x}Ca_xCu_{24}O_{41}$ at small x where hole count on chains is close to 6. After Vuletić *et al.* [2]

short-range order persists up to at least $x = 11.5$. Above this Ca content and at low temperatures an antiferromagnetic order is established with a large magnetic moment of $0.56 \mu_B$, which is typical for localized spins.

Turning to **the ladder subsystem in fully doped materials** (Fig. 1.14 right), at ambient pressure and low Ca content the ground state is a charge-density wave along ladder legs with a gapped spin liquid in spin sector: pairs of spins along ladder rungs form singlets, a correlation which forces doped holes to group in pairs along rungs. The CDW in ladders has been observed through the non-standard, anisotropic frequency-dependent conductivity and dielectric response (Fig. 1.16), [77,17] and a peak in microwave conductivity spectra associated with the CDW pinned mode ((Fig. 1.17) Also, hole ordering with a period of $5c_L$ has been confirmed by resonant soft x-ray scattering measurements tuned to the oxygen peak near 528 eV (Fig. 1.18). [16] No higher harmonics have been found meaning the modulation is not of the fully localized Wigner $4k_F$ type. Here lattice distortions are completely absent which indicates that a predominantly electron-electron interaction is responsible for the density wave. A theoretical prediction exists for the CDW by White *et al.* which starts from a simple $t - J$ model for a half-filled two-legged ladder where t and J are respectively the hopping integral and exchange coupling both between rung and ladder sites. At weak doping the spins are gapped and the low-energy spectrum of hole pairs is well-described by bosonic hole-pairs at each rungs. A completely gapped $4k_F$ CDW can stabilize at a critical value of $J/t \approx 0.25$ which approximately agrees with $J = 130$ meV, $t = 500$ eV in $Sr_{14}Cu_{24}O_{41}$. [2] Such a CDW is characterized by a modulation of charge density $\propto \cos(2\pi\delta j + \alpha + \text{const.})$, where δ is the density of holes per Cu, j is the rung index and α a phase constant. In the case of parent material $Sr_{14}Cu_{24}O_{41}$, a period of $5c_L$ obtained by resonant soft x-ray scattering implies a density of holes of $\delta = 0.2$ per ladder Cu-site (2.8 holes/f.u.), a value much too high when compared with other methods (around

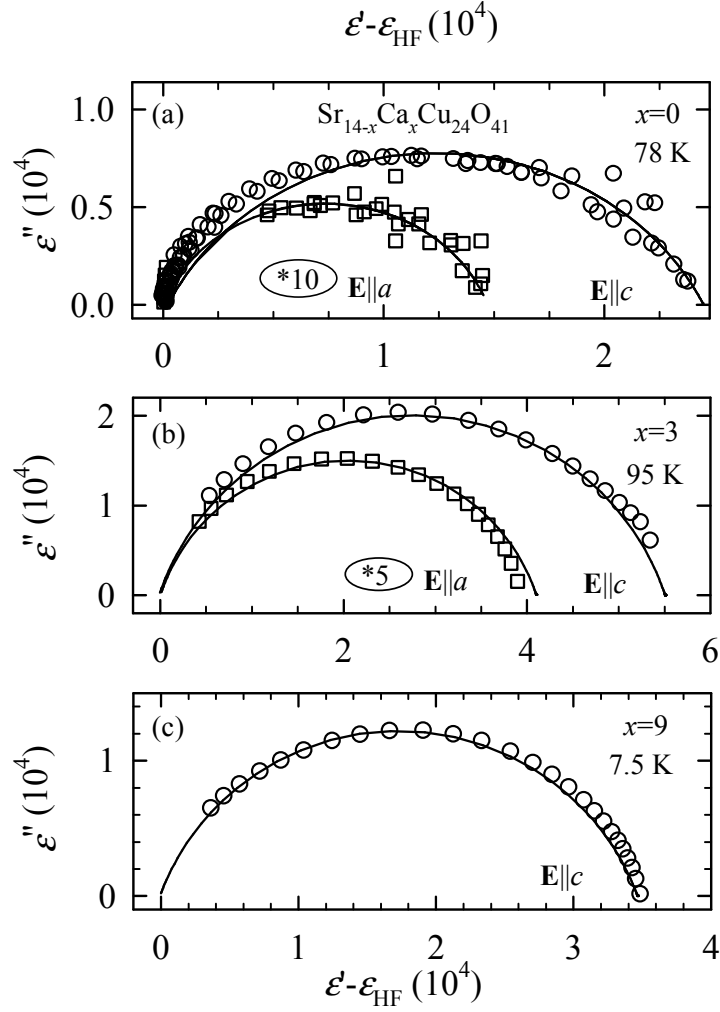


Figure 1.16 – Representative Cole–Cole plots of the real (ϵ') and imaginary (ϵ'') parts of the dielectric function of $Sr_{14-x}Ca_xCu_{24}O_{41}$ for $x = 0$ (a), $x = 3$ (b) and $x = 9$ (c) with the $\mathbf{E} \parallel c$ and $\mathbf{E} \parallel a$. The plots for the response along the a -axis are scaled up by factors of 10 ($x = 0$) and 5 ($x = 3$). The full lines are fits of the generalized Debye function (refer to Eq. 3.2 in Sec. 3.2). The broad dielectric relaxation is associated with the overdamped longitudinal phason mode of ladder CDW. After Vuletić *et al.* [17]

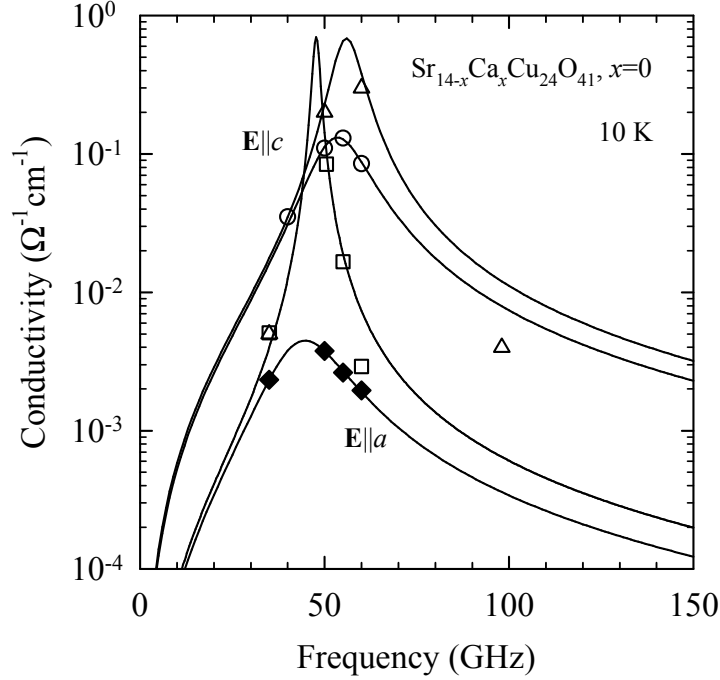


Figure 1.17 – Low-temperature microwave conductivity spectra at 10 K of single crystals taken from different batches of $Sr_{14}Cu_{24}O_{41}$, $\mathbf{E} \parallel c$ and $\mathbf{E} \parallel a$. The full lines are based on fits to Lorentzians with characteristic frequencies of $\Omega_c \approx 1.8 \text{ cm}^{-1}$, $\Omega_a \approx 1.7\text{--}3.5 \text{ cm}^{-1}$. The modes are interpreted as evidence for CDW pinned mode in ladders. Data taken from Kitano *et al.* [15]

0.07 holes per Cu according to NEXAFS data, compare with Fig. 1.13). There are models predicting a $2k_F$ CDW in ladders, [78, 79, 80] with periodicities $2/\delta$, which again overestimates ladder hole counts (0.4 per ladder Cu site) than what is experimentally observed. The exact periodicity of the ladder CDW remains an open question.

An increase of Ca content destroys the charge gap which suppresses the CDW phase in the ladders and introduces a Mott insulating behavior. However, the gapped spin liquid still persists. Further increase of Ca content introduces metallic behavior at high temperatures and an antiferromagnetic ordering at low temperatures. Superconductivity in ladders has experimentally been observed for $10 \leq x \leq 13.6$ at pressures between 3 and 8 GPa. The exact superconducting mechanism and symmetry are still not known. Namely, hole pairing across a ladder rung would imply a d -wave symmetry of the superconducting phase. However, speaking against this option is the enhanced spin-lattice relaxation rate in the superconducting state, interpreted as a Hebel-Slichter coherence peak [81] which is standardly a mark of an s -wave superconducting phase. Also, there is the well-known extreme sensitivity of d -wave superconductivity to disorder, which makes it unlikely to appear in the composite q1D cuprate family. [82]

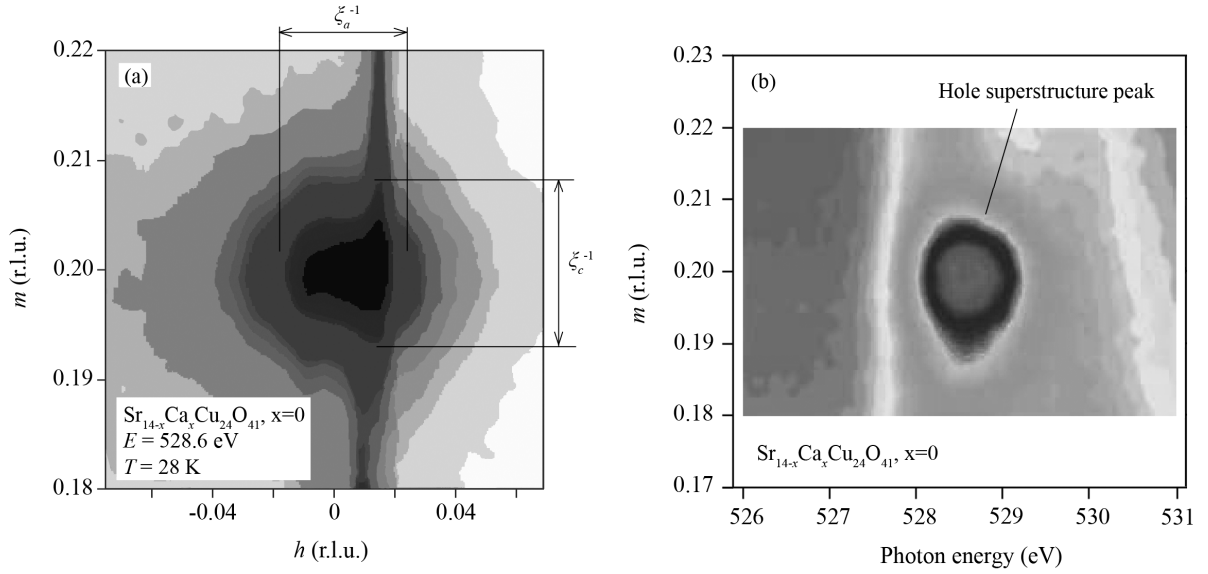


Figure 1.18 – (a) Reciprocal ladder space map around $(h, k, m) = (0, 0, 0.2)$ with the X-ray energy tuned to the ladder hole absorption feature (MCP at 528.6 eV) taken at $T = 28$ K in $Sr_{14}Cu_{24}O_{41}$, $x = 0$. Inverse coherence length ξ_c^{-1} and ξ_a^{-1} are denoted. (b) Hole super-structure peak intensity across the oxygen K edge. After Ref. [16].

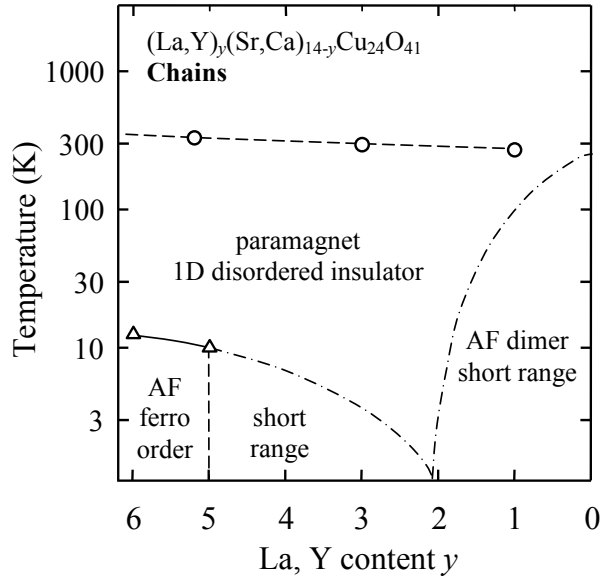


Figure 1.19 – Phase diagram of chains in the underdoped $(La, Y)_y(Sr, Ca)_{14-y}Cu_{24}O_{41}$ materials. From Vuletić *et al.* [2]

Removing holes by non-isovalent La, Y substitution of Sr, Ca atoms brings about a striking change in physics of both ladders and chains. Fig. 1.19 shows the phase diagram of **chains in underdoped materials** $(La, Y)_y(Sr, Ca)_{14-y}Cu_{24}O_{41}$. [2] As mentioned before, the total hole count $n_h = 6 - y$ is solely determined by the substituted ions y . Regarding chains, at low $y \leq 1$ it appears the number of holes on chains remains fixed at approximately 5/f.u., while ladders gradually accept doping to accommodate one hole per f.u. at the parent material $y = 0$. [83] Similar to the fully doped systems, the high-temperature phase of chains is again a paramagnetic 1D disorder-driven insulator. At low temperatures, transport along the chains is that of Mott variable-range hopping in 1D. For $y = 6$ without any self-doped holes left, the magnetism of cuprate chains is dominated by ferromagnetic on-chain nearest-neighbor interaction and antiferromagnetic interchain interaction. This results in ferromagnetic chains with a bulk antiferromagnetic state at low temperatures. Holes doped into the chain by decreasing y quickly destroy the long-range order since they introduce a strong antiferromagnetic interaction between spins of the next-nearest neighbor Cu^{2+} ions separated by a hole. Reintroduction of holes brings about a short-range antiferromagnetic order (short ferro-chains antiferromagnetically correlated across holes) which survives up to $y \approx 2$. The antiferromagnetic interaction is dominant at smaller y and dimers start to form, however the long-range dimer order develops in full only at $y = 0$. This means that any deviations from an almost full set of 6 holes/f.u. in the chains are most likely critical for favoring the Anderson-localized, disorder-driven insulating phase instead of the long-range AF dimer ordering and its complementary charge order. Measurements on $y = 3$ and $y = 5$ monocrystals showed that charge transport on chains happens via hopping between localized states along the chain (see Fig. 1.20). [22, 84] At the beginning of this work, it was known that room temperature conductivity rises drastically with introduction of holes, from $\sigma_c = 0.0007 \Omega^{-1}cm^{-1}$ at $y = 5.2$ to $0.5 \Omega^{-1}cm^{-1}$ at $y = 1$, an increase by orders of magnitude which evidently cannot be explained by transport mechanisms linked solely to the chains. [2]

1.2.3 Open questions

At the beginning of this work there was scarce information about systems with very low La, Y substitution $y < 2$, hence it was unclear how exactly does the far-underdoped phase diagram join with the fully doped materials. The main questions revolve around the introduction of new holes into the underdoped structure: do the newly-added holes prefer to settle on the ladders or chains? How does the long-range dimer order form in

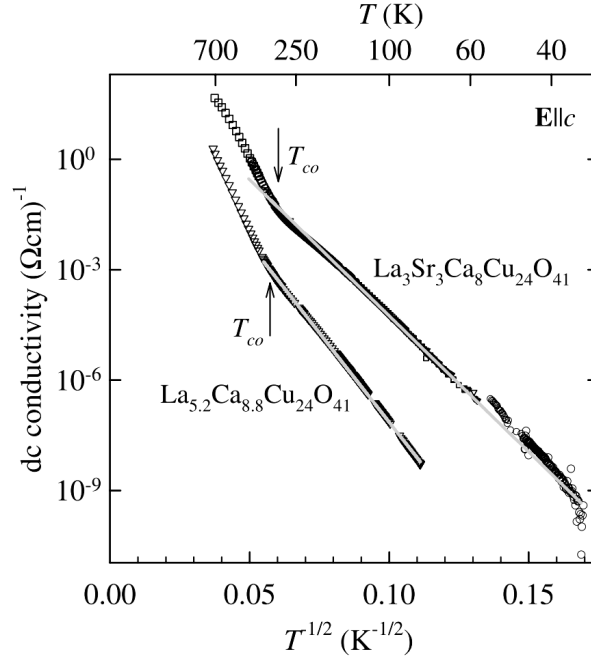


Figure 1.20 – The dc conductivity along the c -axis in the underdoped $(\text{La}, \text{Y})_y\text{-(Sr}, \text{Ca})_{14-y}\text{Cu}_{24}\text{O}_{41}$, $y = 3, 5$. The low-temperature conductivity is in the one-dimensional variable-range hopping regime characterized by the temperature dependence $\sigma_{\text{dc}} \propto \exp -(T_0/T)^{1/(1+d)}$, $d = 1$. From Vuletić *et al.* [2]

chains? As the hole doping is increased, can we regard the formation of ladder CDW as a gradual crossover or a narrow second-order phase transition? One of the main goals of the study presented here is to fill in the missing part of the phase diagrams by mapping the way transport properties vary with La, Y content and temperature in an attempt to pinpoint the substitution levels at which newly-added holes start populating ladders instead of localizing on chains. Somewhat surprisingly, the results infer a cooperative interdependence between ground states of the two subsystems.

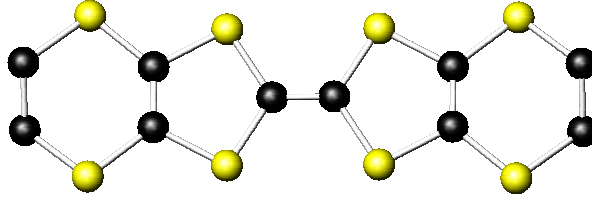


Figure 1.21 – Schematic display of a bis(ethylenedithio)tetrathiofulvalene (BEDT-TTF) molecule. Black spheres represent carbon and yellow spheres sulfur atoms.

1.3 Charge ordering in the quasi-2D organic conductor α -(BEDT-TTF) $_2$ I $_3$

1.3.1 2D (BEDT-TTF) $_2$ X charge-transfer salts

Owing to the superconductivity and insulating charge-ordered states, the (BEDT-TTF) $_2$ X family of salts is prominent among the A_2B organic conductors. BEDT-TTF stands for the bis(ethylenedithio)tetrathiofulvalene molecule shown in Fig. 1.21. With acceptor ions being X^- , the BEDT-TTF $^{1/2+}$ form two-dimensional planes of 3/4-filled electronic systems on average, i.e., 1/4-filled in terms of holes. There exist many polytypes in this family, each representing a different arrangement of BEDT-TTF molecules with different electronic properties, with the θ -, β -, κ -, λ -, and α -types most extensively studied. The spatial arrangements of molecules in the unit cells of these polytypes are schematically shown in Fig. 1.22. θ - and β -type represent polytypes with two molecules per unit cell, while the lower-symmetry α -, κ - and λ -type have four molecules per unit cell. Setting the stage for the charge-ordered α -(BEDT-TTF) $_2$ I $_3$, the following is a brief overview of the rich phenomena observed in various (BEDT-TTF) $_2$ X polytypes.

θ -type: Structurally the simplest of the BEDT-TTF salts, a series of θ -type materials has been synthesized [86,87] and can be classified in a phase diagram of temperature and dihedral angle ϕ (angle between molecules of two neighboring columns in the herringbone structure). As shown by Fig. 1.23, in the region of large ϕ the system undergoes a metal-insulator transition simultaneously with a structural transition, [88,89] marking the onset of charge order. [89] At lower temperatures a spin gap opens [87,88,90]. On the other hand, materials with a smaller ϕ also show a minimum in resistivity, however there is no sharp transition to an insulator [87,91] and the charge ordering is absent, as evidenced by ^{13}C -NMR measurements. [92,85] When ϕ is further decreased, a normal metallic state is stabilized in the only θ -material with a SC ground state, the θ -(BEDT-

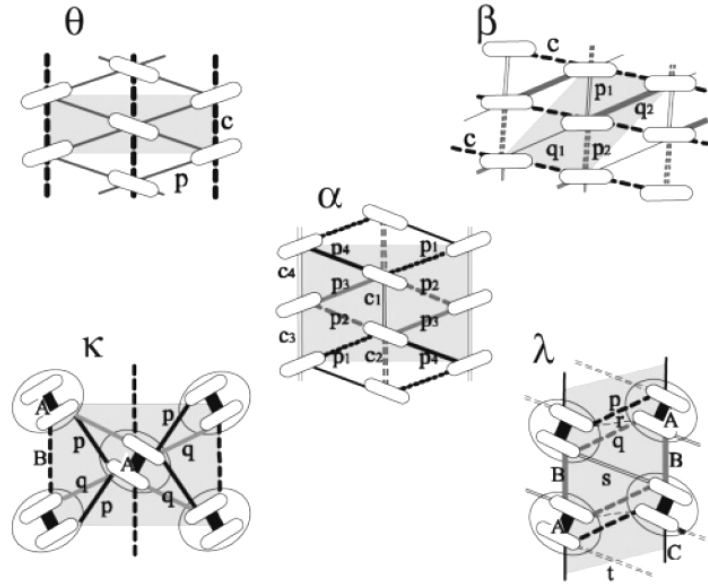


Figure 1.22 – Schematic representation of the planar structure and different transfer integrals between molecules for the five basic (BEDT-TTF) $_2$ X and (BEDT-TSF) $_2$ X polytypes. Unit cells are marked grey. From Seo *et al.* [85]

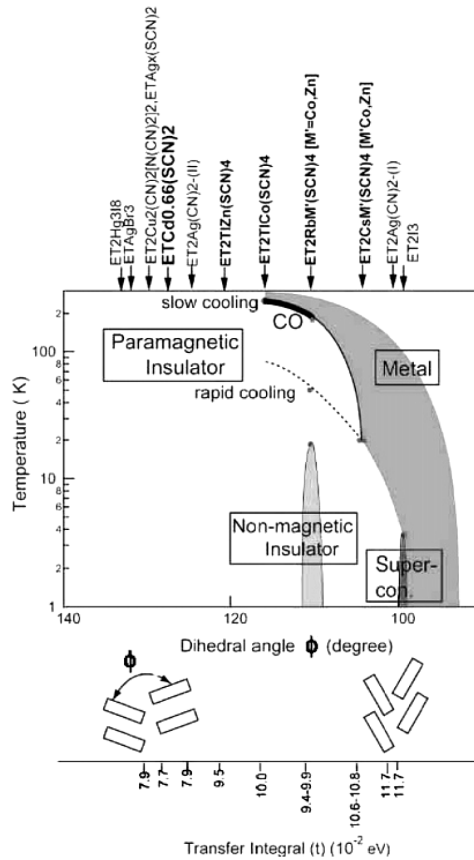


Figure 1.23 – Experimental phase diagram of the θ -(BEDT-TTF) $_2$ X classified by the dihedral angle ϕ . After Seo *et al.* [85]

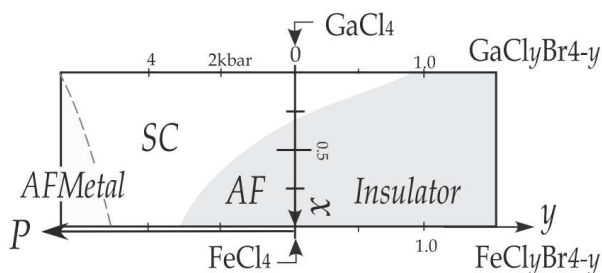


Figure 1.24 – Experimental phase diagram of the λ -(BEDT-TSF) $_2$ Fe $_x$ Ga $_{1-x}$ Cl $_{4-y}$ Br $_y$ as a function of Ga content and hydrostatic or chemical pressure. From Hotta *et al.* [92]

TTF) $_2$ I $_3$.

β -type: The β -type materials are known for their superconducting state; β -(BEDT-TTF) $_2$ I $_3$ has two superconducting phases with different critical temperatures (1.5 and 8 K) which are related to the two different types of conformation of terminal ethylene groups. [93, 94, 95] Other systems like β -(BEDT-TTF) $_2$ IBr $_2$ ($T_c = 2.7$ K) and β -(BEDT-TTF) $_2$ AuI $_2$ (3.8 K) are also superconducting whereas β -(BEDT-TTF) $_2$ I $_2$ Br remains a normal metal due to the structural disorder of inhomogeneously aligned anions. This generates a random electrostatic potential which leads to the weak localization of electrons and suppresses the formation of superconductivity. [96, 97, 98]

κ -type: The κ -salts are often cited as having interesting parallels with the physics of superconducting cuprate planes. As the pressure is varied at low temperatures a commensurate antiferromagnetic insulating phase, most likely of Mott type, [99] and the superconducting phase appear next to each other. [100, 92] A representative material is the κ -(BEDT-TTF) $_2$ Cu[N(CN) $_2$]Cl with $T_N = 26$ K. [101, 99] The salts become superconducting through a first-order transition by the application of pressure, while anion replacement and/or deuteration acts as “negative chemical pressure”. [102, 103] In this sense the κ -(BEDT-TTF) $_2$ Cu[N(CN) $_2$]Br salt is superconducting but is positioned very close to the phase boundary: its fully deuterated form is an insulator. [104] The metallic phase of κ -compounds above the SC phase is reportedly unconventional. [105] The drop in the linewidth and the peak structure of $(T_1T)^{-1}$ at $T^* \approx 50$ K in 13 C-NMR are assigned to the formation of a pseudo gap. [106, 107] Interestingly, a second-order phase transition at T^* has been proposed where a density-wave fluctuation is likely to occur. [108]

λ -type: There are only a few BEDT-TTF-based λ -type materials, most notably the insulating λ -(BEDT-TTF) $_2$ GaI $_4$ and λ -(BEDT-TTF) $_2$ InBr $_4$. [109] Systematic studies do exist of materials based on the BEDT-TSF [bis(ethylenedithio)tetraselenafulvalene], the λ -(BEDT-TSF) $_2$ Fe $_x$ Ga $_{1-x}$ Cl $_{4-y}$ Br $_y$ family (see phase diagram in Fig. 1.24. The ground state here primarily depends on the Fe content. The ground state of GaCl $_4$ salt is superconductivity, which turns into an AFI by the introduction of Fe with spin 5/2. Superconducting and insulating phases of the GaCl $_{4-y}$ Br $_y$ are next to each other at low temperatures as the effective pressure is varied, analogous to the κ -materials. However, the magnetic behavior in the insulating phase differs between the two polytypes: where κ -(BEDT-TTF) $_2$ X shows AF ordering, the λ -(BEDT-TTF) $_2$ X has a maximum in magnetic susceptibility at similar temperatures but without any signal of clear antiferromagnetic ordering. [85] The FeCl $_4$ salt on the other hand becomes metallic under high pressure, concomitantly with an AF ordering of Fe spins. [110]

α -type: The α -type materials have a herring-bone-structured molecular plane similar to the θ -type, but with a doubled periodicity along the stacking axis. There are two characteristic members of the α -type: α -(BEDT-TTF) $_2$ I $_3$ and α -(BEDT-TTF) $_2$ MHg(SCN) $_4$. Among the α -(BEDT-TTF) $_2$ MHg(SCN) $_4$ materials ($M = \text{K, Rb, Tl, NH}_4$) the NH $_4$ salt becomes superconducting, [111] while the K, Rb and Tl-compounds present density-wave-like anomalous ground states at low temperatures. [112]

The α -(BEDT-TTF) $_2$ I $_3$ behaves quite differently from its Hg-based counterparts. It was the first organic material which showed highly conducting properties in two dimensions. [114] The compound undergoes a metal-insulator transition at $T_{\text{CO}} = 136$ K, with a sudden opening of a charge and spin gap. Originally the gap was attributed to formation of a charge- or spin-density wave [115, 116], but an absence of a Peierls-like instability contradicts these early assignments. Rather, a two-dimensional charge ordering develops at low temperatures, with a pronounced modulation of molecular charge as well as transfer integrals between the BEDT-TTF sites. Under small uniaxial strain the system undergoes a phase transition from the charge-ordered phase to superconductivity, and then again at large strains into a narrow gap semiconducting state (see Fig. 1.25. [113] Worth noting is the peculiar property of the α -(BEDT-TTF) $_2$ I $_3$ metallic state stabilized by high pressure: the temperature dependence of the resistivity is almost flat, and yet the mobility and carrier number deduced from the transport measurements have very strong temperature dependences. [113]

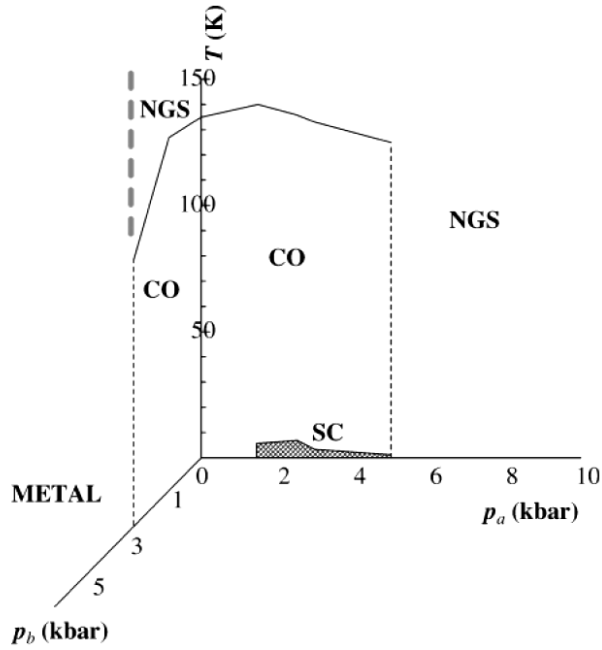


Figure 1.25 – Phase diagram of α -(BEDT-TTF) $_2$ I $_3$ under strains along the a -axis (1), and along the b -axis (b). CO denotes charge ordering, SC superconductivity and NGS the narrow gap semiconducting state. From Tajima *et al.* [113]

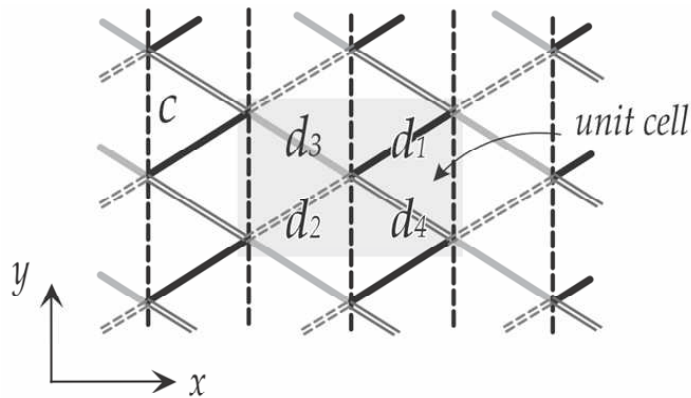


Figure 1.26 – Anisotropic triangular lattice used to model the different BEDT-TTF polytypes. Five different transfer integrals are shown by different lines, denoted as c and $d_1 - d_4$. From Hotta *et al.* [92]

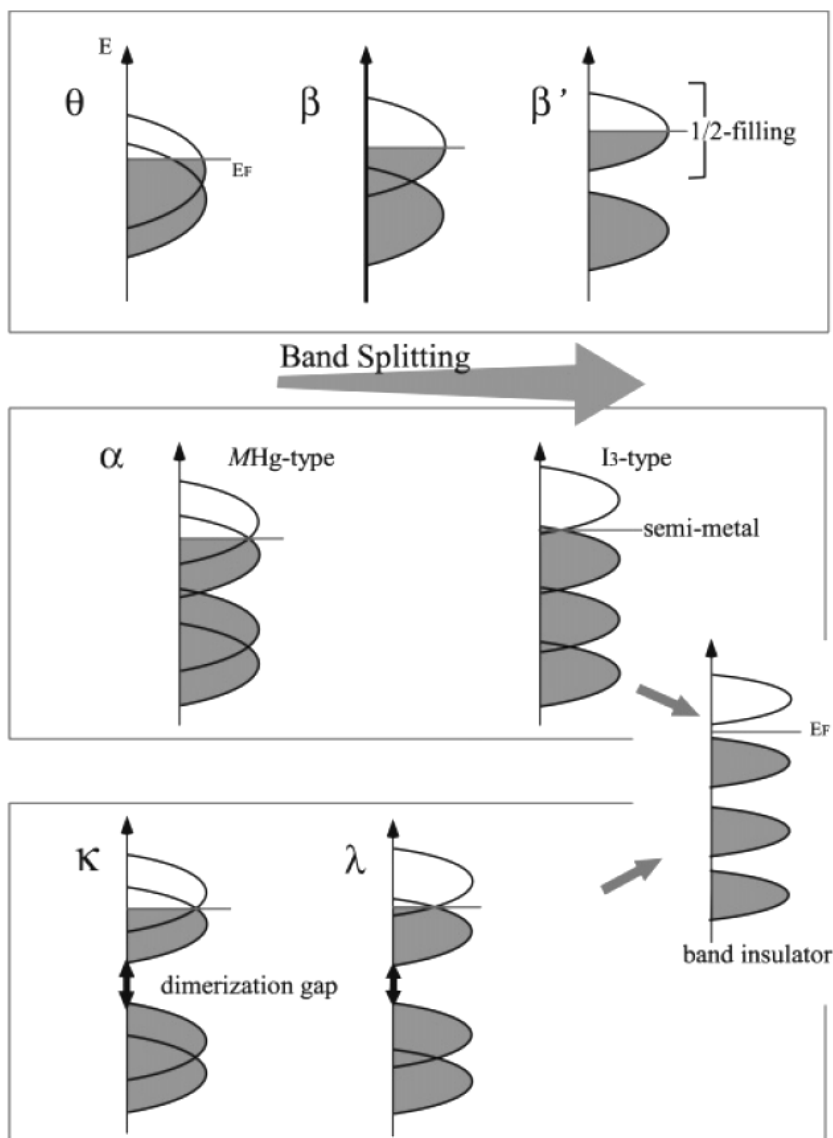


Figure 1.27 – Relationship between different BEDT-TTF polytypes. Density of states schematically show band splitting. Polytypes are classified into three groups: those with only two bands (top), with four bands but without dimerization (middle), and both with four bands and with dimerization (bottom). In the limit of large band splitting, the latter two systems are expected to become a band insulator. α -(BEDT-TTF) $_2$ I $_3$ is best described as a semi-metal. From Seo *et al.* [85]

In a unifying theoretical treatment of the various BEDT-TTF polytypes (Fig. 1.22), Hotta proposed a mapping to a tight-binding anisotropic triangular lattice with five tunable hopping parameters, as shown in Fig. 1.26. [92] Different polytypes are treated based on the level of dimerization and band splitting, which classifies them into three groups: those with only two bands, those with four bands but without dimerization, and those with both four bands and dimerization (see Fig. 1.27). Within this model the α -types are generally treated as a dimerized structure not unlike the κ - and λ -types, which explains well the properties of α -(BEDT-TTF) $_2$ MHg(SCN) $_4$. Unfortunately, the procedure is not fully valid for the α -(BEDT-TTF) $_2$ I $_3$ since the dimer model does not account for the appearance of charge ordering. Because of this α -(BEDT-TTF) $_2$ I $_3$ is treated as an intermediary polytype approximately analogous to the θ -type (see below, Section 1.3.3). [92, 85]

1.3.2 Crystallographic structure of α -(BEDT-TTF) $_2$ I $_3$

The α -(BEDT-TTF) $_2$ I $_3$ is a 2D organic conductor made of I $_3^-$ anions and BEDT-TTF $^{0.5+}$ cations (donors) on average. The triclinic crystal structure is a sandwich-like alternation of I $_3$ insulating layers and BEDT-TTF conduction layers. The space group at room temperature is $P\bar{1}$, with four molecules per unit cell, and cell parameters $a = 9.211 \text{ \AA}$, $b = 10.850 \text{ \AA}$, $c = 17.488 \text{ \AA}$, $\alpha = 96.95^\circ$, $\beta = 97.97^\circ$, $\gamma = 90.75^\circ$. [114] The BEDT-TTF layer at room temperature consists of two types of stacks with molecular sites denoted as A and A' in one stack, B and C in the other (see Fig. 1.28). Stack I is weakly dimerized and composed of crystallographically equivalent molecules A and A', while the stack II is a uniform chain composed of B and C molecules. At T_{CO} the structural changes are subtle - there are no translations of molecules, only a shift in dihedral angles is observed which results in breaking of inversion symmetry between A and A' sites, with space group changing from $P\bar{1}$ to the P1. This non-equivalency of A and A' allows for crystal twinning in the low-temperature acentric structure. [27]

1.3.3 Electronic properties and charge ordering in α -(BEDT-TTF) $_2$ I $_3$

The original and rather rough first-principle calculations for α -(BEDT-TTF) $_2$ I $_3$ at room temperature were done by Mori. [23] The molecular orbitals were calculated by means of extended Hückel method which in turn provides the overlap integrals of the highest occupied molecular orbital (HOMO) for the tight-binding method. The authors

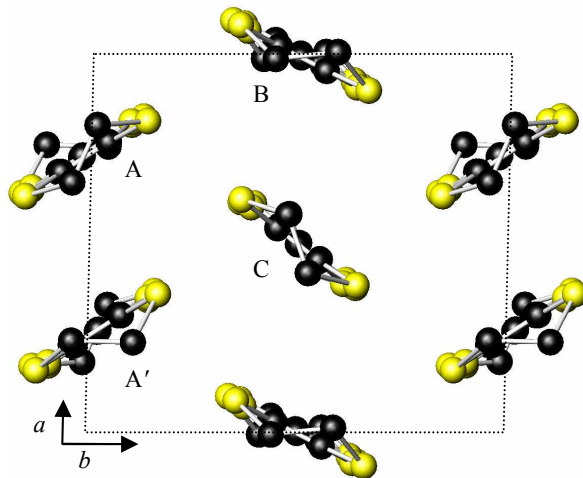


Figure 1.28 – Schematic representation of donor layer in α -(BEDT-TTF) $_2$ I $_3$. Molecular sites belonging to the stack I and stack II are denoted as A, A' and B, C, respectively.

of this early study note that the four-band, 1/4-filled system should be regarded as either a semimetal or narrow-gap semiconductor, depending on whether or not there opens a gap between the third and fourth band. On the basis of the A-site HOMO being about 0.1 eV higher than those of B- and C-sites, at room temperature the electrons are easily activated across this gap: they conclude that α -(BEDT-TTF) $_2$ I $_3$ is a narrow-gap semiconductor which acts as a 2D semimetal at high temperatures. As mentioned in Section 1.3.1, Hotta's unified model for BEDT-TTF systems cannot interpret the ground state or MI transition of α -(BEDT-TTF) $_2$ I $_3$ in a straightforward manner. Figure 1.29 shows the α -(BEDT-TTF) $_2$ I $_3$ band structure obtained by Hotta's model from the θ -type calculations (left), and dimerized model (right). If only the two largest transfer integrals t_{p3} and t_{p4} are taken into account, the four bands of α -(BEDT-TTF) $_2$ I $_3$ are essentially separated with three completely filled bands and an empty single band, and a band-insulating state is expected. In reality, a semimetallic state with small pockets is realized due to the small modifications of the band structure coming from other transfer integrals.

From the examination of bond length Mori's early first-principle calculations also predict a low-temperature charge disproportionation with holes localized at the A and A' sites. [23] Indeed, at $T_{CO} = 135$ K the α -(BEDT-TTF) $_2$ I $_3$ undergoes a metal-to-insulator phase transition [117] with a temperature-dependent gap opening in charge and spin sector which indicates the ground state is insulating and diamagnetic. Molecular deformations are observed in the insulating phase which are at the origin of charge disproportionation. The first experimental evidence of a charge disproportionation was

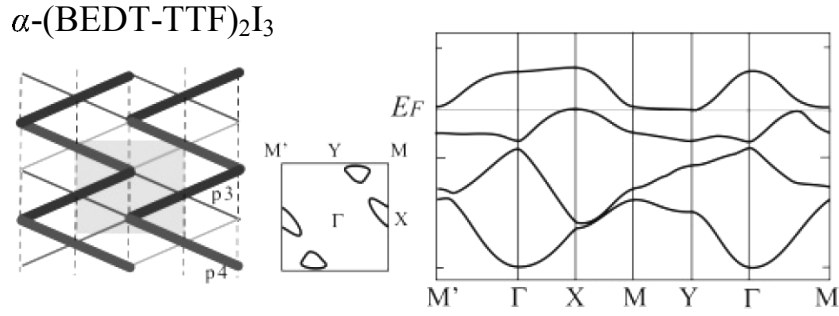


Figure 1.29 – Simplified 2D plane of α -(BEDT-TTF) $_2$ I $_3$ together with its band structure and Fermi surface based on Hotta’s unified model. [92] From Seo *et al.* [85]

the ^{13}C -NMR measurements by Takano *et al.* [25]. In the metallic phase the relaxation rate T_1^{-1} has only one component and indicates all molecules have the same charge density. However, below T_{CO} the T_1^{-1} consists of two components which decrease exponentially at low temperatures. The two relaxation components are each associated with a so-called Pake doublet appearing in the low-temperature ^{13}C -NMR. A Pake doublet standardly appears as a split resonance signal due to dipolar interaction between ^{13}C sites, however, it can also further split into quartets if the difference in Knight shift and chemical shift is large. Two Pake doublets and two associated relaxation components indicate the existence of two non-equivalent environments around the ^{13}C sites, i.e., a BEDT-TTF molecule which is almost neutral, and one with a larger charge density.

Charge disproportionation, albeit with different values of charge, has also been confirmed by vibrational infrared and Raman spectroscopy. [28, 118, 119, 29] Frequencies of certain intramolecular vibration modes of BEDT-TTF crystals are sensitive to the oxydation number of molecules, in other words to the molecular charge. [118] Systematic Raman scattering studies have been performed at room temperature on various BEDT-TTF salts in different oxidation states. [120, 121, 122] Vibrational modes based on intramolecular vibrations of the central C=C bonds practically do not depend on the particular salt or polytype. Indeed, a significant shift to lower frequencies is found for the $\nu_2(A_g)$, $\nu_3(A_g)$ and $\nu_6(A_g)$ modes as the charge of a BEDT-TTF molecule changes from neutral to $+2e$ (see Fig. 1.30). Also, the infrared-active $\nu_{27}(B_{1u})$ mode, an out-of-phase contraction of the C=C double bonds in the BEDT-TTF rings, can be observed with electric field perpendicular to the molecular planes of single crystals, in powder pellets, or on symmetry breaking in Raman scattering. [123] The frequency of this mode is sensitive to the molecular charge population (see Fig. 1.31) and splits upon passing through a charge-ordering phase transition. [28, 124] In particular, infrared spectroscopy experiments on α -(BEDT-TTF) $_2$ I $_3$ powder samples by Moldenhauer *et al.* have shown

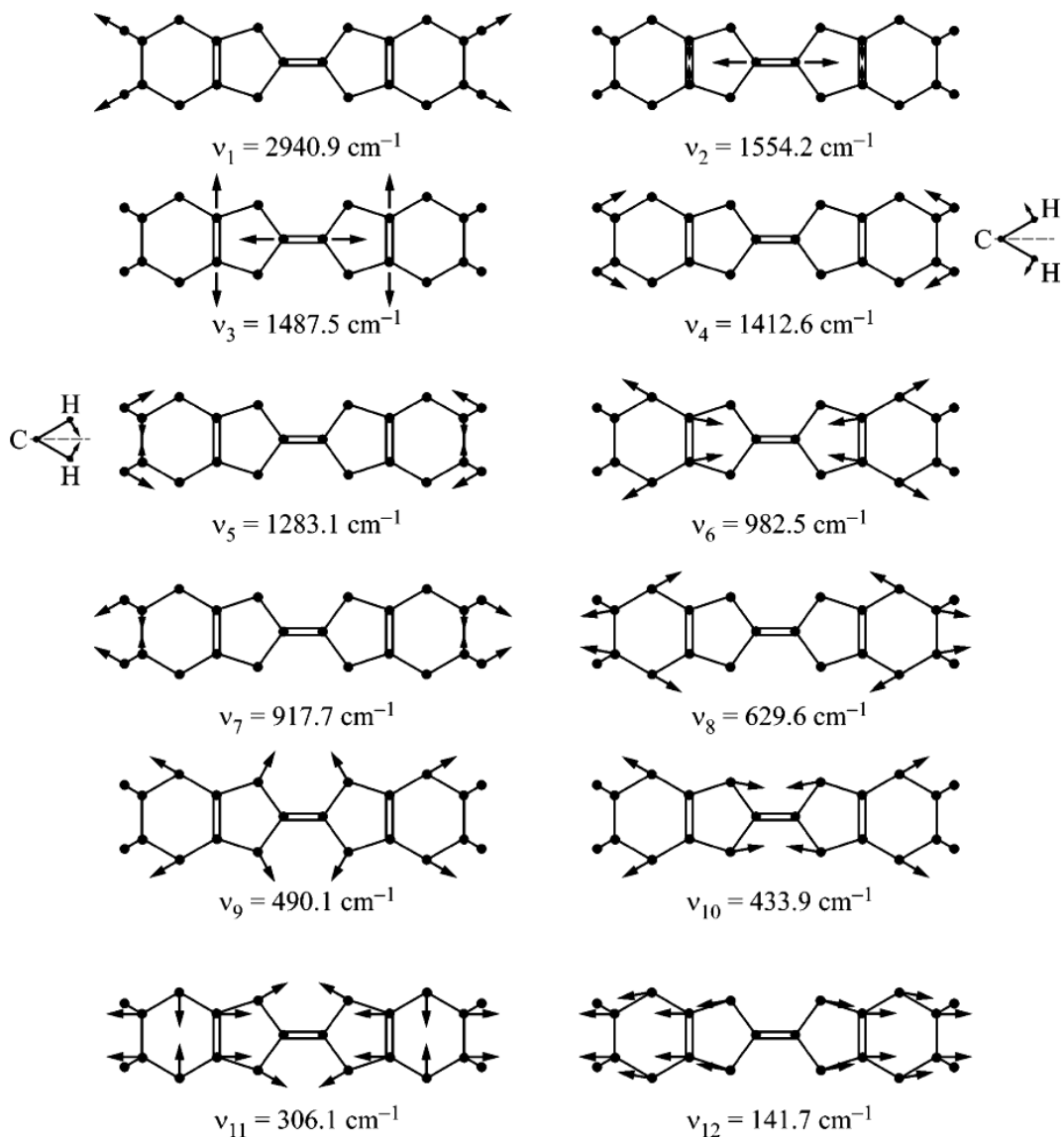


Figure 1.30 – Atomic displacements and frequencies for the 12 totally symmetric A_g modes of the neutral BEDT-TTF molecule. All of the modes are in-plane except the C-H bends in ν_4 and ν_5 . From Dressel *et al.* [118]

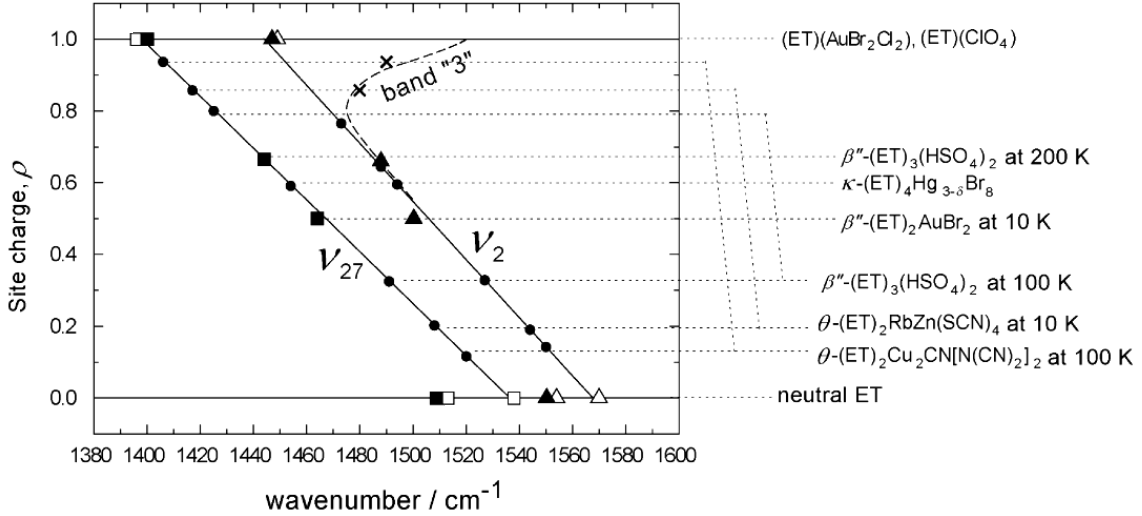


Figure 1.31 – Infrared frequencies of the $\nu_{27}(B_{1u})$ mode as well as Raman shift of the $\nu_2(A_g)$ mode as a function of molecular charge in different BEDT-TTF salts. After Yamamoto *et al.* [124]

that due to charge disproportionation two new bands emerge at the metal-insulator transition T_{CO} which are arranged symmetrically around the $\nu_{27}(B_{1u})$ at 1477 cm^{-1} . The frequencies of the $\nu_{27}(B_{1u})$ modes allow for an evaluation of average charge per donor molecule: $+0.15e$, $+0.52e$ and $+0.9e$ [28] meaning that a charge localization takes place in two crystallographically different molecules, while the others maintain an average charge of approximately $+0.5e$. These findings are also confirmed by Raman scattering measured by Wojciechowski *et al.* [29] By observing the splitting of the $\nu_2(A_g)$ mode into two bands, the Raman spectroscopy experiment finds a low-temperature charge disproportionation of $+0.2e$ to $+0.8e$ in a so-called horizontal-stripe arrangement with charge-rich sites being either (A,B) or (A',B).

The long-range formation of a horizontal-stripe charge order has further been investigated by Kakiuchi *et al.* using synchrotron x-ray diffraction. [27] On the basis of anomalous scattering effects the information about charge can be extracted for each BEDT-TTF site in the unit cell (see Fig. 1.32). Most notably, a small but discernable long-range charge disproportionation is already present in the metallic phase ($A=A' = 0.49(3)e$, $B = 0.57(4)e$, $C = 0.41(3)e$) which remains almost constant down to T_{CO} . At the phase transition an abrupt development of large charge disproportionation ($A = 0.82(9)$, $A' = 0.29(9)$, $B = 0.73(9)$, $C = 0.26(9)$) leads to a charge order comprising “horizontal” charge stripes of charge-poor (CP) sites, the A' and C molecules, and charge-rich (CR) sites (A and B molecules) along the b crystallographic axis, as depicted in Fig. 1.33. Kakiuchi *et al.* have also calculated the overlap integral $|S|$ between the

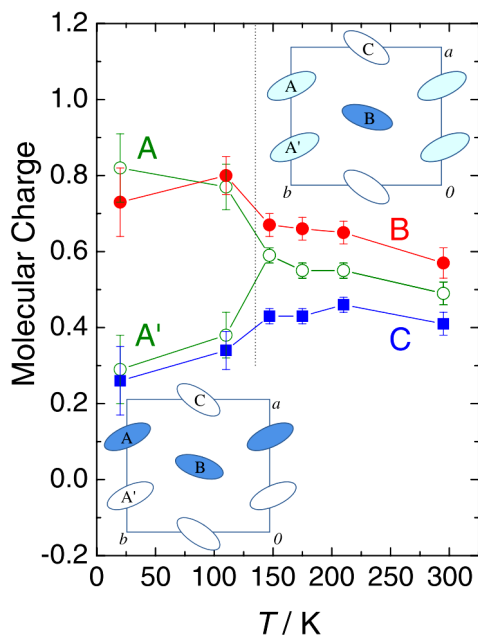


Figure 1.32 – Temperature dependence of molecular charges obtained by anomalous x-ray scattering effects. The charge disproportionation increases significantly at T_{CO} . From Kakiuchi *et al.* [27]

neighboring molecules, which is approximately proportional to the transfer integrals, based on tight-binding approximation and a molecular orbital calculation with the extended Hückel method. [27] Their results indicate a 2D modulation of overlap integrals between the BEDT-TTF sites. Based on the zig-zag path of largest overlap integrals they propose a $2k_F$ charge ordering structure, which would result in both charge and spin gap. Most notably, such a charge ordering evidently lacks strong nesting effects crucial for a standard Peierls instability.

The effects of charge ordering are visible as a drastic change in electrical transport properties. At the phase transition a significant drop of α -(BEDT-TTF) $_2$ I $_3$ conductivity has been reported within the conducting molecular ab plane (see Fig. 1.34). The onset of frequency-dependent transport in the microwave region is also intriguing, however no clear evidence was found for a collective mode analog to e.g. those found in CDWs. [117] Various authors reported a temperature-dependent transport gap (about 50 meV at 50 K) in the insulating phase within the conducting plane, as well as an at least 1000 times smaller conductivity perpendicular to the molecular planes. [24, 117] Early transport measurements did not note the electric field orientation within the ab plane, which leaves open the possibility of anisotropic conduction. Apart from a THz study on carefully oriented crystals, [125] no systematic exploration of transport anisotropy had been attempted.

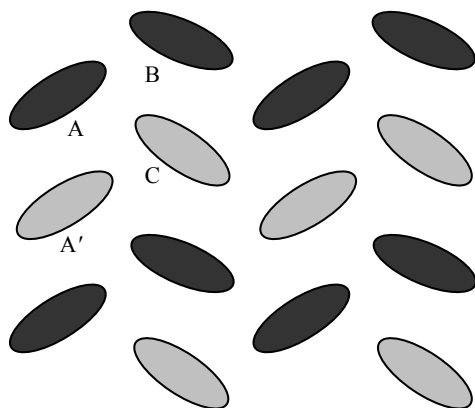


Figure 1.33 – Stripe arrangement in the ab conducting donor layer of α -(BEDT-TTF) $_2$ I $_3$ in the charge-ordered state. Dark- and light-gray ovals denote charge-rich and charge-poor molecules, respectively.

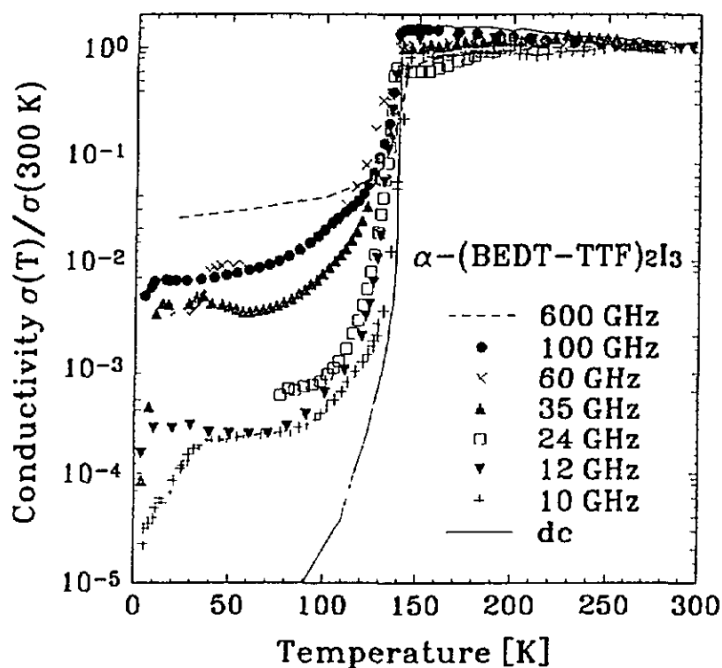


Figure 1.34 – The temperature-dependent conductivity of α -(BEDT-TTF) $_2$ I $_3$ at various frequencies from dc to microwave range. From Dressel *et al.* [117]

Lastly, applied hydrostatic pressure has been found to reduce the T_{CO} of α -(BEDT-TTF) $_2$ I $_3$, eventually suppressing the phase transition completely at 20 kbar and rendering the resistivity almost temperature-independent from 300 down to 1.5 K. [126] Hall effect measurements at such pressures suggest that the carrier density decreases from 10^{21} cm^{-3} (at 300 K) to 10^{15} cm^{-3} (at 1 K), while the carrier mobility increases from $10 \text{ cm}^2/(\text{V}\cdot\text{s})$ (at 300 K) to $10^5 \text{ cm}^2/(\text{V}\cdot\text{s})$ (at 1 K). This has been interpreted as evidence of a narrow-gap semiconducting state with the gap $E_g \sim 1 \text{ meV}$. Further, recent band calculations [127, 128] claim that the electrons in the metallic phase of α -(BEDT-TTF) $_2$ I $_3$, even at ambient pressure, can be considered massless, the so-called zerogap or Dirac fermions. Dirac fermions are well known in graphite, where their cone-like dispersion is centered around high-symmetry points in the first Brillouin zone. In metallic α -(BEDT-TTF) $_2$ I $_3$ due to inversion symmetry two Dirac cones are expected which are tilted (energy depends on direction of impulse) and centered at non-high-symmetry points $(k_x, k_y) \approx \pm(-0.23, 0.30)$. This has been corroborated by latter-date Hall effect measurements. [129]

1.3.4 Open questions

Of many open questions in α -(BEDT-TTF) $_2$ I $_3$, the ones to be tackled here are once again closely related to its electrical transport properties. The first is a basic question of conductivity anisotropy and its behavior with temperature. A systematic study of the dependence of electric transport on direction of electric field requires samples cut from a single monocrystal oriented along the crystal a - or b -axis. A far-reaching problem is that of the type of charge ordering in α -(BEDT-TTF) $_2$ I $_3$: the literature does not agree whether it is of Wigner-type (with electron charges localized at molecular sites), or some other state with a perhaps more delocalized nature. Additionally, and similar to the case of BaVS $_3$, to the best of our knowledge no work has been reported on possible collective modes above the ground state.

Chapter 2

Overview of theory

2.1 Standard charge-density waves: The Peierls transition

Due to the particular geometry of Fermi surface in conductive systems with highly anisotropic band structures, the correlation effects lead to phase transitions and to different collective modes at low temperatures. As already noted in the introduction, different ground states emerge such as superconductivity, spin- or charge-density waves, depending on the details of interactions the electrons are subjected to.

Before delving into insulating ground states induced by strong Coulomb interactions between electrons, it is beneficial to first examine the relatively simple case where the electron-phonon coupling is the dominant interaction. Back in 1955 it was pointed out by Peierls that a one-dimensional electron gas coupled to the lattice cannot be stable at low temperatures. [130] Instead of being a metal, its ground state is characterized by a gapped single-particle spectrum. Also, a collective mode appears which can be described by electron-hole pairs involving double the Fermi wave vector, $Q = 2k_F$. The charge density of such a system varies sinusoidally with the modulation vector $2k_F$. In fact, this feature was at the time considered a plausible explanation of superconductivity: Frölich noted that in the absence of pinning and damping this electron-hole condensate could in principle facilitate a superconducting current. [131] Here we set up this simple one-dimensional model and show its electrodynamic properties.

Starting from a one-dimensional metal with lattice constant a at zero temperature, in the absence of electron-electron or electron-phonon interaction the ground state corresponds to the simple situation shown by Fig. 2.1(a): electrons occupy all the states up to

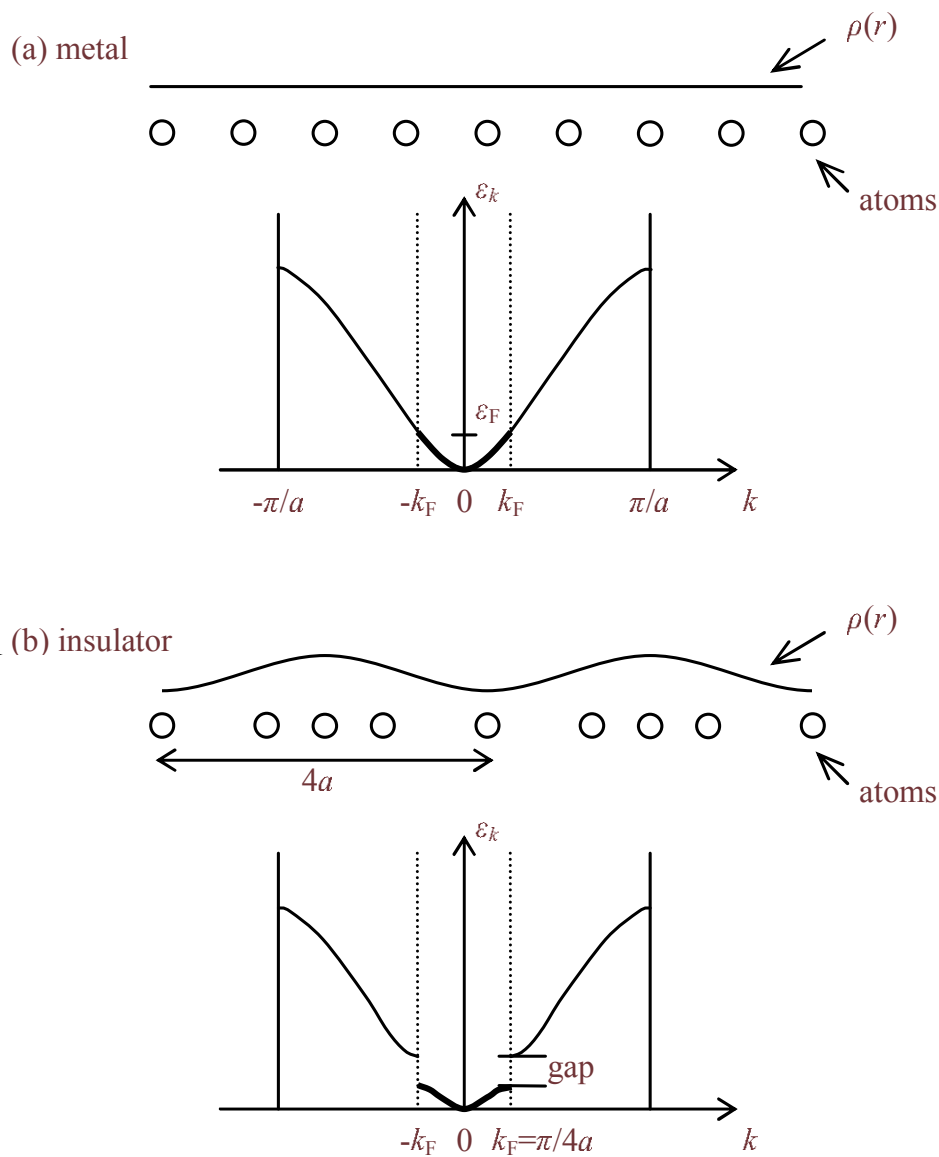


Figure 2.1 – Peierls distortion in a one-dimensional metal with a quarter-filled band: the effect on charge density $\rho(r)$, atomic positions and electron band structure for (a) undistorted metal above the Peierls transition, (b) Peierls charge-density wave insulator.

the Fermi energy ϵ_F with no influence on the lattice. In the presence of electron-phonon coupling it becomes energetically favorable to introduce a sinusoidal lattice distortion with period

$$\lambda = \frac{2\pi}{2k_F} \quad (2.1)$$

directly related to the Fermi wave vector k_F . This new superstructure opens up a gap at the Fermi level [see Fig. 2.1(b)]. Since the single-particle energy of occupied states near the newly-opened gap are being reduced, the electronic contribution to total energy is lowered. For small lattice displacement amplitude u it can be shown that the single-particle gap Δ is proportional to u , and that the decrease of electronic energy behaves as $\propto u^2 \ln u$. The concomitant increase of elastic energy is proportional only to u^2 and the total energy of the distorted system is smaller than that of an undistorted metal: **the one-dimensional metal is inherently unstable to static $2k_F$ distortions.**

Going now to finite temperatures, the electrons excited above the single-particle gap screen the electron-phonon interaction. When this effect is taken into account, the gap and lattice distortion become reduced. This eventually leads to the Peierls transition at temperature T_P where the system behaves metallic above the transition, and as a semiconductor below it with a temperature-dependent gap $\Delta(T)$. [130] The Frölich 1D electron-phonon Hamiltonian captures the main features of a charge-density wave in a real material, i.e., in the presence of electron-phonon coupling:

$$H = \sum_{k,\sigma} \epsilon_k c_{k,\sigma}^\dagger c_{k,\sigma} + \sum_q \hbar\omega_q (b_q^\dagger b_q + b_{-q}^\dagger b_{-q}) + \sum_{k,q,\sigma} g(k) c_{k+q,\sigma}^\dagger c_{k,\sigma} (b_q + b_{-q}^\dagger). \quad (2.2)$$

Here $c_{k,\sigma}^\dagger$ and b_q^\dagger are the creation operators for 1D Bloch electron and a longitudinal phonon of wave vector q with respective dispersions ϵ_k and ω_q . $g(k)$ is the coupling constant of electron-phonon interaction. The mean-field approach simplifies this problem so that only the phonon at $Q = 2k_F$ needs be considered. Introducing the complex order parameter

$$\Delta e^{i\varphi} = g(2k_F) \langle b_{2k_F} + b_{-2k_F}^\dagger \rangle \quad (2.3)$$

allows us to write the lattice displacement as

$$\langle b_{2k_F} + b_{-2k_F}^\dagger \rangle + \text{c.c.} = \frac{2\Delta}{g(2k_F)} \cos(2k_F x + \varphi) \quad (2.4)$$

where c.c. indicates the complex or hermitian conjugate.

The electronic part of the Hamiltonian can be self-consistently diagonalized in the

mean-field approximation by replacing phonon operators b_{2k_F} by averaged $\langle b_{2k_F} \rangle$ and linearizing the electron dispersion near Fermi level, $\epsilon_k = v_F(|k| - k_F)$. In a procedure analogous to BCS treatment of superconductivity, the gap can then be expressed using the dimensionless electron-phonon coupling constant $\Lambda = g^2(2k_F)(\omega_{2k_F}\epsilon_{k_F})^{-1}$, and at zero temperature is equal to

$$\Delta = 2D \exp(-1/\Lambda). \quad (2.5)$$

As opposed to BCS, where cutoff D is defined by the characteristic Debye frequency, here D is the one-dimensional bandwidth. From the BCS-like temperature dependence of Δ , the ordering parameter vanishes at the transition temperature $T_P = \Delta(T = 0)/1.76k_B$. The lattice superstructure at $2k_F$ is accompanied by a spatially-dependent electron charge modulation $n(x)$ which is at zero temperature evaluated to

$$n(x) = n_0 + \frac{\Delta n_0}{\Lambda v_F k_F} \cos(2k_F x + \varphi). \quad (2.6)$$

Here $n_0 = \pi/k_F$ is the electron density when electron-phonon coupling is turned off. A CDW wavelength is given by $\lambda = \pi/k_F = Na$ when expressed in terms of the original lattice constant a . If N is an integer multiplier, the CDW is called commensurate. When N is non-integer or a very large integer, the system is considered to be incommensurate.

The appearance single-particle gap and the form of complex order parameter are reminiscent of BCS superconductivity. As opposed to the BCS theory, where electrons of opposite spin and wave vectors form Cooper pairs responsible for superconductivity, the collective mode in Peierls CDWs is formed by combining electron-hole pairs from opposite sides of the Fermi surface (separated in impulse space by $2k_F$). As a point of interest, the cutoff frequency D , which appears in the gap equation (2.5), is typically large compared to the characteristic phonon frequencies which define the superconducting gap. Hence, the Peierls transition happens at higher temperatures larger than the BCS superconducting transitions.

Generally, the mean field description ignores the one-dimensional fluctuations and, consequently, leads to a finite transition temperature even for a strictly one-dimensional metal. It is well-known that 1D fluctuations strongly suppress the transition, and for a single metallic chain a phase transition does not occur at finite temperatures. Coupling between neighboring chains, either due to overlap integrals or Coulomb repulsion, restores the phase transition at a finite temperature, with most of the 1D correlations preserved in the ordered phase. [131] Generally one can expect that chain-structured, i.e., quasi-1D materials which are metallic at high temperatures actually show strong

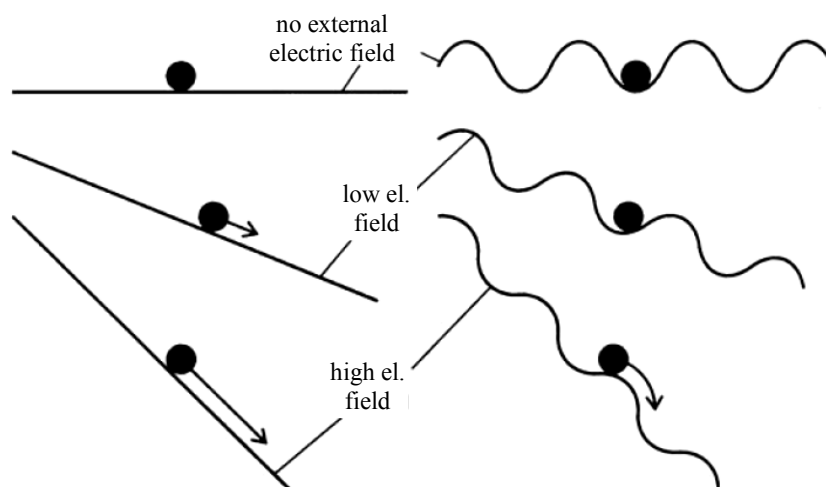


Figure 2.2 – An external constant electric field applied to (left) a free charged particle, and (right) a charged particle representing the CDW condensate in the pinning potential. The CDW condensate participates in dc, i.e., sliding transport only when the electric field is larger than a threshold field.

1D correlations along the chain direction in the form of a wide fluctuating region around the Peierls transition. Below the ordering temperature for single chains the correlations between neighboring chains couple together, further leading to a three-dimensional long-range order: perpendicular to the chains the periodic charge/lattice modulations are either in-phase or out-of-phase on neighboring chains, depending on the relative magnitude of the perpendicular electron bandwidth and Coulomb interactions. [132, 133, 131]

2.1.1 Charge-density wave sliding motion

At the beginning of this chapter we mention Frölich’s idea that the motion of the CDW condensate could contribute to the total conductivity of the system. All that is needed is to unpin the relatively massive CDW condensate from the background by a sufficiently strong electric field.

In the case of a commensurate CDW we can utilize a classical approximation to describe its dynamics. We are interested in sliding of the condensate an applied constant electric field. We describe the density wave condensate as a massive charged particle positioned at a minimum of the periodic pinning potential of the lattice $V_{\text{pinning}} = -V_0 \cos Kx$, where K is the pinning potential wave vector. A linear external potential $V_{\text{ext}} = -Ex$ is applied as shown in Fig. 2.2 which tilts the pinning potential:

$$m^* \frac{d^2x}{dt^2} + \gamma \frac{dx}{dt} = -e \frac{d(V_{\text{pinning}} + V_{\text{ext}})}{dx} \quad (2.7)$$

where m^* is the condensate mass, γ the damping constant. When the external field is large enough that no local minima remain in the total potential, the CDW becomes free to slide. It is not difficult to see that this amounts to taking all the derivations $d^i x/dx^i$ to be zero, which gives the so-called threshold field

$$E_T = KV_0. \quad (2.8)$$

At fields below E_T only single-particle transport contributes to total conductivity. Above E_T the condensate slides as well and enhances the conductivity.

For the incommensurate CDWs, the pinning to the lattice is infinitesimally small since the CDW and lattice periods do not match and on average there are no clear spatial minima of their interaction. In such a case pinning to randomly distributed impurities becomes important, [134] giving non-zero but small E_T typically on the scale of 10 meV/cm. By a similar token, commensurate pinning becomes less relevant as the commensurability $N = \lambda/a$ of the density waves rises, and at $N \geq 4$ impurity pinning becomes the dominant effect. [135]

2.1.2 Phason response

Excitations above the CDW condensate involve fluctuations of the order parameter Δ , Eq. (2.3), as a function of position and time. Fluctuation of its amplitude and phase are usually assumed to be decoupled and are presented in the form $\Delta(x, t) = (\Delta_0 + \delta)e^{i\varphi'}$. Lee, Rice and Anderson have evaluated the dispersion relations $\omega(q)$ of these modes. [134] The amplitude mode is Raman-active with an optical dispersion ($\omega(q=0) \neq 0$), while the phason mode is infrared-active with an acoustic (gapless) dispersion ($\omega(q=0) = 0$). Since phase excitations carry a dipole moment, the gapless phason mode is closely related to the experimentally observable dc and ac conductivity in a CDW phase.

The coupling of neighboring chains in real materials alters somewhat the phason mode dispersion to the following form: [133, 136]

$$\omega_{\text{ph}}^2 \propto v_{\text{ph}}^2 q_z^2 + \omega_L^2 \frac{q_z^2}{q_z^2 + q_{\perp}^2}. \quad (2.9)$$

where the second term is the screened Coulomb singularity. In an insulator with no free carriers, the Coulomb interaction is screened when the charge/lattice modulations on neighboring chains are locked in phase ($q_{\perp} < q_z$) which raises the phason frequency to $\omega_{\text{ph}}(q=0) \approx \omega_L$. Phasons with other wave vectors, $q_{\perp} > q_z$, remain acoustic.

In real materials where free carriers screen the Coulomb interaction, the translational invariance is lifted through the interactions of CDW with lattice and impurities, which locally distorts the phase of the condensate around pinning centers. Since free carrier screening is weak at $2k_F$, pinning effectively shifts the collective mode to a finite pinning frequency usually denoted as Ω_0 .

A more realistic analysis by Fukuyama, Lee and Rice takes into account that the pinning background in real materials not only gives a pinned mode but also an additional overdamped low-frequency relaxation. [137] They regard an incommensurate CDW as a deformable classical medium which is free to oscillate parallel to external field E along the chains:

$$m^* \frac{d^2\varphi}{dt^2} + \gamma_0 \frac{d\varphi}{dt} - \kappa \nabla^2 \varphi + \sum_i V(\mathbf{r} - \mathbf{R}_i) \rho_0 \sin[\mathbf{Q} \cdot \mathbf{r} + \varphi(\mathbf{r})] = \rho_c E_z / Q_z \quad (2.10)$$

where κ is the elastic modulus of the CDW when deformed due to pinning, \mathbf{Q} is the nesting vector, and the charge modulation is given by $\rho(\mathbf{r}) = \rho_c + \rho_0 \cos[\mathbf{Q} \cdot \mathbf{r} + \varphi(\mathbf{r})]$. This problem is treated as linear response of a two-fluid model in which the ‘‘CDW-fluid’’ and free carriers interact only via the electromagnetic field. Introducing the variable $u = \varphi/Q_z$ and linearizing Eq. (2.10) around a static equilibrium state $u_0(\mathbf{r})$ gives

$$\sum_{q'} [G_0^{-1}(\mathbf{q}, \omega) \delta_{q, q'} + V(\mathbf{q} - \mathbf{q}')] u(\mathbf{q}', \omega) = \rho_c E_z(\mathbf{q}, \omega) \quad (2.11)$$

where $G_0^{-1}(\mathbf{q}, \omega) = -m^* \omega^2 - i\gamma_0 \omega + \mathbf{q} \cdot \kappa \cdot \mathbf{q}$ is the response function in the absence of interaction V . Writing the response function in the presence of field $G_E^{-1}(\mathbf{q}, \mathbf{q}'; \omega) = G_0^{-1}(\mathbf{q}, \omega) + V(\mathbf{q} - \mathbf{q}')$ gives of course the formal solution $u(\mathbf{q}, \omega) = \rho_c \sum_{q'} G_E(\mathbf{q}, \mathbf{q}'; \omega) E_z(\mathbf{q}', \omega)$. This can be inserted into the expression for total induced current, $\mathbf{j}(\mathbf{r}, t) = \tilde{\sigma} \mathbf{E} + \rho_c \dot{u} \hat{\mathbf{z}}$ where $\tilde{\sigma} = \sigma - i\omega \varepsilon$ is the complex conductivity tensor which accounts for the (real) conductivity and dielectric tensors σ and ε , and which is assumed to be diagonal. Finally, the CDW condensate conductivity along the electric field

$$[\sigma_{\text{tot}}(\mathbf{q}, \mathbf{q}'; \omega)]_z = \tilde{\sigma}_z \delta_{\mathbf{q}, \mathbf{q}'} - i\omega \rho_c^2 G_E(\mathbf{q}, \mathbf{q}'; \omega). \quad (2.12)$$

First let us see if the Fukuyama-Lee-Rice model reproduces the pinned mode. If we assume a simple uniform pinning potential $V(\mathbf{q}) = V_0 \delta_{\mathbf{q}, 0}$, the previous expression is simplified to

$$\sigma_{\text{tot}}(0, \omega) = -i\omega \varepsilon_{\text{tot}} = \sigma_z - i\omega \varepsilon_z - \frac{i\omega \rho_c^2}{G_0^{-1}(0, \omega) + V_0}. \quad (2.13)$$

The total dielectric function ε_{tot} can now be separated into a longitudinal and transverse response. The transverse response is easily found by searching for singularities of the dielectric function, which appear at the pinning frequency

$$\Omega_0^2 = V_0/m^*. \quad (2.14)$$

The longitudinal response corresponds to zeros of total dielectric function ε_{tot} . At high frequencies, $\omega \gg \sigma_z/\varepsilon_z$, and the plasmon-like longitudinal mode is found at $\omega_L^2 = V_0/m^* + \rho_c^2/m^*\varepsilon_z$, above the pinned transverse mode. At low frequencies the longitudinal mode is found at

$$\tau_0^{-1} = \gamma/V_0 \approx \rho_c^2/\sigma_z V_0 \quad (2.15)$$

where we note that free carriers also increase the effective damping $\gamma = \gamma_0 + \rho_c^2/\sigma_z$.

Uniformly-pinned Fukuyama-Lee-Rice model indeed gives us a transverse pinned mode which can be identified with the one found in the classical model. The longitudinal response obtained in this way is surprising: strictly longitudinal excitations should not be observable due to being at the zeros of the dielectric function. On the contrary, a longitudinal overdamped relaxation is experimentally observed. We account for this fact by introducing nonuniform, random pinning of the CDW. Disorder of local phase in a pinned CDW has a typical length scale ξ , the Lee-Rice length below which the CDW phase can be considered constant. We are going to introduce the disordered nature of CDW response in a nonuniformly pinned configuration by calculating local response to external charge, namely the free carriers which are always present in real materials. The response function now takes the form

$$G_\rho^{-1}(\mathbf{q}, \omega) = G_E^{-1}(\mathbf{q}, \omega) - i\omega\rho_c^2 R(\mathbf{q}, \omega) \quad (2.16)$$

with the shorthand

$$R(\mathbf{q}, \omega) = \frac{q_z^2 - i\omega\mu_0\tilde{\sigma}_\perp}{\mathbf{q} \cdot \tilde{\sigma} \cdot \mathbf{q} - i\omega\mu_0\tilde{\sigma}_\perp\tilde{\sigma}_z} \quad (2.17)$$

It is reasonable to assume that skin depths $\omega\mu_0\tilde{\sigma}_0$ are larger than CDW localization lengths along and perpendicular to the chains, which leads to $R(\mathbf{q}, \omega) = \tilde{\sigma}_z^{-1} [1 + (\tilde{\sigma}_\perp/\tilde{\sigma}_z)(\mathbf{q}_\perp/\mathbf{q}_z)^2]^{-1}$. Further simplification is possible taking large conductivity anisotropy $\tilde{\sigma}_z/\tilde{\sigma}_\perp > (\xi_z/\xi_\perp)^2$ where we finally get $R(\mathbf{q}, \omega) = 1/\tilde{\sigma}_z(\omega)$. In such a situation the local mode appears essentially longitudinal in character, contributes in transport and can be observed by low-frequency spectroscopic techniques.

2.2 Strongly interacting electrons in 1D

Up to now we have relied on the electron-phonon interaction to facilitate the transition from metal to a new phase, the charge-density wave. In this we have did not invoke the electron-electron interaction. However, in a number of phenomena - high-temperature superconductivity, Mott insulator, charge ordering, orbital ordering - the Coulomb interaction between electrons becomes crucial.

One of the earliest and simplest examples which demonstrates the importance of electron-electron interactions can be seen in the electron gas at low densities. It was predicted by E. Wigner in 1934 that an electron gas would crystallize and form a lattice when the density is less than a critical value. [138] If electrons were classical particles, interactions at low density would be negligible: low density means long distances between electrons, and since the interactions decay with distance (as inverse distance for Coulomb law, and exponentially if screening is in effect) one could disregard or treat them perturbatively.

Electrons however are quantum particles, and quantum theory gives a fundamentally different answer. Taking n as the average density of electrons, the average distance between them is $a \sim n^{-1/3}$. For Coulomb interactions, the typical scale of the potential energy is $E_{\text{Coulomb}} \sim e^2/a$. The kinetic energy is as always given as $E_{\text{kin}} = k^2/2m$, but for electrons as Fermi-particles the only relevant values of the momenta lie close to the Fermi surface. If one estimates the Fermi momentum from the electron density as $\alpha \sim \hbar/a$, the kinetic energy scale is of the order of $E_{\text{kin}} \sim \hbar^2/(2ma^2) \propto 1/a^2$. Hence, at low densities n (large distances a) the interaction term clearly remains the dominant contribution to total energy.

The ground state of a low-density interacting electron system is an insulating electron crystal, the so-called Wigner crystal. Quantum Monte Carlo simulations indicate that the uniform 3D electron gas crystallizes into a cubic body-centered lattice at $a = 106r_b$ (r_b is the Bohr radius), and a 2D gas into a triangular lattice at roughly $a = 35r_b$. [139, 140] In 1D the system crystallizes into a uniformly-spaced arrangement of localized electrons. Experimental realizations are difficult and scarce due to the sensitivity of Wigner crystal to disorder: sample impurities induce Anderson localization before a Wigner crystal can form, or quantum fluctuations destroy the ordering. Notable solid-state systems displaying Wigner crystallization include the organic quarter-filled quasi-1D conductor (DI-DCNQI)₂Ag, [141] quantum well systems [142] and 2D electron systems based on GaAs/AlGaAs semiconductors. [143]

2.2.1 Extended Hubbard model in 1D

We further examine the effects of Coulomb interaction on electrons in the 1D tight-binding approximation. A common description starts with the simplest Hubbard Hamiltonian: [144, 145]

$$H = -t \sum_{j,\sigma} \left(c_{j,\sigma}^\dagger c_{j+1,\sigma} + \text{c.c.} \right) + U \sum_j n_{j,\uparrow} n_{j,\downarrow}. \quad (2.18)$$

This is a model of tight-binding type with one atomic orbital per lattice site j with spin $\sigma = \uparrow$ or \downarrow . The creation operator $c_{j,\sigma}^\dagger$ inserts an electron into the atomic orbital at site j and the annihilation operator $c_{j+1,\sigma}$ removes it from the nearest-neighbor site $j + 1$. The first term of the Hamiltonian (2.18) describes the kinetic energy due to electron hopping, i.e., it is the effect of orbital overlap between the neighboring sites. t is the overlap integral of the tight-binding theory which gives the bandwidth of $4t$. The second, interaction term competes with the first one by adding extra energy U whenever two electrons occupy the same site ($n_{j,\sigma} = c_{j,\sigma}^\dagger c_{j,\sigma}$ is the standard particle number operator). Increasing the parameter U/t traverses the whole range from the independent electron band theory to the fully localized Mott insulator (see Fig. 2.3). [146, 147, 148, 149].

The extended Hubbard model further takes into account the Coulomb interaction between neighboring sites V . It gives a particularly simple picture of possible states in a system with large U in which t and the inter-site interaction V -terms are treated as perturbations: [150, 151]

$$H = -t \sum_{j,\sigma} \left(c_{j,\sigma}^\dagger c_{j+1,\sigma} + \text{c.c.} \right) + U \sum_j n_{j,\uparrow} n_{j,\downarrow} + V \sum_{j,\sigma,\sigma'} n_{j,\sigma} n_{j+1,\sigma'}. \quad (2.19)$$

The properties of the system depend upon the sign of U . Positive U corresponds to repulsive on-site interaction between the electrons of the opposite spin occupying the same orbital. Doubly-occupied sites are thus made energetically unfavorable and in the ground state all sites are either singly occupied or empty. However, the effective on-site Coulomb repulsion may be reduced and can even lead to the attraction, i.e. $U < 0$. It is instructive here to schematically present the possible orderings in the one-dimensional (1D) electron gas of a single chain. [152]

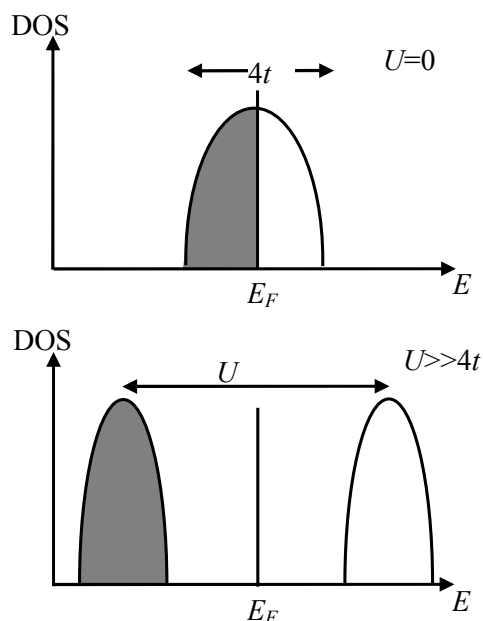


Figure 2.3 – The electronic density of states (DOS) as a function of the on-site Coulomb interaction U . Upper panel: For the case of entirely independent electrons (bandwidth is $4t$, no Coulomb interaction $U = 0$) and half filling, the Fermi level E_F is located in the middle of the band and the system is metallic. Lower panel: Large on-site Coulomb repulsion $U \gg 4t$ splits the band into a lower and upper Hubbard band separated by the Mott-Hubbard gap, making the system an insulator.

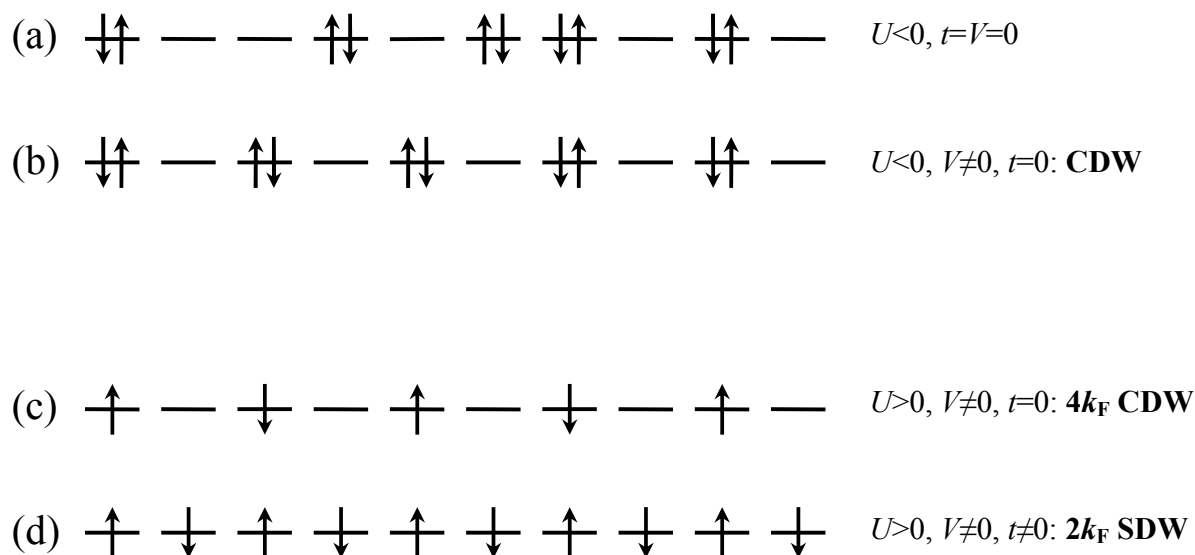


Figure 2.4 – Different configurations of electrons, spin up (\uparrow), or spin down (\downarrow) on a separated chain in the presence of a strong on-site interaction U , as suggested by Emery. [152]

On-site attraction, $U < 0$

On-site attraction makes it advantageous for electrons with opposite spins to form pairs, preferring either empty or doubly-occupied sites [see Fig. 2.4(a), (b)]. In the case of zero transfer integral t and inter-site interaction V , the ground state is highly degenerate because the energy does not depend on the choice of occupied sites [Fig. 2.4(a)]. The charge-density wave states occur in an extreme form when there is a finite inter-site repulsion $V > 0$ but still no hopping t , i.e., $t = 0$, as shown in Fig. 2.4(b) for the half-filled band. The pairs are then equally spaced to minimize energy. Along the chain the charge density varies periodically from 1 to 0 with the wave vector of $2k_F$. More realistically, for non-zero hopping (not shown) the amplitude of the charge density modulation is significantly smaller. The density modulation does not even have to be commensurate with the inter-site distance. Nevertheless, the wave vector $2k_F$ always characterizes the periodicity of the CDW. For the case of inter-site attraction, $V < 0$ (not shown), singlet superconductivity can arise when hopping term t is included. The electron pairs are bound in a singlet state and behave as bosons which may become superfluid (and hence superconducting since they are charged) at low enough temperatures. Triplet superconductivity with parallel spins will not occur because the electrons are bound into singlet pairs before long-range triplet correlations can build up.

On-site repulsion, $U > 0$

Anderson first pointed out that in the strongly repulsive case, $U > 0$, and $U \gg t$ in a half-filled band, when all sites are singly occupied, the extended Hubbard model can be mapped onto a spin-1/2 Heisenberg chain with electrons Mott-localized on the sites. [153] Virtual hopping produces an effective antiferromagnetic exchange interaction $J = (4t^2/U) > 0$ between the neighboring spins. Such an antiferromagnetic insulator is described by a $t - J$ Hamiltonian:

$$H = -t \sum_{j,\sigma} \left(c_{j,\sigma}^\dagger c_{j+1,\sigma} + \text{c.c.} \right) + J \sum_j \mathbf{S}_j \cdot \mathbf{S}_{j+1}. \quad (2.20)$$

The first term describes hopping as in Eq. (2.18). The new term contains spin-1/2 operators for fermions, \mathbf{S}_j , where we restrict the interaction to nearest-neighbor spins. Emery analyzed the Heisenberg chain with inter-site interaction included and derived electronic correlation functions, which are used to discuss long range order in the ground state. [150] The ground state here exhibits a $2k_F$ modulation of the spin density, i.e., a

spin-density wave instability, which is illustrated by Fig. 2.4(d). With weaker coupling and a different number of electrons per site the ground state is not visualised as easily, but the instability still happens at the wave vector of $2k_F$. CDW states can occur again when inter-site repulsion $V > 0$ is enabled, but in the absence of hopping. As opposed to the $U < 0$ case, single electrons rather than pairs are equally spaced so the period of the CDW is halved and its wave vector is $4k_F$. This is the Wigner crystal already explained in simple terms, or the so-called $4k_F$ CDW. The stabilization of a $4k_F$ CDW is usually indicative of strong Coulomb interactions with respect to the hopping terms. This case is shown in Fig. 2.4(c) for a quarter-filled band.

In the presence of non-zero hopping, numerical calculations have shown that different density waves are possible: in addition to the both $2k_F$ and $4k_F$ CDW, $2k_F$ and $4k_F$ bond-density waves (BOW) can be also stabilized. While the coexistence of some of these phases is possible for the quarter-filled band, [154] only an excluding competition is found among $2k_F$ SDW, CDW and BOW for the half-filled band. [155]

As a rule, in quasi-one-dimensional materials structural instabilities are linked to $2k_F$ and $4k_F$ electronic instabilities. [156, 157] Variations in t , U and V produced by lattice distortions lead to modified phonon dispersions which depend on electronic polarizabilities. [158] In particular, the electron-phonon-induced modulation of the site energy yields charge modulation on sites, i.e., a CDW, whereas the modulation of the overlap integrals between sites produces a BOW: [155, 159] the intra-site electron-phonon coupling induces CDW formation, but it is the inter-site coupling which is necessary for a BOW.

2.2.2 Cuprates - the strong coupling limit

There is a general consensus that the strong electronic correlations are the driving force behind the complex phase diagram of cuprates. The electron Hamiltonian of layered cuprate systems should incorporate terms related to the copper $\text{Cu}3d_{x^2-y^2}$ and oxygen $\text{O}2p_{x,y}$ orbitals oriented within the CuO_2 plane. Starting from an Extended Hubbard hamiltonian and going through a series of physical simplifications Zhang and Rice derive explicitly a single-band effective Hamiltonian for cuprates. [160] Their main working assumption is that doping creates holes primarily on oxygen sites, i.e., that Cu-O hybridization strongly binds a hole on each square of O atoms to the central Cu^{2+} ion to form a local singlet. In this way the singlet can then move through the lattice of Cu^{2+} ions similarly to a hole in the single-band Hamiltonian of the strongly interacting

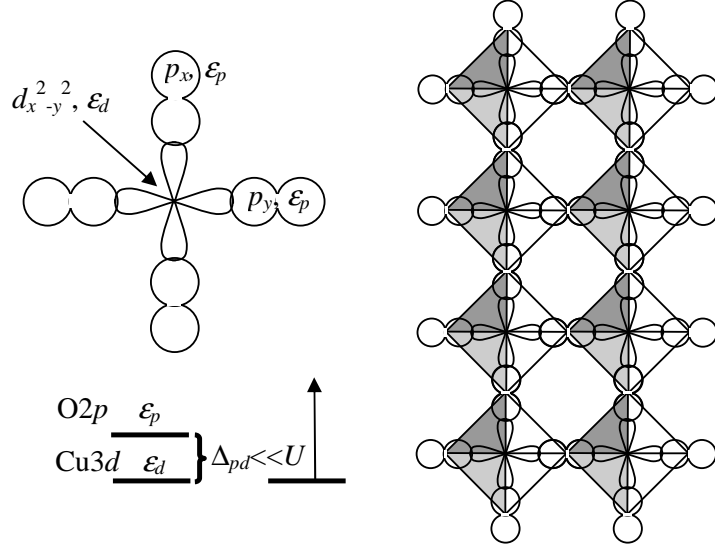


Figure 2.5 – Hybridization of the $O2p^5$ hole and $Cu3d^9$ hole within the CuO_4 square. At the oxygen sites only one of the two orbitals (p_x or p_y) is shown. The splitting of the energy levels is denoted on the lower left side. On the right, the squares assembled into a ladder structure are shown. From Vuletić *et al.* [2]

Hubbard model.

The initial assumption of Zhang and Rice was the degeneracy of oxygen orbitals $2p_{x,y}$, thus they started from a model given by

$$\begin{aligned}
 H = & \epsilon_d \sum_{j,\sigma} d_{j,\sigma}^\dagger d_{j,\sigma} + \epsilon_p \sum_{l,\sigma} p_{l,\sigma}^\dagger p_{l,\sigma} + \\
 & + U \sum_j n_{j,\uparrow} n_{j,\downarrow} + t_0 \sum_{j,\sigma} \sum_{l \in j} \left(d_{j,\sigma}^\dagger p_{l,\sigma} + \text{c.c.} \right). \quad (2.21)
 \end{aligned}$$

ϵ_d and ϵ_p are the energy levels of holes at copper sites j and oxygen sites l , respectively, and the vacuum is defined by filled $Cu3d^{10}$ and $O2p^6$ states upon which the operator $d_{j,\sigma}^\dagger$ creates a hole in the $Cu3d_{x^2-y^2}$ orbital, and $p_{l,\sigma}^\dagger$ a hole in the $O2p_x$ ($2p_y$) orbitals. The third term takes into account the Coulomb repulsion at the copper sites. The hybridization is described by the last term. The amplitude t_0 of the wave-function overlap between Cu and O orbitals does not depend of the specific cuprate lattice geometry. Its sign alternates depending on the phases of the p_x (p_y) and $d_{x^2-y^2}$ wave functions, and also on the specific lattice geometry. At exactly half-filling and for $t_0 = 0$, each Cu site is occupied by a single $Cu3d^9$ hole due to the strong on-site Coulomb repulsion represented by the third term, and consequently all the O sites are empty ($2p^6$) in the hole representation.

If the overlap integral t_0 is finite but small compared to the interaction terms (as is commonly the case in cuprates), the virtual hopping processes involving the doubly occupied Cu-hole states produce an antiferromagnetic superexchange interaction between the neighboring $\text{Cu}3d^9$ holes. The Hamiltonian (2.21) is then simplified to a spin-1/2 Heisenberg model on the lattice of Cu sites.

$$H_S = J \sum_{i,j} \mathbf{S}_i \mathbf{S}_j, \quad J = \frac{4t_0^4}{\Delta_{pd}^2 U} + \frac{4t_0^4}{2\Delta_{pd}^3}. \quad (2.22)$$

In Eq. (2.22) $\mathbf{S}_{i,j}$ are spin-1/2 operators of $\text{Cu}3d^9$ holes, with the interaction between the nearest neighbor spins, U is the Coulomb repulsion at copper sites and $\Delta_{pd} = \epsilon_p - \epsilon_d$ denotes the energy difference between the $\text{O}2p$ and $\text{Cu}3d$ states (see Fig. 2.5).

If the system is doped, the physical situation strongly depends on the energy splitting Δ_{pd} , wave-function overlap t_0 between Cu and O orbitals, and the ratio between the on-site repulsive interaction U and Δ_{pd} . In a typical cuprate systems, Coulomb interaction and energy splitting are much larger than the overlap integral. Upon doping holes into the crystal, the charge is transferred into the cuprate lattice and located either at the $\text{Cu}3d^9$ sites (rendering a $3d^8$ configuration) if $U < \Delta_{pd}$, or at the oxygen orbitals if $U > \Delta_{pd}$. In the first case (Hubbard limit), the O sites are not relevant and can be eliminated from the picture: the effective Hamiltonian describes the hole motion on Cu sites alone. [161] In the opposite case $U > \Delta_{pd}$ (charge-transfer limit), which Zhang and Rice have taken as more relevant for cuprate layers, it is favorable to have the doped holes located in oxygen orbitals $2p^6$ surrounding the Cu site and form a singlet state (ZR singlet) with the $\text{Cu}3d^9$ hole in the copper orbital - a situation applicable to chains and ladders in $(\text{La}, \text{Y}, \text{Sr}, \text{Ca})_{14}\text{Cu}_{24}\text{O}_{41}$. Zhang and Rice have shown that in this case the Hamiltonian H_{eff} reduces to the effective $t - J$ Hamiltonian of the single-band Hubbard model (as in Eq. (2.20)) in the large- U limit, but considering only the $\text{Cu}3d^9$ holes

$$H_{\text{eff}} = \sum_{i \neq j, \sigma} t_{ij} (1 - n_{i, -\sigma}) d_{i, \sigma}^\dagger d_{j, \sigma} (1 - n_{j, -\sigma}) + J \sum_{i,j} \mathbf{S}_i \cdot \mathbf{S}_j. \quad (2.23)$$

The operator $d_{i, \sigma}^\dagger$ creates a hole of spin σ on Cu-site i . Here the projection operator $(1 - n_{i, -\sigma})$ brings in the correlations which would otherwise have to be supported by the Hubbard term (hoppings between a doubly-occupied site and an empty site, or between two singly-occupied sites, are forbidden). It becomes apparent that a singly-occupied site carries a spin 1/2, while at a doubly-occupied site (no spin) a ZR singlet is formed. The second term describes the magnetic interaction between the singly occupied sites.

The Hubbard model in its strong coupling limit, the $t - J$ model, is most likely the simplest form to capture strong correlations in cuprates. It can also be applied to better understand the two-leg cuprate ladders. With this in mind Dagotto *et al.*, [54, 162, 56] have coupled two $t - J$ chains by $t' - J'$ hopping and interaction (Fig. 2.6):

$$\begin{aligned}
 H = & J \sum_{i,\lambda=-1,1} \mathbf{S}_{i,\lambda} \cdot \mathbf{S}_{i+1,\lambda} + J' \sum_i \mathbf{S}_{i,1} \cdot \mathbf{S}_{i,-1} \\
 & - t \sum_{i,\sigma,\lambda=-1,1} (c_{i,\lambda,\sigma}^\dagger c_{i+1,\lambda,\sigma} + \text{c.c.}) - t' \sum_{i,\sigma} (c_{i,1,\sigma}^\dagger c_{i,-1,\sigma} + \text{c.c.}).
 \end{aligned} \tag{2.24}$$

The $c_{i,\lambda,\sigma}^\dagger$ operator is the creation operator for a hole with spin σ on a given site i along the legs of ladders. The index $\lambda = -1, 1$ denotes sites on the same rung, at one or the other leg of the ladder. It is noteworthy that an approximation has been made in going from Eq.(2.23) to (2.24), in that the projection operators have been removed, although the same hoppings are allowed (and forbidden) in both models. In the large J' limit at half filling the ground state consists of a set of spin singlets in each rung of the ladder. To flip a spin costs energy, hence there is a spin gap in the excitation spectrum which is of the order of J' ; it corresponds to the creation of a spin triplet in one of the rungs. The prediction of a gapped spin-liquid ground state was experimentally confirmed for the quasi-1D cuprate ladder materials. [163, 164] If the ladder system is now doped by holes, we find that at low hole concentration and in the limit $J' > J$ the system prefers to combine two holes in the same rung, in order to lower the energy. Otherwise, the two holes have to break two singlets, which produces a substantial energy cost. Therefore, each added pair of holes forms a bound state in a given rung (Fig. 2.6).

Once triplets are forbidden across rungs, we recognize that rung singlets may be mapped onto a linear chain as shown in Fig. 2.6. The sites in this chain are either doubly occupied (mapped from the bound holes on the rung) or empty (mapped from the two spins which form a rung singlet). In this subspace the effective on-site interaction $|U_{\text{eff}}|$ is similar to J' , and $U_{\text{eff}} < 0$, which implies that U_{eff} is attractive. There is an important analogy of this model with the Hubbard model for a linear chain (see Fig. 2.4). The attractive Hubbard model exhibits superconducting or CDW correlations. Indeed, Dagotto *et al.* [54] have discussed the ladder model away from half-filling (i.e., hole-doped ladders) and argued that this model predicts superconducting or CDW ground states, but under the unrealistic condition $J' > t'$. In particular, their numerical calculations have shown that the spin gap and pairing correlations exist for $t'/t = 0.1$ and $J' \leq J$. It is not evident that the picture of pairing on the same rung should be valid for arbitrary J' and t' . Indeed, Noack *et al.* [165] examined the ground state properties of a Hubbard

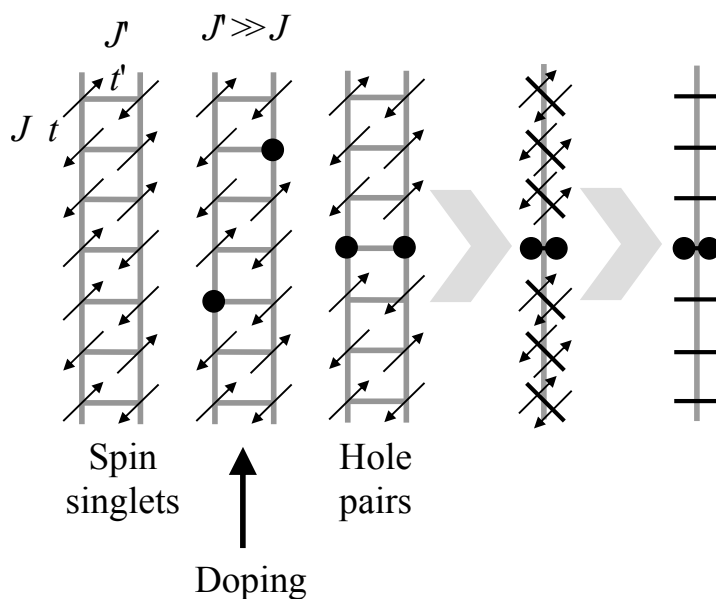


Figure 2.6 – Schematic description of the $t - J - t' - J'$ model of a cuprate spin-ladder. Hopping and coupling along the legs, and along the rungs of the ladders are denoted by t and J , and by t' and J' , respectively. The arrows indicate sites occupied by spin $1/2$, while the full dots denote doped holes which carry no spin due to formation of Zhang-Rice singlets with $\text{Cu}3d^9$ holes. From Vuletić *et al.* [2]

model on a hole-doped ladder (close to half-filling) for $t = 1$ and $U = 8$ (strong coupling limit). They have shown that while the spin gap exists at half-filling for a broad range of t' and U , in the doped system the spin-gap and pairing correlations develop only for a restricted range of parameters (t' values between 0.5 and 1.7). In addition, both the spin gap and pairing correlations become negligibly small for small t' . They have also shown that the pairing in the spin liquid is strongest across the rung, while it is weaker along the ladder legs.

2.2.3 More than one orbital per site

In the previous section the idea of two orbitals per site was introduced through the $t - J$ model for two-leg ladders. Effectively, a ladder was mapped onto a chain with each rung, now a site on the chain, carrying two singlet-bound orbitals. The idea can naturally be expanded to a chain of atoms with more than one degree of freedom, or orbital, on each site.

In fact, such a model is needed to attempt a description of BaVS_3 , a system with three electron bands coexisting at the Fermi level. Even though in principle adding more orbitals makes the problem less tractable, an interesting attempt has been made

to construct a minimal model of electron instabilities in BaVS₃ starting from the main symmetry properties of a single vanadium electron together with the electron-electron interactions. [183] In BaVS₃ the crystal field lifts the fivefold degeneracy of vanadium d -orbitals. Judging by ARPES data [49] a broad A_{1g} band (5 eV) forms of d_{z^2} orbitals, together with the narrow E_g bands (0.1 eV) composed of the two $e(t_{2g})$ orbitals e_{g1} and e_{g2} . The narrow bands pin the Fermi level in such a way that roughly half of the electrons populate the wide band and the narrow bands. The Hubbard U term is typically about 1 eV for $3d$ electrons, which is of the same order of magnitude as the bandwidth of A_{1g} states but larger than the narrow bands. This makes the simplified model in question quite interesting to compare with experimental observations.

The localized limit is a good starting approximation for strong coupling models. The Hilbert space is restricted by constructing four different states for a unit cell of two vanadium sites:

$$\begin{aligned} \left| \frac{1}{2}, \frac{1}{2} \right\rangle &:= |d_{z^2}, e_{g1}\rangle \\ \left| -\frac{1}{2}, \frac{1}{2} \right\rangle &:= |e_{g1}, d_{z^2}\rangle \\ \left| \frac{1}{2}, -\frac{1}{2} \right\rangle &:= |d_{z^2}, e_{g2}\rangle \\ \left| -\frac{1}{2}, -\frac{1}{2} \right\rangle &:= |e_{g2}, d_{z^2}\rangle. \end{aligned}$$

The spanned Hilbert space provides enough degrees of freedom to describe both the structural phase transition at T_S and the metal-insulator transition T_{MI} . Now, pseudo-spin operators $\tau = 1/2$ and $\eta = 1/2$ can be introduced which act separately on the d_{z^2} and $e_{g1,2}$ subspaces, respectively. With the help of these operators, 15 independent local order parameters in total can be defined, e.g., the operator “is the d_{z^2} present on the left or right vanadium?” $\tau^z |\pm\frac{1}{2}, e_g\rangle = \pm\frac{1}{2} |\pm\frac{1}{2}, e_g\rangle$. [183] Similarly, η operators act on the e_g electrons, and there are still 9 remaining order parameters to construct by combining the τ, η operators.

The somewhat inspired choice of operators makes it easier to express the reduction of symmetry at the phase transitions. Namely, at the second order phase transition the number of irreducible representations of the order parameters is lowered. Operators belonging to the base of an irreducible representation which was removed at the phase transition become suitable to realize the corresponding reduction of symmetry. For example, at the structural transition the order parameter can be constructed as a linear



Figure 2.7 – Different orbital and spin configurations of the V1-V2-V2-V1 order in BaVS₃. See text. From Barišić. [183]

combination of $\eta^{x,y}$, removing the symmetry to 120° rotations around the c -axis.

At the MI transition the order parameter τ^z brings about the tetramerization and a V1-V2-V2-V1 order (which, granted, does not fully agree with the experiments [9]). If we now introduce interactions between two unit cells, it can be seen that below T_S four situations between two unit cells are favored as shown by Fig. 2.7. At the right side the spin is irrelevant for the configuration energy. The left side displays energetically more favorable configurations due to spin pairing, resulting in spin correlations with an effective antiferromagnetic interaction between two neighboring e_g electrons.

The final Hamiltonian which includes spin pairing through direct coupling and direct interactions between orbital parameters regulated by parameter K can be written down in the following form: [183]

$$H_{12} = \left(\frac{1}{2} - \tau_1^z\right) \left(\frac{1}{2} + \tau_2^z\right) J \mathbf{S}_1 \cdot \mathbf{S}_2 + \left(\frac{1}{2} + \tau_1^z\right) \left(\frac{1}{2} - \tau_2^z\right) J \mathbf{S}_1 \cdot \mathbf{S}_2 + K \tau_1^z \tau_2^z - \mathbf{H} \cdot (\mathbf{S}_1 + \mathbf{S}_2) \quad (2.25)$$

where the index 1,2 denotes position inside the unit cell, $\mathbf{S}_{1,2}$ are spin operators and \mathbf{H} is the external magnetic field.

Models should be compared with measurements, and spin susceptibility calculated from Eq. (2.25) agrees well with the experiment (compare Fig. 2.8 with Fig. 1.5).

Based on the above model of symmetry breaking, we can summarize that below T_S the unit cells start to form local spin singlets, an interaction that is eventually going to produce a four-vanadium unit cell and a V1-V2-V2-V1 ordering. At T_{MI} the intrachain interactions between the 4V unit cells produce a 3D order and the system becomes insulating.

The model certainly has flaws, e.g., hopping is almost completely neglected (save for the superexchange J), it disagrees with the orbital ordering proposed by diffuse x-ray scattering experiments [9] and masks the complexity of the particular situation in BaVS₃. It however serves as an interesting qualitative alternative to the *ab ini-*

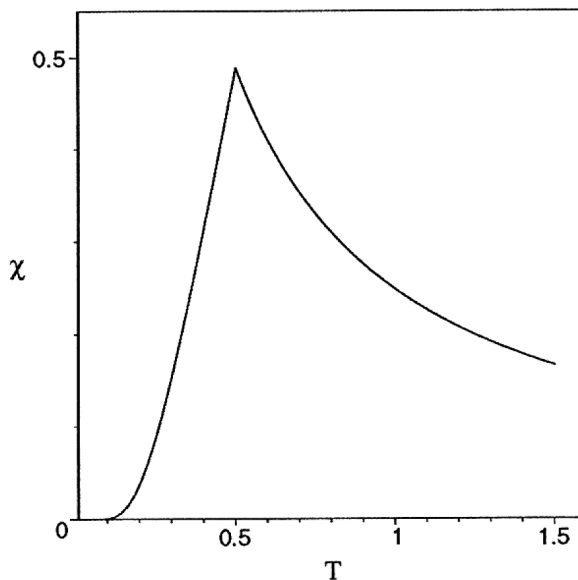


Figure 2.8 – Spin susceptibility of BaVS₃ calculated after Eq. (2.25) using $J = 0.8$, $K = 2$. From [183].

tio itinerant calculations which provide a quantitative description of various phases in the material (see Section 1.1.2) but fail to establish a more general framework for its understanding. [5]

2.3 Charge order on a 2D anisotropic triangular lattice

The local approach, where electrons or holes are considered localized on molecular sites, seems to be well-suited as a starting point in understanding organic charge-transfer salts. Namely, the large size of molecules (as opposed to atoms in inorganic materials) leads to smaller local amplitudes of electron wave functions, and consequently results in a smaller transfer integral t between neighboring molecules. Also, the van der Waals bonding between molecules leads to smaller t than in materials composed of atoms with stronger bonding. Therefore, in organic salts the energy separation between molecular orbitals Δ is typically larger than the transfer integral t , i.e., the resulting bands are well separated in energy. In such cases, either HOMO (highest occupied molecular orbital) or LUMO (lowest unoccupied molecular orbital), are the determining factors of the electronic properties in molecular solids. The notable feature of molecular solids is that t between HOMO or LUMO always have strong anisotropy. This anisotropy

reflects particular shapes of molecules (planar in most cases) and leads to various band structures and electronic properties in systems depending on arrangement of molecules in the unit cell. In particular, here we concentrate on the phenomenon of charge order in molecular planes of quarter-filled θ - and α -BEDT-TTF₂X salts.

2.3.1 Identifying the charge pattern of ground state

α -(BEDT-TTF)₂I₃ was the first quarter-filled 2D BEDT-TTF system for which a theoretical possibility of a charge order was suggested. Kino and Fukuyama [166, 167] have treated the Hubbard model, i.e., Eq. (2.19) with $V = 0$, and have found that in the limit of large U a slight charge disproportionation emerges between the neighboring stacks. A short while later, ¹³C-NMR measurements on another BEDT-TTF system, the θ -(BEDT-TTF)₂RbZn(SCN)₄, presented the first experimental evidence of a CO state in these systems. [89] However, the Hubbard model for this compound predicted a different, so-called dimer-Mott state in the slightly dimerized low-temperature θ_d -structure, rather than a CO state. [168] This was a strong indication that a simple Hubbard term cannot completely account for the charge ordering effects in 2D lattices. A later set of ¹³C-NMR measurements have indeed observed the CO in α -(BEDT-TTF)₂I₃, [25] but the exact charge pattern or the relevant interactions for its formation were still unknown.

In an effort to improve the theoretical description, Seo investigated the stabilization of charge-ordered ground states in the θ -, θ_d - and α -(BEDT-TTF)₂I₃-type structures by using an extended Hubbard model analogous to Eq. (2.19). The Hamiltonian models an anisotropic triangular lattice with particular attention to the effect of intersite Coulomb interaction, V_{ij} : [169]

$$H = \sum_{\langle ij \rangle, \sigma} (t_{ij} c_{i, \sigma}^\dagger c_{j, \sigma} + \text{c.c.}) + U \sum_i n_{i, \uparrow} n_{i, \downarrow} + \sum_{\langle ij \rangle} V_{ij} n_i n_j \quad (2.26)$$

A mean-field approach provides some level of insight into the ground state of model (2.26). All three structures, θ -, θ_d - and α -(BEDT-TTF)₂I₃-type, show the stabilization of CO when the value of intersite Coulomb repulsion V_{ij} approaches $U/4$. Two kinds of values for nearest-neighbor V_{ij} are assumed: V_c for bonds along the stacking direction, and V_p along the inter-stack directions (it is customary to label directions after the θ -structure axes, i.e., the molecular stacking direction is the c -direction corresponding to the crystallographic a -axis of α -(BEDT-TTF)₂I₃, and the directions towards nearest neighbors in the adjoining stacks are the two p -directions). Judging by the intermolecu-

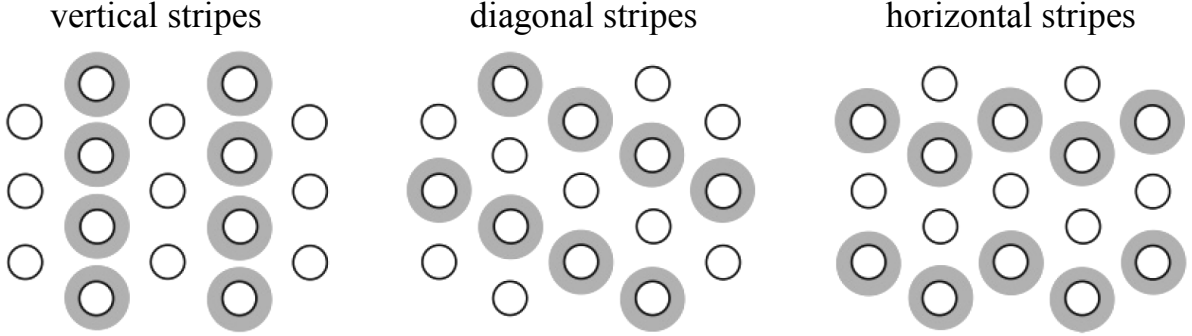


Figure 2.9 – Three possible stripe-type charge-ordered states in the vertical, diagonal and horizontal direction. Charge-rich sites are emphasized by gray circles. After Seo *et al.* [85]

lar distances, V_c and V_p should take similar values. [170] Three possible charge patterns were found for the θ - and α -type structure, the so-called horizontal, vertical and diagonal stripe charge order, akin to a 2D lattice extensions of Wigner-type charge order found in 1D systems (see Figure 2.9).

The extended Hubbard studies by Seo left several unresolved issues. First and foremost, stripe-type CO states in the mean-field calculation are very close in energy and quite sensitive to the value of intersite Coulomb energies as well as to the degree of anisotropy of transfer integrals. [169] It is therefore hard to conclude which charge pattern is realized in the actual compounds solely on the basis of mean-field results in a purely electronic model. In case of the θ -structure, the mean-field approach also fails to explain an additional low-temperature spin gap transition as evidenced in, e.g., θ -(BEDT-TTF)₂RbCo(SCN)₄, as well as neglects dimerization effects along the stacking direction. [169, 171] Seo proposed that including the electron-phonon interaction would lead to bond alteration inside individual charge-rich or charge-poor stripes which in turn would produce a spin gap, analogous to the 1D spin-Peierls transition. [169] An alternative explanation for the spin gap is a frustrated spin model proposed by Seo and Fukuyama which however cannot explain the coexistence of CO and frustrated states in a satisfying manner. [168] The failure of mean-field approximation to explain CO in the quarter-filled BEDT-TTF salts came as no surprise, after all it was known to give incorrect behavior in some aspects of Eq. 2.19, e.g., in 1D it shows erroneous behavior of $4k_F$ CDW transitions as a function of U and V . Extended Hubbard models for anisotropic 2D triangular lattices are difficult to treat beyond mean-field approximation, which limits detailed theoretical investigations. Radically simplified models also appeared: Calandra *et al.* kept only the nearest-neighbor terms, [172] while McKenzie *et al.* managed an exact diagonalization when they excluded the hopping integrals and

interaction terms along the stacking direction; [171] both groups arrive at the vertical stripe CO. Seo's latter approach was to utilize magnetic properties of real materials in regimes where quantum fluctuations among localized spins are expected, and incorporate quantum fluctuations through appropriate Heisenberg models. [85] By this procedure the charge pattern in the insulating phases of both θ -(BEDT-TTF)₂RbZn(SCN)₄ and α -(BEDT-TTF)₂I₃ was identified as the horizontal stripe-type.

An improvement over previous approximations, Clay *et al.* studied a small cluster of the θ -type structure by numerical Lanczos exact diagonalization. [173] For the more complex α -(BEDT-TTF)₂I₃ with lower symmetry, such analysis is still missing. Nevertheless, work by Clay *et al.* offers an important insight into the formation of stripes. They included a small electron-phonon interaction term inspired by the knowledge that electron-phonon coupling is vital in reproducing experimental phonon dynamics of the superconducting κ -(BEDT-TTF)₂I₃. [174] Now the Hamiltonian comprises the usual extended Hubbard terms, and adds the small electron-phonon coupling term:

$$H = \sum_{\langle ij \rangle, \sigma} t_{ij} c_{i, \sigma}^\dagger c_{j, \sigma} + U \sum_i n_{i, \uparrow} n_{i, \downarrow} + V \sum_{\langle ij \rangle} n_i n_j + H_{e-ph} \quad (2.27)$$

In the above, i and j are site indices, $\langle \dots \rangle$ implies nearest neighbors, $n_j = n_{j, \uparrow} + n_{j, \downarrow}$, σ is the index of spin and H_{e-ph} represents the electron-phonon coupling. The average number of holes per site equals 1/2 for the quarter-filled θ -materials. In accordance with extended Hückel calculations, [87] the two hopping integrals of θ -structure are assumed to be $t_c > 0$, $t_p < 0$, and $|t_c| \ll |t_p|$. V_p and V_c should be roughly the same value since the Coulomb integrals depend only on the distances between site-charges. Phonon effects H_{e-ph} are approximated by a site energy component $\sum_i \epsilon_i n_i$, with ϵ_i negative for charge-rich sites and positive for charge-poor sites. This is equivalent to including an on-site electron-phonon coupling within the classical approximation of fixed spring constants. Clay *et al.* proceed by calculating the lowest energy corresponding to each specific CO for the smallest spring constants that still give measurable energy differences between the three stripe structures. In the limit of vanishing electron-phonon coupling this provides a consistent measure of relative stabilities of the different CO patterns. [173] Parameters are chosen consistently with numerical estimates by Mori *et al.*: [170] $t_p = -0.14$ eV, $t_c = 0.01$ eV, $U = 0.7$ eV, V variable in the region $V < U/2$ and $|\epsilon_i| = 0.01$ eV.

Fig. 2.10 shows the energy gain upon formation of the three stripe CO patterns in the θ -structure. As a rule, vertical stripes are suppressed by either horizontal or diagonal stripes. Horizontal stripes dominate the phase diagram above a certain value of inter-

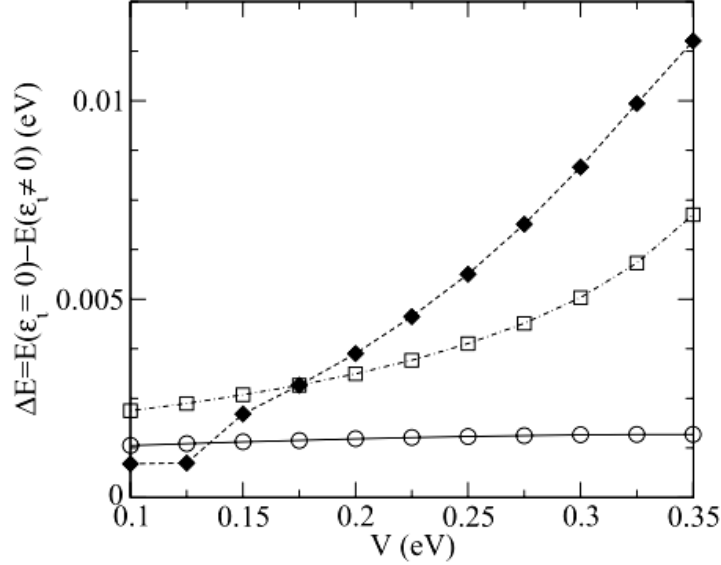


Figure 2.10 – Energy gain upon formation of the three stripe CO patterns. Circles, squares and diamonds correspond to vertical, diagonal and horizontal stripe patterns, respectively. For $V > 0.18$ eV, the ground state has the horizontal stripe CO. From Clay *et al.* [173]

site Coulomb interaction, in this case $V > 0.18$ eV. Clay *et al.* make an instructive observation concerning the stabilized horizontal stripe ground state. Let us denote charge-rich sites as 1 and charge-poor as zero. In a 1D system, the classical energy of a 1010 charge order is lower than that of 1100. However, for all V below a critical $V_{\text{cr}}(U) > 2|t|$ the 1100 ordering is predominant. This observation for 1D strongly suggests that the critical inter-site Coulomb term at which the horizontal stripes form should be smaller than that of diagonal or vertical stripes.

Exact charge densities n_j predicted by this model strongly depend on the on-site electron-phonon coupling and can be very large ($\Delta n \sim 0.3e$ for $\epsilon_i = 0.01$ eV). The interesting result however is emergence of alternating bond orders (overlap integrals), $b_{ij} = \sum_{\sigma} (c_{i\sigma}^{\dagger} c_{j\sigma} + c_{j\sigma}^{\dagger} c_{i\sigma})$ within the horizontal stripe CO. Bonds are spontaneously distorted along all three directions: tetramerized in the p -directions and dimerized in the stacking c -direction. The tendency of spontaneous modulation of bonds next to the charge ordering throughout the lattice can be interpreted as a consequence of co-operative bond-charge density wave (BCDW) nature of the horizontal stripe phase within the θ -structure. Finite intra- and inter-site electron-phonon interactions would further lower the energy of such a cooperative BCDW, which makes it more likely that even in the low- V region the horizontal stripes would dominate.

It is interesting to note that the model above also gives insight into the spin singlet

transition of θ -(BEDT-TTF)₂RbCo(SCN)₄. In short, between the MI and spin gap transitions this particular θ -system is ferromagnetic and charge-ordered. Calculations in the ferromagnetic excited state of the horizontal stripe predict that bond dimerization occurs immediately below the MI not only in c -direction but p -directions as well. A spin gap is not expected immediately below MI transition since dimerization in a quarter-filled band does not open a spin gap in 1D. [175] At low enough temperatures high-spin states become thermally inaccessible, leading to a second transition accompanied by a large dimerization of molecular stacks and a tetramerization of p -direction bonds. It is plausible to expect a spin gap in this state, even though its existence still needs to be demonstrated explicitly. [173,176]

2.3.2 Excitations in a charge-ordered phase with horizontal stripes

As we have seen, in 1D systems there is an established body of knowledge covering possible ground states and excitations. Going from one to two dimensions however we face a distinct lack of theoretical work on (collective) excitations in a 2D charge order, mainly due to the untractability of the extended Hubbard models in two dimensions. Here we briefly present two models describing possible excitations and transport in a horizontal stripe CO: the so-called “pinball liquids” proposed by Hotta *et al.* [177] and the excitonic picture by Yamaguchi *et al.* [178,179]

Hotta *et al.* have tackled the problem of strongly interacting spinless fermions on an anisotropic triangular lattice. Taking into account strong nearest-neighbor repulsion, part of the fermions localize in a striped charge order, and the others form a “pinball liquid”, i.e., a metal on the remaining sites. Movement of the free fermions is significantly restricted by the presence of localized fermions. Hence, in effect the frustrations stemming from electronic interactions tune of the effective dimensionality and metallicity. [177] In the case of a half-filled, horizontally-striped spinless fermion system, doped particles can hop along the stripes with no cost of energy. An additional propagation perpendicular to stripes can also take place which includes deforming of the stripes themselves. Namely, doped particles interact with stripes in the vertical direction through two bonds which can separate orthogonally to the stripes without increase of potential energy, fractionalizing the charge so that each of them is carrying a charge of $e/2$ (see Fig. 2.11). Fourth-order perturbative calculations utilizing the so-called plaquette processes result in collective excitations which can be regarded as a decay of the

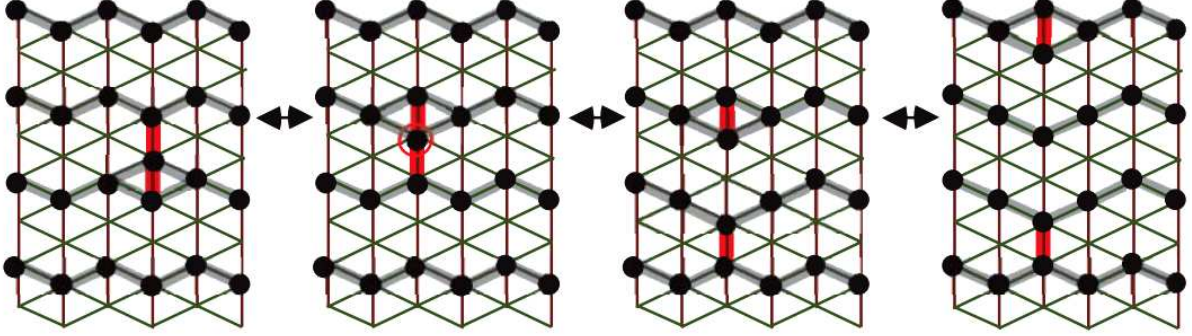


Figure 2.11 – Charge fractionalization in the pinball liquid atop a horizontal stripe configuration, illustrated by the separation of two bold vertical bonds perpendicular to the stripes. From left to right, a doped particle propagates perpendicular to stripes. It separates into two quasiparticles with fractionalized charge which deform the striped charge order in their wake. After Hotta *et al.* [177]

doped particle into bound pairs of fractional charges with a large spatial extent. The dispersion of the quasiparticle is a combination of 1D free propagation along the stripes, and the 1D collective propagation perpendicular to stripes. The effective dimensionality is tuned between 1D and 2D depending on the anisotropy of transfer integrals and on the original interaction strength. However, the serious drawback of this model is that it does not lend itself easily to workable predictions about observables accessible in electric transport, dielectric and infrared experiments: namely, it is not clear which telltale experimental features would identify the pinball liquid.

The rather simple excitonic model used by Yamaguchi *et al.* is a single-particle picture devised to explain dielectric properties and nonlinear conductivity in the low-temperature phase of θ -BEDT-TTF₂MZn(SCN)₄ ($M = \text{Cs, Rb}$) with horizontal-stripe CO. [178,179] This model considers a charge-ordered square-lattice system with quarter filling in which excitations are created by moving a localized hole to a site where no hole was originally present, thus creating a pair of a localized electron and hole. Due to their electric fields being confined to the polarizable plane of ET molecules, the attractive Coulomb potential between a bound electron and hole is of a logarithmic form: the potential is modeled as

$$U = \begin{cases} U_0 \ln(r/a) & \text{for } r < \lambda, \\ U_0 \ln(\lambda/a) & \text{for } r > \lambda. \end{cases} \quad (2.28)$$

where the spatial scale a is the distance between neighboring BEDT-TTF sites, typically $a \approx 0.5$ nm, and λ is the screening length. At finite temperatures bound pairs are thermally excited. The potential barrier for a pair to unbind under an electric field E

is given by

$$\begin{aligned} 2\Delta(E) &= \max [U_0 \ln(r/a) - eEr] \\ &\approx U_0 \ln \{U_0/(eEa)\}, E \ll U_0/(ea). \end{aligned} \quad (2.29)$$

In the excitonic picture a transport gap $2\Delta(E=0) = U_0 \ln(\lambda/a)$ naturally follows from the cutoff of logarithmic potential. [179] From this we get a nonlinear conductivity $\sigma(E)$,

$$\sigma(E) \approx \sigma_0(ea/U_0)^{U_0/2k_B T} E^{U_0/2k_B T}. \quad (2.30)$$

The thermally excited but bound pairs are polarized in the presence of an electric field and give rise to a temperature-dependent dielectric constant

$$\varepsilon(T; \omega = 0) = 1 + \frac{n_0}{\varepsilon_0} \int_0^\lambda r dr \frac{(er)^2}{2k_B T} \exp \left\{ -\frac{U(r)}{k_B T} \right\} / \int_0^\lambda r dr \exp \left\{ -\frac{U(r)}{k_B T} \right\}, \quad (2.31)$$

where n_0 is the electron-hole density at $T \rightarrow \infty$ which can be taken as equal to half the BEDT-TTF density. [179]

This model describes well both the observed nonlinear conductivity and dielectric properties of θ -BEDT-TTF₂MZn(SCN)₄ below 2 K, yielding the values of $U_0/k_B = 5.8 \pm 0.4$ K, $\lambda = 47 \pm 10$ nm (CsZn), and $U_0/k_B = 400 \pm 40$ K, $\lambda = 7 \pm 1$ nm (RbZn). It is plausible that the excitonic mechanism might also explain dielectric properties measured in the charge-ordered α -(BEDT-TTF)₂I₃.

Chapter 3

Experimental techniques

3.1 DC conductivity

Low-temperature dc transport measurements have been performed in the temperature range 300 K – 4.2 K in a double liquid N₂ - liquid He cryostat. Temperature is measured by a Pt-100 and a Lakeshore CarbonGlass 500 thermometer. In the case of (La,Y,Sr,Ca)₁₄Cu₂₄O₄₁ high-temperature measurements (300 K – 750 K) have also been performed in an oven with a simple on-off thermostat for temperature regulation, and a Pt/Pt-Rh10% thermocouple as a thermometer. Thermometry was carefully calibrated and verified to match between the cryostat and oven.

Resistances from mΩ to GΩ range are measured with three separate setups. The first is the low-frequency ac setup where a Stanford Research Systems SR830 lock-in together with a Keithley 6221 ac current source is used for resistances of 10 mΩ – 10 kΩ. The current is sourced at 77 Hz to avoid powerline noise at 50 and 100 Hz. The voltage drop is then measured in the standard four-probe configuration using the lock-in, with current source internal clock as a phase and frequency reference signal. Resistance range of 1 Ω – 100 MΩ is covered by a second setup consisting of a dc current source Keithley 220 and Keithley 181/2182 nanovoltmeters, also used in the four-probe configuration. The dc setup also measures resistances up to 50 GΩ by replacing the nanovoltmeter with the Keithley 617 electrometer (internal resistance of 200 TΩ), however this solution suffers from very long time constants - that is, the measured resistance $R > 10$ GΩ combined with the input capacitance $C \sim 1$ nF of the voltmeter give time constants RC measured in minutes. In such cases, notably with cuprates, a third setup was used consisting either of Keithley 617 electrometer or Keithley 487 picoammeter in the two-probe V/I

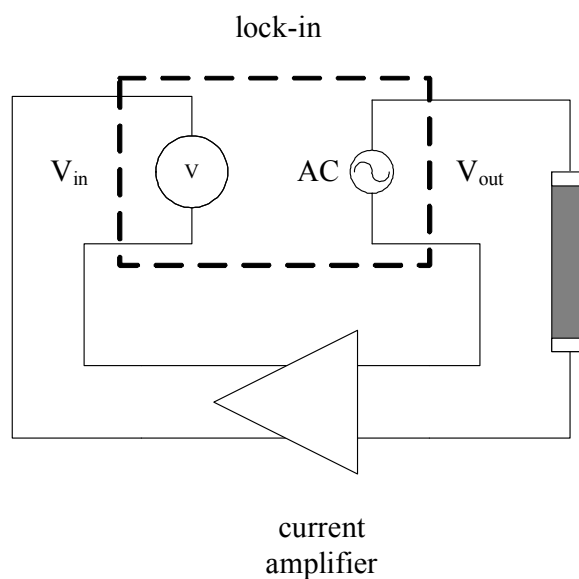


Figure 3.1 – Lock-in based low-frequency dielectric spectroscopy setup.

mode with applied voltage and measured current.

Additionally, the resistance has been measured as a function of applied electric field to check for possible nonlinear effects at various temperatures. These measurements have been performed in the four-contact configuration, using a current source and nanovoltmeter in the continuous dc regime. Special care has been taken to avoid sample heating by keeping the Joule power below $1 \mu\text{W}$ at all times.

3.2 Dielectric spectroscopy

Dielectric spectroscopy is a two-contact transport method used to determine frequency dependence of the sample impedance and extract the complex dielectric function. Measurements have been performed in two-contact configuration from the room temperature to 4.2 K in the same cryostat as the dc transport experiments, and on the same crystals. Two setups cover a wide range of frequencies, and results obtained by both setups routinely agree in the overlapping frequency range. The low-frequency setup is used in the 10 mHz – 3 kHz range for impedances up to $1 \text{ T}\Omega$. Sine voltage is applied to the sample. The current response is transformed to voltage by the Stanford Research Systems SR570 current preamplifier and detected by dual-channel digital lock-in Stanford Research Systems SR830 (see Fig. 3.1).

At higher frequencies (20 Hz – 10 MHz) Hewlett-Packard 4284A and Agilent 4294A

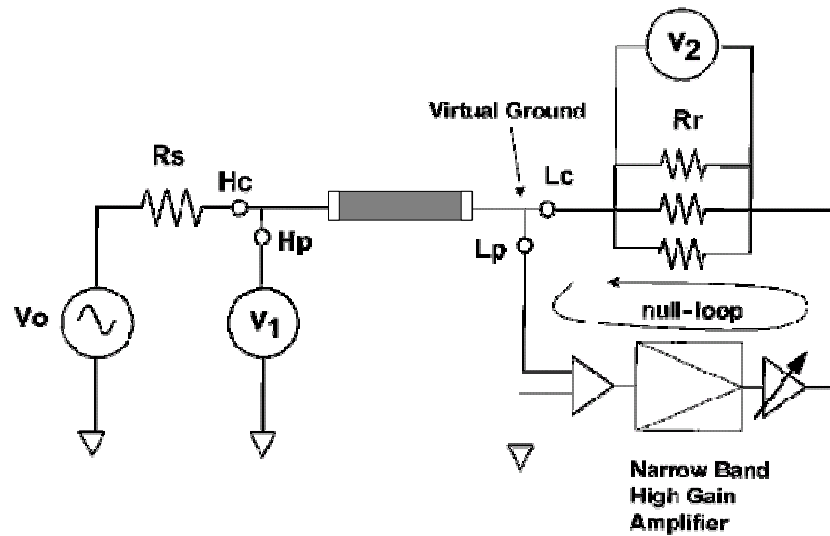


Figure 3.2 – A basic auto-balancing bridge. See text.

auto-balancing bridges are used, allowing measurement of impedances from $\sim 1 \text{ k}\Omega$ up to $1 \text{ G}\Omega$. Even though Agilent 4294 reaches the maximum frequency of 110 MHz , we are limited to $F \approx 10 \text{ MHz}$ by cabling length L : the rule of the thumb is $F \cdot L < 15 \text{ m}\cdot\text{MHz}$ where F is the high frequency limit and cable length L is in our case 1.5 m . The principle of operation of the two impedance analyzers is shown by Fig. 3.1. In order to perform precise impedance measurements, the voltage applied to the sample and the current which flows through it need to be accurately measured, both in amplitude and in phase. The High-Current (Hc) terminal is the output of signal source. Current flows from the Hc terminal, through the DUT and into the Low-Current (Lc) terminal where it is measured. If there exists a non-zero potential at the Lc terminal, any stray capacitance between the terminal and ground may cause part of the current to flow to ground, and therefore not be picked up by the current measurement circuit. To avoid such current leaks through stray capacitances (which become significant at higher frequencies), the Low terminal is kept as near as possible to the voltage level of ground. This technique is called “Virtual Ground” and it is functionally dependent on a feedback loop, a so-called “null-loop”. The null amplifier commonly consists of an input amplifier, a narrow-band, high-gain amplifier, and an output amplifier. It is important that the input amplifier has a near-infinite input resistance in order to prevent current flowing from the Low terminal(s) to ground. The output of null amplifier is a voltage signal which maintains the virtual ground level at the Low-Potential (Lp) terminal and helps to pull the whole DUT current to a range resistor. By detecting the voltage of the range resistors, the current which flows through the DUT is measured. Impedance analyzers

usually have several range resistors in order to achieve high resolution for various current measurements. Since the Low-terminal voltage is at the virtual ground, the voltage drop across DUT is detected at the High-Potential (Hp) terminal of the instrument relative to ground. Typically, the measurement circuit behind the Hp terminal is isolated from the Hc terminal, which enables more accurate detection of the voltage applied to the DUT.

Amplitude of the applied voltage has always been within the linear response regime of the samples. Depending on geometry of samples typical levels of 10 – 50 mV have been used, resulting in electric fields of up to 500 mV/cm.

In order to account for and remove background influences, we have routinely subtracted the open-circuit admittance $Y_{\text{open}}(\omega)$ from all measured sample admittances $Y(\omega)$. [180] This procedure removes stray capacitances due to sample holder construction and cabling which can never be completely avoided. The background capacitance of our setup corresponds to 350 fF at all measured temperatures.

Dielectric function $\varepsilon(\omega) = \varepsilon'(\omega) - i\varepsilon''(\omega)$ can be deduced from the real and imaginary parts of conductivity $Y - Y_{\text{open}} = G(\omega) + iB(\omega)$ using the following expressions:

$$\varepsilon'(\omega) = 1 + \frac{l}{S} \frac{B(\omega)}{\varepsilon_0 \omega}, \quad \varepsilon''(\omega) = \frac{l}{S} \frac{G(\omega) - G(0)}{\varepsilon_0 \omega} \quad (3.1)$$

where l is the sample length and S sample cross section. Dielectric relaxation of systems studied in this work can be fitted with a generalized Debye function, which is widely used to describe (overdamped) dielectric relaxation in disordered systems: [181]:

$$\varepsilon(\omega) - \varepsilon_{\text{HF}} = \frac{\Delta\varepsilon}{1 + (i\omega\tau_0)^{1-\alpha}}, \quad (3.2)$$

where $\Delta\varepsilon = \varepsilon(0) - \varepsilon(\infty)$ is the dielectric relaxation strength, τ_0 the mean relaxation time, and $1 - \alpha$ the symmetric broadening of relaxation time distribution. Fig. 3.3 shows the typical form of generalized Debye relaxations for various broadening parameters. The fits to cuprate and BaVS₃ measurements utilize a single generalized Debye function, while the α -(BEDT-TTF)₂I₃ requires a sum of two generalized Debye function.

Since dielectric spectroscopy is at its core a two-contact transport method, the possibility of extrinsic influences is always present in the form of contact resistance and surface layer capacitance. A procedure was devised to consistently verify if the measured response is predominantly intrinsic to the sample, i.e., stems from sample bulk with negligible contact contribution. See Appendix A for further details.

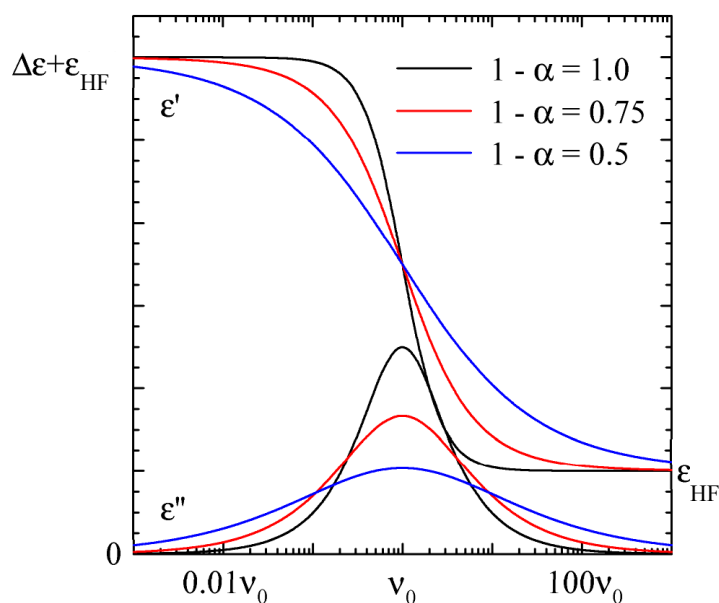


Figure 3.3 – Typical form of the real (step-like curves) and imaginary part (bell-like curves) of generalized Debye function Eq. (3.2) centered around a frequency ν_0 .

3.3 THz spectroscopy

Complex transmission measurements at frequencies $5\text{--}25\text{ cm}^{-1}$ ($150\text{--}750\text{ GHz}$) have been provided by B. Gorshunov in the group of prof. M. Dressel at the University of Stuttgart, Germany. The technique was applied to samples of $(\text{La,Y,Sr,Ca})_{14}\text{Cu}_{24}\text{O}_{41}$ and $\alpha\text{-(BEDT-TTF)}_2\text{I}_3$. However, after the experiments it became apparent that the $\alpha\text{-(BEDT-TTF)}_2\text{I}_3$ results were irreparably influenced by beam diffraction inside the cryostat due to cracking and misalignment of samples and had to be discarded.

The custom THz setup is based on a Mach-Zehnder spectrometer in transmission geometry which measures the phase shift and power transmission coefficient of radiation which passes through a thin insulating sample as functions of frequency. On the basis of phase shift and transmission coefficient, complex dielectric and conductivity spectra are obtained. A set of exchangeable and continuously tunable backward wave oscillators (BWO) are used as coherent millimeter-wave sources. Samples are mounted inside a He-flow optical cryostat which is placed inside one of the two beam paths of the interferometer.

Fig. 3.4 lays out the experiment in more detail. This submm experiment requires nonstandard “optical” elements. Teflon lenses collimate and focus the radiation. Planar wire grids made out of thin tungsten wires spaced at a distance much smaller than the radiation wavelength are used as polarizers, analyzers, semi-transparent mirrors

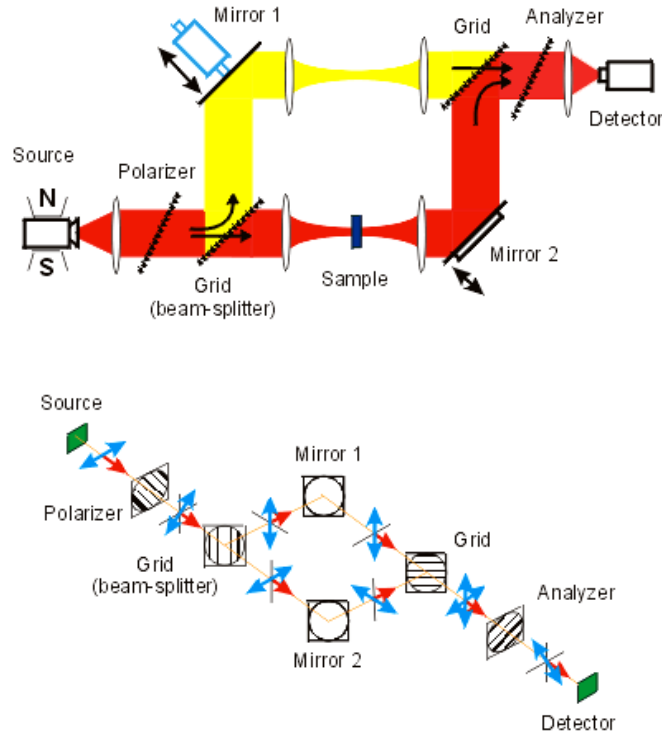


Figure 3.4 – Schematic depiction of the THz Mach-Zehnder spectrometer. Refer to text for details.

and beam-splitters. For each temperature and polarization separate measurements are performed for the phase shift and transmission coefficient.

For measurement of the transmitted power only the beam path marked red in Fig. 3.4 is employed and the signal on the detector is recorded versus frequency two times - without and with the sample. The absolute transmission coefficient is determined as their ratio.

Phase shift is measured using both the yellow and red beam path, in the configuration of a Mach-Zehnder two-beam polarization interferometer. Mirror 1 of the interferometer can be moved; its position is controlled electronically in such a way that during the frequency scanning the interferometer is always kept in a balanced state (equal optical paths in its both arms). The frequency is again scanned twice - without and with the sample - and the phase-shift spectrum is determined based on the difference of two positions of the mirror.

After the transmission coefficient and phase shift have been obtained, standard relations are used to calculate the complex refractive index and from that the complex dielectric function and/or conductivity.

3.4 Infrared spectroscopy

For α -(BEDT-TTF)₂I₃ material, Fourier-transform infrared reflectivity (FTIR) measurements have been performed in the 10–10000 cm⁻¹ range in the group of prof. M. Dressel at the University of Stuttgart, Germany. This wide frequency range is covered by two spectrometers based on the classical Michelson interferometer. In the mid-infrared range, 500–10000 cm⁻¹, a Bruker 66v/s Fourier-transform infrared spectrometer was employed. The sample is mounted in vacuum inside an optical He-flow microcryostat which covers the temperature range 17–300 K. The interferometer is equipped with a beam polarizer and an infrared microscope which enables measurements on a chosen optically clean spot of sample surface (typical spot radius $\sim 100 \mu\text{m}$). Light is reflected from the sample at normal incidence, returned back through the microscope into the interferometer, and detected with a nitrogen-cooled bolometer. Absolute values of sample reflectivity are obtained by also measuring at each temperature the reflectivity of a reference mirror which is mounted in the cryostat near the sample. Additional measurements in the far-infrared range, 10–7000 cm⁻¹ have been performed by C. Clauss from the group of prof. M. Dressel using a Bruker IFS 113v FTIR spectrometer with an optical liquid N₂ - liquid He cryostat (4.2–300 K). C. Clauss is also credited for the following data analysis.

For each temperature and selected polarization FTIR measurements provide absolute values of reflectivity $R(\omega)$. Dielectric constant and conductivity are obtained through Kramers-Kronig relations in the following way. Measured reflectivity provides us with the phase shift $\phi(\omega)$ of the reflected light as

$$\phi(\omega) = \frac{\omega}{\pi} \int_0^{\infty} \frac{\ln R(\omega') - \ln R(\omega')}{\omega^2 - \omega'^2} d\omega'. \quad (3.3)$$

The phase shift can in turn be used to calculate the real part of conductivity

$$\sigma'(\omega) = \frac{\omega}{4\pi} \frac{4\sqrt{R(\omega)}[1 - R(\omega)] \sin \phi(\omega)}{[1 + R(\omega) - 2\sqrt{R(\omega)} \cos \phi(\omega)]^2}, \quad (3.4)$$

and real part of the dielectric function

$$\varepsilon'(\omega) = \frac{[1 - R(\omega)]^2 - 4R(\omega) \sin^2 \phi(\omega)}{[1 + R(\omega) - 2\sqrt{R(\omega)} \cos \phi(\omega)]^2}. \quad (3.5)$$

When calculating the integral (3.3) care must be taken in extrapolating data beyond

the high- and low-frequency end of experimental data. Extrapolation towards infinite frequencies is usually not problematic as most commonly an extrapolation of $R(\omega) \propto \omega^{-2}$ is assumed. The low-frequency extrapolation requires more care. For an insulator the reflectivity is assumed to remain constant as frequency is extrapolated to zero. However, this means that zero-frequency conductivity vanishes. For α -(BEDT-TTF)₂I₃ a finite low-frequency optical conductivity σ'_0 was obtained by extrapolating the data to the Hagen-Rubens law $R(\omega) \approx 1 - (2\omega/\pi\sigma'_0)^{1/2}$ which describes the reflectivity of metals at frequencies below scattering rates.

3.5 Sample preparation and protocols

A note is in order on properly determining conductivities of anisotropic conductors. Here, the concept of the equivalent isotropic sample is very useful since it provides a simple visualisation of current distribution in the anisotropic sample. [182] The basic idea behind the concept is to remap the current distribution, contacts applied to the sample, and the sample shape itself to an imagined isotropic sample and verify there if the current distribution is homogenous. The equivalent isotropic sample is obtained by a coordinate scaling according to the formula $l'_i = l_i \sqrt{\sigma/\sigma_i}$, $\sigma = \sqrt[3]{\sigma_1\sigma_2\sigma_3}$, where l_i is the sample dimension along the i -th principal axis of the diagonalized conductivity tensor σ_i . An example of such a rescaling is shown in Fig. 3.5 for an α -(BEDT-TTF)₂I₃ sample at room temperature, with $\sigma_a : \sigma_b : \sigma_c \approx 1000 : 2000 : 1$ and dimensions $l_a = 1.5$ mm, $l_b = 0.2$ mm, $l_c = 40$ μ m. This particular example shows that the otherwise needle-like α -(BEDT-TTF)₂I₃ $\mathbf{E} \parallel a$ sample shape maps to a very thick equivalent isotropic sample. However, the geometry remains elongated and acceptable due to wide voltage contacts covering the sides of the sample, as well as current contacts capping the sample ends. As we shall see, α -(BEDT-TTF)₂I₃ shows a further increase of ab -plane anisotropy in the insulating phase. For the $\mathbf{E} \parallel a$ geometry this only means that the equivalent isotropic sample becomes more elongated and narrow along the a -axis, which is the desired effect. The $\mathbf{E} \parallel b$ seems to be more problematic as its equivalent isotropic shape becomes shorter and thicker. Still, this poses no significant deviations down to $\sigma_a : \sigma_b \approx 1 : 20$ which is approximately the range of our low-temperature data. A similar verification validates the needlelike (La,Y,Sr,Ca)₁₄Cu₂₄O₄₁ geometries.

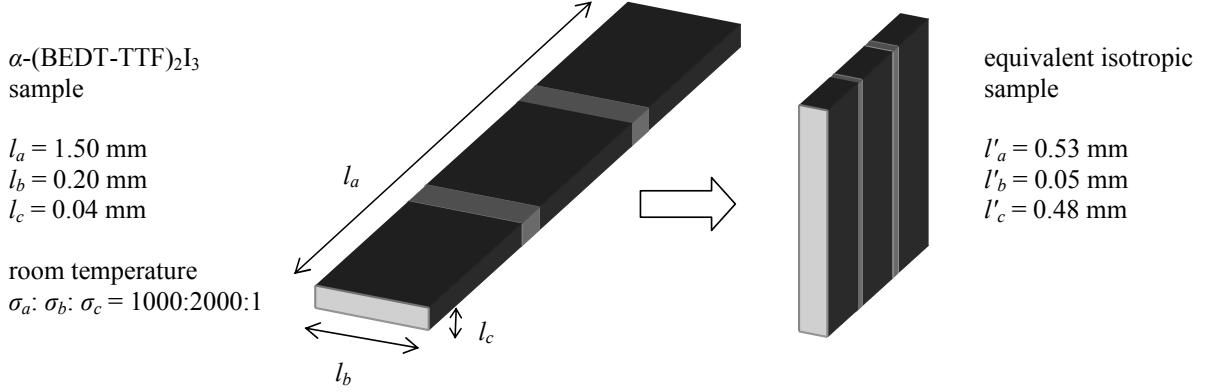


Figure 3.5 – Example of an equivalent isotropic sample mapping. Contacts are marked light gray. See text.

3.5.1 BaVS₃

On BaVS₃ we have performed dc transport and dielectric measurements. High-quality crystals and prepared contacts were found to be crucial for reliable and reproducible results. Already the first work on BaVS₃ [6] notes a strong dependence of resistivity on purity of the crystals. Further work on magnetic and transport properties [4, 183] has confirmed a need for high-quality samples. Namely, stoichiometric samples are antiferromagnetic at low temperatures and display very high residual resistance ratios under pressure where the metal-insulator transition is completely suppressed. Non-stoichiometric, sulfur-depleted samples on the other hand show low-temperature ferromagnetic behavior and a high influence of impurities on transport properties. According to the work of N. Barišić, [183] high quality samples display all of the following:

1. metallic behavior at high temperatures,
2. a well-defined change of the slope in resistivity *vs.* temperature at structure transition T_S ,
3. a sharp MI transition
4. no sign of saturation of resistivity in the insulating phase which could be attributed to an impurity band,
5. complete suppression of metal-insulator phase transition under pressure of 20 kbar,
6. high residual resistance ratio (RRR) at 20 kbar

Our samples of BaVS_3 were synthesized by H. Berger at the École Polytechnique Fédérale de Lausanne. Single crystals were grown in melted tellurium as flux [184], typically as large needles 4–6 mm long, with a hexagonal cross-section of about 1 mm in width, oriented along the crystallographic c -axis. Standard silver paint contacts were not suitable due to sulfur content in the samples. The following method was employed in Lausanne has been proven to give contacts with resistances of $\sim 10 \Omega$ at room temperature. First, the samples are masked with mylar strips, leaving uncovered the area for future contacts along the needles, for measurements with $\mathbf{E} \parallel c$. Approximately 500 Å of chrome and then 500 Å of gold is evaporated. Wires are fixed by conducting silver paint DuPont 6838. This particular silver paint needs to be cured at 350 °C for 10 min, which is the lowest temperature and duration under which it becomes conducting. At higher temperatures BaVS_3 degrades by releasing sulfur, which reacts with silver paint and chemically ruins the contacts. Curing is performed in vacuum to prevent oxidation of the epoxy. However, this process also causes loss of sulfur from the samples, which is then repleted in the last step of treatment by a cycle of heating and cooling in a saturated sulfur atmosphere.

A total of 10 samples have been measured, however 8 had to be discarded either due to large contact influence on the two-contact dielectric measurements (see Appendix A for a detailed description), or due to poor RRR under pressure (≈ 10 , as compared to 20 and 80 for good samples). The two remaining high-quality samples with good contacts show qualitatively the same dielectric response, which ensures it is intrinsic. The following chapter presents and discusses results obtained on one of these two single crystals.

3.5.2 $(\text{La}, \text{Y}, \text{Sr}, \text{Ca})_{14}\text{Cu}_{24}\text{O}_{41}$

Single crystals of $\text{Y}_y\text{Sr}_{14-y}\text{Cu}_{24}\text{O}_{41}$ ($y = 0, 0.55, 1.6$) and $\text{La}_3\text{Sr}_3\text{Ca}_8\text{Cu}_{24}\text{O}_{41}$ were synthesized by the group of J. Akimitsu, T. Sasaki and T. Nagata from the Department of Physics, Aoyama-Gakuin University, Kanagawa, Japan. Single crystals of $\text{La}_{5.2}\text{Ca}_{8.8}\text{Cu}_{24}\text{O}_{41}$ were synthesized by the group of C. Hess and B. Büchner from Leibniz-Institut für Festkörper- und Werkstofforschung, Dresden, Germany, where we reused samples from our previous work on underdoped quasi-1D cuprates. [22, 58] Initially a stoichiometric mixture of dried powdered CuO , CaCO_3 , SrCO_3 together with Y_2O_3 and/or La_2O_3 is prepared. This mixture may be melted, [52, 53] or calcined (heated and grinded) at high temperature, [19] which induces a solid-state reaction resulting in polycrystalline samples. These are regrinded and sintered into polycrystalline rods which are recrystal-

lized using the floating zone method, [185], i.e., by local melting and recrystallization of the material. The whole synthesis was performed in the controlled atmospheres of either oxygen, hydrogen, or inert gasses, in order to control oxydation/reduction levels in the material. The obtained single-crystal rods are quite large (around 5 mm wide, up to 10 cm long) and may consist of several domains. The formation of single crystals and their orientation is verified by X-ray diffraction.

Single crystal samples for transport measurements were cut from the X-ray-oriented larger rods. We are interested in transport properties inside the ac plane. The most suitable sample geometry for $\mathbf{E} \parallel a$ and $\mathbf{E} \parallel c$ measurements is the shape of rectangular parallelepipeds elongated along a - or c -axis, edges parallel to crystallographic axes. For each cuprate composition ($\text{Y}_y\text{Sr}_{14-y}\text{Cu}_{24}\text{O}_{41}$, $y = 0, 0.55, 1.6$, $\text{La}_3\text{Sr}_3\text{Ca}_8\text{Cu}_{24}\text{O}_{41}$ and $\text{La}_{5.2}\text{Ca}_{8.8}\text{Cu}_{24}\text{O}_{41}$) and orientation along the a - or c -axis, two single-crystal samples were cut, typically 3–5 mm in length and a rectangular cross-sections of 0.12–0.20 mm². Orientation of their edges along the axes was also subsequently verified by XRD, and were never found to deviate from the crystallographic axes more than the experimental error of the XRD equipment used, 1–3°. Routinely, for each composition and orientation both samples were measured to verify sample and contact quality, and in all cases have given consistent results.

For complex THz transmission spectroscopy, crystals with plane-parallel faces were polished to a thickness of about 0.5 mm with transverse dimensions about 7×7 mm².

In case of dc and dielectric spectroscopy measurements, four annular contacts were applied along the length of the samples (in the two-contact dielectric spectroscopy only the end-covering contacts were used). The contacts were prepared as follows. [186] All surfaces of a sample were first lightly cleaned with fine sandpaper, washed in ethanol and left to dry. Annular contacts themselves were applied using DuPont 6838 silver paint directly on the surface, and cured for one hour at 750 K in oxygen-flow atmosphere. Thin gold leads (20 μm diameter) were pasted to the cured contact areas with standard DuPont 4929 silver paint. Contact resistances were routinely checked in three- and two-contact configurations approximately every 20 K during measurements to exclude any possible measurement artefacts.

3.5.3 α -(BEDT-TTF)₂I₃

α -(BEDT-TTF)₂I₃ samples were synthesized by electrical oxidation of BEDT-TTF in a tetrahydrofuran solution containing $(n\text{-C}_4\text{H}_9\text{O})_4\text{N}^+\text{I}_3^-$ as electrolyte, where α -(BEDT-

TTF)₂I₃ was deposited as flat planar monocrystal plates with a thickness of approximately 35–55 μm and an area of about 10–30 mm². As a rule, the pronounced sample plane is in the *ab* plane of the crystal structure. *c*-axis of the crystal structure corresponds to the direction perpendicular to sample plane. α-(BEDT-TTF)₂I₃ crystals are easily oriented using IR spectroscopy, which is particularly suitable due to its nondestructability and the characteristic anisotropic IR spectra of α-(BEDT-TTF)₂I₃ at room temperatures along *a*- and *b*-axes.

The infrared and THz reflectivity measurements were performed on as-grown surfaces; for the *c*-axis investigation infrared microscope was employed. Optical properties were found to be consistent without significant sample dependence.

As opposed to optical properties, sample-dependent transport properties have been previously been reported [117]. Our own preliminary measurements have found a significant sample dependence of the activation energy below the charge-ordering phase transition. It became apparent that extracting reliable information on in-plane transport anisotropy required well-oriented samples cut from the same single crystal. Therefore we have chosen a high-quality single crystal with a homogenous surface and used it to cut all of the transport samples. The cut samples are thin and needle-shaped, ensuring a homogenous flow of current. The original crystal was first oriented under the FTIR microscope setup. It was then covered in carbon paint and left to dry, to provide mechanical support during cutting. A slow, low-pressure wire saw was used to cut four needle-like samples in total, two along both *a*- and *b*-axis, of typical dimensions 1.5 × 0.2 × 0.04 mm³. The resulting well-oriented needles were cleaned of carbon paint in the carbon paint solvent and shortly in tetrahydrofurane solution, which again gave a highly reflective clean surface with good IR spectra. Four gold wires were applied on the surface using carbon paint for current and voltage contacts, taking care to cap the sample ends with the paint for better current injection.

Separate transport and dielectric measurements were also done on another high-quality sample, with contact orientation confirmed by infrared reflectivity and subsequent x-ray diffraction to be at an angle of approximately 45° to the crystal axes, along [1 $\bar{1}$ 0]. Hence these measurements will be denoted as “diagonal” or “**E** || [1 $\bar{1}$ 0]”

Chapter 4

Evidence of orbital ordering in BaVS₃

4.1 Transport and dielectric response

dc transport and dielectric spectroscopy measurements have been performed with electric field parallel to vanadium chains, $\mathbf{E} \parallel c$. Figure 4.1 displays the temperature dependence of dc resistance. The structural transition to orthorhombic phase happens at $T_S \approx 250$ K and is marked by a change of slope in the metallic behavior of transport [Fig. 4.1(a), inset]. The resistance curve reaches its minimum at 156 K. The transition to insulating state happens at $T_{\text{MI}} = 67$ K, indicated by a pronounced peak at T_{MI} in the logarithmic derivative of resistivity [Fig. 4.1(b)].

Fig. 4.2 shows frequency dependence of the complex dielectric response at three selected temperatures. A pronounced dielectric relaxation is present in the insulating phase and in the metallic phase up to about 80 K, with a symmetric screened loss peak ε'' centered at τ_0^{-1} which moves toward lower frequencies and smaller amplitudes with decreasing temperature. The main features of the dielectric response are well-described by fits to the generalized Debye expression (3.2), where the high-frequency dielectric constant ε_{HF} is found negligible and the symmetric widening parameter $1 - \alpha = 0.8$ temperature-independent. The found behavior clearly demonstrate that a huge dielectric constant $\Delta\varepsilon$ is associated with the metal-to-insulator phase transition (see Fig. 4.3). On decreasing temperature, a sharp rise in $\Delta\varepsilon$ starts in the close vicinity of T_{MI} and reaches the huge value of the order of 10^6 at $T_{\text{MI}} = 67$ K [Fig. 4.3(a)]. This T_{MI} value perfectly matches the phase transition temperature as determined in the dc resistivity measurements.

The observed dielectric relaxation by itself points toward the formation of a charge-

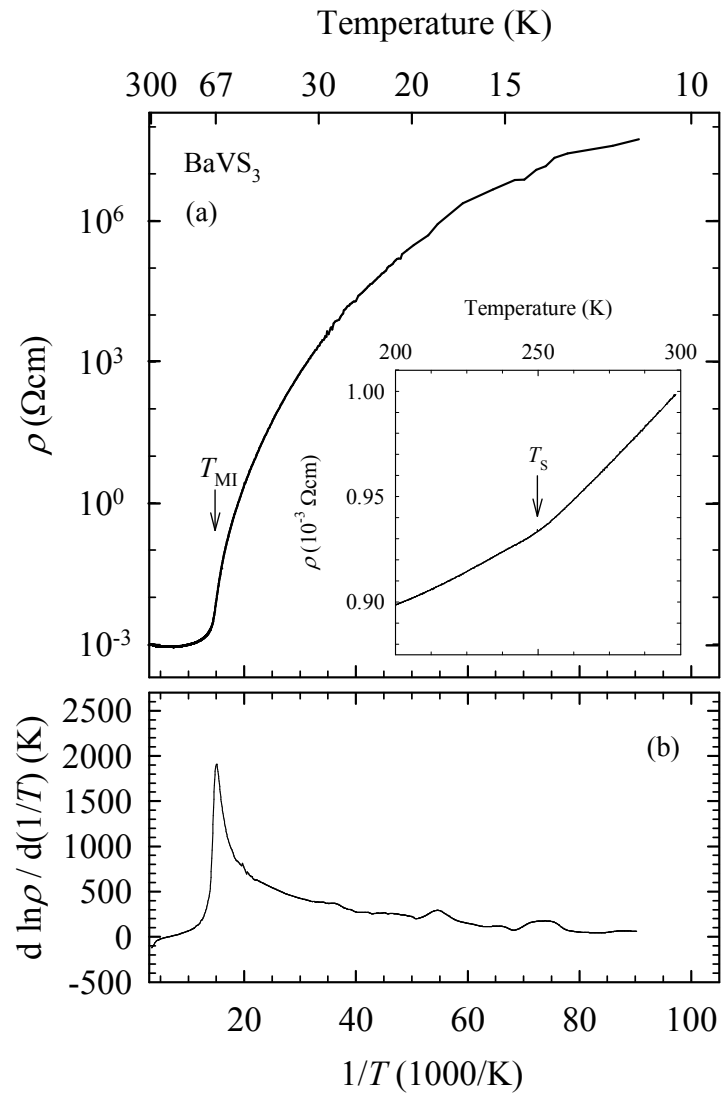


Figure 4.1 – Temperature dependence of (a) dc resistivity and (b) its logarithmic derivative in BaVS₃. The arrows indicate the structural and MI transition temperature.

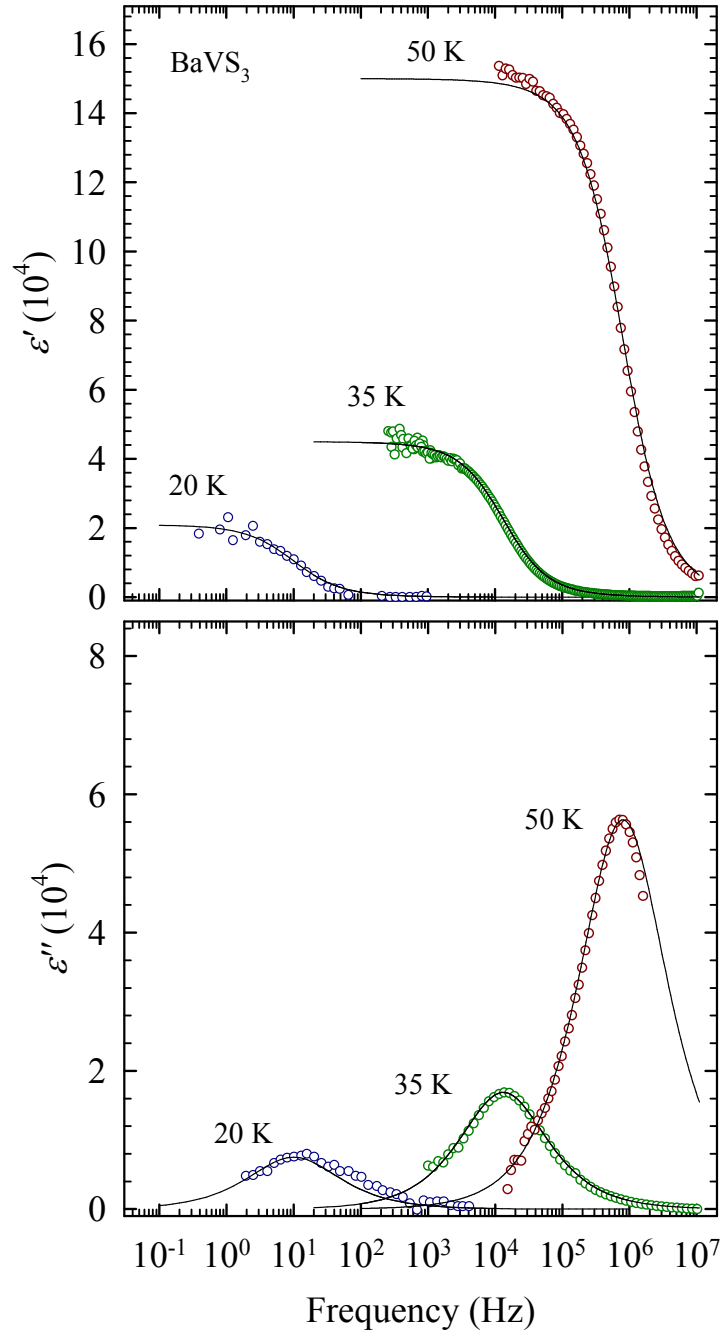


Figure 4.2 – Real (upper panel) and imaginary parts of the dielectric function of BaVS₃ (lower panel) measured at three representative temperatures as a function of frequency with the ac electric field applied along the *c*-axis. The full lines are fits by the generalized Debye expression (3.2).

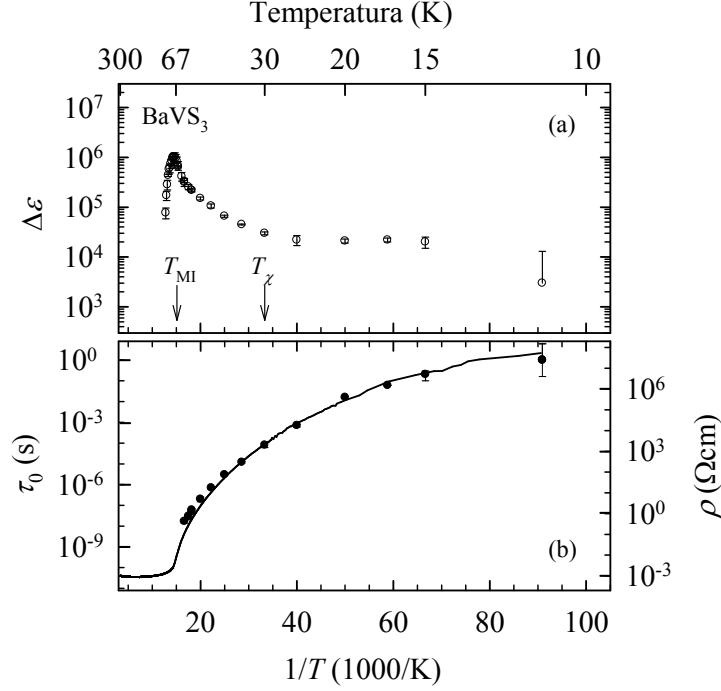


Figure 4.3 – BaVS_3 , fit parameters for the generalized Debye model in Eq. (3.2): (a) dielectric relaxation strength $\Delta\epsilon$, and (b) mean relaxation time τ_0 (points) superimposed to the dc resistivity ρ (full line). The arrows indicates the MI and magnetic transition temperature.

density wave at T_{MI} . It was mentioned in Section 2.1.2 that a standard deformable CDW pinned in a non-uniform impurity potential features two modes, transverse and longitudinal. [187] The former couples to the electromagnetic in the microwave region and yields an unscreened pinned resonance, unfortunately no microwave data is available on BaVS_3 as of yet. The latter, longitudinal mode couples to the electrostatic potential and due to screening of non-uniform pinning centres can be observed as an overdamped low-frequency relaxation at τ_0^{-1} . The low-frequency dielectric mode bears two features expected of such a relaxation. The first is that the relaxation time distribution is symmetrically broadened, $1 - \alpha \approx 0.8$ at all measured temperatures. The second is that the mean relaxation time τ_0 closely follows a thermally activated behavior similar to the dc resistivity $\tau_0(T) = \tau_{00} \exp(2\Delta/2k_{\text{B}}T) \propto \rho(T)$ (see Fig. 4.3(b)). $\tau_{00} \approx 1$ ns describes the microscopic relaxation time of the collective mode and the gap $2\Delta \approx 500$ K agrees with the optical conductivity spectra. [34] Screening can be attributed to single-particle excitations from the wide A_{1g} band.

However, this dielectric relaxation also has features which stand out from the standard phason response. The dielectric constant $\Delta\epsilon$ weakens significantly below T_{MI} and only levels off at temperatures below about 30 K, while the behavior expected in a CDW

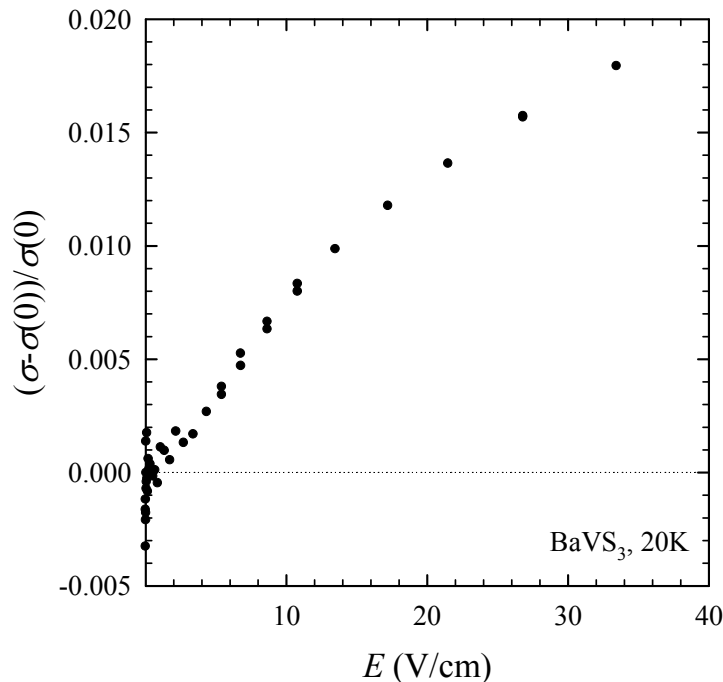


Figure 4.4 – BaVS₃, relative change in dc conductivity $\sigma(E)$ as a function of electric field E at a representative temperature of 20 K.

condensate would be to follow the CDW condensate density n , $\Delta\varepsilon(T) \propto n(T)$, which would intuitively increase with cooling. The drop in $\Delta\varepsilon$ between the MI transition T_{MI} and the magnetic transition T_{χ} is substantial and amounts to two orders of magnitude. One possible explanation for this discrepancy is the very nature of the standard model for the response of the conventional CDW to applied electric fields in which phasons plays a prominent role. Namely, this model is worked out for the incommensurate CDW in a random impurity potential, whereas the density wave in BaVS₃ is associated with the observed lattice modulation is commensurate with the order of commensurability, i.e. the ratio of superstructure and lattice periodicity, $N = 4$. However, the order of commensurability is not as high to impose the commensurability pinning and forbid the phason excitations. [134] Indeed, the fact that the dielectric relaxation is broader than pure Debye response ($1 - \alpha \approx 0.8$) indicates a significant randomness of the background structure.

Another puzzling feature is brought by the dc electric-field dependent measurements. In the standard 1D CDW compounds, the collective charge modulation couples to an applied dc electric field and gives a nonlinear contribution to the electrical conductivity. [131] Measurements with electric fields as high as 100 V/cm in the dc regime between 15 K and 40 K have revealed only a negligibly small non-linear conductivity

which emerges from the background noise, as shown in Fig. 4.4. No clear threshold field is apparent, effectively excluding the standard density wave sliding.

4.2 Discussion

Judging by the dielectric response, the long-wavelength density-wave collective excitations are not fully appropriate for the case of BaVS_3 , i.e., they are frozen or strongly renormalized. A different kind of collective excitations should be responsible for the observed dielectric relaxation. In this section the most plausible scenario for above results is constructed by going through the possible sources of the large dielectric relaxation.

We start with the possibility that the hopping conduction causes the large dielectric constant. In disordered systems with reduced dimensionality Anderson localization can bring about Mott's dc variable-range hopping (VRH) transport, and in the ac limit a power-law dependence on frequency. Even though BaVS_3 may be regarded as a quasi-1D system, the hopping scenario does not seem realistic for two reasons. First, the frequency marking the onset of frequency-dependent transport is known to be roughly proportional to the dc conductivity, i.e., to the inverse of the dc resistivity. [188] In the diverse systems with dc resistivities of similar orders of magnitude to BaVS_3 , the ac conductivity power law is observed only at frequencies above 1 MHz, whereas below 1 MHz an influence of hopping on dielectric dispersion is detected only for dc resistivities much higher than $10^{10} \Omega\text{cm}$ [189, 77] (see the discussion on $(\text{La}, \text{Y})_y(\text{Sr}, \text{Ca})_{14-y}\text{Cu}_{24}\text{O}_{41}$, $y > 2$ in Chapter 5 and Ref. [77]). A crude estimate for the crossover frequency in BaVS_3 may be attempted in the following way. [77] Generally, conductivity due to hopping can be expressed as the sum of two terms,

$$\sigma(\nu, T) = \sigma_{\text{dc}}(T) + A(T) \cdot \nu^s, \quad (4.1)$$

where ν denotes frequency, exponent s is typically close to 1, and both the frequency-independent term $\sigma(T)$ and prefactor of the frequency-dependent term $A(T)$ are allowed to depend on temperature T . The cross-over frequency ν_{co} from frequency-independent to frequency-dependent conductivity can be estimated from the condition that the ac hopping length R_ν becomes smaller than the dc hopping length R_0 . [190] For one-dimensional variable-range hopping, the dc hopping length is given by

$$R_0 = \sqrt{(\Delta c)/(2\alpha T)}, \quad (4.2)$$

and the ac hopping length by

$$R_\nu = \alpha^{-1} \ln(\nu_{\text{ph}}/\nu_{\text{co}}). \quad (4.3)$$

Here c is the distance between two neighboring sites, α^{-1} is the electron localization length and ν_{ph} attempt frequency. We assume that near Fermi level the energy of the sites available for hops has a uniform distribution in the range $+\Delta$ to $-\Delta$. The crossover frequency estimated in this way at temperature T is

$$\nu_{\text{co}} = \nu_{\text{ph}} \exp\left(-\sqrt{\frac{\Delta c \alpha}{2T}}\right). \quad (4.4)$$

Localization length α^{-1} can be taken as comparable to quasi-1D cuprates, $\alpha^{-1} = 0.5 \text{ \AA}$ (see Chapter 5 and Ref. [2]). The distance between two neighboring sites is comparable to lattice parameters, and for this calculation can be taken as equal to the orthorhombic lattice parameter along the c -axis: $c = 5.6 \text{ \AA}$. Further, Δ is estimated from the logarithmic derivation of resistivity at 25 K: $\Delta = 24 \text{ meV} = 280 \text{ K}$. The frequency of hopping attempts is set to be approximately equal to the lowest phonon frequency, $\nu_{\text{ph}} \approx 10^{12} \text{ Hz}$. Using these values Eq. 4.4 gives $\nu_{\text{co}}(25 \text{ K}) = 360 \text{ MHz}$ and $\nu_{\text{co}}(50 \text{ K}) = 3.8 \text{ GHz}$ which is significantly above the frequency window of the experimental setup, meaning the frequency-dependent term in the ac conductivity is unlikely to stem from hopping of localized charges. The second important result which excludes hopping comes from the observed optical spectra. [34] Namely, a simple indication for existence of a hopping mechanism would be a significantly enhanced optical conductivity compared to the dc conductivity, whereas in the case of BaVS_3 the optical conductivity, even at temperatures lower than T_{MI} , is at best comparable to the dc conductivity, as shown by Fig. 4.5. [34]

In the general case of a quarter-filled band with a Peierls-like $2k_{\text{F}}$ distortion no electric dipoles appear. However, in BaVS_3 a secondary $4k_{\text{F}}$ order parameter is present which allows for a dipole moment. Hence, the ferroelectric nature of the MI transition might be responsible for the dielectric response. Simple space group considerations indicate that below the MI transition the structure of BaVS_3 is noncentrosymmetric with a polar axis in the reflection plane containing the VS_3 chains: the symmetry of this low-temperature superstructure is Im , which implies that the distortions of the two chains of the unit cell are out of phase, [33] and a charge disproportionation would generate a dipole moment. Bond-valence sum (BVS) calculations of these x-ray data have indicated some charge disproportionation at low temperatures, below T_{x} , amounting to -0.17, +0.14, +0.31 and

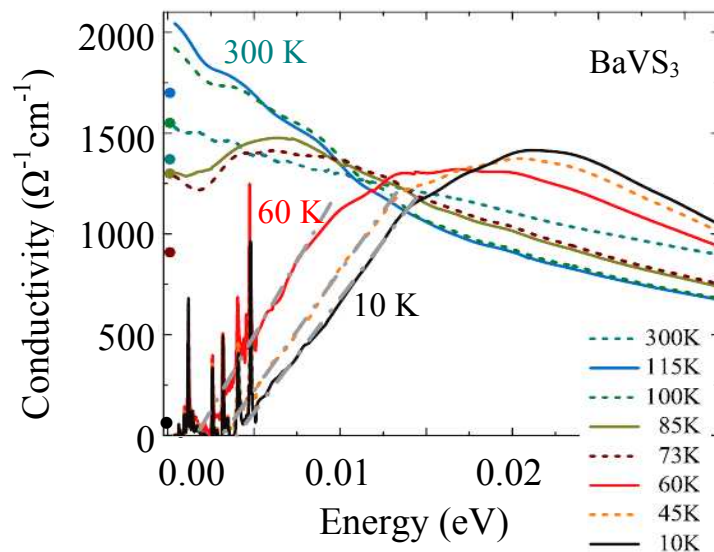


Figure 4.5 – DC (points) and optical conductivity (lines) in BaVS₃ at various temperatures with electric field along the chains $\mathbf{E} \parallel c$. After Kezsmarki *et al.* [34]

+0.13 for V1-V4, respectively. However, it was argued by Foury-Leylekian [191] that the BVS method overestimated the charge disproportionation due to several reasons: a nonsymmetric V⁴⁺ environment, lack of corrections for thermal contraction, and rather imprecise atomic coordinates used in the calculations. As already pointed out in Section 1.1.1, x-ray anomalous scattering in fact shows only a negligible charge redistribution, not larger than 0.01 electron below T_{MI} . [9] It can therefore safely be concluded that ferroelectricity cannot provide an explanation of the dielectric response in BaVS₃.

Yet another option to explain the dielectric relaxation is to consider phason excitations in a commensurate density wave phase; indeed, a description of BaVS₃ in terms of an $N = 4$ density wave has been proposed. [183] Here the $2k_{\text{F}}$ instability of d_{z^2} electrons occurs at T_{MI} and its local magnetic field also induces the density-wave ordering on the narrow e_g electrons. This picture seems to be supported by the phase boundary analysis as a function of magnetic field, where magnetic-field-induced suppression of MI transition has been found to agree well with effects found in organic and inorganic compounds as well as theoretical predictions. [192] Assuming strong commensuration effects, the density wave would be commensurably pinned to the lattice. The behavior of $\Delta\varepsilon$ with temperature could then be understood as reflecting the commensurability gap: the initial drop of the dielectric response below T_{MI} indicates that excitations across this gap are progressively less likely, and its settling to a constant value below T_{χ} might be due to the competing magnetic incommensurability taking over. It has to be noted however that the order of the $N = 4$ commensurability is typically not enough to impose

a strong commensurate pinning of a density wave: [135] the observed dielectric strength $\Delta\varepsilon \sim 10^4\text{--}10^6$ is orders of magnitude lower than values typical for a SDW ($\sim 10^7\text{--}10^9$). [193, 194] Additionally we observe a wide dielectric relaxation, $1 - \alpha \approx 0.8$ which implies a disordered pinning background and makes the respective excitations more akin to phasons of an incommensurately-pinned density wave.

Finally, orbital ordering should be taken into consideration as a plausible ground state with collective excitations which might cause the observed dielectric relaxation. This is a good place to again review the arguments by Fagot *et al.* who associate orbital ordering with the MI transition to consistently explain structural data of BaVS₃. [9] Results in favor of an orbital ordering scenario at T_{MI} are an almost non-existent charge modulation in the insulating phase together with a qualitative structural analysis of the VS₆ octahedron distortions, which reveals an out-of-phase modulation of the occupancy of V sites by the d_{z^2} and $e(t_{2g})$ orbitals. In particular, dominant E_{g1} and A_{1g} occupancies are proposed for V1 and V3 sites respectively, while no definitive preferential occupancy was found for V2 and V4 sites [see Fig. 1.6(d)]. Supporting this assignment of orbital occupancies are recent x-ray absorption spectroscopy measurements at the V L₃ edge which discern four inequivalent V-sites below the MI transition. [195] Further, LDA+DMFT calculations for the monoclinic insulating phase of BaVS₃ have qualitatively confirmed an orbital-ordering scenario showing a V-site-dependent orbital occupancy and only minor, if any, charge disproportionation. [45] However, these calculations predict a different orbital ordering where the (V3,V4) pair forms a correlated dimer with mixed A_{1g} and E_{g1} occupancy, while the V1 and V2 ions bear major E_{g1} occupancy with negligible coupling. The LDA+DMFT study indicates that the electronic structure is very sensitive to change of temperature despite only small changes in local environment of the V sites. Orbital ordering below T_{MI} , if any, should be corroborated by magnetic ordering. ⁵¹V NMR and NQR measurements also suggested an orbital ordering below T_{MI} which fully develops at long length scales only below T_{χ} . [10]. The magnetic phase transition at T_{χ} is preceded by long-range dynamic AF correlations all the way up to T_{MI} and this phase bears features of a gapped spin-liquid-like phase. Mihály *et al.* pointed out that the lack of magnetic long-range order between T_{MI} and T_{χ} might be due to the frustrated structure of a triangular array of V chains, which also prevents the orbital long-range order, so that the long-range spin and orbital orders can develop only well below T_{MI} . [7] The AF static order below T_{χ} is not a conventional Néel phase: an AF domain structure is suggested by the magnetic anisotropy measurements. [196] The existence of domains is also supported by muon spin rotation (μSR) experiments. Two independent measurements by Higemoto *et al.* and Allodi *et al.* show

an essentially random distribution of sizeable static electric fields below T_χ which implies an incommensurate or disordered magnetism. [197, 198]

Based on the considerations above the following scenario emerges as the most plausible. The primary order parameter for the MI phase transition is 1D Peierls-like density wave instability. It drives the orbital ordering *via* structural changes involving a reduction from orthorhombic to monoclinic symmetry, with internal distortions of VS_6 octahedron and tetramerization of V^{4+} chains. The imposed orbital order is coupled with the spin degrees of freedom and drives the spin ordering into an AF-like ground state below 30 K. In other words, the orbital ordering transition happens at T_{MI} , domains of orbital order gradually consolidate and grow with lowering temperature (at the same time their number diminishes) and the long-range order eventually stabilizes below T_χ , albeit with a persisting domain structure. In this picture the collective excitations responsible for the observed dielectric relaxation would have to be short-wavelength ones, such as domain walls in the random AF domain structure. We note that the domain wall and soliton both stand for short wavelength excitations; solitons are usually one-dimensional objects, while domain walls are not dimensionally restricted. Similar short-wavelength excitations associated with domain structure have previously been invoked as the origin induced dipoles and their dielectric relaxation in diverse systems. [199, 200] The relaxation happens between different metastable states which correspond to local changes of the spin configuration, which in turn is intimately connected with the charge and orbital degrees of freedom. Since the dielectric constant measures density of collective excitations, its anomalous temperature behavior below T_{MI} indicates that the relaxation-active number of domain walls decreases with lowering temperature and eventually becomes well-defined below T_χ . In other words, the dynamics of domain walls becomes progressively more restricted as the temperature lowers and becomes constant below T_χ . Unfortunately, there are no models or calculations which would predict the dispersion of collective excitations in an orbitally-ordered phase such as the one of $BaVS_3$.

Chapter 5

(La,Y,Sr,Ca)₁₄Cu₂₄O₄₁ - crossover of electrical transport from chains to ladders

5.1 Anisotropy of dc transport

Fig. 5.1 shows the behavior of dc resistivity and its logarithmic derivative for different La,Y content ranging from $y = 5.2$ to $y = 0$ along the c -axis [panels (a) and (b)] and the a -axis [panels (c) and (d)] in the wide temperature range from 50 K (the lowest temperature obtained in our experiment) up to 700 K. While for two compounds with high $y = 5.2$ and 3 the dc resistivity curves along the c -axis and the a -axis markedly differ below about 300 K, the one along the c -axis presenting a much smaller increase with lowering temperature, one finds an almost identical behavior of dc resistivity along the both axes for $y = 1.6$, 0.55 and 0. An immediate conclusion that can be drawn from observed behaviors is that the conductivity anisotropy becomes significantly enhanced for high La,Y content $y \geq 3$ (i.e., low hole count $n_h \leq 3$), whereas it remains small and temperature-independent for low y (high n_h), as depicted in Fig. 5.2. The qualitative difference between the two kinds of behavior is emphasized in Fig. 5.2, which shows conductivity anisotropies normalized to the corresponding RT values. The conductivity anisotropy at RT is in the range of 1-30 and basically does not correlate with La,Y content.

The next significant difference between low and high La,Y contents is found in the temperature dependence of the dc conductivity curves. As already reported for $y = 5.2$

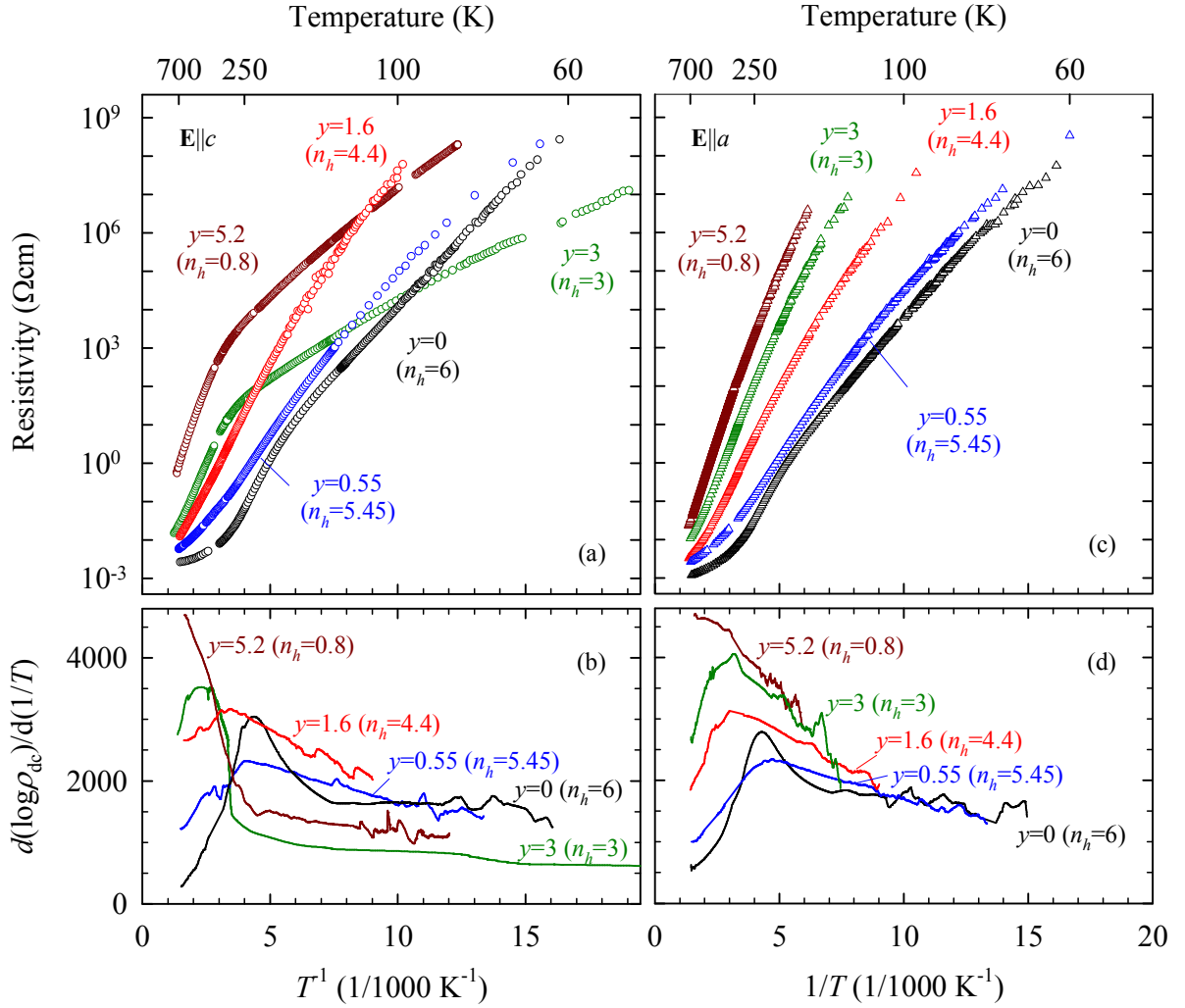


Figure 5.1 – dc resistivity and logarithmic derivatives of $(\text{La,Y,Sr,Ca})_{14}\text{Cu}_{24}\text{O}_{41}$ for various La,Y content y along the c [panels (a) and (b)] and the a [panels (c) and (d)] crystallographic directions.

and 3, the dc conductivity along the c -axis $\sigma_{\text{dc}}(c)$ follows a variable-range hopping behavior with the dimension of the system $d = 1$, and crosses over around T_{co} to nearest neighbor hopping at high temperatures. [22, 2, 58] The observation of $d = 1$ type of VRH conduction is in accord with a rather small interchain coupling in $(\text{La}, \text{Y}, \text{Sr}, \text{Ca})_{14}\text{Cu}_{24}\text{O}_{41}$. Conversely, VRH fits

$$\sigma_{\text{dc}}(T) = \sigma_0 \exp \left[- \left(\frac{T_0}{T} \right)^{1/(1+d)} \right] \quad (5.1)$$

to the $\sigma_{\text{dc}}(c)$ curves for $y = 1.6$ and $y = 0.55$ fail to give a meaningful description: the respective values of the VRH activation energy $T_0^{\text{exp}} = 13400$ meV and 9000 meV, obtained from the fit of our data by expression (5.1) are much larger than those for $y = 5.2$ and 3 . This result is at variance with the behavior expected in the VRH mechanism: the more conductive the sample, the lower T_0 is expected. Indeed, these T_0^{exp} values are markedly different from the ones expected theoretically: $T_0^{\text{th}} = 2 \cdot \Delta \cdot c_{\text{C}} \cdot \alpha \approx 1900$ meV and 700 meV, see Table 5.1. Here the energy of sites available for hops near the Fermi energy is assumed to be uniformly distributed in the range $-\Delta$ to Δ , c_{C} is the distance between the nearest Cu chain sites and $\alpha^{-1} = 2c_{\text{C}} \cdot T_{\text{co}}/\Delta$ is the localization length. In particular, the experimental values T_0^{exp} are so high that the usual interpretation of the hopping parameters also leads to values too low for the density of states for $y = 1.6$ and 0.55 , when compared with $y = 5.2$ and 3 . It can be noted that the one-dimensional VRH conducting channel along the c -axis, which is present in $y \geq 3$, is more efficient when compared with the transport in $y < 3$.

When one compares high- and low- y compounds, the dc resistivity changes with y in a similar manner for both $\mathbf{E} \parallel c$ and $\mathbf{E} \parallel a$. The slope of $\log \rho_{\text{dc}}$ vs. T^{-1} curves for $y = 5.2$ and 3 shows that the activation energy is much larger at high temperatures and becomes smaller with decreasing T , whereas for $y = 0.55$ and 0 we find an opposite behavior: a smaller activation energy at high temperatures and a larger one at low temperatures. It appears that the $y = 1.6$ compound is situated somewhere at the border between these two distinct behaviors. As a reminder, for $y = 0$ a smaller activation energy at high temperatures and a larger at low temperatures is a feature associated with an insulator-to-insulator phase transition into the CDW phase of ladders. [17]

Another difference between compounds with low and high y contents becomes obvious when looking at the logarithmic derivative curves (Fig. 5.1, panels (b) and (d)). For $y = 0.55$ (but not $y = 3$ and 5.2), both $\mathbf{E} \parallel a$ and $\mathbf{E} \parallel c$ orientation show a broad and flat maximum in $d(\ln \rho)/d(1/T)$ centred at about 210 K, similar to $y = 0$ where this

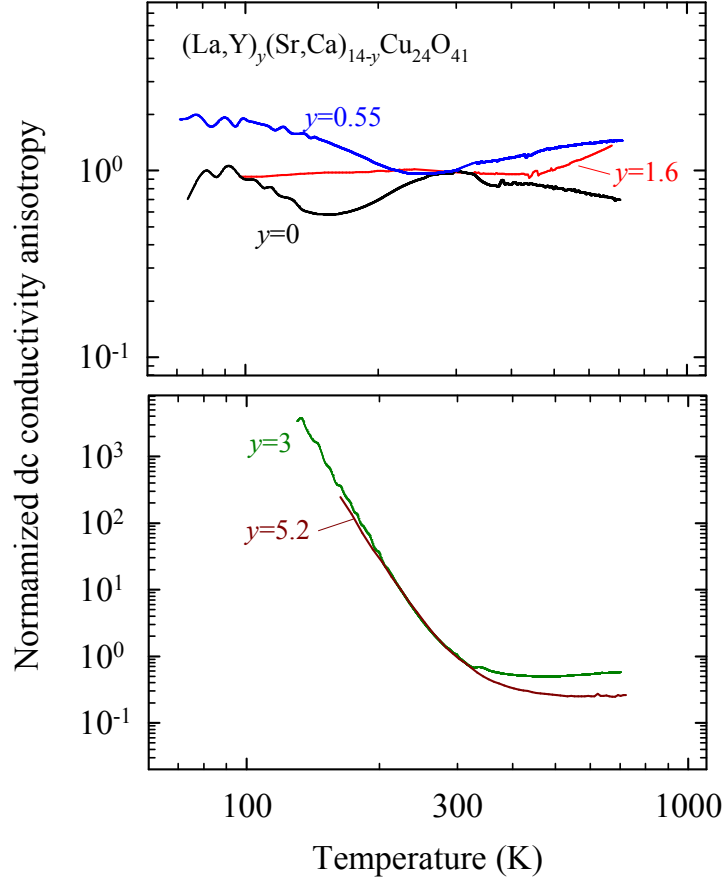


Figure 5.2 – Temperature dependence of the conductivity anisotropy of $(\text{La},\text{Y},\text{Sr},\text{Ca})_{14}\text{Cu}_{24}\text{O}_{41}$ for various La,Y content y normalized to the corresponding room temperature value.

Table 5.1 – dc transport parameters of $(\text{La},\text{Y},\text{Sr},\text{Ca})_{14}\text{Cu}_{24}\text{O}_{41}$ for various La,Y content y along the c -axis.

Compound	y	Δ (meV)	T_{co} (K)	T_0^{exp} (meV)	α^{-1} (Å)	T_0^{th} (meV)
$\text{Y}_{0.55}\text{Sr}_{13.45}\text{Cu}_{24}\text{O}_{41}$	0.55	130 ± 40	280 ± 15	9000 ± 100	0.960	750
$\text{Y}_{1.6}\text{Sr}_{12.4}\text{Cu}_{24}\text{O}_{41}$	1.6	230 ± 10	330 ± 30	13400 ± 100	0.677	1900
$\text{La}_3\text{Sr}_3\text{Ca}_8\text{Cu}_{24}\text{O}_{41}$	3	280 ± 10	295 ± 5	2500 ± 100	0.481	3400
$\text{La}_{5.2}\text{Ca}_{8.8}\text{Cu}_{24}\text{O}_{41}$	5.2	370 ± 50	330 ± 5	4300 ± 100	0.435	4600

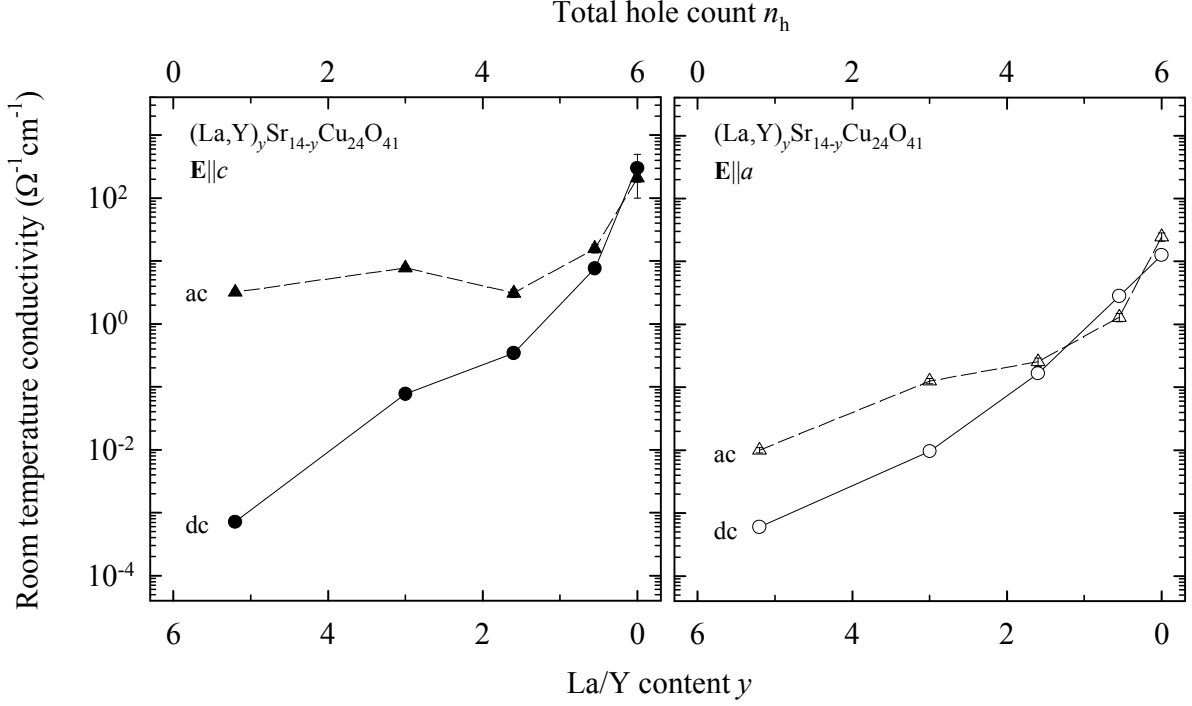


Figure 5.3 – Room temperature dc (circles) and ac conductivity at 10 cm^{-1} (triangles) along the c -axis (left panel) and the a -axis (right panel) as a function of La,Y content y and total hole count n_h . The full and dashed lines are guides for the eye for dc and ac data, respectively.

feature, albeit more narrow, is recognized as a signature of the CDW phase transition in the ladders. This feature remains visible for $y = 1.6$; however it is now extremely broad and flat, shifted to 300 K and more pronounced for $\mathbf{E}||a$ than in $\mathbf{E}||c$ orientation.

Finally, an unusual result concerns the magnitude of RT conductivity along both axes which increases substantially with total hole count (see Fig. 5.3). It is evident that the increased number of holes per formula unit cannot account completely for this orders-of-magnitude rise in conductivity. Theoretically, doping could create a finite density of states at the Fermi level by shifting the Fermi level from the gap into the region with high density of states, which then might partially account for the observed conductivity rise. Nevertheless, an overall rise hints to an extraordinary increase of mobility which happens for y smaller than two.

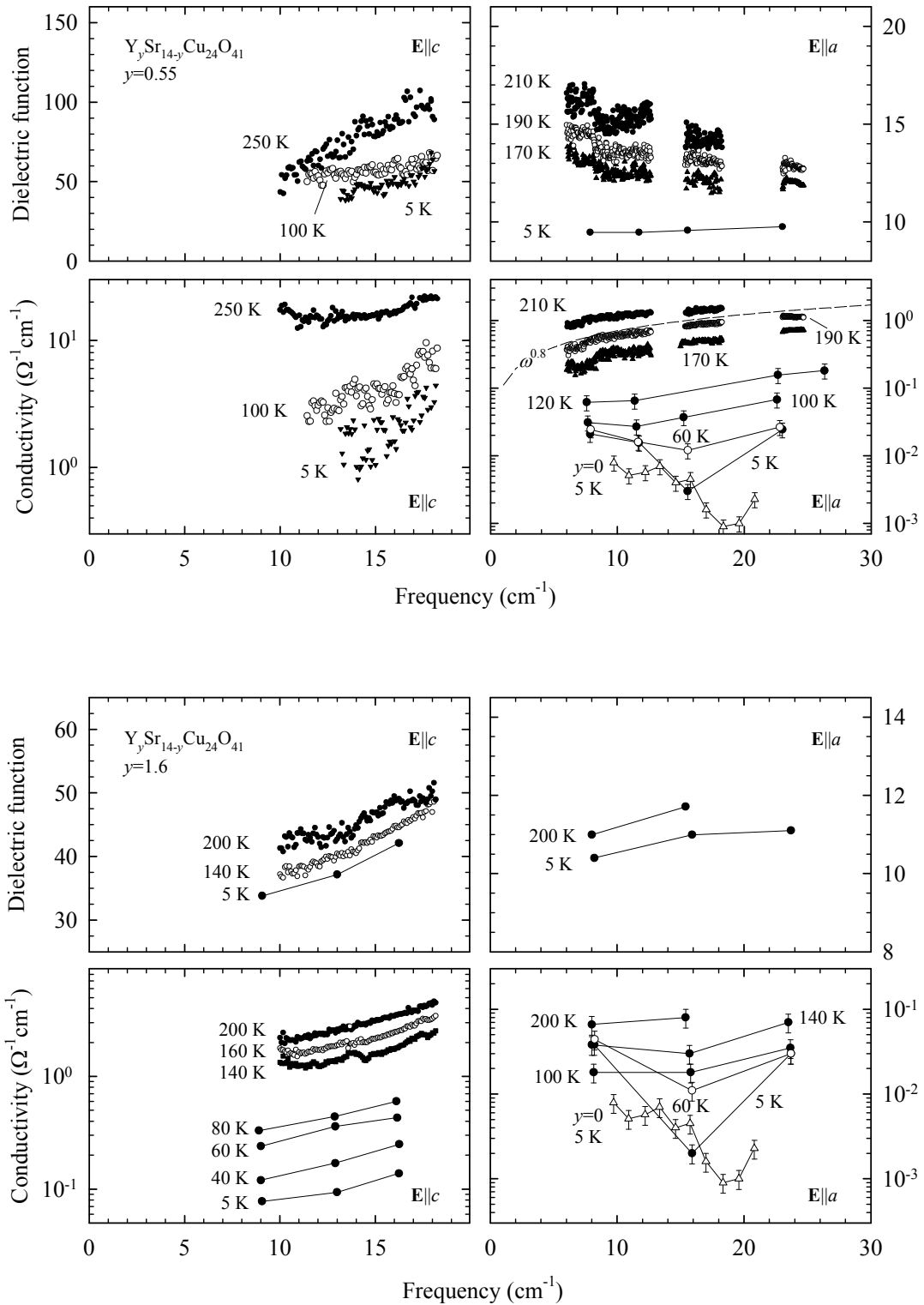


Figure 5.4 – Dielectric function and infrared conductivity in THz region of $Y_ySr_{14-y}Cu_{24}O_{41}$ for various Y content $y = 0.55$ (upper panel) and 1.6 (lower panel) along the c - and a -axis at several temperatures as indicated. Conductivity data for $y = 0$ along the a -axis at 5 K (denoted as open triangles) are shown for comparison.

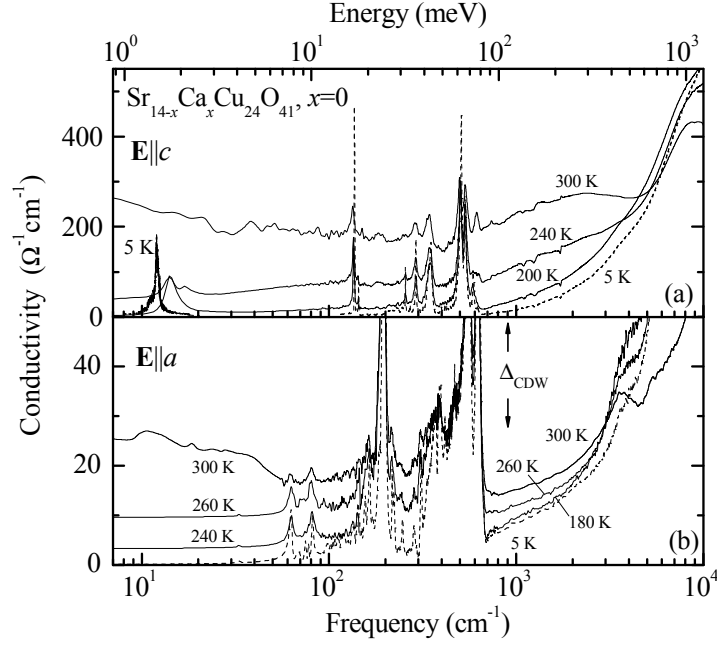


Figure 5.5 – Optical conductivity of the parent compound $\text{Sr}_{14}\text{Cu}_{24}\text{O}_{41}$, $x = 0$ along the c -axis (a) and along the a -axis (b) at several representative temperatures. Vertical arrows show the charge-density wave gap obtained from the activated dc resistivity. After Refs. [13, 17, 12, 2]

5.2 Frequency-dependent conductivity and dielectric function

A comparative analysis of dc and ac conductivity data is in order. The conductivity spectra of $(\text{La}, \text{Y}, \text{Sr}, \text{Ca})_{14}\text{Cu}_{24}\text{O}_{41}$ for $y = 0.55$ and 1.6 in the frequency range between 5 and 25 cm^{-1} at several representative temperatures are shown in Fig. 5.4. An almost dispersionless conductivity spectrum at RT reveals the existence of a metallic response of $y = 0$ in the infrared conductivity along both c -axis and a -axis (see Fig. 5.5). [13, 17, 12, 2] Such a metallicity is also evident for $y = 0.55$ and 1.6 , indicating the appearance of a certain amount of free charges not detected in $y = 3$ and 5.2 (Ref. [22]). Hence, the observed spectra could be attributed to the charge excitations in the ladders similarly as for $y = 0$. [2] Cooling below 200 K clearly suppresses the Drude weight in the conductivity spectra of $y = 0.55$ and 1.6 along the c - and a -axis, which means that metallicity gives way to insulating behavior.

In all studied cases, and particularly in $y = 0.55$ and $y = 1.6$, the dc conductivity (see Fig. 5.1) is followed by an increase well into the infrared range. A mechanism standardly responsible for such a conductivity rise is electronic hopping conduction characterized

by a power-law dispersion of Eq. (4.1), as already employed in the discussion of BaVS₃. Indeed, hopping conduction with power $s \approx 1$ has already been established in the ladders of $y = 0$ compound for $\mathbf{E}||c$ and $\mathbf{E}||a$, as well as in the chains of $y = 3$ and 5.2 for $\mathbf{E}||c$. [22, 2, 58] In this study, the power-law behavior is found only for $y = 0.55$ ($\mathbf{E}||a$) between 200 K and 100 K, freezing out at lower temperatures. There are two reasons which prevented detection of hopping conduction for other cases. The first is related to the phonon tail masking the hopping dispersion for $\mathbf{E}||c$ orientation, which is not surprising and actually expected since at low temperatures a low-energy phonon can easily prevail over frozen electronic contributions. Indeed, for the c -axis response of $y = 0.55$ and 1.6, at the lowest temperature ($T = 5$ K) we see a typical phonon tail in the THz range. It seems that for these two compositions the lowest frequency phonon is located at about 25 cm^{-1} , i.e., at the same frequency where the lowest frequency phonon for the $y = 3$ (see Fig. 3 in Ref. [22]) and for Sr₁₁Ca₃Cu₂₄O₄₁ compound was found.

The second reason which prevents detection of electronic hopping for $\mathbf{E}||a$ below about 100 K is due to a clear conductivity increase below 20 cm^{-1} . This increase might be an indication of a transversal pinned CDW mode located in the microwave range. It is noteworthy that this feature is also visible for $y = 0$ compound (see Fig. 5.4 for $\mathbf{E}||a$). Since only the higher frequency slope of the mode is visible, extraction of parameters like eigenfrequency, dielectric strength and damping are unfortunately not feasible. Nevertheless, it is safe to estimate these parameters would be much different from those of the pinned CDW mode as inferred for fully doped compound Sr₁₄Cu₂₄O₄₁ by Kitano *et al.* [15] based on distinct microwave points. On the other hand, for $\mathbf{E}||c$ we do not detect any signature of this mode in the THz range, which might be either due to its location at lower frequencies, or the mode being masked by a contribution of free carriers or a nearby phonon. Even though we observe it in a rather narrow frequency range and is therefore at delicate grounds, it can tentatively be attributed to the pinned ladder CDW mode, especially so since it is notably absent in the THz spectra of $y = 3$ and 5.2 compounds. The issue of pinned CDW mode and its evolution in Y_ySr_{14-y}Cu₂₄O₄₁ obviously deserves more attention in the future, where bridging the gap between GHz and THz region is going to be important. As far as dielectric constant ε' of $y = 0.55$ and 1.6 is concerned, we note that it coincides well with the dielectric constant of the fully doped compound Sr₁₁Ca₃Cu₂₄O₄₁ (see Fig. 66 in Ref. [2]) with short-range CDW correlations in ladders, meaning that the infrared phonon spectra of all these three materials could be very similar.

We turn now to the radio-frequency results. As is well-known, [13, 2] in the $y = 0$

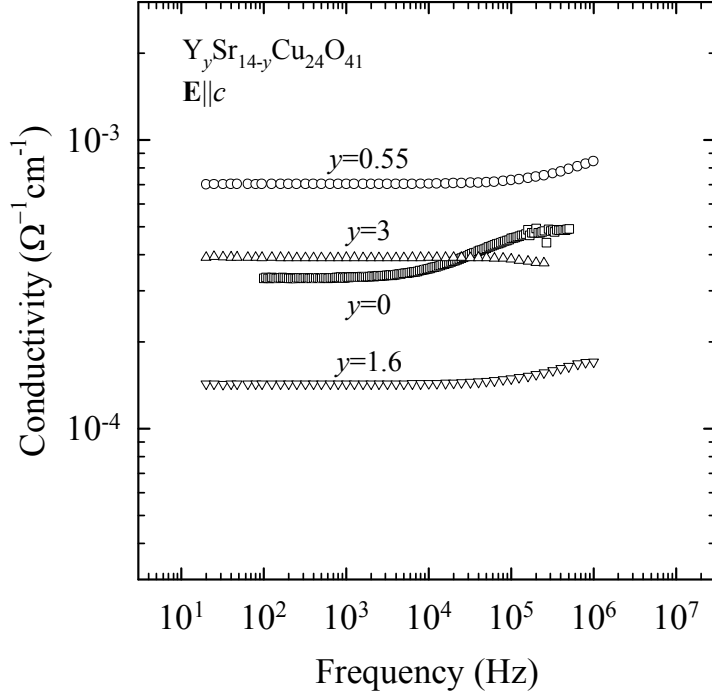


Figure 5.6 – Conductivity spectra of $y = 0, 0.55, 1.6$ and 3 , $\mathbf{E}||c$ in the radio-frequency range at representative temperatures (95 K, 125 K, 165 K and 132.5 K, respectively) with comparable dc conductivities.

compound the CDW develops in the ladders and yields a pronounced step-like conductivity increase in the radio-frequency range. A corresponding frequency dependence is much weaker for $y = 0.55$ and 1.6 and even comparable to the $y = 3$ compound (see Fig. 5.6). We recall that for $y = 3$ as well as for $y = 5.2$ the frequency independent behavior is found in the radio-frequency range for all temperatures. [22, 2, 58] However, unlike $y = 3$ and $y = 5.2$ with its power-law hopping term, when the complex dielectric function for $y = 0.55$ and 1.6 is calculated from complex conductivity, a weak dielectric relaxation mode emerges (see Fig. 5.7): a characteristic step-like drop in the real part of dielectric function and a wide maximum in the imaginary part, resembling that of the fully-doped $\text{Sr}_{14}\text{Cu}_{24}\text{O}_{41}$ parent system ($y = 0$), where CDW is fully developed. A similar behavior is observed for both polarizations $\mathbf{E}||c$ and $\mathbf{E}||a$, as in the case of $y = 0$. Also, the mean relaxation time τ_0 has comparable values and temperature dependence when measured along both the c - and a -axis (Fig. 5.8). [17, 2] However, contrary to the $y = 0$ case, the temperature range in which we were able to track the mode for $y = 0.55$ and 1.6 was rather narrow (see Fig. 5.8). Still, a systematic trend in the behavior upon doping is clearly visible. In this range the dielectric strength is small (10^3 and 10^2 for $y = 0.55$ and 1.6 , respectively) when compared to the value for $y = 0$ (10^4 at same

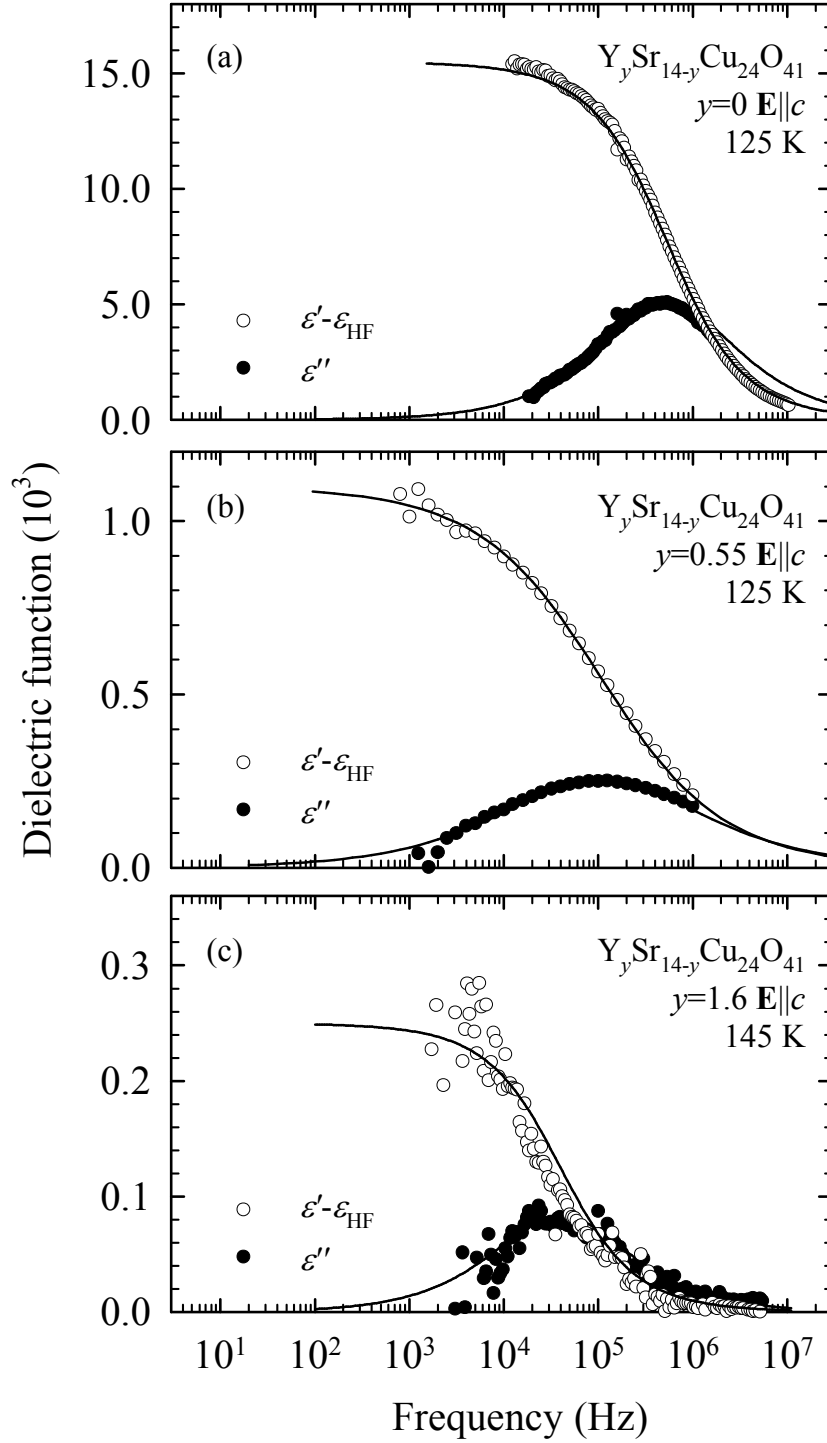


Figure 5.7 – Real (ϵ') and imaginary (ϵ'') parts of the dielectric function of $\text{Y}_y\text{Sr}_{14-y}\text{Cu}_{24}\text{O}_{41}$ for $y = 0$ [panel (a)], $y = 0.55$ [panel (b)] and $y = 1.6$ [panel (c)] at representative temperatures of 125 K ($y = 0$ and $y = 0.55$) and 145 K ($y = 1.6$) as a function of frequency, with the ac electric field applied along the c -axis. The full lines are fits to data using the generalized Debye expression 3.2, $\epsilon(\omega) - \epsilon_{\text{HF}} = \Delta\epsilon / (1 + (i\omega\tau_0)^{1-\alpha})$.

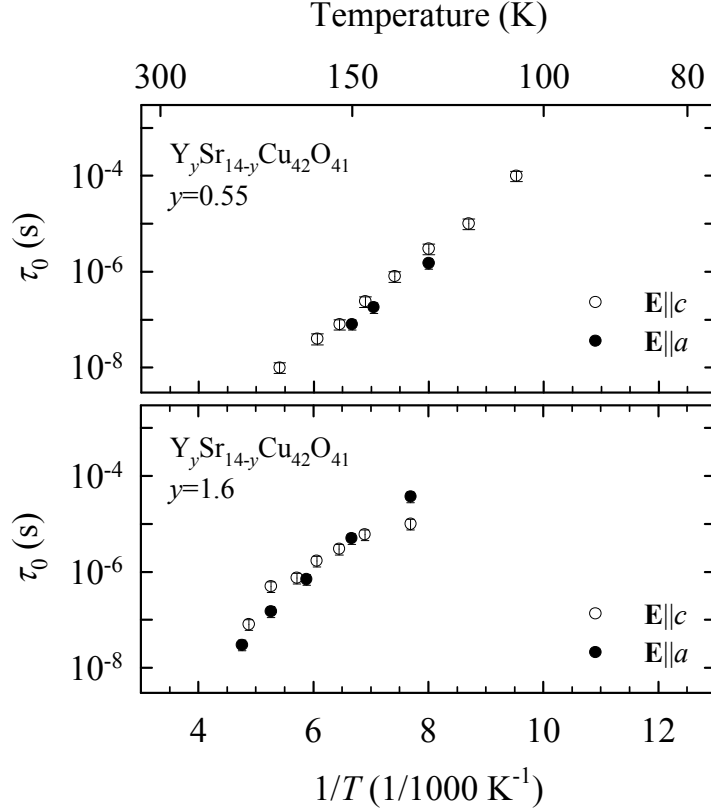


Figure 5.8 – Temperature dependence of mean relaxation times τ_0 for $y = 0.55$ and 1.6. Open and full circles are for $\mathbf{E}||c$ and $\mathbf{E}||a$, respectively.

temperatures). Another worrisome issue is that, because of the small low-frequency capacitance, we were not able to follow its disappearance. Nevertheless, we are tempted to qualitatively associate this weak mode with a ladder CDW order which persists only at short length scales for $y = 0.55$ and 1.6, whereas it fully disappears for $y = 3$ and 5.2.

Finally, coming back to the crossover from metallic to insulating behavior upon doping (i.e., increasing y), we compare the room-temperature ac conductivity at 10 cm^{-1} with dc conductivity and find the following interesting feature (see Fig. 5.3). RT conductivity data clearly show how the metallic-like character of charge transport in $y = 0$ (σ_{ac} is close to σ_{dc}) gradually deteriorates with y (σ_{ac} values differ from σ_{dc}) and becomes typical for dielectrics for $y = 3$ and 5.2. It is hard to quantify where this change starts since for $y = 0.55$ and 1.6 the highest temperatures at which σ_{ac} was measured were 210 K and 250 K, respectively (the reason for this limit is purely technical, namely high conductivity values caused the transmittivity to become too low for reliable measurement). This means the actual RT σ_{ac} are higher than those shown in Fig. 5.3. Taking this into account, the dc and ac conductivity contributions differ substantially along

both orientations for $y \gtrsim 2$, i.e., when the total hole count is smaller than 4. At temperatures lower than about 200 K, reliable estimates of infrared conductivity are prevented due to either a phonon or a pinned CDW-like mode influence. However, we can say that $\sigma_{ac}(10 \text{ cm}^{-1})/\sigma_{dc}$ ratio for all La,Y contents increases with lowering temperature, indicating the evolution of the insulating behavior.

5.3 Discussion

From the above analysis a picture presents itself where the one-dimensional hopping transport along the chains for $2 < y \leq 6$ (hole-doping from zero to three injects holes uniquely into chains) crosses over into a quasi-two-dimensional charge conduction in ladders for smaller y . Supports for this conjecture are:

- a weak and temperature-independent conductivity anisotropy (see Fig. 5.2) for $0 \leq y \leq 1.6$,
- a maximum in $d(\ln \rho)/d(1/T)$ centered around 210 K (see Fig. 5.1) which becomes broader and flatter going from $y = 0$ to 1.6,
- a smaller activation energy at high temperatures and larger at low temperatures: this difference disappears for $y = 1.6$.

These results might be attributed to the ladder CDW, whose long-range order as developed in $y = 0$ compound (coherence length of about 260 Å) [16] is destroyed as holes are removed, but domains developed at short range scale still persist until $y \approx 1.6$. Indeed, a weak dielectric relaxation mode is detected in the radio-frequency range which resembles a CDW loss peak. The increase of conductivity below 20 cm^{-1} and its considerably larger value compared to the dc limit infer an additional mode somewhere in the microwave range. One might be tempted to ascribe it to the pinned CDW mode, although the parameters should be different (most likely of larger spectral weight and shifted to higher frequencies) than those of the peak that was proposed to be the pinned mode in $y = 0$ compound (see Fig. 1.17).

Further, recall that neutron scattering and static susceptibility measurements show a gradual destruction of AF dimer long-range order in chains (AF dimers separated by a site occupied by a localized hole) as y increases from zero to one ($0 < y \leq 1$). [201,83,202] In addition, NMR measurements of spin-lattice relaxation rate revealed that the spin

gap associated with AF dimer order in chains persists until $y = 2$. [203] The latter result tells us that antiferromagnetic and charge correlations for $y = 2$ (total hole count $n_h = 4$) are already strong enough to dynamically form domains of AF dimers and the related charge order and so persist at short time scales. Concomitantly, chains cease to be a favorable charge transport channel and the beginning of hole transfer to ladders is induced. A partial hole transfer from chains into ladders starts once the total hole count becomes close to and over 4. Although probably only a tiny amount of holes is transferred to ladders for $y = 1.6$, from likeness with the parent compound it appears that the observed conduction with a weak and temperature-independent anisotropy happens predominantly in ladders. For $y = 0.55$ charge transport along the chains becomes almost completely frozen due to the rather well-developed AF dimers and CO. It is taken over by two-dimensional ladders with significantly more mobile holes which give an important conductivity rise toward $y = 0$.

Our results therefore suggest that ladders at La,Y content $y \lesssim 2$ prevail over chains as the conduction channel. A question arises why do holes, which are doped exclusively into the chains as La,Y content is varied from $y = 6$ to $y \approx 2$, start to be distributed between chains and ladders once their total count is larger than 4? In other words, it appears that doping more than 4 holes in the chains is energetically favorable only if at least a tiny amount of holes is concomitantly doped in the ladders. Fully-doped systems already demonstrate that there is a subtle interaction between chains and ladders and their electronic phases: the chain CO and AF dimer pattern on one side and ladder CDW on the other are both being suppressed at a similar rate. [204, 2] Here-presented results in the underdoped series strengthen this idea and additionally reveal that the stability of these two distinct electronic phases is also mutually interdependent, in the sense that one cannot develop without the other.

As a final remark, the proposed scenario fits perfectly well to the hole distribution proposed by Nücker *et al.* [14] for $y = 0$ compound, $\text{Sr}_{14}\text{Cu}_{24}\text{O}_{41}$: close to 5 holes per formula unit in the chains and close to 1 hole per formula unit in the ladders. However, this hole distribution cannot account for the observed periodicity of CDW in ladders. [16] Conversely, a hole distribution of close to three hole per formula unit in both ladders and chains, as proposed by Rusydi *et al.*, [74] demonstrates opposite problems in explaining formation of electronic phases in the underdoped series towards fully doped systems when La,Y content decreases from $y = 3$ to $y = 0$, i.e. when the total hole count increases from three to six. Namely, a gradual doping of holes from zero to three in ladders nicely explains formation of the CDW in ladders and its eventual

periodicity found in $y = 0$ compound when long-range order is developed. On the other hand, a fixed hole count in chains in the range $0 \leq y < 3$, cannot concisely explain the short-range AF dimer and CO domains therein which dynamically appear at $y \approx 2$ and grow in size as La,Y content decreases to $y = 0$. It also stays in contradiction with magnetic susceptibility which show that on decreasing y in the range $0 \leq y \leq 3$ the number of spins in chains decreases, meaning a gradual increase of hole count in chains. [83,202] Obviously, more experimental efforts are needed to clarify and reconcile these contradictory findings in order to construct a self-consistent picture of physics of chains and ladders in $(\text{La},\text{Y},\text{Sr},\text{Ca})_{14}\text{Cu}_{24}\text{O}_{41}$.

Chapter 6

Collective excitations in the charge-ordered α -(BEDT-TTF) $_2$ I $_3$

6.1 Optics

Despite the numerous reports on the optical properties of α -(BEDT-TTF) $_2$ I $_3$, [205, 206, 207, 208, 209, 210, 211, 28, 117, 119, 212] a few aspects of the development right at or below the charge-order transition are worthwhile to be reconsidered in the present context. The first issue to tackle is the behavior of anisotropy and energy gap in the highly conducting ab molecular plane at the metal-to-insulator phase transition. The second issue concerns the redistribution of charge on the molecular sites. As explained in Section 1.3.3, certain vibrational features of BEDT-TTF molecules and their evolution on cooling depend on their charge. By observing vibrational spectra with light polarized $\mathbf{E} \parallel c$ (perpendicular to the BEDT-TTF planes) the infrared-active $\nu_{27}(B_{1u})$ vibrational mode is targeted. In addition, vibrational features of the BEDT-TTF molecule are discussed in metallic and the CO state as seen with $\mathbf{E} \parallel a$ and b polarizations (along the BEDT-TTF stacks and perpendicular to them, respectively).

Electronic contributions

The experimentally accessible frequency range extends from 10 to 5000 cm^{-1} and covers the bands formed by the overlapping orbitals of neighboring molecules. Fig. 6.1 shows the optical properties for the two polarizations $\mathbf{E} \parallel a$ and $\mathbf{E} \parallel b$ in the highly conducting plane at different temperatures above and below T_{CO} . The optical spectra are dominated by a broad band in the mid-infrared in both directions that is different in

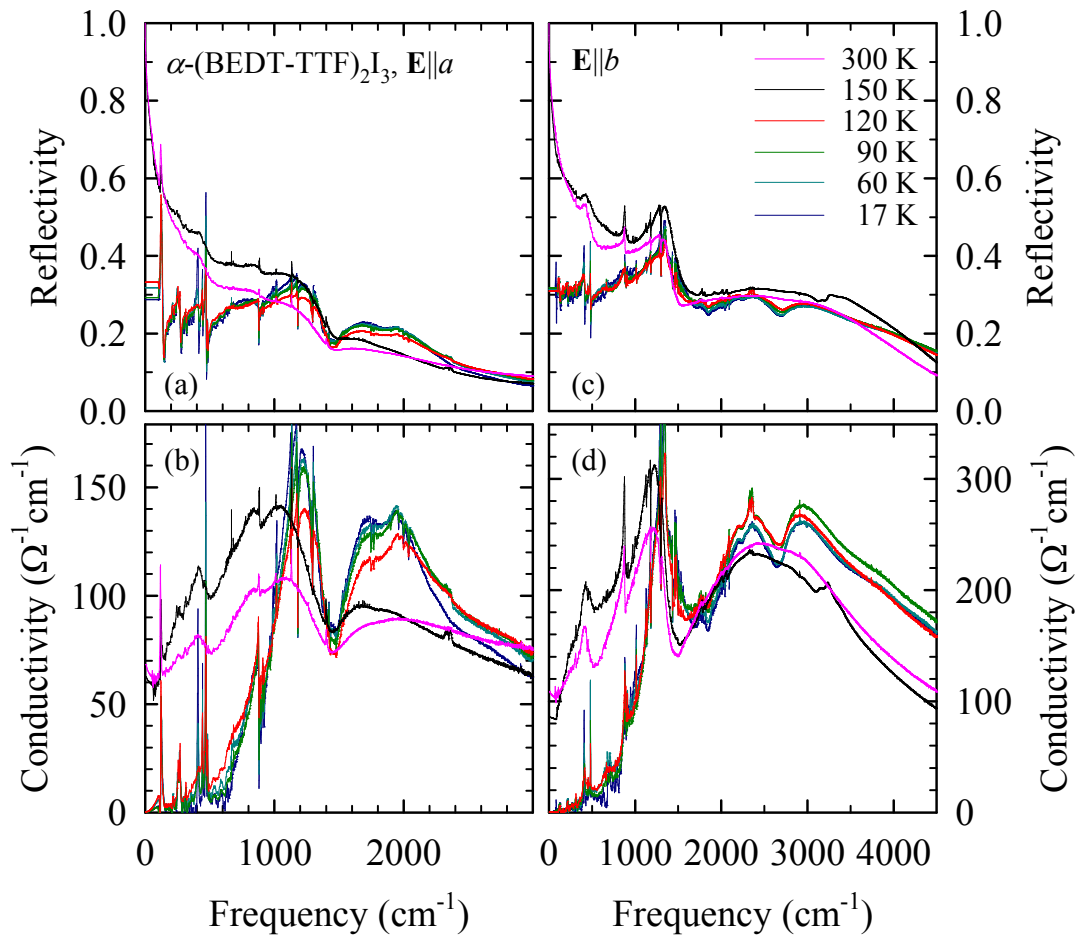


Figure 6.1 – Optical properties of α -(BEDT-TTF)₂I₃ for different temperatures as indicated. The upper panels (a) and (c) show the reflectivity, the lower panels (b) and (d) the corresponding conductivity. On the left side (a) and (b) measurements are shown with the electric field polarized parallel to the stacks ($\mathbf{E} \parallel a$); the panels on the right side display the data for the polarization perpendicular to stacks ($\mathbf{E} \parallel b$).

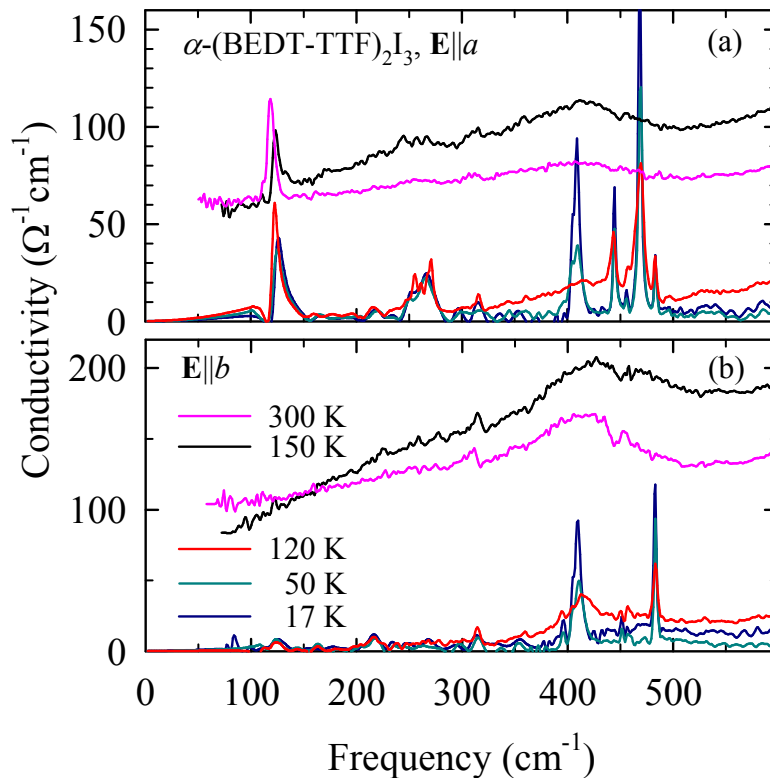


Figure 6.2 – The far-infrared conductivity for (a) $\mathbf{E} \parallel a$ and (b) $\mathbf{E} \parallel b$ for different temperatures above and below the charge order transition at $T_{CO} = 136$ K.

strength by about a factor of 2. A shoulder in $R(\omega)$, which shows up as a pronounced dip in the conductivity spectra around 1450 cm^{-1} , is due to the strong electron-molecular vibrational (emv) coupling of the $\nu_3(A_g)$ mode. [118]

At room temperature the reflectivity clearly shows a metallic response. However, no clear Drude-like response of the quasi-free carriers can be separated from the wing of the mid-infrared band [Fig. 6.1(b), (d) and Fig. 6.2]. The conductivity above the MI transition depends weakly on temperature and is characterized by a small spectral weight compared to the large scattering rate, which is best described as an overdamped Drude response.

Upon decreasing the temperature from room temperature down to T_{CO} , the reflectivity slightly increases due to reduced phonon scattering. In the CO state, the far-infrared reflectivity drops dramatically and the corresponding optical conductivity decreases as the energy gap opens in the density of states (Fig. 6.2). The spectral weight shifts to the mid-infrared range where it piles up in a band with maxima around 1500 cm^{-1} for $\mathbf{E} \parallel a$ and 2000 cm^{-1} for $\mathbf{E} \parallel b$. The maxima in optical conductivity are obscured by the antiresonance at these frequencies, leaving only two side peaks: when screening by

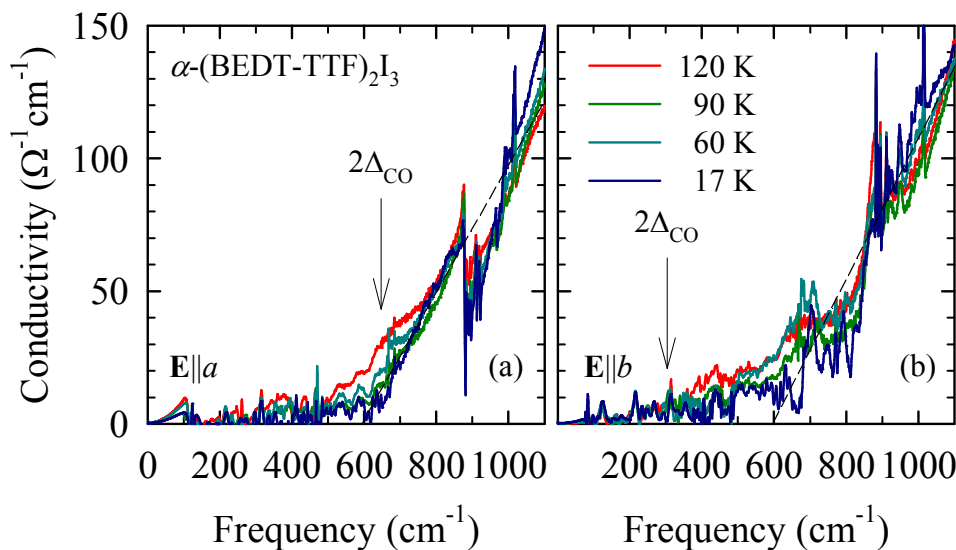


Figure 6.3 – Temperature dependence of the optical conductivity of α -(BEDT-TTF) $_2$ I $_3$ for $T < T_{CO}$ measured for the polarization (a) $\mathbf{E} \parallel a$ and (b) $\mathbf{E} \parallel b$. In order to illustrate the development of the charge-order gap, the phonon lines have been subtracted to some extent. Dashed line shows the linear extrapolation which gives the optical gap value of about 600 cm^{-1} . Arrows denote the anisotropic dc transport gap.

the conducting charge carriers is reduced at $T < T_{CO}$, the Fano-shaped antiresonances due to the emv coupled molecular vibrations become even more pronounced and split the mid-infrared peaks.

At the metal-insulator phase transition the optical gap opens rather abruptly. The conductivity in the overdamped Drude region drops to very low values, as shown in Fig. 6.2. In order to illustrate the low-temperature electronic behavior more clearly, fits of vibrational features to Lorentz and Fano curves have been subtracted from the measured spectra. The results for both polarizations are plotted in Fig. 6.3 for different temperatures. Optical gap can be obtained by linear extrapolation of the drop in $\sigma(\omega)$ below 1000 cm^{-1} and for both polarizations it amounts to $2\Delta_0 \approx 600 \text{ cm}^{-1} \approx 75 \text{ meV}$ for $T \rightarrow 0$. It is worth noting that the conductivity for $\mathbf{E} \parallel a$ is indeed close to zero at frequencies below 600 cm^{-1} , but the conductivity for $\mathbf{E} \parallel b$ remains finite down to about 400 cm^{-1} . Thus taking only the range up to 800 cm^{-1} into account, we can extract gap values of 600 and 400 cm^{-1} from the linear extrapolation, which corresponds rather well to the one extracted from the dc conductivity measurements (see Fig. 6.7).

For $T < T_{CO}$ spectral weight still moves from the gap region to higher frequencies as T is reduced: it is enhanced around 1000 cm^{-1} and higher (Fig. 6.4). Interestingly, not only the region of the gap changes, but spectral weight in the entire range shifts to higher frequencies. The maximum of the mid-infrared band moves up slightly which is

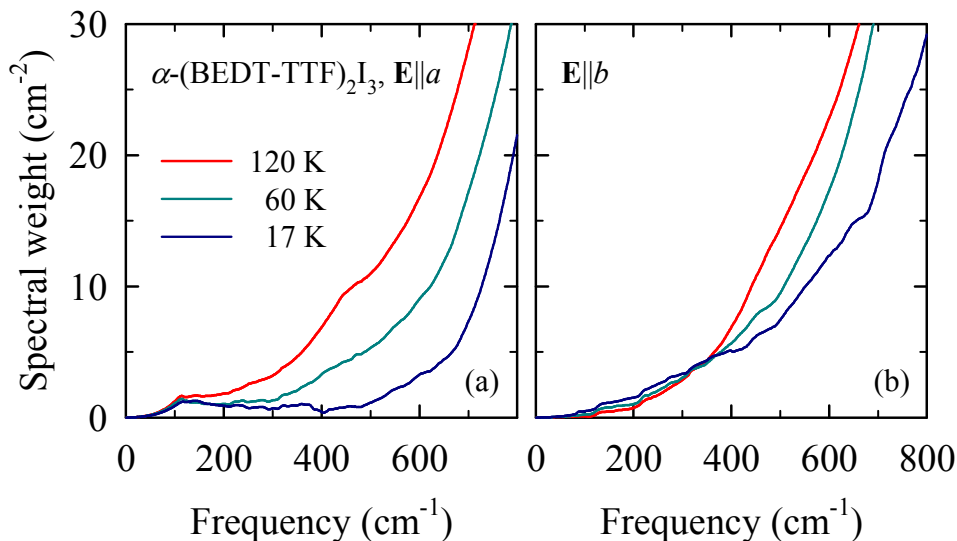


Figure 6.4 – Development of the spectral weight $SW(\omega_c)$ as a function of cut-off frequency ω_c , calculated by $SW(\omega_c) = 8 \int_0^{\omega_c} \sigma_1(\omega) d\omega = \omega_p^2 = 4\pi n e^2 / m$ for both directions of α -(BEDT-TTF) $_2$ I $_3$.

only in part due to thermal contraction, and mainly can be ascribed to the redistribution of spectral weight.

Vibrational features

The redistribution of charge on molecular sites associated with the charge ordering can be followed by the behavior of the infrared-active $\nu_{27}(B_u)$ charge-sensitive mode by measuring perpendicular to the conducting plane. In the metallic state ($T > T_{CO}$) a wide single band is evident at about 1445 cm^{-1} . This frequency corresponds to an average charge of $+0.5e$ per molecule (refer to Fig. 1.30). The charge diproportionation happens abruptly at $T_{CO} = 136 \text{ K}$. In the CO insulating state the mode splits in two pairs of bands at 1415 and 1428 cm^{-1} , and at 1500 and 1505 cm^{-1} (the waterfall plot of Fig. 6.5). Following the explanation given in Section 1.3.3, as shown by Fig. 1.31 the lower-frequency bands correspond to approximately $+0.8$ and $+0.85e$ charge on the molecule, the upper-frequency modes to $+0.2$ and $+0.15e$. This charge redistribution remains constant on further cooling and is in agreement with the charges estimated by x-ray for the four different sites in the unit cell. [27] The comprehensive recent infrared and Raman experiments of Yue *et al.* [208] confirm our findings.

Further, for \mathbf{E} polarized parallel to a and b , we observe changes in shape of some modes at the metal-insulator transition. Due to screening, no molecular vibrations can be seen above the metal-to-insulator phase transition. Below T_{CO} , the modes detected in

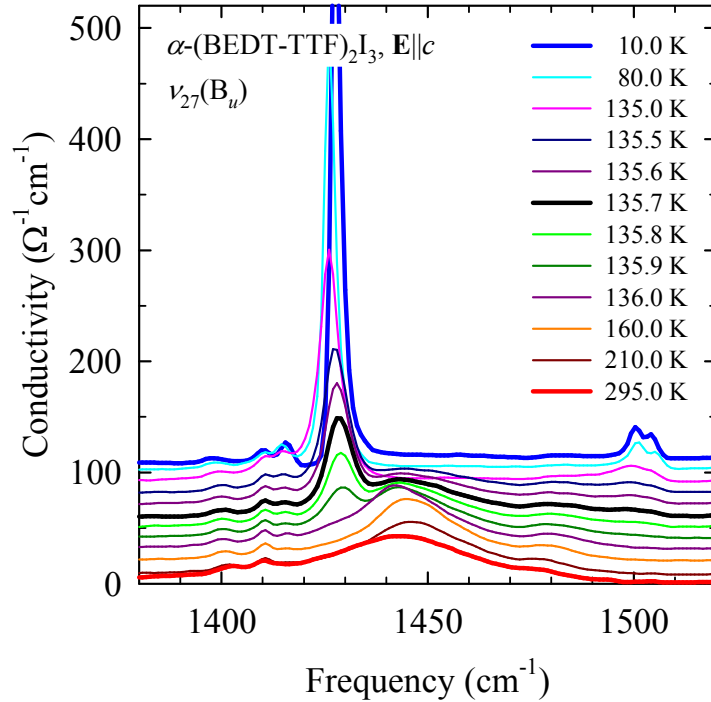


Figure 6.5 – Temperature dependence of the intramolecular vibrations of the BEDT-TTF molecule measured for the perpendicular direction $\mathbf{E} \parallel c$. The curves for different temperatures are shifted by $10 (\Omega\text{cm})^{-1}$ for clarity reasons. The ν_{27} mode becomes very strong right at the charge order transition ($T = 295, 210, 160, 136.0, 135.9, 135.8, 135.7, 135.6, 135.5, 135.0, 80,$ and 10 K).

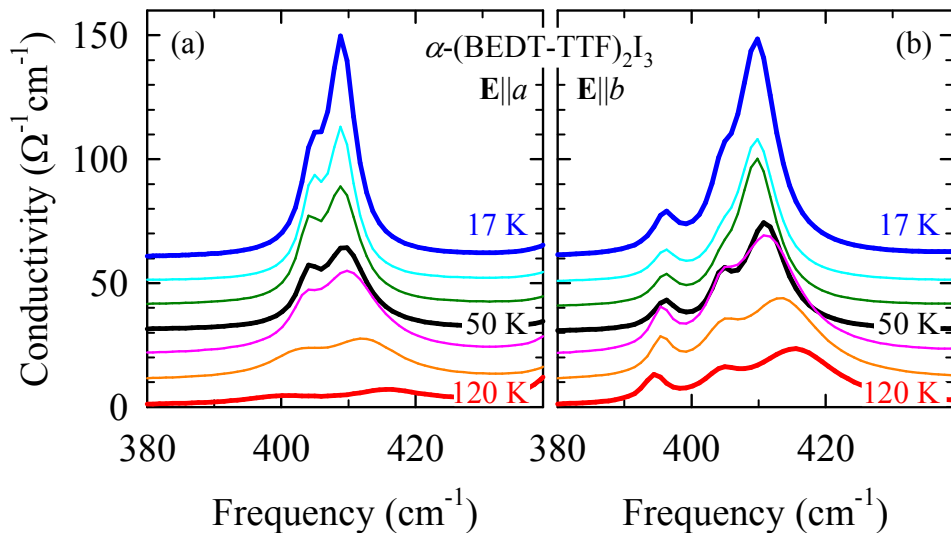


Figure 6.6 – Temperature dependence of the intramolecular vibrations $\nu_{14}(A_g)$ of the BEDT-TTF molecule. The curves for different temperatures are shifted by $10 (\Omega\text{cm})^{-1}$ for clarity reasons. For the polarizations (a) $\mathbf{E} \parallel a$ and (b) $\mathbf{E} \parallel b$ the ν_{14} grows and is splits in three distinct peaks ($T = 120, 90, 60, 50, 40, 30,$ and 17 K).

the in-plane spectra are the features of totally symmetric vibrations of BEDT-TTF molecule emv coupled with electronic charge-transfer transitions which have been observed and assigned previously [206] down to 300 cm^{-1} . As a result of interaction with electronic transition they have a Fano-shape: [213] an anti-resonance at frequencies where they coincide with the electronic excitations and an asymmetric peaks shape when the electronic feature is separated in frequencies. Thus, for example the $\nu_3(A_g)$ feature and several symmetric and asymmetric CH_3 vibrations [206] at about 1400 cm^{-1} not only shows a shift to higher frequencies together with charge-transfer band in the mid-infrared range, but also changes shape to become a narrow and slightly asymmetric band (see Fig. 6.1). While the lower-frequency modes are only weakly seen for $T > T_{\text{CO}}$, in the insulating phase the spectra we observe (cf. Fig. 6.2) all of the A_g vibrations predicted by Meneghetti *et al.*: [206] for instance, the $\nu_{15}(A_g)$ mode at 260 cm^{-1} (associated with the deformation of the outer EDT rings), the $\nu_{16}(A_g)$ mode at 124 cm^{-1} (associated with the deformation of the inner TTF rings). These bands are very intense only in the $\mathbf{E} \parallel a$ direction and barely seen in the b polarization. This is in agreement with the symmetry breaking, i.e., both the intrinsic dimerization along the stacks (a direction) and the stripes formed along the b direction in the CO phase.

An interesting observation is that the 410 cm^{-1} mode changes on cooling in the insulating state (see Fig. 6.6). The band is much wider than the other features in this range at temperatures right below the metal-insulator transition and continuously narrows as T is reduced. Following Meneghetti *et al.* [206] it can be assigned to the $\nu_{14}(A_g)$ mode which mainly involves the deformation of the outer rings.

Finally, the strong vibrational feature observed around 1300 cm^{-1} (not shown) is assigned to the emv coupled $\nu_4(A_g)$ mode of the BEDT-TTF molecule. It is sharper and more pronounced for $\mathbf{E} \parallel a$ although the overall conductivity in the mid-infrared is about half compared to $\mathbf{E} \parallel b$. Below 1000 cm^{-1} a large number of molecular and lattice vibrations peak out as soon as the screening by the conduction electrons is lost.

6.2 DC transport

The dc transport measurements reveal that the small dc resistivity anisotropy known to be present at room temperature, [114] $\rho_a/\rho_b \approx 2$, pertains to the whole metallic regime and is approximately constant down to T_{CO} . As a new result, below T_{CO} the anisotropy of resistivity, hence also of conductivity, changes significantly with lowering temperature: the resistivity along the a -axis rises more steeply than along the b -axis,

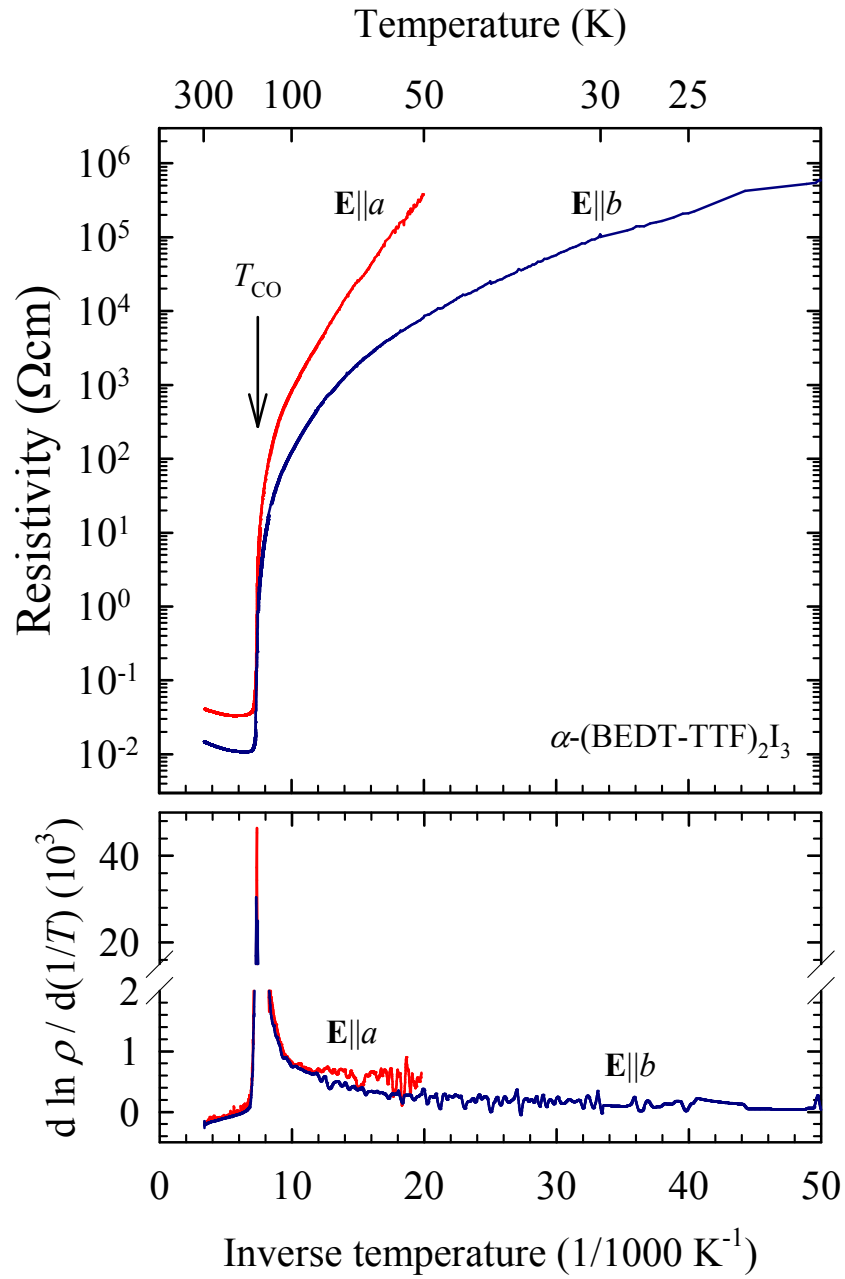


Figure 6.7 – Resistivity (upper panel) and logarithmic resistivity derivative (lower panel) vs. inverse temperature of $\alpha\text{-(BEDT-TTF)}_2\text{I}_3$ for $\mathbf{E} \parallel a$ (red line) and $\mathbf{E} \parallel b$ (blue line).

and at 50 K reaches $\rho_a/\rho_b = 50$ (see Fig. 6.7). In our samples, despite temperature-dependent activation, the anisotropic transport gap in the CO phase for $\mathbf{E}||a$ and $\mathbf{E}||b$ can be estimated to about $2\Delta = 80$ meV and 40 meV, respectively. At a first glance the appearance of an anisotropic transport gap seems to be at odds with the isotropic optical gap extracted from our optical measurements (Fig. 6.3). It is well known that systems with a complex band structure such as α -(BEDT-TTF) $_2$ I $_3$ may exhibit quite different optical and transport gaps: optical measurements examines direct transitions between the valence and conduction band, while dc transport probes transitions with the smallest energy difference between the two bands.

dc resistivity of α -(BEDT-TTF) $_2$ I $_3$ has also been characterized in the conducting ab plane for $\mathbf{E} || [1\bar{1}0]$, i.e., at an angle of approximately 45° to the crystallographic axes. Metallic behavior of resistivity is present from room temperature down to 156 K where the resistance reaches its minimum value. A sharp metal-to-insulator transition is confirmed at $T_{\text{CO}} = 136.2$ K, which is apparent in the peak in $d(\ln \rho)/d(1/T)$ with full width at half-height $2\delta T_{\text{CO}} = 1.5$ K; $2\delta T_{\text{CO}}/T_{\text{CO}} = 0.011$ (Fig. 6.8). Below the transition the resistivity curve rises with a temperature-dependent activation indicating that a temperature-dependent conductivity gap opens of about 80 meV. No significant hysteresis in dc resistivity in the vicinity of T_{CO} could be found.

6.3 Dielectric response

Low-frequency dielectric spectroscopy measurements were performed at various temperatures in the semiconducting phase. Representative spectra for $\mathbf{E} || [1\bar{1}0]$ are shown in Fig. 6.9. Most notably, between 35 K and up to 75 K two dielectric relaxation modes are discerned. The complex dielectric spectra $\varepsilon(\omega)$ can be described by an extension of Eq. (3.2), the sum of two generalized Debye functions

$$\varepsilon(\omega) - \varepsilon_{\text{HF}} = \frac{\Delta\varepsilon_{\text{LD}}}{1 + (i\omega\tau_{0,\text{LD}})^{1-\alpha_{\text{LD}}}} + \frac{\Delta\varepsilon_{\text{SD}}}{1 + (i\omega\tau_{0,\text{SD}})^{1-\alpha_{\text{SD}}}} \quad (6.1)$$

where ε_{HF} is the high-frequency dielectric constant, $\Delta\varepsilon$ is the dielectric strength, τ_0 the mean relaxation time and $1 - \alpha$ the symmetric broadening of the relaxation time distribution function of the large (LD) and small (SD) dielectric mode. The ε_{HF} has been found negligible compared to the static dielectric constant. The broadening parameter $1 - \alpha$ of both modes is typically 0.70 ± 0.05 . The temperature dependences of dielectric strengths and mean relaxation times are shown in Fig. 6.10. The dielectric strength of

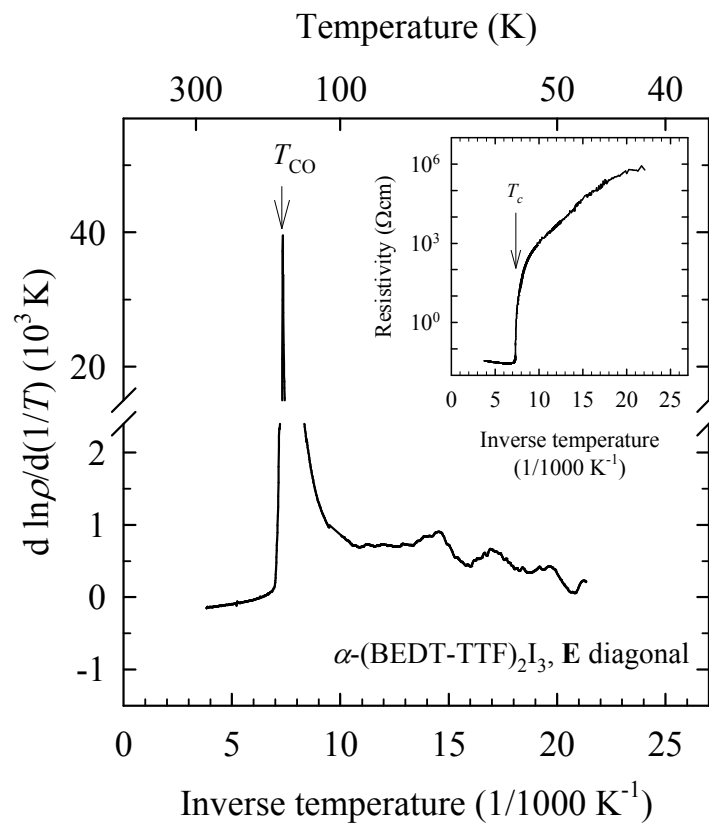


Figure 6.8 – Logarithmic resistivity derivative (main panel) and resistivity (inset) *vs.* inverse temperature of α -(BEDT-TTF) $_2$ I $_3$ for $\mathbf{E} \parallel [1\bar{1}0]$, i.e., in the diagonal direction of the ab plane.

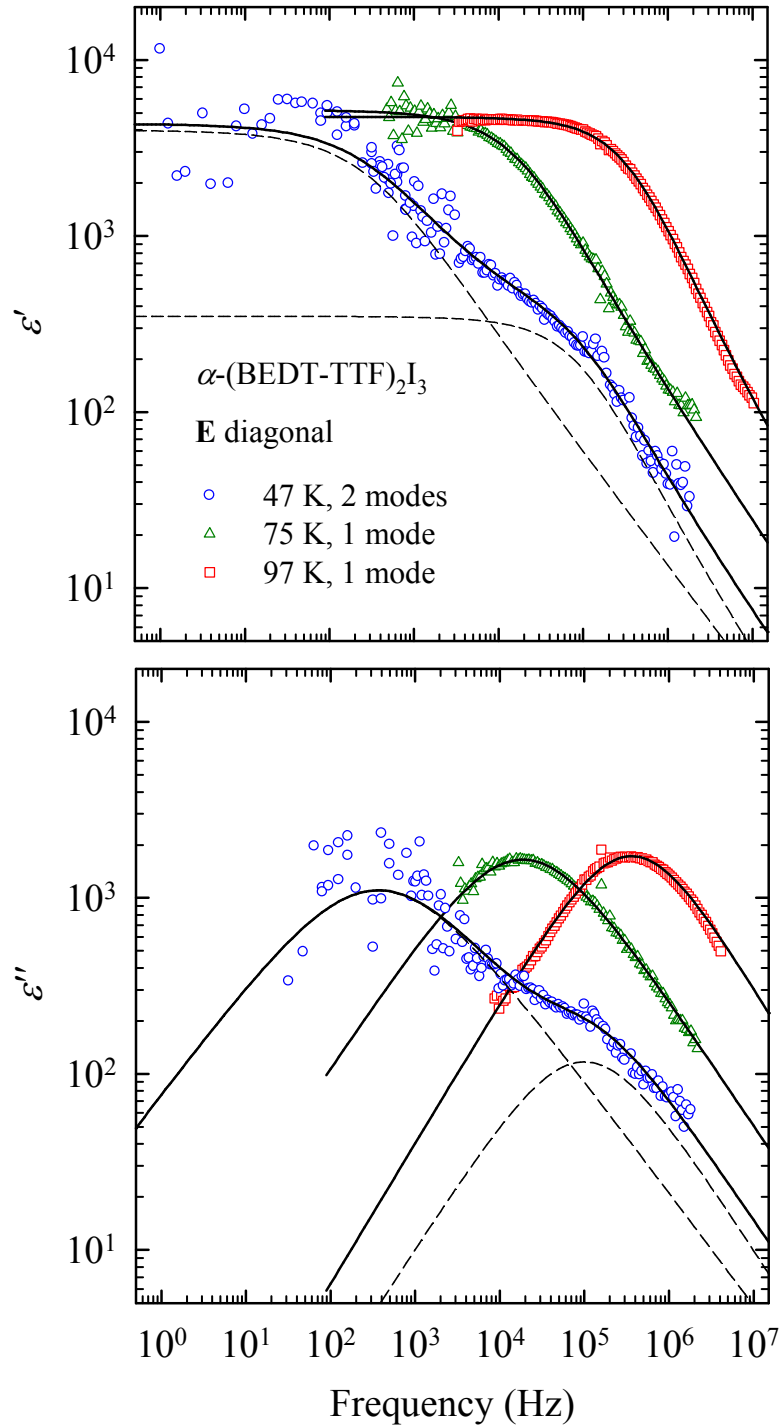


Figure 6.9 – Double logarithmic plot of the frequency dependence of the real (ϵ') and imaginary (ϵ'') part of the dielectric function in α -(BEDT-TTF)₂I₃ at representative temperatures for $\mathbf{E} \parallel [1\bar{1}0]$. Below 75 K two dielectric relaxation modes are observed – full lines for 47 K show a fit to a sum of two generalized Debye functions from Eq. (3.2); dashed lines represent contributions of the two modes. Above 75 K only one mode is detected, and the full lines represent fits to single generalized Debye functions.

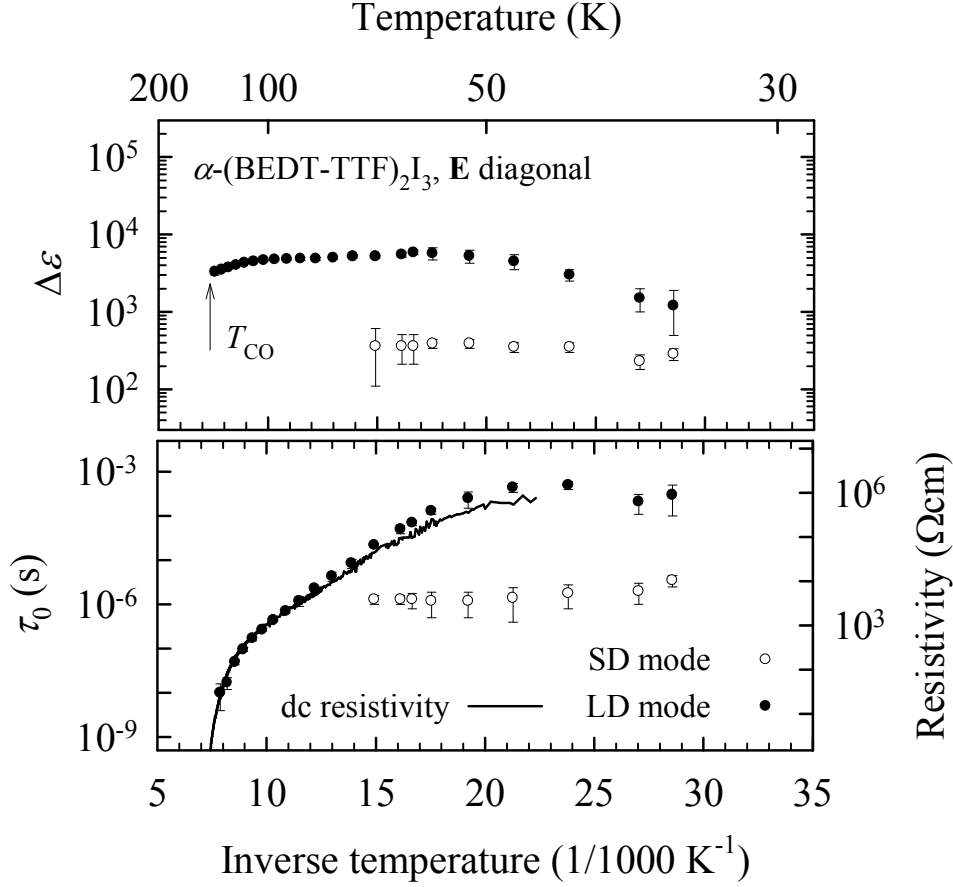


Figure 6.10 – Dielectric strength (upper panel) and mean relaxation time with dc resistivity (points and line, respectively, lower panel) in α -(BEDT-TTF)₂I₃ as a function of inverse temperature, for $\mathbf{E} \parallel [1\bar{1}0]$.

both modes does not change significantly with temperature ($\Delta\epsilon_{LD} \approx 5000$, $\Delta\epsilon_{SD} \approx 400$). At approximately 75 K the large dielectric mode overlaps the small mode. It is not clear whether the small dielectric mode disappears at this temperature or is merely obscured by the large dielectric mode due to its relative size. However, above 100 K, when the large dielectric mode shifts to sufficiently high frequencies, there are no indications of a smaller mode centered in the range 10^5 – 10^6 Hz. Accordingly, above 75 K fits to only a single Debye function are performed that we identify with the continuation of the large dielectric mode. All parameters of the large mode – such as dielectric strength, mean relaxation time, symmetric broadening of the relaxation time distribution function – can be extracted in full detail until it exits our frequency window at approximately 130 K. From 130 K to 135 K (just below $T_{CO} = 136$ K) only the dielectric relaxation strength can be determined by measuring the capacitance at 1 MHz.

One of the most intriguing results is that the temperature behavior of the mean

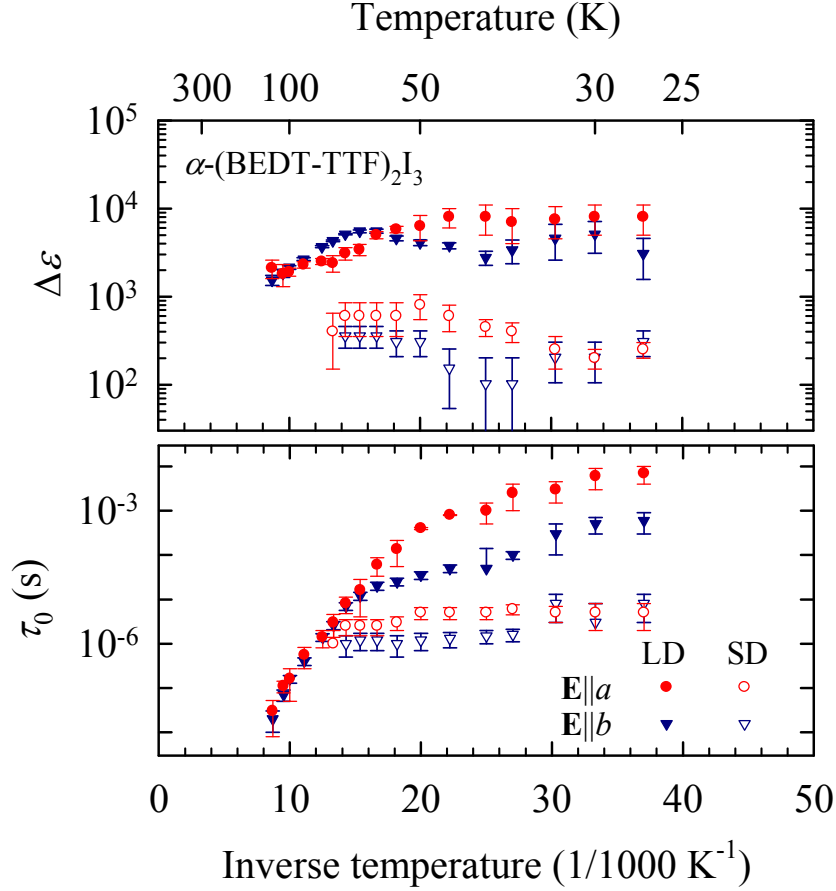


Figure 6.11 – Dielectric strength (upper panel) and mean relaxation time (lower panel) in α -(BEDT-TTF)₂I₃ as a function of inverse temperature; full and empty symbols represent parameters of the large and small dielectric mode, respectively, for \mathbf{E} along the a - (red circles) and b -axis (blue triangles).

relaxation time differs greatly between the two dielectric modes. The large dielectric mode follows a thermally activated behavior similar to the dc resistivity, whereas the small dielectric mode is almost temperature-independent. This unexpected and novel behavior in the charge-ordered phase raised the possibility of anisotropic dielectric response. With this in mind another set of dc and ac spectroscopy measurements has been performed on the needle-shaped samples oriented along the a - and b -axis.

Low-frequency dielectric spectroscopy for both $\mathbf{E}||a$ and $\mathbf{E}||b$ orientation yields results comparable to $\mathbf{E} || [1\bar{1}0]$: a large mode whose mean relaxation time follows dc resistivity, and a small, temperature-independent mode noticeable at temperatures below $T \approx 75$ K. The fit parameters to model (6.1) are displayed in Fig. 6.11 as a function of inverse temperature. Compared to Fig. 6.10, the relatively large error bars are due to a somewhat unfavorable needle-like sample shape which results in higher resistances and

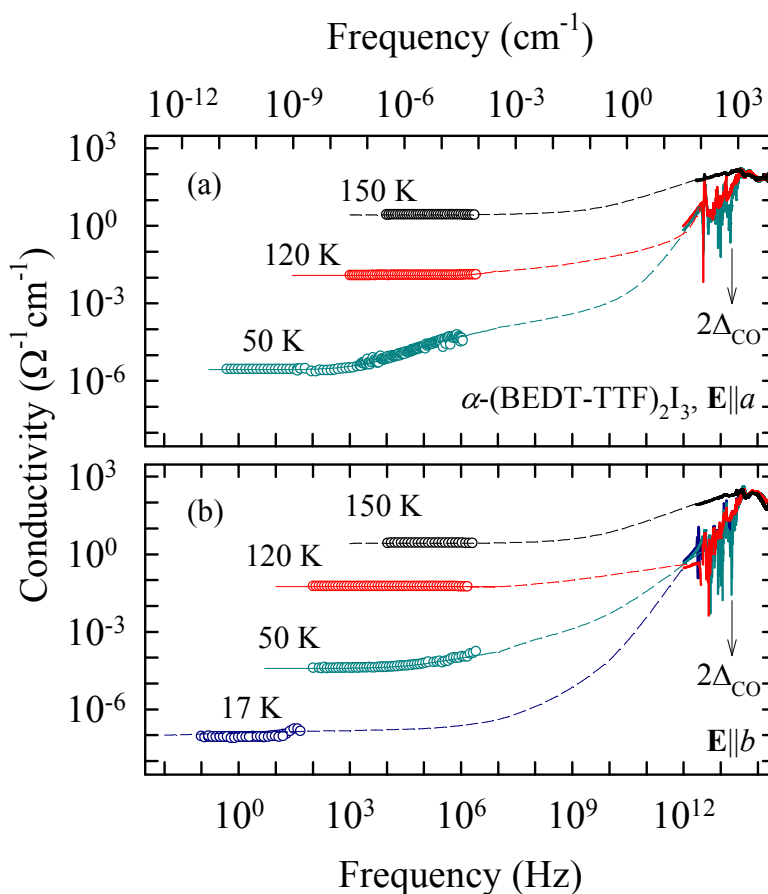


Figure 6.12 – Broad-band conductivity spectra of α -(BEDT-TTF)₂I₃ for (a) $\mathbf{E} \parallel a$ and (b) parallel b at a few selected temperatures. Vertical arrows show the CO optical gap. The dashed lines are guides for the eye.

a smaller capacitive response. The shape however was necessary to ensure a homogeneous and well-oriented electric field. There is no prominent anisotropy or temperature dependence in dielectric strength, and the $\Delta\epsilon$ values of both the large and small dielectric modes correspond to those of the sample measured in \mathbf{E} diagonal orientation. However, an evolution of anisotropy in $\tau_{0,\text{LD}}$ is clearly visible. Figure 6.13 shows that the newly-found anisotropy in $\tau_{0,\text{LD}}$ closely follows the dc conductivity anisotropy.

6.4 Discussion

It is instructive to compare the conductivity of α -(BEDT-TTF)₂I₃ as a function of temperature in the wide frequency range. Fig. 6.12 composes the conductivity spectra of α -(BEDT-TTF)₂I₃ from dc, dielectric and optical measurements for $\mathbf{E} \parallel a$ and b at different temperatures. First, the high-temperature phase is addressed. The

Drude term in room-temperature spectra of organic conductors is known to be commonly very weak, if present at all. [118] The optical conductivity of α -(BEDT-TTF)₂I₃ agrees with this observation, showing along the a - and b -axes an overdamped Drude response at all temperatures above T_{CO} . The absence of a well-defined Drude peak in the vicinity of the CO transition resembles the behavior reported for the CO insulator θ -(BEDT-TTF)₂RbZn(SCN)₄. [214] Mercury-based α -type systems, α -(BEDT-TTF)₂MHg(SCN)₄, do exhibit a zero-energy peak. [215]

Optical, dc resistivity and low-frequency dielectric measurements give mutually consistent values for the conductivity anisotropy $\sigma_b/\sigma_a \approx 2$ at all temperatures above T_{CO} . The electronic part of optical spectra can be compared to calculations of the extended Hubbard model for a quarter-filled square lattice using Lanczos diagonalization. The calculations predict a band with a maximum at approximately $6t$ in the charge-ordered insulating state, [216] which yields $t_a = 0.03$ eV and $t_b = 0.04$ eV for the respective directions. The values are in reasonable agreement with Hückel calculations performed by Mori *et al.* [23] and support the observed anisotropy in transport and optical properties.

Next let us discuss the charge-ordered phase: how it develops on cooling, the ground state features and excitations observed by applied spectroscopic techniques. The vibrational spectra reveal that the static charge disproportionation sets in rather suddenly (Fig. 6.5) at the temperature of MI transition and is accompanied by the respective change in the optical properties of the conducting plane. At high temperatures, a wide single band at about 1445 cm^{-1} is observed whose frequency corresponds to an average charge of $+0.5e$ per molecule. According to Yue *et al.* [208] this band originates from slow fluctuations of the charge distribution at each site reflecting the partial charge ordering at short length scales as detected in NMR and x-ray measurements. [217, 27] Yue *et al.* estimate the site-charge distribution slightly above transition to be $+0.6$, $+0.6$ and $+0.4e$, agreeing well with the x-ray data by Kakiuchi *et al.* The long-range charge diproportionation happens abruptly at $T_{\text{CO}} = 136 \text{ K}$ and remains constant on further cooling. In the CO insulating state the mode splits in two pairs of bands (see Fig. 6.5). The lower-frequency bands correspond to approximately $+0.8$ and $+0.85e$ charge on the molecule, and the upper-frequency modes to $+0.2$ and $+0.15e$, which is in agreement with charge estimation by x-ray for the four different sites in the unit cell. [27]

Interestingly though, optical gap and some of the features of outer ring BEDT-TTF vibrations show a continuous change on cooling in the CO state, indicating that some changes (but not a charge redistribution) happen with temperature in the insulating state. In contrast to the sharp onset of the $\nu_{27}(\text{B}_u)$ vibration that monitors the static

charge order and does not change below T_{CO} (see Fig. 6.5), some development of the gap can be seen and some of the env coupled features on cooling in the charge-ordered state. In the region where the gap has opened ($T < T_{\text{CO}}$), the conductivity drops further and reaches zero only at the lowest measured temperature ($T = 17\text{ K}$). For instance, at $T = 120\text{ K}$ a finite conductivity is found all the way down to 200 cm^{-1} and even below, in accord with previous microwave measurements. [117, 212] The optical gap is more or less isotropic, in contrast to the pronounced anisotropy of the dc gap, which is explainable taking into account that different transitions are involved in optics and dc. Nevertheless, as mentioned in Section III, there is some weak indication that for $\mathbf{E} \parallel b$ excitations are possible to lower frequencies. The increase of the anisotropy at lower temperatures, which was observed in the dc limit, is not that clear in the optical data possibly due to strong phonon features and the low-conductivity base line. A similar dc conductivity anisotropy has been observed in the CO phase of $(\text{TMTTF})_2\text{AsF}_6$. [218]

In the charge-ordered phase we observe novel processes at lower frequencies, including CDW responses. As soon as the CO phase is entered, the low-frequency conductivity drops strongly leading to a step in the radio-frequency range (see Fig. 6.12). This corresponds to the broad and strongly temperature-dependent CDW relaxation mode (visible only below 120 K), which can be clearly seen in the spectra of imaginary part of dielectric function (Fig. 6.9). It is followed by a power law dispersion attributed to hopping transport that leads to relatively high ac conductivity in the microwave and far-infrared region, as compared to the conductivity in dc limit (see Fig. 6.12). In the microwave region, the most prominent feature is the continuous increase of conductivity with rising frequency, while the far-infrared and infrared regions are mainly characterized by the suppression of the Drude weight, below either the CO gap and strong phonon features. Such behavior of conductivity is similar to the one observed for fully doped ladders in the $(\text{Sr,Ca})_{14}\text{Cu}_{24}\text{O}_{41}$ cuprates in which CDW is established. Conversely, comparable dc and optical conductivities were found in BaVS_3 systems in which CDW is also observed. [34] In this way, the latter system can be classified as fully ordered, while ladders and $\alpha\text{-(BEDT-TTF)}_2\text{I}_3$ show features known for disordered systems.

The ac conductivity data demonstrate a complex and anisotropic dispersion in the charge-ordered state. First, similar to the Peierls CDW state, we observe broad screened relaxation (large dielectric) modes along diagonal and both a - and b -axis of BEDT-TTF planes. These modes can be interpreted as signatures of long-wavelength charge excitations possessing an anisotropic phason-like dispersion. In $\alpha\text{-(BEDT-TTF)}_2\text{I}_3$ Kakiuchi *et al.* were the first to suggest a $2k_{\text{F}}$ CDW which forms along the zig-zag path CABA'C

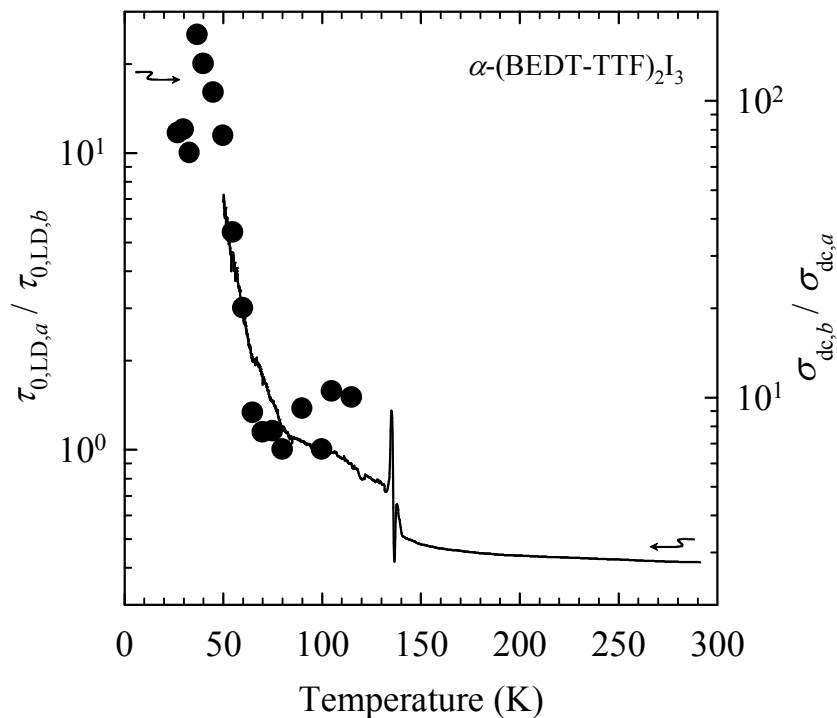


Figure 6.13 – Anisotropy of the large-dielectric-mode mean-relaxation time (points) closely follows the temperature behavior of dc conductivity anisotropy (line) in α -(BEDT-TTF) $_2$ I $_3$.

of large overlap integrals detected in their x-ray diffraction measurements [27]. However, the presence of a $2k_F$ modulation of overlap integrals along the p_1 - and p_2 -directions, ACA'BA and ABA'CA (see Fig. 6.14), hints at an additional complexity and makes the zig-zag paths a somewhat arbitrary choice. An alternative and likely more appropriate theoretical model was proposed by Clay *et al.* as described in Section 2.3.1, which originally described the related quarter-filled θ -ET $_2$ X. [173] In their model the CO in a horizontal stripe phase can be thought of as a combined $2k_F$ bond-CDW along the two BEDT-TTF plane p -directions with bond dimerization in stacking direction. Indeed, a similar albeit more complex tetramerization of overlap integrals does develop along the p -directions of α -(BEDT-TTF) $_2$ I $_3$. Using x-ray diffraction data, Kakiuchi *et al.* calculated overlap integrals between neighboring molecules based on the tight-binding approximation and a molecular orbital calculation with the extended Hückel method. [27, 219] As shown in Fig. 6.14, along the p_2 -direction, ABA'CA, the strongest overlap integral is obtained between the two charge-rich sites A and B, quite alike the model bond order for the θ -material. Also, bond dimerization along the stacking b -direction and its pattern in the ab plane of α -(BEDT-TTF) $_2$ I $_3$ agree with the model. However, in the p_1 -direction, ACA'BA, the order is shifted by one bond: the largest overlap integral is between the

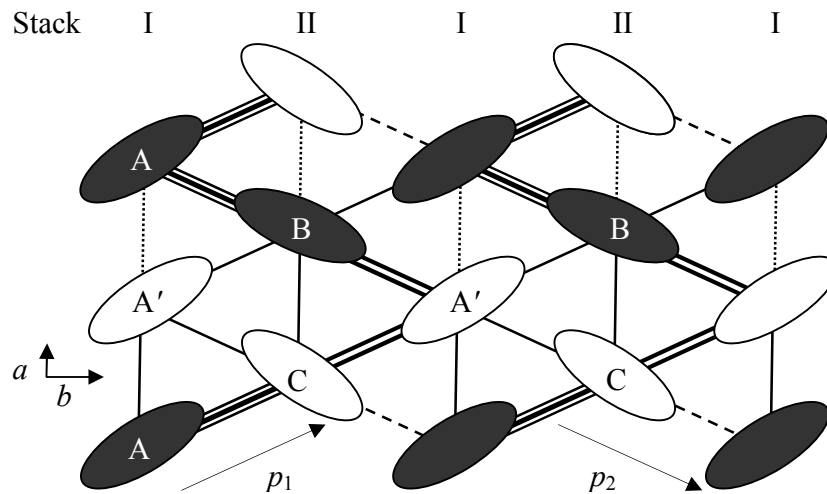


Figure 6.14 – Schematic representation of a $2k_F$ bond-CDW in α -(BEDT-TTF)₂I₃. Triple, double, single and dashed lines show relative strengths of overlap integrals, from strongest to weakest, along p_1 - and p_2 -directions [27]. Also denoted are dimerized bonds along the a -axis in the AA' and BC stacks.

charge-rich A site and the charge-poor C site. Additionally, the overlap integrals are not perfectly $2k_F$ sine-modulated along each p -direction. While these deviations of α -(BEDT-TTF)₂I₃ bond order from the θ -ET₂X model should be recognized, they are hardly surprising. α -(BEDT-TTF)₂I₃ has a lower symmetry than a θ -structure which may well induce slight differences in bond patterns. Also, the overlap integrals obtained from x-ray diffraction could somewhat depend on the employed method of calculation. This leaves the main physical result of the model by Clay *et al.*, the formation of a bond-CDW within the conducting molecular planes, fully applicable and relevant to the case of α -(BEDT-TTF)₂I₃. It is plausible to look for the origin of phason-like dielectric relaxation in such a $2k_F$ bond-CDW. In this case the energy scale of barrier heights is close to the single-particle activation energy indicating that screening by single carriers responsible for the dc transport is effective for this relaxation. The fact that the temperature behavior of the $\tau_{0,LD}$ anisotropy closely follows the dc conductivity anisotropy has important implications: while the CDW motion is responsible for the dielectric response, the single electron/hole motion along the two p -directions, possibly zig-zagging between them, is responsible for the observed dc charge transport.

Further, the small dielectric mode needs to be addressed. Its features are characteristic of short-wavelength charge excitations. The origin of this relaxation might be in the twinned nature of the CO phase due to breaking of the inversion symmetry, with one domain being (A,B)-rich and the other (A',B)-rich. [27] Indeed, a ferroelectric-like character to the charge-ordered phase is suggested by bond-charge dimerization along

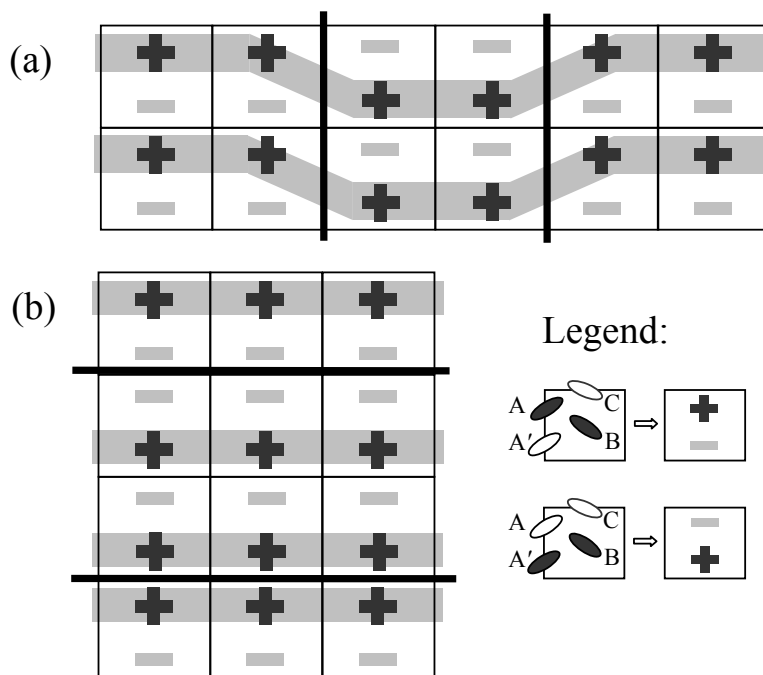


Figure 6.15 – Two different types of domain wall pairs in the charge-ordered phase of α -(BEDT-TTF) $_2$ I $_3$. (A,B)- and (A',B)-rich unit cells are symbolically represented as $+ -$ or $- +$ cells which form CO stripes. For simplicity B and C molecules are omitted. Gray thick lines stand for charge-rich stripes. Thin black lines denote a domain wall pair.

the a -axis together with optical second-harmonic generation and photoinduced CO melting. [220,221,222] The dielectric data can be most naturally attributed to the motion of charged kink-type defects – solitons or domain walls in the charge order texture. Both domain walls and solitons stand for short wavelength excitations; however whereas a soliton is usually a one-dimensional object, the domain wall is not dimensionally restricted. Charge neutrality constraint of the CO in α -(BEDT-TTF) $_2$ I $_3$ (a change of stripes equivalent to strictly replacing unit cells of one twin type with another) suggests two types of solitons and/or domain walls. The first one is the domain wall in pairs (a soliton-antisoliton pair) between CR and CP stripes along the b -axis, which we get if the constraint along the b -axis is imposed [Fig. 6.15(a)]. The second type of domain-wall pair is given by applying the constraint along the a -axis so that the domain walls' interior contains both charge signs [Fig. 6.15(b)]. The motion of such entities induces a displacement current and can therefore be considered as the microscopic origin of polarization in the CO state. Namely, in the presence of an external electric field perpendicular to the horizontal stripes, $\mathbf{E} \parallel a$, coupling to the AA' dipole moments of each unit cell breaks the symmetry between the two orientations of the dipole. Due to first-neighbor interactions the AA' dipoles can most easily be flipped at the domain wall,

causing the wall pairs to move. Coupling to a field in the $\mathbf{E} \parallel b$ configuration, parallel to stripe direction and therefore perpendicular to the AA' dipoles, seems to be more troublesome. However, one only needs to remember that A and A' also interact with B and C sites. At the energetically unfavorable domain wall the B and C molecules effectively couple AA' dipoles to perpendicular external fields and allow for solitonic motion along the b -axis as well. Theoretically, a domain wall should be independent on position, however in a real crystal it gets pinned to defect sites. [223] Such a pinning causes the domain wall to sit in a local energy minimum. The broad distribution of relaxation times might then be ascribed to a distribution of activation energies associated with pinning sites. A weak ac electric field induces a dielectric response which can be attributed to the activation between different metastable states over energies barriers. These metastable states correspond to local changes of charge distribution across the length scale of domain wall thickness. A nearly temperature-independent mean relaxation time indicates that resistive dissipation cannot be dominant for domain wall pairs and that the dielectric relaxation is governed by low energy barriers.

A word is in order about alternative microscopic descriptions of excitations which could give rise to the dielectric relaxation in α -(BEDT-TTF)₂I₃. Section 2.3.2 introduces the pinball liquid model proposed by Hotta *et al.* [177] which describes single-particle excitations in an insulating, horizontally-stripped charge order on a triangular lattice. Unfortunately, while the model manages to calculate density of states, it does not lend itself easily to workable predictions of dc transport, dielectric or infrared properties. Another possibly suitable single-particle description is the excitonic model used by Yamaguchi *et al.* to explain dielectric properties below $T = 2$ K as well as nonlinear conductivity of θ -BEDT-TTF₂MZn(SCN)₄ ($M = \text{Cs, Rb}$). [178, 179] They consider a charge-ordered quarter-filled square-lattice system in which excitations are created by moving a localized hole to a site where no hole was originally present. This creates a pair of a localized electron and hole which can unbind due to thermal excitations and, as worked out in Section 2.3.2, give rise to a temperature-dependent dielectric constant

$$\varepsilon(T; \omega = 0) = 1 + \frac{n_0}{\varepsilon_0} \int_0^\lambda r dr \frac{(er)^2}{2k_B T} \exp\left\{-\frac{U(r)}{k_B T}\right\} / \int_0^\lambda r dr \exp\left\{-\frac{U(r)}{k_B T}\right\}, \quad (2.31)$$

where n_0 is the electron-hole density at $T \rightarrow \infty$ which is equal to half the BEDT-TTF density. [179] The above expression can be compared with the measured dielectric properties of α -(BEDT-TTF)₂I₃. Namely, the total dielectric constant $[\varepsilon(\omega = 0)]$ is well-approximated by the $\Delta\varepsilon$ of LD mode (see Figs. 6.10 and 6.11). A two-parameter

(λ, U_0) fit to, e.g., our $\mathbf{E} \parallel a$ data above $T = 25$ K reproduces adequately the general temperature dependence, but gives a rather small $\lambda = 2.2 \pm 0.1$ nm and $U_0 = 1.6 \pm 1.5$ meV. The fit value of U_0 is in stark contrast with the value extracted from transport gap, $U_0 = \Delta / \ln(\lambda/a) \approx 50$ meV (further, substituting λ from the previous expression gives an unsatisfactory one-parameter fit). A similar discrepancy can be seen in $\mathbf{E} \parallel [1\bar{1}0]$ and $\mathbf{E} \parallel b$ fits. Also, it is not clear whether this model (here shown only in the static limit) reproduces the complex shapes of our experimental dielectric spectra and their temperature dependence. Thus the excitonic picture, while nicely applicable to θ -BEDT-TTF₂MZn(SCN)₄ below 2 K, does not seem to account for general dielectric features of α -(BEDT-TTF)₂I₃ in the charge-ordered phase.

It needs to be stressed again that certain properties of the 2D striped charge-ordered phases carry an uncanny resemblance to the standard 1D charge-density waves. The observation of a Peierls-like broad screened dielectric mode in 2D represents an important experimental result which clearly indicates that the charge order in α -(BEDT-TTF)₂I₃ cannot be of the fully localized Wigner type as predicted by a number of theoretical models. [166, 167, 3] Rather, the bond-CDW delocalized picture appears as the most appropriate one. This is indeed not the first instance of a phason-like response observed in two dimensions. As reported in Sections 1.2 and 5, a similar observation was made in the ladder CDW phase of quasi-1D Sr₁₄Cu₂₄O₄₁, [13, 17, 16] which the theory predicts to be either of $2k_F$ or $4k_F$ type [54, 82, 224] and resonant x-ray diffraction measurements [16] confirm a sinusoidal, delocalized modulation and exclude a fully localized Wigner-type ordering. Apart from the phason-like dielectric response in α -(BEDT-TTF)₂I₃, recently some other experimental evidence also started to point out tantalizing similarities between excitations in 1D density-wave systems and 2D charge orders. As already noted above, nonlinear conductivity (a hallmark of CDW and SDW phases) has also been reported in charge-ordered θ -BEDT-TTF₂MZn(SCN)₄ ($M = \text{Cs, Rb}$), but was explained within an excitonic model rather than invoking collective sliding motion. [179] A recent study by Tamura *et al.* on α -(BEDT-TTF)₂I₃ discovered a significant nonlinear conductivity below R_{CO} in all three crystallographic directions. [225] Most intriguingly, a negative differential resistance regime is found (currents above ~ 2 Acm⁻²) in which current pulses of 5 ms produce rapid voltage oscillations parallel to the molecular stacks. The effect superficially evokes the narrow-band noise standardly associated with the sliding motion of density waves in 1D systems [226, 227] and the authors interpret the anisotropic oscillations in α -(BEDT-TTF)₂I₃ as due to collective sliding of charge in the AA' stacks. Whatever the cause of oscillations may be, the negative differential resistance regime can be explained in a very down-to-Earth manner - through Joule

heating. [228] Even though this shuts off one possibly very interesting line of exploration as a mere artefact of measurements, a very weak nonlinear conductivity still seems to remain before the heating becomes dominant. [228] This definitely opens up new avenues of exploring analogies in electrical transport between the 2D charge order and the well-explored standard 1D density waves, and emphasizes the need for a better understanding of excitations in CO systems such as α -(BEDT-TTF)₂I₃. Further work is needed on the theoretical front to identify normal excitation modes in the CO phase and link them to the observables.

Chapter 7

Concluding remarks

This thesis presents experimental work on three structurally distinct electron systems. Even though their chemical composition is unrelated, every one presents a playground of interacting electrons on lattices with reduced dimensionality, in other words, which correlates them toward novel collective behaviors. Vanadium sulfide BaVS_3 , underdoped cuprates $(\text{La}, \text{Y}, \text{Sr}, \text{Ca})_{14}\text{Cu}_{24}\text{O}_{41}$ and the organic charge-transfer salt α - $(\text{BEDT-TTF})_2\text{I}_3$ all present their own rich “physics with at least one twist”.

The primary experimental techniques employed to learn about their non-standard ground states and excitations were dc conductivity measurements as well as dielectric spectroscopy. These were complemented with spectroscopic methods in the THz and infrared ranges.

What follows is a short recapitulation of the obtained results and questions which remain open or have opened for further exploration.

Orbital ordering in BaVS_3

BaVS_3 is a perovskite material composed of vanadium-sulfide chains. Structurally, it is an almost deceptively simple system which then develops a beautiful interplay between the lattice, orbital degeneracy, electron spins and charges. It exemplifies interwoven degrees of freedom which need to be taken into account to fully understand the origin of the metal-to-insulator phase transition and low-temperature phases of transition-metal compounds in general. The vanadium orbitals in BaVS_3 hybridize to form a wide quasi-1D electron band, and two narrow bands with a more localized character. All three bands intersect the Fermi level. This fact together with strong Coulomb effects and lattice coupling brings about a series of phase transitions when BaVS_3 is cooled: the

initial structural transition at 250 K which leaves the system a metal, followed by an appearance of a Peierls-like superstructure and a transition to an insulator at 68 K, and lastly at 30 K an appearance of incommensurate magnetic ordering.

The exact nature of the ground state is still not completely resolved, but most evidence points toward an ordering of orbital degrees of freedom on vanadium sites. In BaVS_3 this kind of ordering is characterized by varying orbital occupancies at vanadium sites, however in such a way that total amount of charge on each remains approximately the same. This can be thought of as having two charge-density waves almost exactly canceling each other's variation in charge. Our measurements in this phase reveal a huge dielectric constant of the order $10^5 - 10^6$ associated with the metal-to-insulator phase transition. Cooling below the metal-insulator transition dramatically decreases the dielectric response which finally levels off below the magnetic transition. The observed broad, screened relaxation is certainly similar to the one generated by long-wavelength collective excitations called phasons in standard CDWs. However, there are crucial differences. Based on the temperature behavior of this dielectric relaxation and experimental results by other authors we assign it to a domain-wall-like short-wavelength excitations of the orbital ordering. The orbital ordering sets in at the metal-to-insulator transition, but only develops a long-range order below the magnetic transition.

Up to now no theoretical framework has been presented which would link up excitations above an orbitally-ordered state with transport observables. Further theoretical work is warranted, as well as experiments which would refine our understanding of orbital order and the associated superstructure in BaVS_3 .

Going from fully-doped to underdoped $(\text{La},\text{Y},\text{Sr},\text{Ca})_{14}\text{Cu}_{24}\text{O}_{41}$

Cuprates of the rather large $(\text{La},\text{Y},\text{Sr},\text{Ca})_{14}\text{Cu}_{24}\text{O}_{41}$ consist of a large composite crystalline structure composed of two subsystems: cuprate ladders and cuprate chains. The system is hole-doped with 6 holes in the parent $\text{Sr}_{14}\text{Cu}_{24}\text{O}_{41}$ material per formula unit. The distribution of holes between chains and ladders dictates their physics and ground state.

In the fully doped systems without La,Y atoms the ladder subsystem receives approximately 1 hole per f.u. and develops either a charge-density wave ground state at low Ca content, or a superconducting ground state under pressure for high Ca content. The chains with their five holes on the other hand form an antiferromagnetic dimer order with accompanying complementary charge ordering. Judging by high-La,Y content

systems, removing holes leaves the ladders completely undoped destroying the density wave there and the AF dimers in chains. The remaining holes conduct exclusively along chains by hopping processes. In the THz spectra at low y we also find signatures of a mode which we assign to the pinned CDW mode of the doped ladders.

The impressively large body of both theoretical and experimental work on this quasi-1D cuprate family still leaves many unsolved problems. Among those is also the question of hole distribution in low- y $(\text{La,Y})_y(\text{Sr,Ca})_{14-y}\text{Cu}_{24}\text{O}_{41}$, i.e., the bridging of doped and underdoped phase diagrams. This work demonstrates the crossover from a one-dimensional hopping charge transport in the chain subsystem for $y \geq 3$ to a quasi-two-dimensional charge conduction in the ladder planes for $y \lesssim 2$. Our results suggest that holes are doped exclusively into the chains for low hole counts, but also start populating ladders once the total hole count n_h exceeds four. The factor which determines hole distribution between subsystems is most likely associated with an interdependent formation of long-range orders in the two subsystems: antiferromagnetic dimer order in chains and charge-density wave in ladders. We confirm once more a profound interdependence between chain and ladder sub-units which shows that any decent theoretical model attempting to give a complete and consistent description of electronic phases in $(\text{La,Y,Sr,Ca})_{14}\text{Cu}_{24}\text{O}_{41}$ should take this into account.

Horizontal-stripe charge order in α -(BEDT-TTF) $_2\text{I}_3$

The planar organic conductor α -(BEDT-TTF) $_2\text{I}_3$ was first described as an insulating sibling of the superconducting β - and κ -(BEDT-TTF) $_2X$ salts. Soon afterwards its charge-ordered phase was discovered, an interesting phenomenon in its own right. It was not clear whether the charge ordering was of fully localized, Wigner type, or more akin to density waves commonly found in 1D systems. Also, apart from more recent optical studies not a lot has been known on the anisotropy of electrical properties and transport in the insulating phase. Recent experimental confirmation and calculations on the two Dirac cones in the conducting BEDT-TTF plane have additionally sparked interest in this material.

We have investigated properties of the electrodynamic response in α -(BEDT-TTF) $_2\text{I}_3$ in a broad range of frequencies using dc conductivity, dielectric spectroscopy and infrared spectroscopy setups. In the normal phase, we observe an overdamped Drude response and a weak optical conductivity anisotropy. This is consistent with an almost isotropic, weakly temperature-dependent dc conductivity inside the conducting layers. We follow through the abrupt charge-ordering phase transition where static charge order

sets in, indicated by a dramatic drop of the optical conductivity. At the same temperature charge disproportionation also becomes noticeable in vibrational spectra and remains constant on further cooling. The observed charge values are $+0.8$ and $+0.85e$ on charge-rich sites, and $+0.2$ and $+0.15e$ on charge-poor sites, consistent with the charges estimated by x-ray. Below the charge-order transition we also demonstrate a strong development of in-plane dc conductivity anisotropy as well as a dc gap anisotropy. This is in contrast to the weak optical conductivity which remains only weakly anisotropic and similar to high temperatures. Further, we observe a complex anisotropic dielectric relaxation within the conducting layers in kHz–MHz frequency range. The two distinct dielectric modes we associate with concomitant anisotropic phason-like excitations and a behavior reminiscent of domain walls. As the most consistent picture of charge order in α -(BEDT-TTF)₂I₃, our results favor an interesting view of horizontal stripes as a cooperative bond-charge density wave with a ferroelectric-like nature, rather than a fully localized Wigner-crystal.

Of the three above systems, the organic layered conductor α -(BEDT-TTF)₂I₃ brings out in a most apparent way the need for a model which would describe not only the ground state but also low-lying excitations and associated electrodynamic observables. At the moment experiment supersedes theoretical work with tantalizing parallels between the 2D charge order and 1D density waves. Future work should examine the extent of these analogies and refine the microscopic description of both metallic and insulating phase of α -(BEDT-TTF)₂I₃.

Poglavlje 8

Sažetak

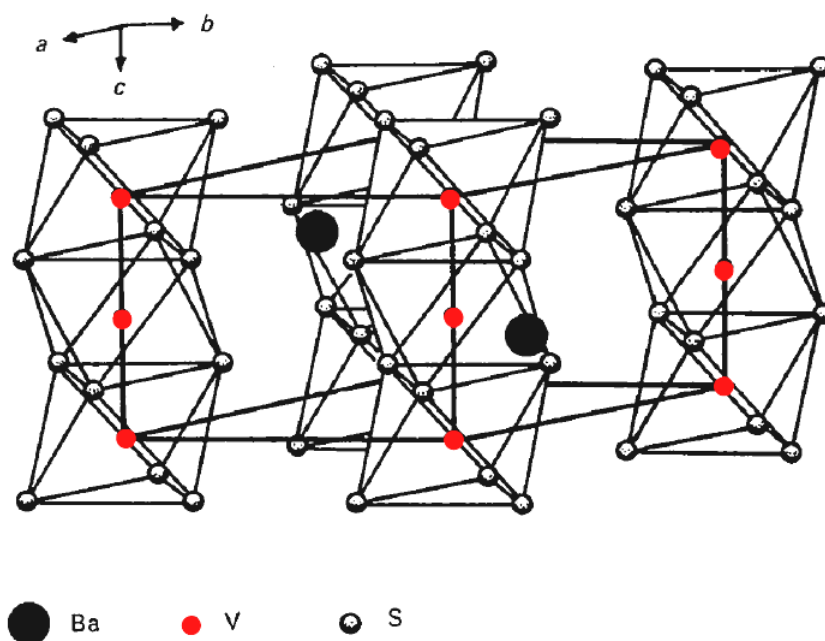
Jako korelirani sustavi, u kojima kulonska interakcija zajedno s reduciranom dimenzionalnošću uzrokuje nova kolektivna elektronska stanja slomljene simetrije, u centru su istraživanja današnje fizike kondenzirane materije. Stanja poput vala gustoće naboja, spina ili veza, lokaliziranog uređenja naboja i orbitalnog uređenja javljaju se kako u oksidima i sulfidima prijelaznih metala tako i u organskim (molekularnim) vodičima. Kompleksna dinamika koja regulira transportna, magnetska i optička svojstva stvara čitavu lepezu efekata i bogatih faznih dijagrama. U ovom doktorskom radu promatramo transportna svojstva lančastog spoja BaVS_3 s ciljem karakterizacije osnovnog stanja, kvazi-1D kompozit kupratnih lanaca i ljestvica $(\text{La,Y,Sr,Ca})_{14}\text{Cu}_{24}\text{O}_{41}$ u svrhu upotpunjavanja faznog dijagrama na prijelazu iz potpuno dopiranih u poddopirane spojeve, te slojnog kvazi-2D organskog metala $\alpha\text{-(BEDT-TTF)}_2\text{I}_3$ kao prvi pokušaj opisa niskoležećih pobuđenja iznad osnovnog stanja tzv. horizontalnih pruga uređenog naboja. Korištene eksperimentalne tehnike pokrivaju transport naboja u malim poljima u frekventnom području od dc granice (mjerjenja istosmjernom četverokontaktinom i dvo-kontaktinom metodom), preko područja 10 mHz - 10 MHz (niskofrekventna dielektrična spektroskopija) do spektroskopije u terahertznom ($5 - 33 \text{ cm}^{-1}$) i infracrvenom ($6 - 10000 \text{ cm}^{-1}$) području.

8.1 Dokazi orbitalnog uređenja u BaVS₃

8.1.1 Uvod

Različiti sustavi reducirane dimenzionalnosti s jakim kulonskim interakcijama između slobodnih nosilaca naboja, spinova i orbitala pokazuju bogate fazne dijagrame s novim fenomenima uređenja. [230] U posljednjih nekoliko godina takve kolektivne faze slomljene simetrije, poput valova gustoće naboja i spina te faze nabojnog ili orbitalnog uređenja, u fokusu su intenzivnog znanstvenog istraživanja. U spojevima prijelaznih metala na d -elektrone djeluje kompeticija dva doprinosa: kulonsko odbijanje koje teži lokalizaciji, te hibridizacija s ligandskim valentnim stanjima koja ih želi delokalizirati. [231] Suptilna ravnoteža između dva doprinosa čini te sustave zanimljivima u istraživanju raznolikih faznih prijelaza iz metala u izolator (MI) koje obično prate drastične promjene u svojstvima naboja, spina i orbitala. Za potpuno razumijevanje ključan je utjecaj orbitalne degeneracije i orbitalnog uređenja na električni transport i magnetska svojstva. [232] Na primjer, rezultati anomalnog raspršenja X-zraka na oksidu prijelaznog metala V₂O₃ govore da popunjenost orbitala ima glavnu ulogu u fizici tog sustava. [233] Taj eksperiment govori da prostorno uređenje zauzeća degeneriranih elektronskih orbitala objašnjava anizotropne integrale izmjene u antiferomagnetskoj izolatorskoj fazi. Dodatno, ostaje otvoreno pitanje kolektivnih pobuđenja u fazi orbitalnog uređenja. Može se očekivati da će orbitalni stupnjevi slobode ili uzrokovati nove vrste pobuđenja, npr. orbitalne valove, ili jako renormalizirati druga pobuđenja. [234]

Perovskitski sulfid BaVS₃ predstavlja izniman sustav za proučavanje gore spomenutih pojava i kao takav privukao je mnogo pažnje u eksperimentalnoj fizici jako koreliranih sustava. Oktaedri VS₆ sa zajedničkim plohamo slažu se duž kristalografske c -osi i čine VS₃ spinske lance s jednim $3d$ elektronom po V⁴⁺ ionu (Slika 8.1). Lanci su odvojeni atomima Ba u ab ravninama, što cijelu strukturu čini kvazi-jednodimenzionalnom. Jedinčna ćelija na sobnoj temperaturi je primitivna heksagonalna i sadrži dvije formulske jedinice. Na 240 K struktura prelazi u ortorompsku, međutim svaki lanac još uvijek zadržava dva ekvivalentna V⁴⁺ atoma po jediničnoj ćeliji. Pripadajuća dva elektrona dijele se među dvije hibridizirane vrpce koje su odvojene zbog utjecaja kristalnog polja: široke A_{1g} vrpce koja potječe od d_{z^2} orbitala koje se preklapaju duž c -osi, i kvazi-degenerirane uske E_{g1} vrpce koja nastaje od $e(t_{2g})$ orbitala s izotropnom interakcijom preko V-S-S-V veza. [43, 45] Popunjenost ovih vrpce je izravno uvjetovana on-site kulonskim odbijanjem U i lokalnim vezanjem J preko Hundovog pravila. U granici jakih korelacija popunjenost A_{1g} i E_{g1} orbitala bliska je polupopunjenosti. Spinski stupnjevi slobode lokaliziranih



Slika 8.1 – Strukturu $BaVS_3$ čine lanci oktaedara sumpora koji dijele plohu sa susjednim oktaedrima u lancu. Crni krugovi predstavljaju atome barija, crveni krugovi atome vanadija, a manji prazni krugovi atome sumpora. Heksagonalna jedinična ćelija označena je debelom linijom. Slika prema Gardner *et al.* [30]

elektrona te vezanje vodljivih i lokaliziranih elektrona čini sustav iznimno kompleksnim, s MI faznim prijelazom na otprilike 70 K i magnetskim prijelazom na oko 30 K.

Razumijevanje detalja MI faznog prijelaza i osnovnog stanja $BaVS_3$ još nije potpuno. Difuzno raspršenje X-zraka pokazuje da se na T_{MI} uspostavlja sumjerljiva superstruktura s kritičnim valnim vektorom $\mathbf{q}_c = 0.5c^*$ bliskom $2k_F(A_{1g})$, čemu prethodi režim velikih fluktuacija sve do 170 K. [8] Ovo ponašanje donekle podsjeća na Peierlsov prijelaz u fazu vala gustoće naboja. Međutim, priroda osnovnog stanja je složenija jer je nađen $2\mathbf{q}_c$ harmonik, što sugerira da i lokalizirani $e(t_{2g})$ elektroni također sudjeluju u prijelazu i uređenju ispod T_{MI} . Magnetska susceptibilnost govori tome u prilog: slijedi Curie-Weiss ponašanje ispod sobne temperature i pokazuje vrh sličan antiferomagnetskom na T_{MI} , dok na nižim temperaturama opada. [7] Nema naznaka magnetskog dugodosežnog uređenja do $T_\chi \approx 30$ K, gdje se uspostavlja nesumjerljivo magnetsko uređenje. [41] Sljedeći neobičan rezultat ispod T_{MI} je strukturalni prijelaz iz ortorompskog u monoklinski s internom distorzijom VS_6 oktaedara i tetramerizacijom lanaca V^{4+} [33]. Konačno, anomalno raspršenje X-zraka na K -rubu vanadija nije pokazalo disproporcijaciju naboja u osnovnom stanju. [9] Autori eksperimenta predlažu intrigantnu interpretaciju prema kojoj postoje dva vala gustoće naboja suprotne faze, jedan u d_{z^2} a drugi u $e(t_{2g})$ elektronima, što povlači orbitalno uređenje u popunjenju d_{z^2} i $e(t_{2g})$ orbitala na V atomima.

Ovdje predstavljamo istraživanje izolatorske faze $BaVS_3$ pomoću niskofrekventne dielektrične spektroskopije zajedno s mjerenjem istosmjerne električne vodljivosti. Dobiveni rezultati u skladu su s opisom u kojem na MI prijelazu dolazi do orbitalnog uređenja u osnovnom stanju. Velika dielektrična konstanta koja se javlja u blizini MI prijelaza drastično opada pri hlađenju do oko 30 K, a na nižim se temperaturama ustaljuje i postaje temperaturno neovisna. Takvo bi se ponašanje moglo dobro opisati orbitalnim uređenjem koje se počinje uspostavljati ispod MI i postaje dugodosežno ispod magnetskog prijelaza.

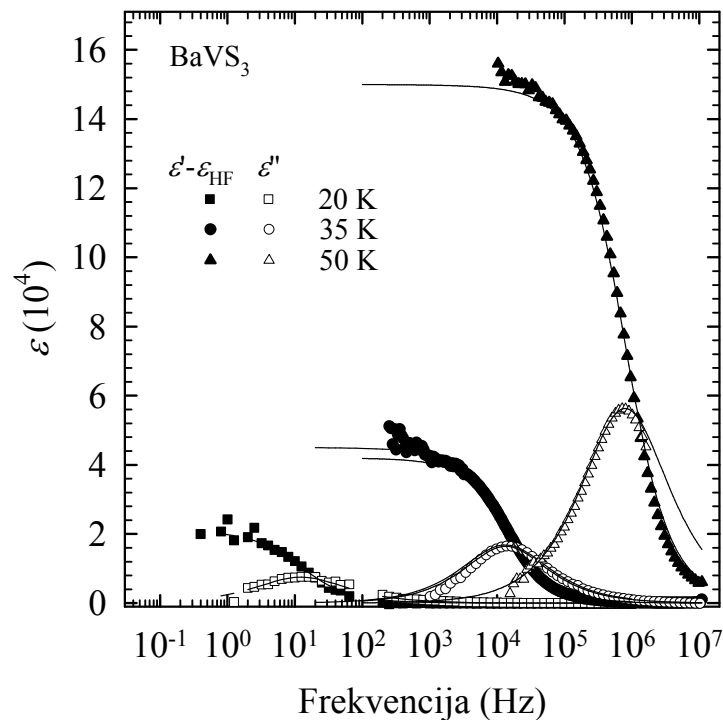
8.1.2 Eksperimentalne metode i uzorci

Mjerenja su vršena između 300 K i 10 K u dvostrukom kriostatu (tekući dušik - tekući helij). Nosač za uzorke opremljen je s četiri koaksijalna kabla čiji centralni vodiči u mjerenju istosmjernog otpora služe kao strujni i naponski vodiči, a u LFDS se na uzorak spajaju dvokontaktno kao što je opisano u prethodnom odjeljku. Vanjski vodiči koaksijalnih kablova kratko su spojeni kako bi se mogao koristiti samobalansirajući most. Temperaturna kontrola izvedena je uz pomoć uređaja Lakeshore 340 koji kontrolira grijač na dnu nosača (žica od manganina opletena tkaninom), i očitava temperaturu uz pomoć dva baždarena otporna termometra, platina 100 i Lakeshore carbon glass 500.

U postavu za dielektričnu spektroskopiju za niske frekvencije i visoke impedancije korišteno je fazno-osjetljivo pojačalo Stanford Research 830 sa strujnim pretpojačalom Stanford Research 570. Mjerenja tim postavom moguća su od 10 mHz do 3 kHz. Gornju granicu frekvencije diktira strujno pretpojačalo koje na velikim transimpedancijama izobličuje spektar vodljivosti na frekvencijama iznad nekoliko kHz.

Za mjerenje na frekvencijama iznad tog područja upotrebljen je analizator impedancije sa samobalansirajućim mostom Agilent 4294A koji nominalno pokriva frekventno područje 40 Hz–110 MHz. Zbog ukupne duljine svakog od koaksijalnih kablova (otprilike 1.5 m) maksimalna frekvencija na kojoj je mjerenje pouzdano ograničena je na oko 10 MHz.

Uzorci su dva monokristala $BaVS_3$ visoke stehiometrijske kvalitete, igličaste geometrije duž kristalografske c -osi odn. lanaca. Sva mjerenja su, dakle, vršena električnim poljem duž kristalografske c -osi. Na oba su uzorka dobiveni kvalitativno isti rezultati. Tipične dimenzije kristala su $(3 \times 0.25 \times 0.25)$ mm³. Kvaliteta samih uzoraka provjerenjena je u laboratoriju EPFL-a u Lausannei mjerenjem električnog otpora pod tlakom od 20 kbar. Na tom je tlaku u visokokvalitetnim uzorcima $BaVS_3$ MI prijelaz potpuno



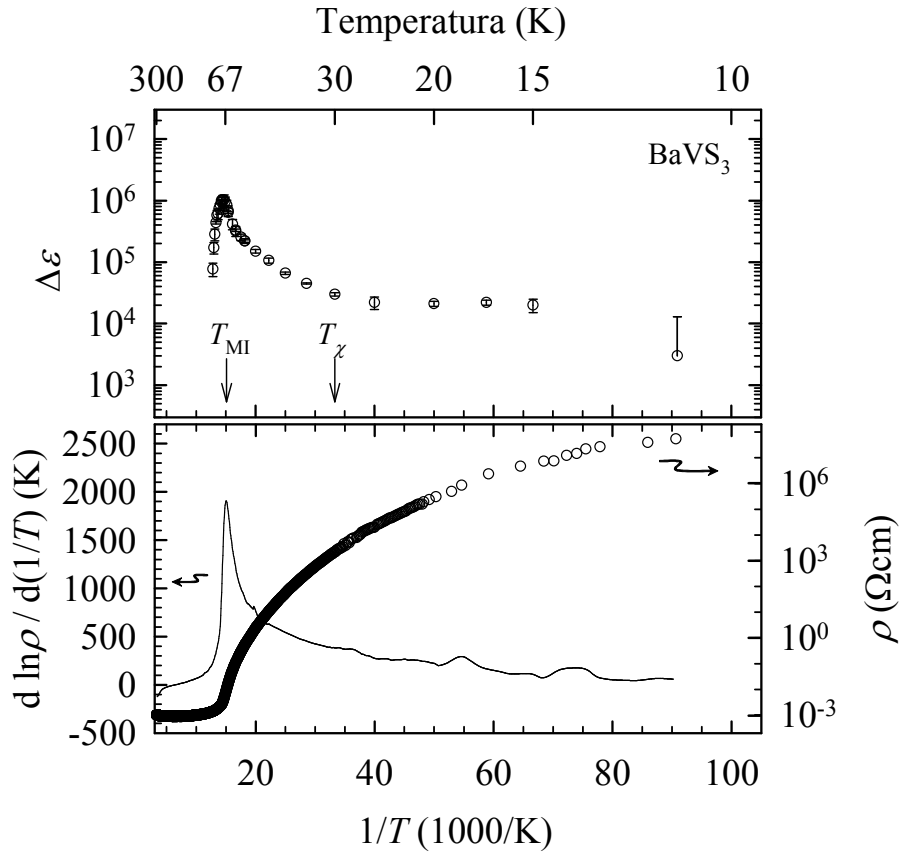
Slika 8.2 – Realni i imaginarni dio dielektrične funkcije u BaVS₃ mjereni na tri reprezentativne temperature kao funkcija frekvencije, s izmjeničnim električnim poljem primjenjenim duž *c*-osi. Puno linije su prilagodbe poopćenog Debyeovog izraza (8.1).

potisnut, tj. ne javlja se izolatorska faza.

Kontakti na uzorcima su pripremljeni na način koji je opisan u doktorskoj disertaciji N. Barišića. [183] Kontakt se sastoji od naparenog sloja kroma debljine 50 nm na samoj površini uzorka, zatim naparenog sloja zlata debljine 50 nm i na kraju srebrne paste kojom su pričvršćene zlatne žice. Srebrna pasta zahtijeva da uzorak bude zagrijan na 350 °C 10 min u vakuumu. Iskustvo je pokazalo da tek kontakti pripremljeni na ovaj način imaju otpor koji je u izolatorskoj fazi prihvatljivo nizak u odnosu na otpor uzorka (kontakti kod kojih je srebrna pasta nanešena direktno na uzorak imali su red veličine veći ohmski otpor).

8.1.3 Rezultati i diskusija

Slika 8.2 prikazuje frekventnu ovisnost kompleksnog dielektričnog odgovora na tri odabrane temperature. Opažena je istaknuta dielektrična relaksacija. Kako se temperatura smanjuje, zasjenjeni disipacijski maksimum u ε'' centriran na τ_0^{-1} kreće se prema nižim frekvencijama i manjim amplitudama. Glavna svojstva ove relaksacije opisuje



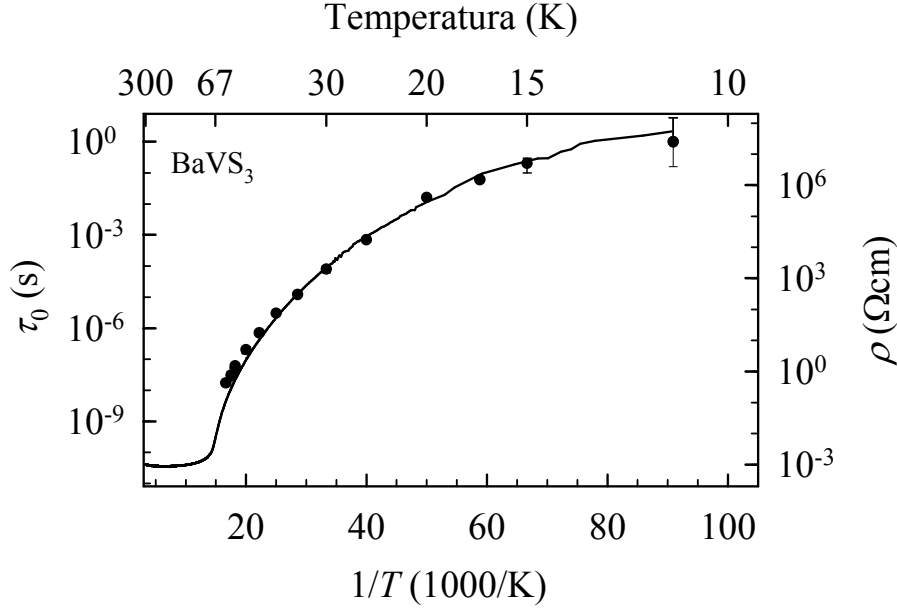
Slika 8.3 – Temperaturna ovisnost dielektrične konstante kolektivnog moda (gore) i istosmjerna otpornost te njena logaritamska derivacija (dolje) u BaVS₃. Strelice označuju temperaturu MI i magnetskog prijelaza.

poopćen Debyeov izraz

$$\epsilon(\omega) - \epsilon_{\text{HF}} = \frac{\Delta\epsilon}{1 + (i\omega\tau_0)^{1-\alpha}}, \quad (8.1)$$

gdje je $\Delta\epsilon = \epsilon_0 - \epsilon_{\text{HF}}$ (ϵ_0 i ϵ_{HF} su statička i visokofrekventna dielektrična konstanta, s time da je posljednja zanemarivog iznosa), τ_0 je srednje relaksacijsko vrijeme, a $1 - \alpha$ simetrično proširenje distribucije relaksacijskih vremena. Izraz (8.1) prilagođava se na dielektrične spektre snimljene pri konstantnoj temperaturi. Korištena je metoda najmanjih kvadrata u kompleksnoj ravnini, istovremeno za realni i imaginarni dio dielektrične funkcije, što znatno smanjuje nepouzdanost parametara prilagodbe u odnosu na klasičnu prilagodbu na svaku komponentu zasebno.

Rezultati jasno pokazuju da je velika dielektrična konstanta $\Delta\epsilon$ vezana uz metal-izolator prijelaz (Slika 8.3). Kako se temperatura spušta, blizu T_{MI} počinje oštri rast $\Delta\epsilon$ koji doseže vrijednosti reda 10^6 na $T_{\text{MI}} = 67$ K (Slika 8.3 gore). Ovako određen T_{MI} savršeno se poklapa s temperaturom faznog prijelaza dobivenom istosmjernim otporom,



Slika 8.4 – Srednje relaksacijsko vrijeme relaxation τ_0 kolektivnog moda (točke) i istosmjerna otpornost (puna linija) BaVS₃ u ovisnosti o inverznoj temperaturi.

gdje je standardno određena kao položaj istaknutog vrha u logaritamskoj derivaciji otpornosti (Slika 8.3 dolje).

Na prvi pogled bez uzimanja u obzir ostalih eksperimentalnih tehnika, opažena dielektrična relaksacija bi sugerirala nastajanje vala gustoće naboja na T_{MI} . [131] Standardni model deformabilnog vala gustoće naboja zapetog na neuniformnom potencijalu nečistoća uzima u obzir postojanje dva moda, transverzalnog i longitudinalnog. [187] Transverzalni se mod veže na elektromagnetsko zračenje i daje nezasjenjeni zapeti mod u mikrovalnom području. Na žalost, za sad još nema mikrovalnih mjerenja na BaVS₃. Longitudinalni mod se veže na elektrostatski potencijal i zbog neuniformnog zapinjanja uključuje i transverzalni odgovor, što uslijed zasjenjenja rezultira pregušenom niskofrekventnom relaksacijom na τ_0^{-1} . Relaksacija detektirana u našim eksperimentima ima dva obilježja koja se očekuju u ovakvoj standardnoj slici. Prvo je da je distribucija relaksacijskih vremena simetrično proširena, $1 - \alpha \approx 0.8$. Druga je da srednje relaksacijsko vrijeme τ_0 slijedi temperaturnu aktivaciju sličnu istosmjernoj otpornosti $\tau_0(T) = \tau_{00} \exp(2\Delta/2k_{\text{B}}T) \propto \rho(T)$ (vidi Sliku 8.4). $\tau_{00} \approx 1$ ns opisuje mikroskopsko relaksacijsko vrijeme kolektivnog moda, a energetski procjep $2\Delta \approx 500$ K odgovara onome u spektrima optičke vodljivosti [34]. Disipacija se prirodno može dodijeliti jednočestičnom zasjenjenju koje potječe iz široke A_{1g} vrpce. Međutim, unutar standardnog modela ne može se naći konzistentno objašnjenje za dielektričnu konstantu $\Delta\epsilon$ koja pokazuje jako opadanje ispod T_{MI} , a zatim se ustaljuje ispod otprilike 30 K. Takvo po-

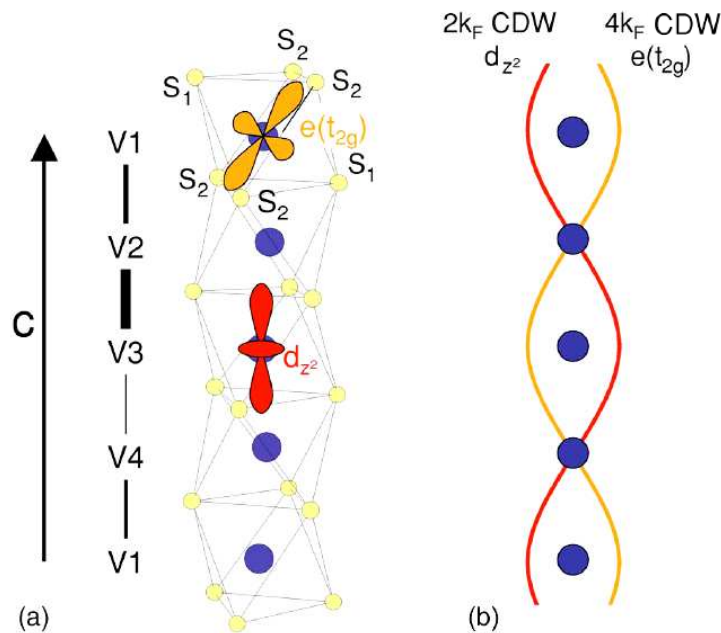
našanje značajno odstupa od očekivanog za gustoću n kondenzata vala gustoće naboja: $\Delta\varepsilon(T) \propto n(T)$ [131]. Pad $\Delta\varepsilon$ od MI prijelaza prema magnetskom prijelazu iznosi čitava dva reda veličine.

Jedno moguće objašnjenje ove diskrepancije leži u pretpostavkama standardnog modela odziva konvencionalnog vala gustoće naboja, koje uzimaju da je dominantni doprinos dugovalnih kolektivnih ekscitacija, tzv. fazona. Model je konstruiran za nesumjerljiv val gustoće naboja u potencijalu slučajno raspodijeljenih nečistoća, dok je val gustoće naboja u BaVS₃ vezan uz opaženu sumjerljivu modulaciju rešetke s redom sumjerljivosti (omjerom periodičnosti rešetke i superrešetke) $N = 4$. Međutim, red sumjerljivosti nije dovoljno velik da bi došlo do sumjerljivog zapinjanja i potiskivanja fazonskih pobuđenja. [134] Zaista, eksperimentalno opažanje široke relaksacije $1 - \alpha \approx 0.8$ svjedoči o neredu pozadinske strukture.

Dodatnu potvrdu da se ne radi o standardnim pobuđenjima vala gustoće donose mjerenja vodljivosti u ovisnosti o istosmjernom električnom polju. S poljima do 100 V/cm između 15 K i 40 K nije primijećena značajna nelinearnost vodljivosti, dok se kod standardnih 1D spojeva u fazi vala gustoće naboja očekuje pojava tzv. klizanja vala gustoće kod koje dolazi do značajnog porasta vodljivosti iznad određenog polja praga. [131]

Dakle, naši rezultati pokazuju da su kolektivne ekscitacije vala gustoće naboja ili zamrznute ili jako renormalizirane, odn. da neka druga vrsta pobuđenja uzrokuje opaženu dielektričnu relaksaciju. To je u slaganju s rezultatima koje daju Fagot *et al.*: izostanak modulacije naboja u izolatorskoj fazi BaVS₃, što implicira orbitalno uređenje. [9] Potvrda dolazi i od kvalitativne strukturne analize deformacija VS₆ oktaedara, koja u V-atomima pokazuje modulaciju popunjenosti d_{z^2} i $e(t_{2g})$ koje su suprotne faze (Slika 8.5). Fagot *et al.* predlažu da su V1 i V3 dominantne E_{g1} i A_{1g} popunjenosti, dok za V2 i V4 nema preferirane popunjenosti. K tome, račun na bazi LDA+DMFT (eng. local density approximation with dynamical mean-field theory, aproksimacija lokalne gustoće u sklopu dinamičke teorije srednjeg polja) [45] daje da u monoklinskoj izolatorskoj fazi BaVS₃ postoji vrlo mala disproporcijacija naboja na V-atomima uz varirajuću orbitalnu popunjenost. Čini se da parovi (V3,V4) formiraju korelirani dimer s miješanom popunjenosti A_{1g} i E_{g1} , dok V1 i V2 ioni nose većinsku E_{g1} i zanemarivo su vezani. Studija u cijelosti poručuje da je elektronska struktura vrlo osjetljiva na temperaturu, iako se okolina atoma vanadija ne mijenja značajno.

Postavlja se pitanje temperaturne ovisnosti parametra orbitalnog uređenja i koja je veza s magnetskim uređenjem. ⁵¹V NMR i NQR mjerenja predlažu orbitalno uređenje ispod T_{MI} koje se u potpunosti ostvaruje tek na $T < T_{\chi}$. [10] Magnetskom faznom



Slika 8.5 – (a) Lanac vanadija s četiri neekvivalentna V atoma i različite duljine veza. (b) Valovi gustoće naboja (eng. charge density wave, CDW) d_{z^2} i $e(t_{2g})$ elektrona koji dovode do orbitalnog uređenja u (a). Slika iz Fagot *et al.* [9]

prijelazu na T_χ prethode dugodosežne dinamičke antiferomagnetske korelacije sve do T_{MI} , i ta faza pokazuje sličnosti sa spinskom tekućinom s procjepom. Mihály *et al.* [7] su predložili da je izostanak dugodosežnog magnetskog uređenja između T_{MI} i T_χ možda posljedica frustrirane strukture trokutaste mreže V lanaca, što također sprečava dugodosežno orbitalno uređenje, pa se ono zajedno sa spinskim može ostvariti tek ispod T_{MI} . U vezi s tim, antiferomagnetsko statično uređenje ispod T_χ nije konvencionalna Néelova faza: mjerenja magnetske anizotropije ukazuju na antiferomagnetsku domensku strukturu [196]. Postojanje domena podržavaju i mjerenja mionske spinske rotacije (μ SR), koja daju slučajnu distribuciju velikih električnih polja ispod T_χ , što je znak nesumjerljivog ili neuređenog magnetizma [197].

Može se provjeriti je li uočeno ponašanje dielektrične konstante možda uzrokovano feroelektričnom prirodom MI prijelaza. Sudeći prema prostornim grupama strukture, ispod MI prijelaza $BaVS_3$ je necentrosimetrična rešetka s polarnom osi u refleksijskoj ravnini Im superstrukture koja sadrži VS_3 lance. BVS proračuni difrakcije X-zraka predviđaju disproporcijaciju naboja na niskim temperaturama. [33] Međutim, P. Foury-Leylekian [191] komentira da BVS metoda precjenjuje disproporcijaciju naboja zbog nekoliko razloga: nesimetrične okoline V^{4+} iona, zanemarivanja termalne kontrakcije i korištenja prilično nepreciznih koordinata atoma u računu. Kad se sve to uzme u obzir zajedno s anomalnim raspršenjem X-zraka (po kojem je redistribucija naboja zanema-

riva, ne veća od 0.01 elektrona ispod T_{MI} [9]), zaključak je da feroelektričnost ne može objasniti veliku dielektričnu konstantu kod $BaVS_3$.

Na kraju, možemo ukratko dotaknuti mogućnost da je vođenje preskakivanjem, čest mehanizam električnog vođenja u neuređenim sustavima niske dimenzionalnosti, zapravo uzrok dielektričnog odgovora. Iako $BaVS_3$ jest kvazi-1D sustav, preskakivanje se ne čini vjerojatnim budući da bi frekvencija na kojoj počinje frekventno ovisna vodljivost trebala ugrubo biti proporcionalna istosmjernoj vodljivosti [188]. Za $BaVS_3$, gruba procjena te frekvencije daje vrijednosti visoko iznad našeg frekventnog opsega. Uz to, optički spektri [34] vode na isti zaključak budući da su optičke vodljivosti usporedivih iznosa s istosmjernom vodljivosti.

Na osnovi svih navedenih razmatranja može se konstruirati vjerojatna slika fizike $BaVS_3$. Primarni parametar uređenja za MI fazni prijelaz je 1D nestabilnost vala gustoće naboja, i ta nestabilnost je uzrok orbitalnog uređenja. S druge strane, orbitalno uređenje je vezano za spinske stupnjeve slobode i tjera spinsko uređenje u osnovno stanje slično antiferomagnetskom ispod 30 K. Drugim riječima, orbitalno uređenje nastaje na T_{MI} i razvija se u dugodosežno uređenje ispod T_χ . U tom scenariju možemo interpretirati opažena svojstva dielektrične relaksacije pozivajući se na kratkovalne kolektivne ekscitacije poput domenskih zidova u slučajnoj antiferomagnetskoj strukturi. Do relaksacije dolazi između različitih metastabilnih stanja, što odgovara lokalnim promjenama spinske konfiguracije, a koja je vezana uz stupnjeve slobode nosilaca naboja i orbitala. Budući da je dielektrična konstanta veličina koja opisuje gustoću kolektivnih ekscitacija, njena anomalna temperaturna ovisnost ispod T_{MI} je indicacija da sa spuštanjem temperature dinamika domenskih zidova postaje sve više ograničena i na kraju postaje konstantna ispod T_χ . Drugim riječima, relaksacijski aktivan broj domenskih zidova smanjuje se s hlađenjem i postaje dobro definiran ispod T_χ .

8.2 Prebacivanje mehanizma transporta s kupratnih lanaca na ljestvice u $(La, Y, Sr, Ca)_{14}Cu_{24}O_{41}$

Kompozitni sustav spinskih lanaca i ljestvica $(La, Y, Sr, Ca)_{14}Cu_{24}O_{41}$ također spada u široku klasu jako koreliranih materijala, oksida prijelaznih metala, i pokazuju iznenađujuće širok skup intrigantnih pojava. [231] Velik broj radova na temu spinskih lanaca i spinskih ljestvica (za pregled vidi Ref. [2]) prvenstveno je potaknut otkrićem supravodljivosti pod tlakom u spoju $Sr_{14-x}Ca_xCu_{24}O_{41}$, $x = 13.6$, zbog činjenica da

je to prvi supravodljivi kupratni spoj s nekvadratnom rešetkom. [11] Roditeljski materijal, $Sr_{14}Cu_{24}O_{41}$, je izolator s valom gustoće naboja (VGN) koji također pokazuje spinski procijep. [12, 235, 16, 203] Izovalentna zamjena stroncijevih atoma kalcijem potiskuje VGN, što je vidljivo u dc i ac transportnim mjerenjima, [13] dok spinski procjep ostaje nepromijenjen. [203, 2] Međutim, nedavni eksperimenti rezonantnog raspršenja X-zraka [236] pokazuju da se VGN možda stabilizira i na višim supstitucijama kalcijem, no s drugačijom periodičnošću, što ukazuje na jake komenzuracijske efekte. Pod tlakom spojevi s visokim udjelom kalcija pokazuju smanjenje spinskog procjepa, no on ne iščezava čak i pri nastanku supravodljivosti. [237] Tlak također povećava vezanje među ljestvicama što dovodi do metalnog transporta duž nogu i prečki ljestvica, [76] te povećava broj mobilnih kvazičestica na niskim temperaturama. [81, 238] Te kvazičestice imaju konačnu gustoću stanja na Fermijevom nivou i mogu doprinijeti supravodljivoj nestabilnosti. Svi ovi rezultati, zajedno s Hebel-Slichterovim koherencijskim vrhom u supravodljivom stanju, kao i značajan nered u dopiranim ljestvicama $Sr_{14-x}Ca_xCu_{24}O_{41}$, ukazuju da mehanizam supravodljivog sparivanja i simetrija ne odgovaraju teoretskim predviđanjima za čiste, zasebne ljestvice.

Poznato je da količina dopiranih šupljina i njena raspodjela među lancima i ljestvicama uvjetuje elektronske faze i dinamiku spina i naboja. U potpuno dopiranom materijalu $Sr_{14}Cu_{24}O_{41}$ ukupni broj šupljina jest $n_h = 6$ po formulskoj jedinki. Raspodjela šupljina među lancima i ljestvicama se direktno može opaziti polarizacijski ovisnom finom strukturom raspršenja X-zraka blizu ruba (eng. near-edge X-ray absorption fine structure, NEXAFS): na sobnoj temperaturi prema Nücker *et al.* [14] postoji otprilike jedna šupljina po formulskoj jedinki u ljestvicama (ekvivalentno $\delta = 0.07$ šupljina po atomu bakra ljestvica) i otprilike pet preostaje na lancima. Nedavno Rusydi *et al.* [74] su predložili drukčiju raspodjelu, po tri šupljine na lancima i ljestvicama. Dvodimenzionalne ljestvice predstavljaju dominantni kanal transporta: vodljivost na sobnoj temperaturi duž nogi ljestvica i lanaca, c -osi, je $\sigma_{dc}(c) \approx 500 \Omega^{-1}cm^{-1}$ i duž a -osi tj. prečki ljestvi $\sigma_{dc}(a) \approx 20 \Omega^{-1}cm^{-1}$. Iako je $\sigma_{dc}(c)$ prilično visokog iznosa, pokazuje izolatorsko ponašanje, tj. spušta se s temperaturom sve do prijelaza u VGN; slično ponašanje se također opazuje u $\sigma_{dc}(a)$. [17] Istovremeno, preostale šupljine u lancima zanemarivo doprinose transportu naboja: između Cu^{2+} spinova formiraju se spinski dimeri koji su odvojeni lokaliziranim Zhang-Rice singletima (Cu^{3+}), tj. ionima bakra na kojima je lokalizirana šupljina. Na taj način je u lancima stvoren uzorak antiferomagnetskih dimera zajedno s uređenjem naboja, i oba zajedno uvode procjeme u spinskom i nabojnom sektoru. [18, 19, 20, 21] Dapače, glavni uvjet za AF dimersko uređenje naboja jest da broj šupljina bude blizak 6. Taj je uvjet zadovoljen prema Ref. [14], a ne može biti pomi-

ren s raspodjelom šupljina u Ref. [74]. S druge strane, u poddopiranim materijalima (La, Y, Sr, Ca)₁₄Cu₂₄O₄₁ ($n_h = 6 - y$) šupljine nisu prisutne u ljestvicama što eliminira VGN fazu i potiskuje uređenje naboja s procjepom u lancima koje je zamijenjeno neuređenom izolatorskom fazom u kojoj se transport odvija preskakivanjem promjenjivog dosega (eng. variable range hopping, VRH). [22, 58] Mehanizam preskakivanja potječe u neperiodičkom potencijalu u kojem se nalaze šupljine, kojeg uzrokuju jake lokalne distorzije lanaca zbog nepravilne koordinacije La³⁺, Y³⁺, Sr²⁺ i Ca²⁺ iona. Vođenje preskakivanjem promjenjivog dosega zbog toga može biti objašnjeno kao rezultat izobličene raspodjele mikroskopskih vodljivosti, kao što predviđa Andersonova teorija lokalizacije: ukratko, kupratni lanci u poddopiranim materijalima se mogu smatrati jednodimenzionalnim sustavom u kojem nered slučajne raspodjele šupljina uzrokuje Andersonovu lokalizaciju.

Prijašnji rad na ovoj obitelji spojeva [22, 2, 58] sugerira intrigantnu mogućnost faznog prijelaza blizu $n_h = 6$ u faznom dijagramu (La, Y, Sr, Ca)₁₄Cu₂₄O₄₁, što bi trebali razjasniti eksperimenti na materijalima s vrlo niskim sadržajem La i Y atoma ($n_h \leq 6$). U ovom radu pokušavamo odgovoriti na pitanje kako i u kojoj točki dopiranja jednodimenzionalni transport preskakivanjem duž lanaca prelazi na kvazi-dvodimenzionalno vođenje u ravninama ljestvica. U svrhu razjašnjavanja tog problema vršena su mjerenja anizotropije ac i dc vodljivosti na monokristalima (La, Y, Sr, Ca)₁₄Cu₂₄O₄₁ d različitim udjelom La odn. Y (posebna pažnja je posvećena La/Y sastavima bliskim $y = 0$) u širokom rasponu frekvencija i temperatura. Pokazujemo da za sustave s $y \lesssim 2$ ($n_h \gtrsim 4$) preskakivanje promjenjivog dosega ne uspijeva objasniti opaženu vodljivost i da nabojni stupnjevi slobode pokazuju slična svojstva kao u potpuno dopiranim sustavima: anizotropija vodljivosti je sličnog reda veličine, a logaritamske derivacije otpornosti pokazuju široke maksimume. Novi rezultat ovog rada je da u poddopiranim sustavima s $n_h \gtrsim 4$ ljestvice počinju doprinositi transportnim svojstvima i nadjačava lance kao dominantni kanal transporta. Frekventno ovisna vodljivost pokazuje začetke kratkodosežnog uređenja naboja u ljestvicama.

8.2.1 Eksperimentalne metode i uzorci

Korišteni su novosintetizirani visokokvalitetni monokristali materijala s niskim sadržajem itrija: $y = 0$ (Sr₁₄Cu₂₄O₄₁), $y = 0.55$ (Y_{0.55}Sr_{13.45}Cu₂₄O₄₁), $y = 1.6$ (Y_{1.6}Sr_{12.4}Cu₂₄O₄₁). Uzorci su prvo karakterizirani difrakcijom X-zraka u prašku, a sadržaj Y je određen elektronskom mikroprobom (eng. electron probe microanalyzer). Za potrebe određivanja niskofrekventnog transporta uzorci su rezani u oblik izduženog kvadra ve-

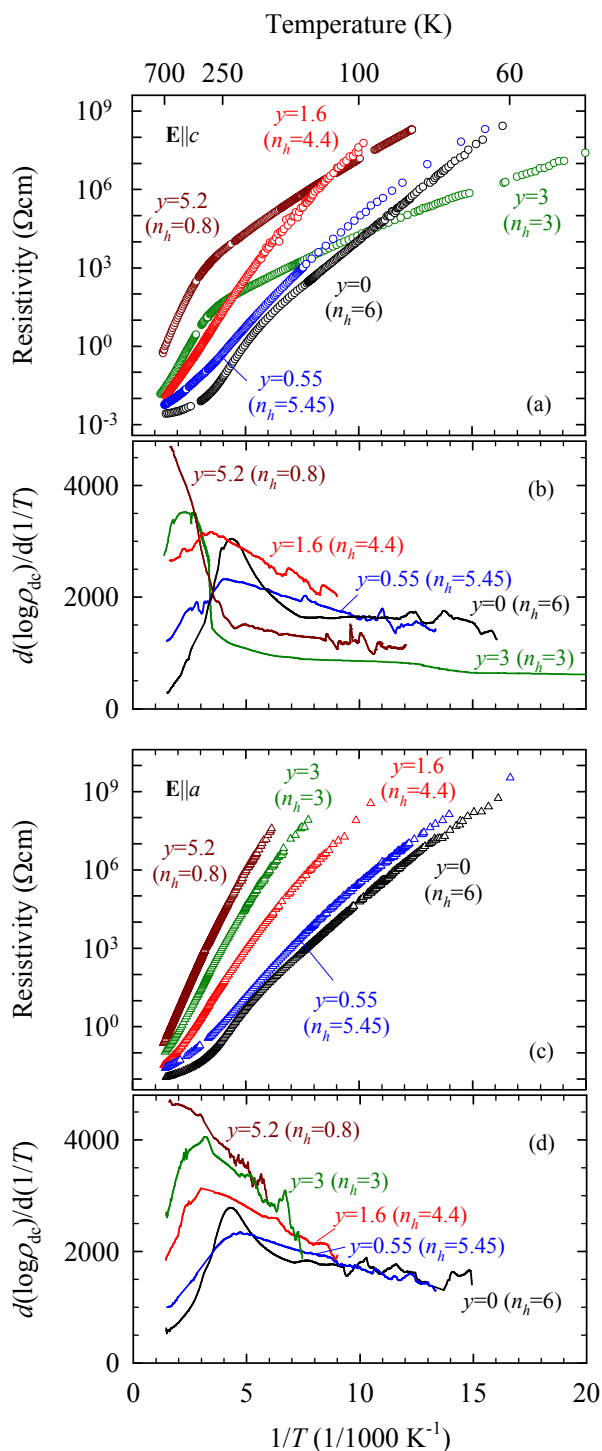
ličine otprilike 0.4 mm^3 . Za transport su također upotrebljeni prethodno sintetizirani i rezani uzorci $y = 3$ ($La_3Sr_3Ca_8Cu_{24}O_{41}$) i $y = 5.2$ ($La_{5.2}Ca_{8.8}Cu_{24}O_{41}$). Orijehtacija rezanih kristala korištenih za anizotropiju vodljivosti je provjerena Laueovom metodom difrakcije X-zraka i simulacijom difrakcijskih slika pomoću programa OrientExpress 3.3. [239] za dvije podćelije ($a = 11.47 \text{ nm}$, $b = 13.37 \text{ nm}$, $c_L = 3.93 \pm 0.03 \text{ nm}$, Fmmm - za ljestvice; $a = 11.47 \text{ nm}$, $b = 13.37 \text{ nm}$, $c_C = 2.73 \pm 0.03 \text{ nm}$, Amma - za lance). Kod svih kristala je ustanovljeno da je kristalografska ac ravnina paralelna najvećoj plohi izduženog kvadra, a c -os ili a -os je postavljena uz najduži brid. dc otpornost mjerena je između 50 K i 700 K.

Hewlett Packard 4284A i Agilent 4294A analizatori impedancije upotrebljeni su u mjerenju kompleksnih vodljivosti $y = 0, 0.55$ i 1.6 između 20 Hz and i 10 MHz. [180] Realni dio vodljivosti na niskim frekvencijama odgovara četverokontaktним dc mjerenjima. Kompleksna dielektrična funkcija na frekvencijama $5\text{--}25 \text{ cm}^{-1}$ dobivena je mjerenjem kompleksne transmitivnosti pomoću koherentnog izvora THz zračenja i spektrometra. [240] za ta su mjerenja ispolirani kristali s planparalelnim plohama debljine oko 0.5 mm , površine oko $7 \times 7 \text{ mm}^2$. Sva su mjerenja obavljena s polarizacijom električnog polja duž dvije kristalografske osi slojeva lanaca i ljestvica: c -osi duž nogi ljestvica i lanaca, te a -osi duž prečki ljestvica.

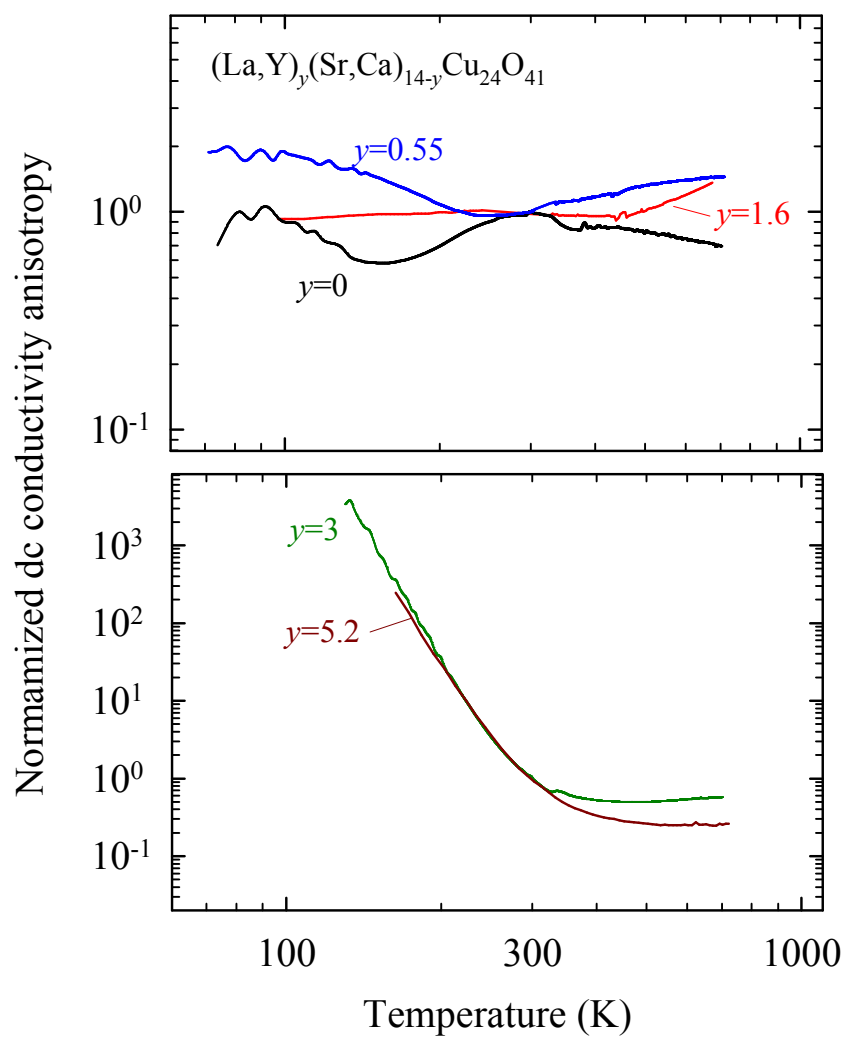
8.2.2 Rezultati i analiza

dc transport

Slika 8.6 pokazuje ponašanje dc otpornosti i njene logaritamske derivacije za različit sadržaj La/Y, od $y = 5.2$ do $y = 0$ duž c -osi [paneli (a) i (b)] i a -osi [paneli (c) i (d)] u širokom rasponu temperatura od 50 K (najniža temperatura s kvalitetnim mjerenjima) sve do 700 K. S jedne strane, za dva spoja visokog $y = 5.2$ i 3 krivulje dc otpornosti duž c - i a -osi se bitno razlikuju ispod 300 K gdje krivulja duž c -osi raste sporije sa spuštanjem temperaturom. S druge strane, $y = 1.6, 0.55$ i 0 pokazuju gotovo identično ponašanje otpornosti duž obje osi. Direktan zaključak jest da anizotropija vodljivosti postaje značajno pojačana za sustave s visokim sadržajem La/Y $y \geq 3$ (odn. niskim brojem šupljina $n_h \leq 3$), a ostaje mala i neovisna o temperaturi za niske y (visoke n_h), kao što prikazuje Slika 8.7. Kvalitativna razlika između ova dva tipa ponašanja naglašena je Slikom 8.7, koja pokazuje anizotropije dc vodljivosti normalizirane na vrijednost na sobnoj temperaturi. Anizotropija na sobnoj temperaturi je u rasponu 1–30 i u biti ne ovisi o sadržaju La/Y.



Slika 8.6 – (color online) dc otpornost i logaritamske derivacije $(\text{La}, \text{Y}, \text{Sr}, \text{Ca})_{14}\text{Cu}_{24}\text{O}_{41}$ za razne sadržaje La/Y y duž c - [paneli (a) i (b)] i a -osi [paneli (c) i (d)].



Slika 8.7 – Temperaturna ovisnost anizotropije vodljivosti $(La, Y, Sr, Ca)_{14-y}Cu_{24}O_{41}$ za razne sadržaje La/Y y normalizirane na vrijednost na sobnoj temperaturi.

Tablica 8.1 – Parametri dc transporta u (La, Y, Sr, Ca)₁₄Cu₂₄O₄₁ za različite sastave La/Y y duž c -osi.

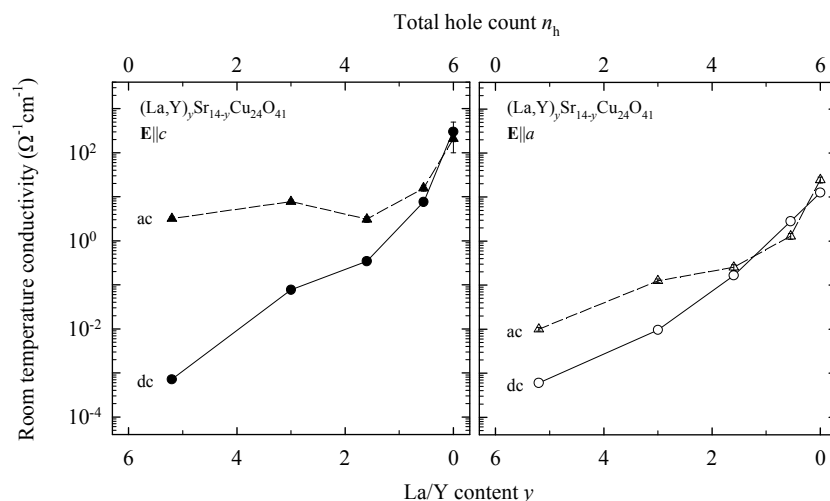
Spoj	y	Δ (meV)	T_{co} (K)	T_0^{exp} (meV)	α^{-1} (Å)	T_0^{th} (meV)
Y _{0.55} Sr _{13.45} Cu ₂₄ O ₄₁	0.55	130 ± 40	280 ± 15	9000 ± 100	0.960	750
Y _{1.6} Sr _{12.4} Cu ₂₄ O ₄₁	1.6	230 ± 10	330 ± 30	13400 ± 100	0.677	1900
La ₃ Sr ₃ Ca ₈ Cu ₂₄ O ₄₁	3	280 ± 10	295 ± 5	2500 ± 100	0.481	3400
La _{5.2} Ca _{8.8} Cu ₂₄ O ₄₁	5.2	370 ± 50	330 ± 5	4300 ± 100	0.435	4600

Sljedeća bitna razlika između niskog i visokog sadržaja La/Y nalazi se u temperaturnoj ovisnosti krivulja dc vodljivosti. Kao što je rečeno za $y = 5.2$ i 3 , duž c -osi vodljivost $\sigma_{dc}(c)$ slijedi ponašanje VRH za dimenziju sustava $d = 1$, te oko T_{co} prelazi na preskakivanje među najbližim susjednima na visokim temperaturama. [22, 2, 58] Opažanje VRH-a tipa $d = 1$ je u skladu s malim vezanjem među lancima u (La, Y, Sr, Ca)₁₄Cu₂₄O₄₁. No, VRH prilagodbe

$$\sigma_{dc}(T) = \sigma_0 \exp \left[- \left(\frac{T_0}{T} \right)^{1/(1+d)} \right] \quad (8.2)$$

na krivulje $\sigma_{dc}(c)$ za $y = 1.6$ i $y = 0.55$ ne pružaju dobar opis: naime, dobivene odgovarajuće VRH aktivacijske energije $T_0^{\text{exp}} = 13400$ meV i 9000 meV su mnogo veće nego za $y = 5.2$ i 3 . Ovaj rezultat ne slaže se s očekivanim ponašanjem u VRH mehanizmu: vodljiviji uzorci bi trebali pokazivati niži T_0 . Zaista, ove vrijednosti T_0^{exp} su različite od onih koje bismo očekivali teoretski: $T_0^{\text{th}} = 2 \cdot \Delta \cdot c_c \cdot \alpha \approx 1900$ meV i 700 meV, vidi Tablicu 8.1. Ovdje energija mjesta dostupnih za preskok blizu Fermijeve energije ima jednoliku raspodjelu u rasponu $-\Delta$ do Δ , c_c je udaljenost između najbližih mjesta Cu atoma u lancima, a $\alpha^{-1} = 2c_c \cdot T_{co}/\Delta$ je lokalizacijska duljina. Konkretno eksperimentalne vrijednosti T_0^{exp} su toliko visoke da uvriježena interpretacija parametara preskakivanja također vodi na prenisu gustoću stanja za $y = 1.6$ i 0.55 u usporedbi s $y = 5.2$ i 3 . Treba istaknuti da je jednodimenzionalni VRH kanal vođenja duž c -osi, koji je prisutan i aktivan kod $y \geq 3$, efikasniji od transporta u $y < 3$.

Otpornost duž a -osi se s promjenom y kvalitativno mijenja slično kao i otpornost duž c -osi. Nagib krivulja $\log \rho_{dc}$ vs. T^{-1} za $y = 5.2$ i 3 pokazuje da je aktivacijska energija mnogo veća na visokim temperaturama i opada sa smanjenjem T , dok za $y = 0.55$ i 0 nalazimo suprotno ponašanje: nižu aktivacijsku energiju na visokim temperaturama i porast prema niskim temperaturama. Čini se da je spoj $y = 1.6$ otprilike na granici među ova dva različita tipa ponašanja. Treba podsjetiti da $y = 0$ ima nižu aktivacijsku energiju na visokim temperaturama i veću na niskim temperaturama, što je osobina koju povezujemo s prijelazom izolator-izolator u VGN fazu ljestvica. [17]



Slika 8.8 – dc (krugovi) i ac vodljivosti za 10 cm^{-1} (trokuti) na sobnoj temperaturi duž c -osi (lijevo) i a -osi (desno) u ovisnosti o sadržaju La/Y y i ukupnog broja šupljina n_h . Pune i isprekidane linije vode oko za dc i ac podatke.

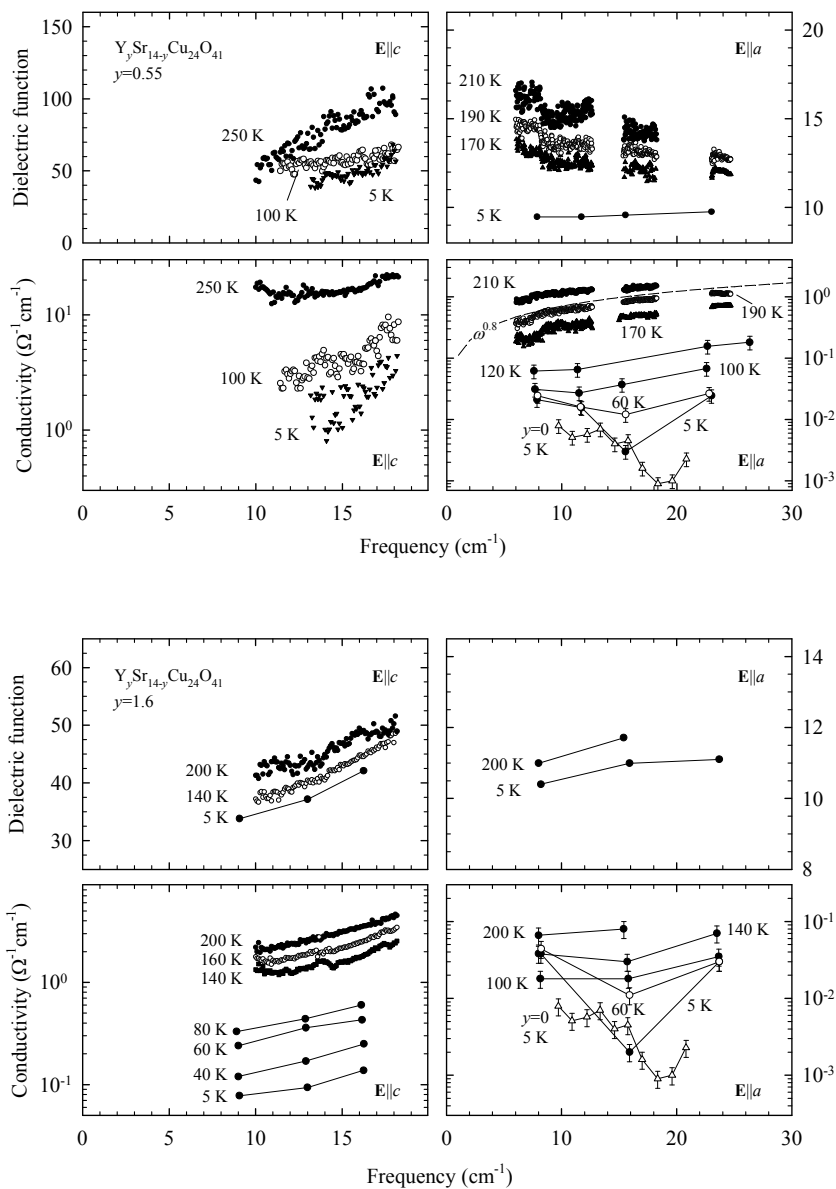
Sljedeća razlika između spojeva s visokim i niskim y postaje očita kad se pogledaju krivulje logaritamskih derivacija [Slika 8.6, paneli (b) i (d)]. Za $y = 0.55$ (no ne $y = 3$ i 5.2), obje orijentacije $\mathbf{E}||a$ i $\mathbf{E}||c$ imaju široki i plosnati maksimum u $d(\ln \rho)/d(1/T)$ centriran oko 210 K, poput $y = 0$ gdje tu pojavu, iako nešto užu, povežemo s potpisom VGN prijelaza u ljestvicama. Maksimum derivacije ostaje vidljiv u $y = 1.6$; no sad je izrazito širok, pomaknut prema 300 K i naglašeniji za $\mathbf{E}||a$ nego $\mathbf{E}||c$.

Na kraju treba pokazati i neobičan rezultat koji se tiče iznosa vodljivosti na sobnoj temperaturi duž obje osi, koja se značajno povećava s brojem šupljina (Slika 8.8). Javno je da povećanje broja šupljina nije dovoljno da objasni rast vodljivosti od nekoliko redova veličine. Teoretski, dopiranje može stvoriti nezanemarivu gustoću stanja na Fermijevom nivou tako da ga pomakne iz procjepa u područje visoke gustoće stanja, što bi moglo doprinjeti rastu vodljivosti. Unatoč tome, ukupni porast ukazuje na izvanredno povećanje mobilnosti za $y < 2$.

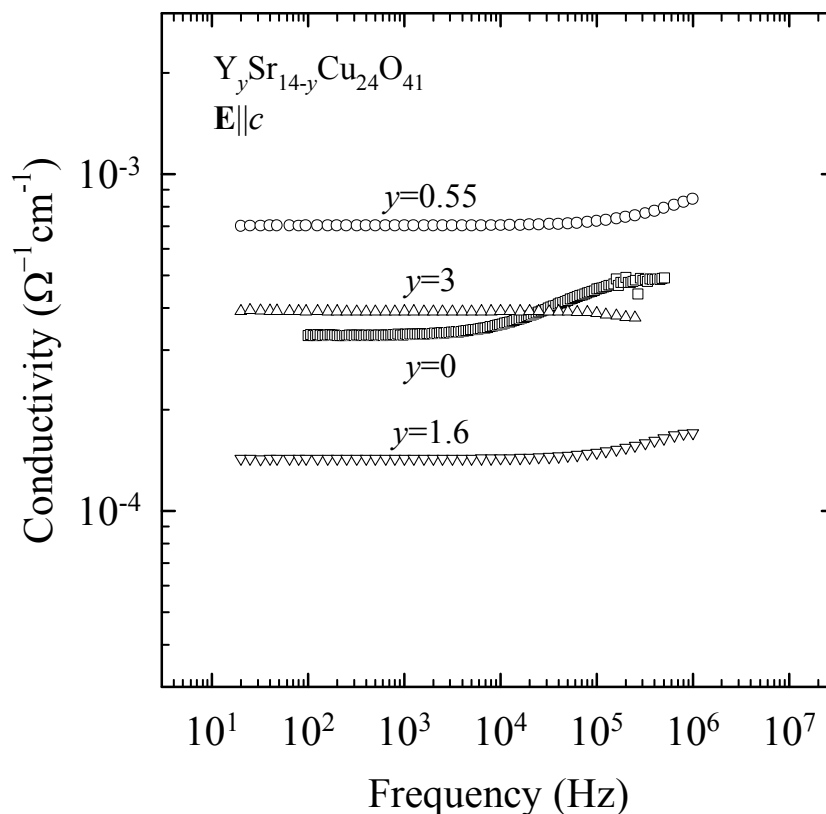
Izmjenična vodljivost i dielektrična funkcija

Usporedimo sad dc i ac podatke. Slika 8.9 prikazuje spektre vodljivosti $(La, Y, Sr, Ca)_{14}Cu_{24}O_{41}$ za $y = 0.55$ i 1.6 u frekventnom opsegu između 5 i 25 cm^{-1} na nekoliko reprezentativnih temperatura. Približno konstantni spektar vodljivosti na sobnoj temperaturi otkriva metalni odziv $y = 0$ u ac vodljivosti duž c - i a -osi (vidi Sliku 67 u Ref. [2]) što je također vidljivo i kod $y = 0.55$ i 1.6 . Ovaj rezultat ukazuje na pojavu određene količine slobodnih naboja koje ne vidimo kod $y = 3$ i 5.2 (vidi umetnutu sliku u Slici 3, Ref. [22])

8.2 Prebacivanje mehanizma transporta s kupratnih lanaca na ljestvice u
 $(La, Y, Sr, Ca)_{14}Cu_{24}O_{41}$



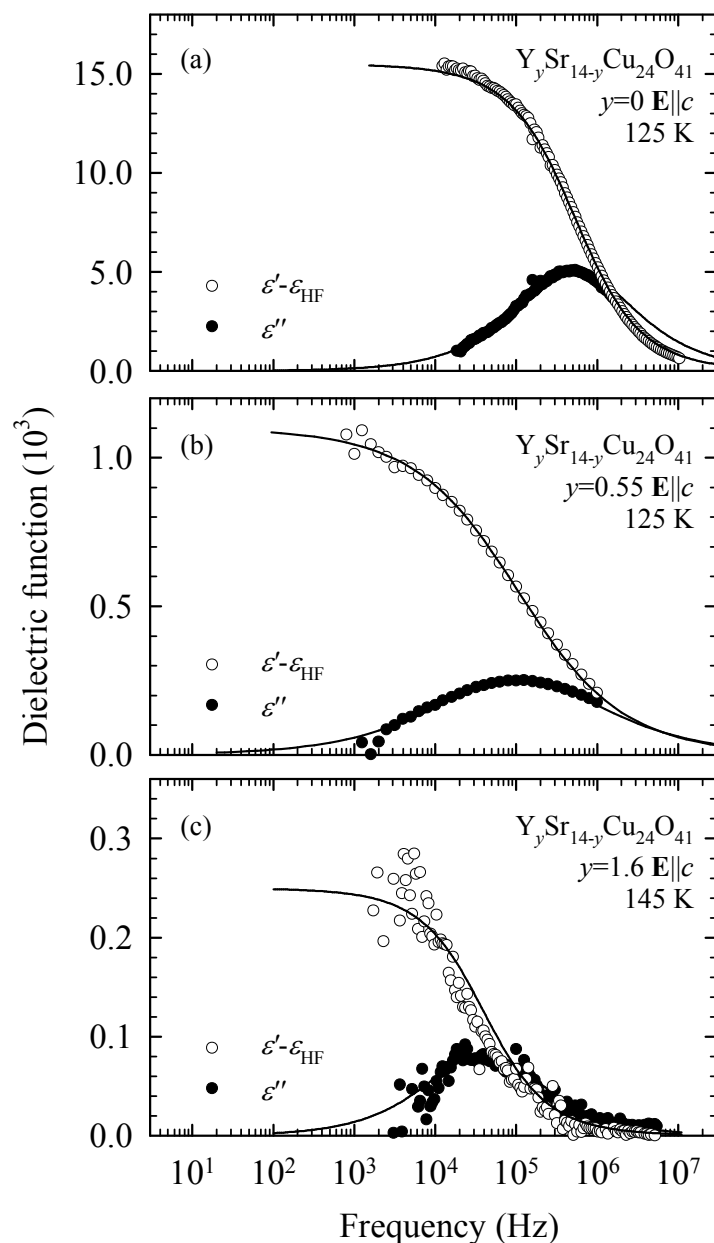
Slika 8.9 – Dielektrična funkcija i vodljivost u THz području za $Y_ySr_{14-y}Cu_{24}O_{41}$ sa sadržajem Y $y = 0.55$ (gore) i 1.6 (dolje) duž c - i a -osi na naznačenim temperaturama. Usporedbe radi prikazani su i podaci za $y = 0$ duž a -osi na 5 K (otvoreni trokuti).



Slika 8.10 – Spektar vodljivosti $y = 0, 0.55, 1.6$ i 3 , $\mathbf{E}||c$ u radiofrekventnom području na reprezentativnim temperaturama (95 K, 125 K, 165 K i 132.5 K u tom redoslijedu) s usporedivim istosmjernim vodljivostima.

i govori da se opaženi spektri mogu pripisati nabojnim pobuđenjima u ljestvicama kao i u $y = 0$. [2] osvrnut ćemo se na ovo ponašanje prema kraju odjeljka. Spuštanjem temperature ispod 200 K zamjetno je potiskivanje Drudeovog doprinosa spektru vodljivosti duž obje osi, što znači da razvoj izolatorskog ponašanja.

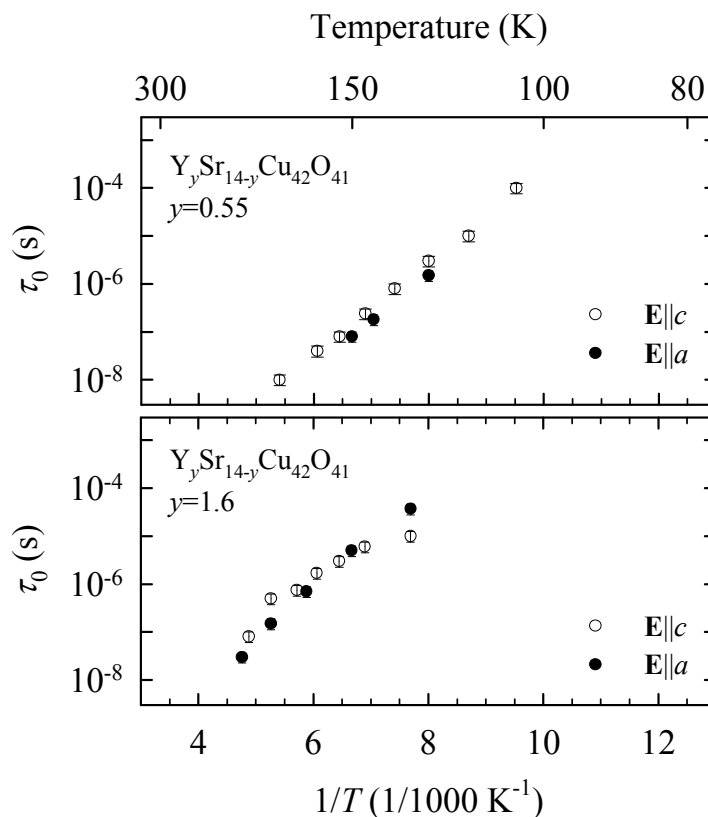
Treba reći da je u svim promatranim slučajevima (uz istaknute $y = 0.55$ i $y = 1.6$) vodljivost u dc granici (Slika 8.6) niža od relativno visoke izmjenične vodljivosti u THz području. Mehanizam koji je standardno odgovoran za takvo ponašanje jest elektronsko preskakivanje opisano potencijskim ponašanjem $\sigma_{ac}(T) \propto A(T) \cdot \omega^s$. Zaista, vođenje preskakivanjem $s \approx 1$ je već pronađeno u ljestvicama spoja $y = 0$ za $\mathbf{E}||c$ i $\mathbf{E}||a$, kao i u lancima $y = 3$ i 5.2 za smjer $\mathbf{E}||c$. [22, 2, 58] U ovom radu potencijska ovisnost je nađena samo kod $y = 0.55$ ($\mathbf{E}||a$) između 200 K i 100 K. Dva su razloga koja sprečavaju detekciju vođenja preskakivanjem u ostalim slučajevima. Prvi je vezan uz fononski rep koji maskira disperziju preskakivanja u smjeru $\mathbf{E}||c$. Za c -os i $y = 0.55, 1.6$ na najnižim temperaturama ($T = 5$ K) vidimo tipični fononski rep u THz području. Čini se da je za ta dva sastava najniži fonon na otprilike 25 cm^{-1} , odn. istoj frekvenciji gdje je najniži



Slika 8.11 – Realni (ϵ') i imaginarni (ϵ'') dijelovi dielektrične funkcije $Y_ySr_{14-y}Cu_{24}O_{41}$ za $y = 0$ [panel (a)], $y = 0.55$ [panel (b)] i $y = 1.6$ [panel (c)] na reprezentativnim temperaturama 125 K ($y = 0$ i $y = 0.55$) i 145 K ($y = 1.6$) u ovisnosti o frekvenciji, s time da je električno polje duž c -osi. Pune linije su prilagodbe na podatke korištenjem generalizirane Debyeovog izraza $\epsilon(\omega) - \epsilon_{HF} = \Delta\epsilon / (1 + (i\omega\tau_0)^{1-\alpha})$.

fonon kod $y = 3$ spoja (vidi Sliku 3 u Ref. [22]) te kod $Sr_{11}Ca_3Cu_{24}O_{41}$. Drugi razlog zbog kojeg se vođenje preskakivanjem teško otkriva kod $\mathbf{E}||a$ ispod oko 100 K je zbog vrlo jasnog porasta vodljivosti ispod frekvencije 20 cm^{-1} . Najvjerojatnija intepretacija jest da je taj porast indikacija tzv. zapetog moda VGN u mikrovalnom području. Ova je značajka također vidljiva kod $y = 0$ (vidi Sliku 8.9 za $\mathbf{E}||a$). Budući da nam preostaje samo visokofrekventni nagib moda, nije moguće dati kvantitativnu prilagodbu i odrediti parametre poput svojstvene frekvencije, dielektričnog intenziteta ili gušenja. Kako bilo, procjene na osnovi dielektrične funkcije i vodljivosti ukazuju na to da bi parametri ovog moda bili bitno različiti od zapetog moda VGN na 1.8 cm^{-1} kojeg su odredili Kitano *et al.* [15] u potpuno dopiranom roditeljskom $Sr_{14}Cu_{24}O_{41}$ na osnovi nekoliko mikrovalnih točki. S druge strane, u smjeru $\mathbf{E}||c$ ne vide se naznake zapetog moda u THz području, što bi moglo značiti da je ili pomaknut na niže frekvencije ili maskiran bilo slobodnim nosiocima bilo fononom. Ovaj mod, kojeg u nedostatku boljeg opisa možemo pripisati zapetom modu VGN, nije prisutan u THz spektrima spojeva s $y = 3$ i 5.2. Upravo ova odsutnost na višim y bi mogla ukazivati alternativnu dodjelu parametara zapetog moda VGN, i, unatoč tome što se za sad temelji samo na indiciji, ne bi trebala biti zanemarena. Pitanje zapetog moda i njegovog razvoja u $Y_ySr_{14-y}Cu_{24}O_{41}$ zaslužuje dodatnu pažnju u budućnosti. Što se tiče dielektrične konstante ε' u $y = 0.55$ i 1.6, treba reći da se dobro poklapa s dielektričnom konstantom potpuno dopiranog $Sr_{11}Ca_3Cu_{24}O_{41}$ (Slika 66 u Ref. [2]), što znači da su infracrveni fononski spektri svih ovih materijala vjerojatno vrlo slični.

Pogledajmo sad rezultate u radiofrekventnom području. U spoju $y = 0$ VGN se razvija u ljestvicama, što daje naglašeni stepeničasti porast vodljivosti na radiofrekvencija, dok je frekventna ovisnost u $y = 0.55$ i 1.6 mnogo slabija i usporediva s onom kod $y = 3$ (Slika 8.10) - ovdje se treba sjetiti da su vodljivosti $y = 3$ i $y = 5.2$ na svim temperaturama neovisne o frekvenciji u radio-frekventnom području. [22, 2, 58] Međutim, za razliku od $y = 3$ i $y = 5.2$, kad se iz kompleksne vodljivosti proračuna kompleksna dielektrična funkcija za $y = 0.55$ i 1.6, ukazuje se slab dielektrični relaksacijski mod (Slika 8.11): primjetan je karakterističan pad poput stepenice u realnom dijelu dielektrične funkcije, te široki maksimum u imaginarnom, što podsjeća na relaksaciju potpuno dopiranog roditeljskog $Sr_{14}Cu_{24}O_{41}$ ($y = 0$) s potpuno razvijenim VGN. Slično ponašanje se vidi u obje polarizacije, $\mathbf{E}||c$ i $\mathbf{E}||a$, kao i kod $y = 0$. Također, srednje relaksacijsko vrijeme τ_0 ima usporediv iznos i temperaturno ponašanje duž c - i a -osi (Slika 8.12). [17, 2] Za razliku od $y = 0$, raspon temperatura u kojem smo uspjeli pratiti razvoj moda u $y = 0.55$ i 1.6 je vrlo uzak (Slika 8.12). Ipak, jasno je vidljiv sistematski trend ponašanja s dopiranjem. Intenzitet dielektrične relaksacije je malen (10^3 i 10^2



Slika 8.12 – Temperaturna ovisnost srednjeg relaksacijskog vremena τ_0 za $y = 0.55$ i 1.6 . Prazni krugovi označavaju podatke za $\mathbf{E}||c$, a puni za $\mathbf{E}||a$.

za $y = 0.55$ i 1.6 u tom redu) kad se uspoređi s $y = 0$ (10^4 na istim temperaturama). Još jedan zabrinjavajući problem je što zbog malih niskofrekventnih kapaciteta nije bilo moguće u pratiti njihovo nestajanje s grijanjem. Unatoč tome opažena slaba relaksacija se kvalitativno može povezati s uređenjem VGN tipa u ljestvicama koje je uspostavljeno samo na kratkim prostornim skalama u $y = 0.55$ i 1.6 , a potpuno je potisnuto kod $y = 3$ and 5.2 .

Na kraju prezentiramo prelaženje iz metalnog u izolatorsko ponašanje sa smanjenjem broja dopiranih šupljina (tj. povećavanjem y). Ovdje je ključna usporedba istosmjerne vodljivosti i one na 10 cm^{-1} na sobnoj temperaturi, gdje se vidi sljedeći zanimljiv efekt (Slika 8.8). Sobnotemperaturna vodljivost jasno pokazuje kako je metalni karakter transporta naboja u $y = 0$ (σ_{ac} blizak σ_{dc}), kako s postupnim porastom y raste razlika među σ_{ac} i σ_{dc} , te konačno kod $y = 3$ i 5.2 odgovara dielektricima. Teško je reći gdje točno počinje ta promjena budući da je kod $y = 0.55$ i 1.6 najviša temperatura mjerenja σ_{ac} 210 K odn. 250 K . Zbog toga treba imati na umu da su prave vrijednosti na sobnoj temperaturi zapravo više od onih sa Slike 8.8. Istosmjerna i zmjenična vodljivost bitno

se razlikuju za obje orijentacije kod $y \gtrsim 2$, tj. kad je ukupni broj šupljina manji od 4. Ispod oko 200 K možemo dati samo grube procjene budući da zbog mogućeg utjecaja fonona ili zapetog moda VGN više ne možemo pravilno procijeniti izmjeničnu vodljivost. Može se reći da omjer $\sigma_{ac}(10 \text{ cm}^{-1})/\sigma_{dc}$ raste za sve La/Y kako temperatura opada, što ukazuje na razvoj izolatorskog ponašanja.

8.2.3 Diskusija

Iz gornje analize može se zaključiti da jednodimenzionalni transport preskakivanjem duž lanaca kod $2 < y \leq 6$ (dopiranje šupljinama od 0 do 3 stavlja šupljine isključivo na lance) prelazi u kvazi-dvodimenzionalno vođenje naboja na ljestvicama pri manjim y . Ovaj zaključak podržavaju: slaba i temperaturno neovisna anizotropija vodljivosti (Slika 8.7) kod $0 \leq y \leq 1.6$; maksimum u $d(\ln \rho)/d(1/T)$ na otprilike around 210 K (Slika 8.6) koji se širi i postaje spljošteniji s porastom $y = 0$ na 1.6; manja aktivacijska energija na visokim temperaturama i viša na nižim temperaturama, razlika koja nestaje kod $y = 1.6$.

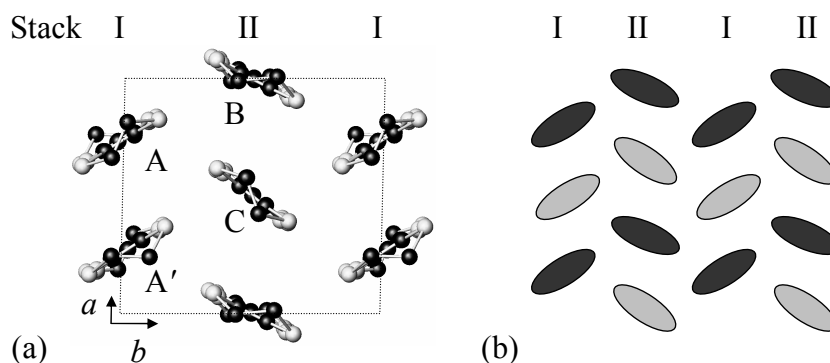
Ove rezultate možemo pripisati VGN ljestvica čije je dugodosežno uređenje u $y = 0$ (koherencijske duljine oko 260 Å) [16] uništeno s porastom y , no uređene domene preostaju na kraćim prostornim skalama sve do $y \approx 1.6$. zaista, slaba dielektrična relaksacija u radiofrekventnom području slična niskofrekventnu relaksaciju VGN. Porast vodljivosti ispod 20 cm^{-1} i iznos primjetno veći od dc vodljivosti govore o postojanju dodatnog pobuđenja negdje u mikrovalnom području. Primamljivo je pripisati ga zapetom modu VGN-a, no tada bi mu parametri (položaj, intenzitet, širina) trebali biti značajno drukčiji od onih za roditeljski spoj $y = 0$.

Nadalje, neutronske raspršenje i magnetska susceptibilnost govore da se s porastom y , $0 < y \leq 1$, također uništava i antiferomagnetsko dimersko uređenje u lancima. [201, 83, 202] Uz to NMR mjerenja relaksacije spin-rešetka razotkrila su da spinski procjep AF dimera preživljava sve do $y = 2$, [203] što znači da su antiferomagnetske i nabojne korelacije kod $y = 2$ (ukupni broj šupljina $n_h = 4$) dovoljno jake da stvaraju dinamičke, kratkoživuće domene AF dimera i s njima vezanog uređenja naboja. Shodno tome lanci prestaju biti preferirani kanal transporta i dolazi do početka transfera šupljina na ljestvice kad je ukupni broj šupljina 4 ili veći. Iako je na $y = 1.6$ vjerojatno na ljestvice prebačen tek mali udio šupljina, čini se da dominantni kanal vođenja postaju upravo ljestvice sudeći po opaženoj slaboj i temperaturno neovisnoj anizotropiji vodljivosti. Kod spoja s $y = 0.55$ očito je da je transport duž lanaca gotovo potpuno smrznut u

usporedbi s $y = 3$ zbog već gotovo potpuno razvijenih AF dimera i uređenja naboja. Transport ovdje u potpunosti preuzimaju ljestvice čije šupljine su bitno pokretljivije i doprinose velikom povećanju vodljivosti prema $y = 0$.

Stoga, dobiveni rezultati svi upućuju na to da ljestvice kod sadržaja La/Y $y \lesssim 2$ preuzimaju primat nad lancima kao vodljivi kanal. Naravno, prirodno je postaviti pitanje zašto se šupljine, koje se inače nalaze na lancima za sadržaj La/Y od $y = 6$ do $y \approx 2$, uopće počinju seliti i na ljestvice jednom kad njihov broj pređe 4 po formulskoj jedinki. Drugim riječima, čini se da je više od 4 šupljine po lancima energetski povoljno tek kad je barem malen udio šupljina istovremeno i na ljestvicama. Potpuno dopirani sustavi su već pokazali da postoji suptilna interakcija među lancima i ljestvicama koja utječe na stabilnost njihovih elektronskih osnovnih stanja: uređenje naboja s AF dimerima u lancima kao i VGN ljestvica na jednak način bivaju potisnuti. [204, 2] Ovi rezultati u poddopiranim sustavima dodatno utemeljuju ideju da je formiranje te dvije istovremeno prisutne elektronse faze međuzavisno i uvjetovano jedno drugim..

Kao konačni komentar, predloženi scenarij savršeno odgovara šupljinskoj raspodjeli koju predlažu Nücker *et al.* [14] kod $y = 0$, $Sr_{14}Cu_{24}O_{41}$: približno 5 šupljina po formulskoj jedinki je u lancima, a 1 na ljestvicama. Međutim, ova raspodjela ne može objasniti periodičnost vala gustoće naboja u ljestvicama. [16] Alternativnu raspodjelu s otprilike 3 šupljine po formulskoj jedinki u lancima i ljestvicama predlažu Rusydi *et al.*, [74] no ona susreće probleme u objašnjavanju uređenja na lancima kako se sadržaj La/Y spušta od $y = 3$ do $y = 0$, odn. kako se ukupni broj šupljina približava 6. Naime, postupno dopiranje šupljinama od 0 do 3 u ljestvicama bi dobro objasnilo formiranje VGN u ljestvicama i konačnu periodičnost kod $Sr_{14}Cu_{24}O_{41}$. Međutim, tada bi broj šupljina u lancima za $0 \leq y < 3$, trebao ostati praktički nepromjenjiv što se ne slaže s kratkodosežnim AF dimerskim uređenjem i dinamičkim domenama s uređenjem naboja u lancima koji se javljaju kod $y \approx 2$ i rastu kako sadržaj La/Y pada prema nuli. Ovakva bi raspodjela šupljina također proturječila mjerenoj magnetskoj susceptibilnosti po kojoj se broj spinova u lancima smanjuje sa spuštanjem y u rasponu $0 \leq y \leq 3$, što znači porast broja šupljina u lancima. [83, 202] Očito je da ovi donekle proturječni rezultati zahtijevaju dodatni eksperimentalni trud kako bi se stvorila samokonzistentna slika lanaca i ljestvica u $(La, Y, Sr, Ca)_{14}Cu_{24}O_{41}$.



Slika 8.13 – (a) Shematski prikaz donorskih slojeva u α -(BEDT-TTF) $_2$ I $_3$. Molekularna mjesta koja pripadaju nizu I označena su kao A, A', a nizu II kao B, C. (b) Raspored pruga u vodljivom ab sloju kod α -(BEDT-TTF) $_2$ I $_3$, u fazi uređenog naboja. Tamni i svijetli ovali redom označavaju molekule bogate i siromašne nabojem.

8.3 Uređenje naboja u α -(BEDT-TTF) $_2$ I $_3$

8.3.1 Uvod

Dok konvencionalni ($2k_F$) VGN znači periodički moduliranu gustoću naboja zbog interakcije između elektrona i fonona, $4k_F$ modulacija tipa Wignerovog kristala, često zvanom uređenjem naboja, potječe od jakog kulonskog odbijanja na jednom kristalnom mjestu U . Zbog toga se najčešće uređenje naboja smatra izmjenom lokaliziranih naboja različitih valencija u kristalnoj rešetki. Konkretno, čitavo bogatstvo uređenja naboja može se pronaći u organskim vodičima koje se može opisati kao jako anizotropne mreže interakcija, što uključuje poznate primjere kvazi-jednodimenzionalnih (TMTTF) $_2$ X (Ref. [241]), (DI-DCNQI) $_2$ Ag (Ref. [242]) te kvazi-dvodimenzionalnih vodiča baziranih na molekuli BEDT-TTF [bis(ethylenedithio)tetrathiafulvalene] kao što su θ -(BEDT-TTF) $_2$ RbZn(SCN) $_4$ i α -(BEDT-TTF) $_2$ I $_3$. [217] Istaknuta je činjenica da svi ti sustavi imaju četvrt-popunjene vrpce i zbog toga čak ni veliko istomjesno kulonsko odbijanje U u odnosu na preskakivanje t nije dovoljno da osnovno stanje pretvori iz metalnog u izolatorsko. Umjesto toga, kulonska interakcija između dva kristalna mjesta V je potrebna kako bi se stabilizirala faza nalik Wignerovom kristalu. [3] Iako svojstva uređenja naboja upućuju na potpunu lokalizaciju naboja u njihovom izmjeničnom uzorku, pojavljuju se teorijski radovi koji zahtijevaju drugačiju interpretaciju, naime, da uređenja naboja treba promatrati kroz delokaliziranu sliku nalik VGN, kao npr. kod θ -(BEDT-TTF) $_2$ X materials. [173]

α -(BEDT-TTF) $_2$ I $_3$, prvi organski materijal koji je pokazao dobra vodljiva svojstva u dvije dimenzije, [114] također je jedan od najpoznatijih primjera uređenja naboja među

dvodimenzionalnim organskim vodičima. Ovaj sustav pokazuje bogati fazni dijagram u tlaku i temperaturi s više intrigantnih kvantnih fenomena, od supravodljivosti, [113], uređenja naboja, [217] preko trajne fotovodljivosti, [243] fotoinduciranog faznog prijelaza, [244] i nelinearnog ultrabrzog optičkog odgovora, [220] do poluvodičkog ponašanja s nultim procjepom [245] i Diracovih stožaca tj. bezmasenih Diracovih fermiona. [246,247]

Triklinska kristalna struktura sastoji se od izmjeničnog slaganja izolacijskih anionskih slojeva (I_3^-) te vodljivih slojeva donorskih molekula (BEDT-TTF $^{0.5+}$ prosječne valencije). Molekule BEDT-TTF tvore strukturu koja podsjeća na uzorak riblje kosti i poredane su u trokutastu rešetku s dvije vrste nizova. Na sobnoj temperaturi niz I je slabo dimeriziran i sastoji se od dvije kristalografski ekvivalentna mjesta A i A', dok je niz II jednolik lanac od B i C molekula [vidi Sliku 8.13(a)]. Jedinичna ćelija stoga sadrži četiri molekule BEDT-TTF. Na visokim temperaturama sustav je polumetal s malim elektronskim i šupljinskim džepovima na Fermijevoj plohi. [24,23] Mala no opaziva disproporcijacija naboja postoji već na sobnoj temperaturi, što znači da se uređenje naboja razvija postepeno prema faznom prijelazu na temperaturi T_{CO} . [27,26]. Kao što nam govori nuklearna magnetska rezonancija [25] i sinkrotronska difrakcija X-zraka, [27] dugodosežno uređenje naboja se potpuno razvija ispod prijelaza iz metala u izolator na $T_{CO} = 136$ K. Na toj temperaturi vodljivost pada za nekoliko redova veličine i otvara se temperaturno ovisni procjep u naboju i spinu, što znači da je osnovno stanje izolatorsko i dijamagnetsko. Difrakcija X-zraka također ukazuje da dolazi do suptilnih strukturnih promjena na T_{CO} . Molekule se ne transliraju, no dolazi do promjene diedralnih kuteva (kuteva između molekula dva susjedna niza), što vodi do lomljenja inverzijske simetrije molekula A i A', i promjene prostorne grupe iz $P\bar{1}$ u P1. Ova promjena dozvoljava tzv. *twinning* u niskotemperaturnoj acentričnoj strukturi. Promjene diedralnih kuteva uzrokuju značajnu modulaciju integrala preklopa u ravnini BEDT-TTF. [27] Konačno, opažene su i molekularne deformacije u izvorištu disproporcijacije naboja. Procjenjuje se da je naboj na svakoj od molekula A, A', B i C $0.82(9)e$, $0.29(9)e$, $0.73(9)e$ i $0.26(9)e$ tim redom. Iznosi variraju od tehnike do tehnike budući da se NMR, vibracijska infracrvena i Ramanova spektroskopija te anomalno raspršenje X-zraka ne slažu savršeno u svojim procjenama, [25, 28, 118, 119, 29, 27] no neovisno o tome svi ti eksperimenti konzistentno govore da se uređenje naboja sastoji od tzv. "horizontalnih" pruga naboja građenih od nabojem siromašnih molekula, A' i C, te nabojem bogatih molekula, A i B, duž kristalografkse *b*-osi, kao što prikazuje Slika 8.13(b). Suprotno uvriježenom pogledu na uređenje naboja kao skup lokaliziranih naboja, raspršenje X-ray zraka daje naslutiti da je za ovaj sustav prikladnija slika delokaliziranih naboja, slična onoj VGN.

U prošlosti je bilo pokušaja da se nađu dokazi kolektivnog pobuđenja u α -(BEDT-TTF) $_2$ I $_3$. Prije više od petnaest godina preliminarna transportna mjerenja [117] su pokazala postojanje široke relaksacije u radiofrekventnom području s velikom dielektričnom konstantom reda 10^5 , kao i nelinearnu vodljivost ovisnu o polju (no i o uzorcima). Tada nije bilo moguće dati koherentni zaključak na osnovi tih rezultata, te je potrebno ponoviti eksperimente, s posebnom pažnjom na orijentaciji električnog polja u odnosu na osi kristala, kako bi se razjasnila elektrodinamika faze uređenog naboja. Dalje, nedavno je objavljeno da α -(BEDT-TTF) $_2$ I $_3$ pokazuje anizotropne oscilacije napona vezane uz nelinearnu vodljivost. [225] Takva pojava slična kolektivno klizanje vala gustoće naboja u kvazi-jednodimenzionalnim vodičima, [131] i time donosi još jedan razlog da se postavi pitanje sličnosti među konvencionalnim valovima gustoće i uređenja naboja u 2D sustavima. Tijekom izrade ovog rada također smo saznali i za nove infracrvene i Raman eksperimente u metalnoj i izolatorskoj fazi α -(BEDT-TTF) $_2$ I $_3$ koje su napravili Yue *et al.* [208]

Kao pokušaj razjašnjavanja otvorenih pitanja postavljenih gore, u ovom radu prikazani su rezultati elektrodinamičkog odgovora normalne i niskotemperaturne faze u slojnom organskom vodiču α -(BEDT-TTF) $_2$ I $_3$. Obavljena su opsežna optička mjerenja duž sva tri kristalografska smjera, kao i mjerenja anizotropije dc i ac vodljivosti unutar vodljivih ravnina, na pažljivo orijentiranim visokokvalitetnim monokristalima α -(BEDT-TTF) $_2$ I $_3$. Dobiveni rezultati pokazuju kompleksnu i anizotropnu disperziju u fazi uređenog naboja, za razliku od gotovo izotropnog i temperaturno neovisnog odziva na visokim temperaturama. Naglo uspostavljanje statičkog uređenja naboja ispod $T_{CO} = 136$ K is najavljuje cijepanje molekularnih vibracija $\nu_{27}(B_u)$ te dramatični pad optičke vodljivosti. Optička anizotropija se ne mijanja značajno, za razliku od anizotropije dc vodljivosti koja strmo raste s hlađenjem. Preraspodjela naboja opažena u uređenoj fazi dobro se slaže s procjenom iz difrakcije X-zraka. [27] Slično Peierlsovoj fazi VGN, opažamo dugovalna nabojna pobuđenja s anizotropnom disperzijom sličnom fazonskoj, koja se pokazuje kao široki zasjenjeni relaksacijski modovi duž a - i b -osi ravnina BEDT-TTF. Dodatno, opažamo i kratkovalna pobuđenja naboja u obliku parova domenskih zidova, opet duž obje osi, koji nastaju uslijed loma inverzijske simetrije. Domenski zidovi su slabo pokretljivi i stvaraju bitno slabiju polarizaciju od faznoskog odziva. Razmotrit ćemo moguće teorijske interpretacije, te dati argumente da je priroda horizontalnih pruga nabojnog uređenja zapravo kooperativni val gustoće naboja i veza umjesto potpuno lokaliziranog Wignerovog kristala.

8.3.2 Eksperimentalne metode i uzorci

Istosmjerna otpornost mjerena je između sobne temperature i 40 K standardnom četverokontaktnom tehnikom. U rasponu frekvencija 0.01 Hz–10 MHz spektri kompleksne dielektrične funkcije određeni su dvokontaktним mjerenjem kompleksne vodljivosti uz pomoć dva postava. Postav za niske frekvencije i visoke impedancije pokriva raspon 0.01 Hz – 3 kHz range. Izmjenični naponski signal primjenjuje se na uzorak, a strujni odgovor pretvara se u napon pomoću strujnog pretpojačala Stanford Research Systems SR570 te očitavan dvokanalnim digitalnim fazno-osjetljivim pojačalom Stanford Research Systems SR830. Na višim frekvencijama (40 Hz – 6 MHz) upotrebljen je analizator impedancija Agilent 4294A koji koristi metodu virtualne zemlje. Iako se Agilentom 4294A mogu doseći frekvencije do 110 MHz, duljina korištenih koaksijalnih kablova nas ograničava na otprilike 6 MHz. Naponski signali, tipično od 50 mV (1000 mV/cm), su provjereno unutar linearnog režima (gornja granica je barem 6000 mV/cm). U području preklapanja frekvencija ova dva postava mjerenja se dobro slažu. Budući da je u dielektričnim mjerenjima uvijek prisutan pozadinski doprinos parazitskih kapaciteta zbog kabela i konstrukcije nosača, u svrhu umanjivanja tih doprinosa sistematski je od svih mjerenja admitancije oduzeta admitancija otvorenog kruga (mjerenja u odsustvu uzorka). Pozadinski kapacitet našeg nosača jest oko 350 fF na svim mjerenim temperaturama. Dalje, na frekvencijama 10–10000 cm $^{-1}$ kompleksna je dielektrična funkcija određena Kramers-Kronigovom analizom temperaturno ovisne infracrvene reflektivnosti mjerene standardnom Fourier-transform spektroskopijom. [118]

Proučavani uzorci su plosnati ravninski monokristali visoke kvalitete. U pravilu je istaknuta ravna ploha uzoraka kristalografska *ab* ravnina. *c*-os kristala odgovara smjeru okomitom na ravninu uzorka. Mjerenja reflektivnosti obavljena su na plohama rasta kristala, dok je za mjerenja duž *c*-osi upotrebljen infracrveni mikroskop. Optička transmisija mjerena je na kristalima poliranima do otprilike debljive od 50 μ m.

Kontakti za mjerenje dc i ac vodljivosti izvedeni su primjenom ugljikove paste (polimerske paste s amorfnim česticama ugljika) izravno na površinu uzoraka. Na prvom proučavanom uzorku kontakti su pripremljeni paralelno bridu uzorka bez prethodne orijentacije. Tek je nakon obavljenih mjerenja ustanovljeno da je smjer kontakata odn. električnog polja paralelan $[1\bar{1}0]$ (dijagonalnom) smjeru, uz pomoć Laueove metode difrakcije X-zraka. U simulaciji difrakcijskih maksimuma korišten je program OrientExpress3.3 [239] Daljnji eksperimenti obavljeni su na igličastim uzorcima rezanim iz jedinstvenog monokristala koji je prethodno bio orijentiran infracrvenom spektroskopijom. Igličasti uzorci su rezani duž *a*- i *b*-osi što osigurava da je električno polje u

transportnim mjerenjima njima paralelno.

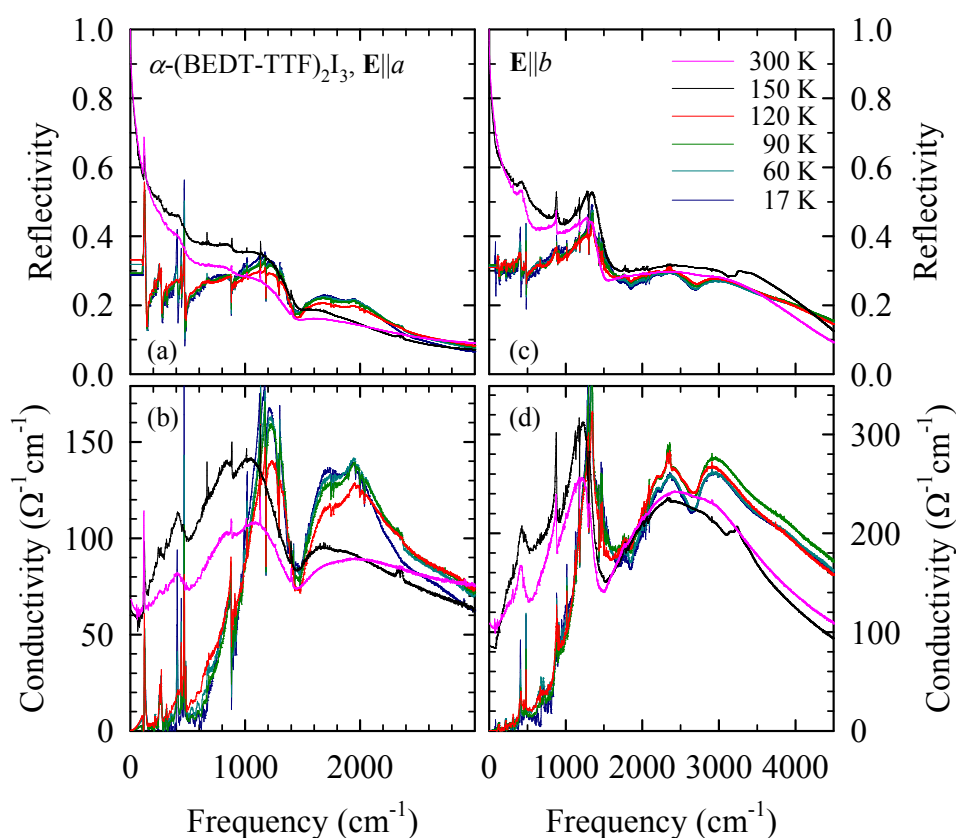
Pažljivo smo isključili bilo kakvu mogućnost ekstrinzičnih efekata u rezultatima dielektrične spektroskopije, pogotovo onih koji bi potjecali od kontaktnih otpora ili kapaciteta površinskog sloja uz materijal kontakta. Od dva detektirana dielektrična moda, manji je neovisan o temperaturi i zbog toga se može pripisati intrinzičnom odgovori uzoraka. S druge strane, svojstva većeg moda bi mogla potjecati od Maxwell-Wagnerove relaksacije na kontaktima [229] što zahtijeva detaljnu provjeru kvalitete kontakata. S tim na umu, obavljena su dc mjerenja u standardnim četvero- i dvokontaktne konfiguracijama. Kad se uzme u obzir razlika među tim dvjema geometrijama, četverokontaktne otpor se može skalirati i oduzeti od dvokontaktne u svrhu procjene kontaktnih otpora (R_c) u odnosu na otpor samog kristala (R_s). U izolatorskoj fazi omjer R_c/R_s postupno raste, od 0.1 tik pod prijelazom pa sve do reda 10 na temperaturama ispod 50 K. Mešutim, neovisno o omjeru R_c/R_s , intenzitet dielektričnog odgovora ostao je približno konstantan i konačan u izolatorskoj fazi, što dokazuje da je mjereni kapacitet dominantno određen intrinzičnim svojstvima uzoraka. Sumnja u kvalitetu dielektričnih spektara ostaje tek u blizini T_{CO} , te smo ih zbog toga odbacili.

8.3.3 Rezultati i analiza

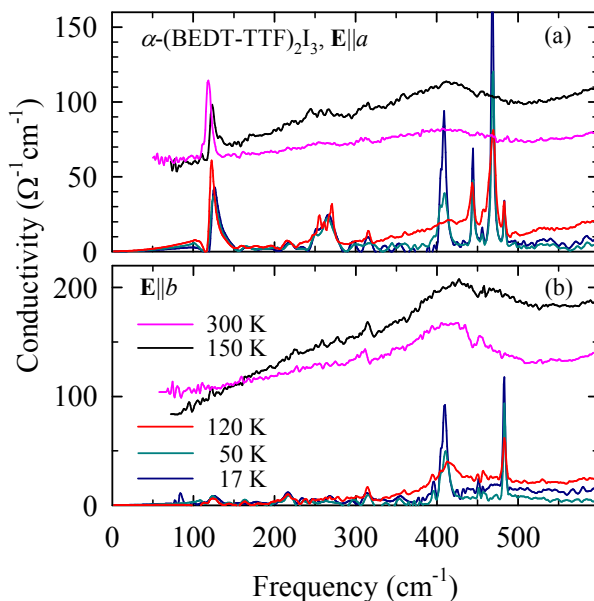
Optika

Usprkos mnogim izvještajima o optičkim svojstvima α -(BEDT-TTF) $_2$ I $_3$, [205, 206, 207, 209, 210, 211, 28, 117, 119, 212] vrijedi ponovo razmotriti neke aspekte tih svojstava tik ispod prijelaza u fazu uređenog naboja. Usredotočujemo se na dva problema. Prvi se tiče istraživanje vodljivosti i reflektivnosti dobro vodljive(ab) ravninena prijelazu iz metala u izolator, što će dati podatke o anizotropiji i energetsom procjepu. Drugi je problem preraspodjele naboja na različitim molekulskim mjestima, što se može pratiti kroz vibracijska svojstva tih različito deformiranih molekula i njihovu evoluciju tokom hlađenja. Vibracijska spektroskopija s polarizacijom $\mathbf{E} \parallel c$ jest najosjetljivija na uređenje naboja. [118, 124] Dodatno, ovdje ćemo predstaviti i diskutirati vibracijske značajke molekula BEDT-TTF u metalnom i izolatorskom stanju sa svjetlom polariziranim $\mathbf{E} \parallel a$ i b .

Elektronski doprinosi Eksperimentalno dostupan raspon frekvencija proteže se od 10 do 5000 cm^{-1} i pokriva vrpce koje tvore prekrivajuće orbitale susjednih molekula. Slika 8.14 pokazuje optička svojstva za dvije polarizacije $\mathbf{E} \parallel a$ i $\mathbf{E} \parallel b$ u dobro vodljivoj



Slika 8.14 – Optička svojstva α -(BEDT-TTF) $_2$ I $_3$ na naznačenim svojstvima. Gornji paneli (a) i (c) pokazuju reflektivnost, a donji (b) i (d) odgovarajuće vodljivosti. Treba svratiti pažnju na različite vertikalne skale. Na lijevoj strani (a) i (b) dani su podaci za električno polje duž molekulskih nizova ($\mathbf{E} \parallel a$); paneli zdesna prikazuju podatke za polje okomito na nizove ($\mathbf{E} \parallel b$).

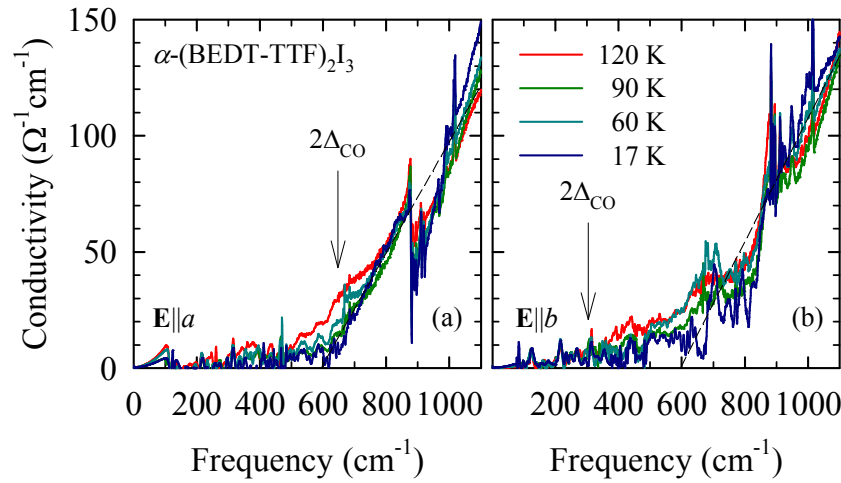


Slika 8.15 – Vodljivost u dalekom infracrvenom području za (a) $\mathbf{E} \parallel a$ i (b) $\mathbf{E} \parallel b$ na različitim temperaturama ispod i iznad faznog prijelaza na $T_{CO} = 136$ K.

ravnini na temperaturama ispod i iznad T_{CO} . Optičkim spektrima dominira široka vrpca u srednjem infracrvenom području koja se za dva smjera po intenzitetu razlikuje za otprilike faktor 2. Detalj u $R(\omega)$ koji izvira kao naglašeni pad u vodljivosti na oko 1450 cm^{-1} potječe od jakog elektronsko-vibracijskog vezanja (eng. electron-molecular vibrational coupling, emv) $\nu_3(A_g)$ moda. [118]

Iako reflektivnost pokazuje metalni odziv na sobnoj temperaturi, koji vodi konačnoj vodljivosti, nema Drudeovog odziva kvazi-slobodnih nosioca koji bi se odvajao od krila vrpce u srednjem infracrvenom području [Slike 8.14(b), (d) i 8.15]. Shodno tome, temperaturno slaba istosmjerna vodljivost iznad faznog prijelaza je opisana pregušenim Drudeovim odzivom. Tajima *et al.* [248] predlažu da je α -(BEDT-TTF) $_2$ I $_3$ polumetal na sobnoj temperaturi, što bi objasnilo nekonvencionalni optički odaziv. Izostanak dobro definiranog Drudeovog vrha u blizini prijelaza uređenja naboja podsjeća na ponašanje izolatora s uređenjem naboja θ -(BEDT-TTF) $_2$ RbZn(SCN) $_4$. [214] Treba reći da ostale α -faze iz obitelji BEDT-TTF, poput α -(BEDT-TTF) $_2$ MHg(SCN) $_4$, [215] ipak pokazuju vrh na nultoj energiji. Ovi optički podaci daju niskofrekventnu anizotropiju otprilike $\sigma_b/\sigma_a \approx 2$ što je konzistentno s dielektričnim i dc mjerenjima (Slike 8.18 i 8.21).

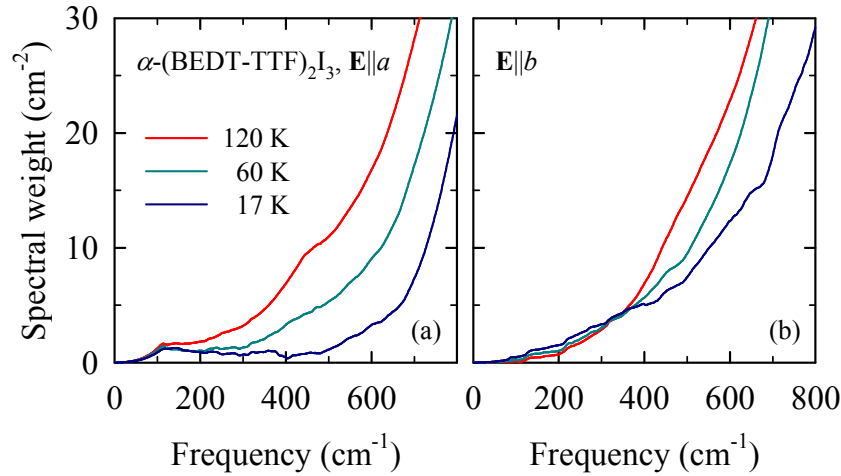
Sa spuštanjem temperature od 300 K prema T_{CO} , reflektivnost lagano raste zbog smanjenog fononskog raspršenja. U fazi uređenog naboja reflektivnost u dalekom infracrvenom području dramatično pada dok se odgovarajuća vodljivost smanjuje uslijed otvaranja energetskog procjepa (Slika 8.15). Spektralna težina se pomiče u srednje in-



Slika 8.16 – Temperaturna ovisnost optičke vodljivosti u α -(BEDT-TTF) $_2$ I $_3$ za $T < T_{CO}$ s polarizacijama (a) $\mathbf{E} \parallel a$ i (b) $\mathbf{E} \parallel b$. Kako bi se pokazao razvoj procjepa nabojnog uređenja, fononske linije su oduzete od prikazanih podataka. Crtkane linije su linearne ekstrapolacije koje daju optički procjep od otprilike 600 cm^{-1} . Strelice označavaju procjep u istosmjernom transportu.

fracrveno područje, gdje se nakuplja oko vrpce s maksimumima na 1500 cm^{-1} za $\mathbf{E} \parallel a$ (paralelno nizovima) i 2000 cm^{-1} za $\mathbf{E} \parallel b$ (okomito na nizove). Kad se zasjenjenje vodljivih nosioca naboja smanji na $T < T_{CO}$, antirezonance Fanovog oblika u vodljivosti, koje nastaju zbog emv-vezanih molekulskih vibracija, postaju još istaknutije i dijele vrhove u srednjem infracrvenom području. Elektronski dio spektara može se usporediti s računima u proširenom Hubbardovom modelu za četvrt-popunjenu kvadratnu rešetku [216] koji predviđaju vrpcu s maksimumom na otprilike $6t$ u izolatorskoj fazi s uređenim nabojem, što daje $t_a = 0.03 \text{ eV}$ i $t_b = 0.04 \text{ eV}$ za odgovarajuće smjerove. Ove su vrijednosti suglasne s Hückel-računima koje su proveli Mori *et al.* [23] i pslažu se s opaženom anizotropijom transporta i optike.

Na faznom prileazu između metala i izolatora vidimo naglo otvaranje optičkog procjepa, pri čemu vodljivost u pregušenoj Drudeovoj regiji opada na veoma niske vrijednosti, kao što prikazuje Slika 8.15. Kako bismo jasnije prikazali niskotemperaturno elektronsko ponašanje, na vibracijska su svojstva prilagođene Lorentzove i Fanoove krivulje koje su zatim oduzete od mjerenih podataka. Rezultati za obje polarizacije daje Slika 8.16 na različitim temperaturama. Pad $\sigma(\omega)$ ispod 1000 cm^{-1} može biti linearno ekstrapoliran kako bi se dobila vrijednost procjepa $2\Delta_0 \approx 600 \text{ cm}^{-1}$ na $T \rightarrow 0$, što odgovara 75 meV , za obje polarizacije. Treba spomenuti da vodljivost za $\mathbf{E} \parallel b$ ostaje konačna iznad do 400 cm^{-1} , iako je vodljivost $\mathbf{E} \parallel a$ bliska nuli na frekvencijama ispod 600 cm^{-1} . Zbog toga, uzimanjem u obzir frekvencija samo do 800 cm^{-1} možemo

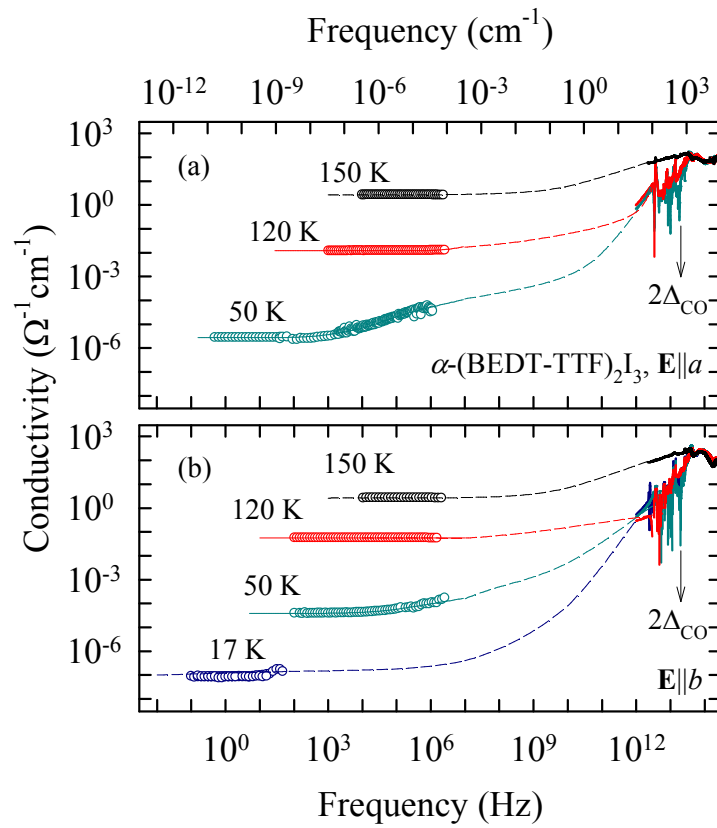


Slika 8.17 – Razvoj spektralne težine $SW(\omega_c)$ u ovisnosti o gornjoj *cut-off* frekvenciji ω_c , koja se računa kao $SW(\omega_c) = 8 \int_0^{\omega_c} \sigma_1(\omega) d\omega = \omega_p^2 = 4\pi n e^2 / m$ za oba smjera ravnina α -(BEDT-TTF) $_2$ I $_3$.

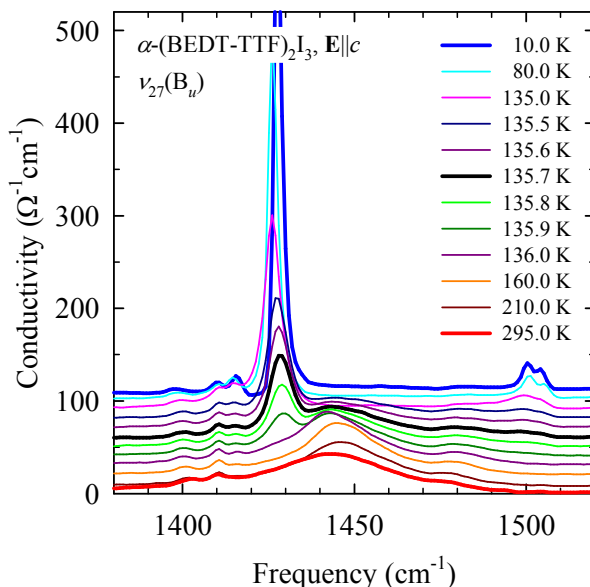
linearnom ekstrapolacijom dobiti procjepe od 600 i 400 cm^{-1} što dobro odgovara dc transportnim procjepima (vidi Sliku 8.21).

Na $T < T_{CO}$ spektralna težina se još uvijek miče iz područja procjepa prema višim frekvencijama kako se T spušta: nakuplja se oko 1000 cm^{-1} i više (Slika 8.17). Interesantno je za opaziti kako ne samo da se područje procjepa mijenja, već se i spektralna težina u cijelom području miče prema višim frekvencijama. Pomicanje maksimuma vrpce u srednjem infracrvenom području može se djelomice pripisati termalnoj kontrakciji, no dominantno preraspodjeli spektralne težine.

Slika 8.18 prikazuje spektre vodljivosti u širokom frekventnom pojasu od istosmjerne granice, preko dielektričnih i optičkih mjerenja za $\mathbf{E} \parallel a$ i b na raznim temperaturama. Optička vodljivost je pregušenog Drudeovog tipa u metalnoj fazi i odgovara vrijednostima u istosmjernoj granici. Porast anizotropije na niskim temperaturama, vrlo očit u istosmjernoj granici, ne vidi se jasno u optičkim podacima [Slika 8.14, (b) i (d)]. Čim sustav uđe u fazu uređenog naboja, niskofrekventna vodljivost značajno pada što vodi do stepenice u radiofrekventnom području. Širok i jako temperaturno ovisnan relaksacijski mod, inače opažan u VGN fazama, jasno se vidi u spektrima imaginarnog dijela dielektrične funkcije (Slika 8.23). Slijedi ga disperzija po zakonu potencije koju pripisujemo transportu preskakivanjem, što vodi do visoke vodljivosti u mikrovalnom i dalekom infracrvenom području. U mikrovalnom području najznačajnija je osobina kontinuiran porast vodljivosti s frekvencijom, dok je u infracrvenom području značajno potiskivanje Drudeove težine ispod procjepa nabojnog uređenja i jačih fononskih potpisa. Takvo je ponašanje slično onom u potpuno dopiranim ljestvicama $(\text{Sr,Ca})_{14}\text{Cu}_{24}\text{O}_{41}$ kuprata



Slika 8.18 – Širokopolasni spektri vodljivosti α -(BEDT-TTF) $_2$ I $_3$ za (a) $\mathbf{E} \parallel a$ i (b) parallel b na nekoliko odabranih temperatura. Okomite strelice pokazuju procjep uređenja naboja. Crtkane linije vode oko.

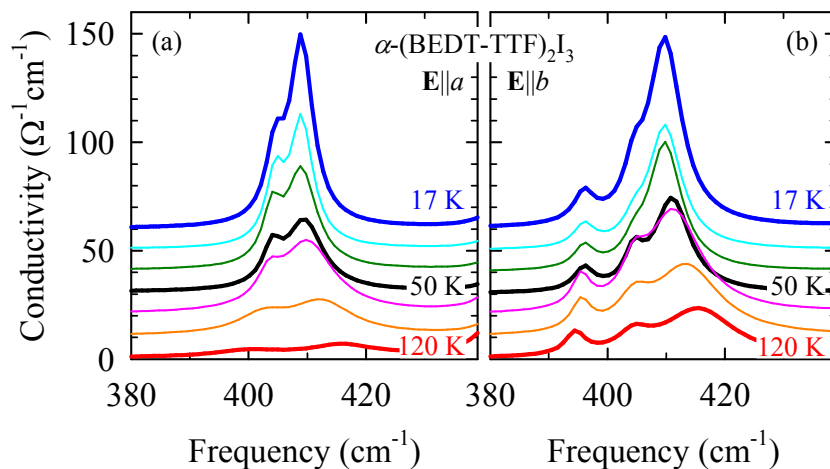


Slika 8.19 – Temperaturna ovisnost intramolekularnih vibracija BEDT-TTF mjerena u okomitom smjeru $\mathbf{E} \parallel c$. Krivulje različitih temperatura pomaknute su za $10 (\Omega\text{cm})^{-1}$ jasnoće radi. Mod ν_{27} postaje veoma naglašen odmah ispod faznog prijelaza ($T = 295$, 210, 160, **136.0**, 135.9, 135.8, **135.7**, 135.6, 135.5, **135.0**, 80, i **10** K).

u kojima dolazi do uspostavljanja VGN. S druge strane, dc i optičke vodljivosti kod BaVS $_3$ su usporedivih iznosa, a i tamo je opažen svojevrsan VGN. [34] Ovakvom usporedbom BaVS $_3$ možemo klasificirati među potpuno uređene sustave, dok ljestvice i α -(BEDT-TTF) $_2$ I $_3$ pokazuju svojstva koja pripadaju neuređenim sustavima.

Vibracijska svojstva

razvoj uređenja naboja pratili smo preko IR-aktivnog $\nu_{27}(B_u)$ moda osjetljivog na količinu naboja na molekuli mjerenjima okomitim na vodljivu ravninu. Radi se o vibracijskom modu u kojem C=C dvostruke veze u prstenovima BEDT-TTF titraju suprotno u fazi, što vodi do dipolnog momenta paralelno s dugom osi molekule. Frekvencija tog moda je osjetljiv na ukupni naboj molekule i poznato je da se cijepa s faznim prijelazom uređenja naboja. [28, 124] U metalnoj fazi ($T > T_{CO}$) opažamo široku vrpce na otprilike 1445 cm^{-1} ; ta frekvencija odgovara naboju od $+0.5e$ po molekuli. U izolatorskoj fazi taj se mod cijepa na dva para vrpce smještenih na 1415 i 1428 cm^{-1} , te na 1500 i 1505 cm^{-1} , kao što prikazuje Slika 8.19. Vrpce na nižim frekvencijama odgovaraju otprilike naboju $+0.8e$ i $+0.85e$ po molekuli, dok dva viša odgovaraju $+0.2e$ i $+0.15e$. Ova redistribucija naboja slaže se s procjenom anomalnog raspršenja X-zraka na četiri nezavisna molekulska mjesta u jediničnoj ćeliji. [27] Do disproporcijacije naboja dolazi naglo na



Slika 8.20 – Temperaturna ovisnost intramolekulskih vibracija $\nu_{14}(A_g)$ u molekulama BEDT-TTF. Krivulje različitih temperatura pomaknute su za $10 (\Omega\text{cm})^{-1}$ jasnoće radi. U polarizacijama (a) $\mathbf{E} \parallel a$ i (b) $\mathbf{E} \parallel b$, intenzitet moda ν_{14} raste, i mod se cijepa u tri odvojena vrha ($T = 120, 90, 60, 50, 40, 30,$ and 17 K).

$T_{\text{CO}} = 136$ K, te ostaje stalna s hlađenjem. Za razliku od oštrog statičkog uređenja naboja koje pratimo kroz $\nu_{27}(B_u)$ i koje se ne mijenja više s hlađenjem ispod faznog prijelaza, ipak opažamo promjene u procjepu i nekim emv-vezanim značajkama kroz hlađenje u izolatorskoj fazi. U podrulu otvaranja procjepa ($T < T_{\text{CO}}$), vodljivost nastavlja padati i doseže praktičnu nulu tek na najnižoj dosegnutoj temperaturi ($T = 17$ K). Npr. na $T = 120$ K konačna vodljivost postoji iznad 200 cm^{-1} , čak i niže, u skladu s prethodnim mikrovalnim mjerenjima. [117, 212] Opaženo razvijanje i promjene u fazi uređenog naboja slažu se sa strukturnim podacima [27] i istosmjerenom vodljivošću.

Vratimo se na vibracijska svojstva; za \mathbf{E} duž a - i b -osi opažamo promjene u obliku nekih modova na prijelazu iz metala u izolator. Zbog zasjenjenja ne vide se molekulske vibracije u metalnoj fazi. Ispod T_{CO} , modovi u spektrima unutar vodljive ravnine su potpuno simetrične vibracije molekula BEDT-TTF emv-vezane s elektronskim prijelazom disproporcionacije naboja, koji su opaženi i dodijeljeni ranije [206] sve do 300 cm^{-1} . Kao rezultat interakcije s elektronskim prijelazom imaju karakteristični Fano-oblik: [213] pojavljuju se kao antirezonancije na frekvencijama koje odgovaraju elektronskim pobuđenjima, te kao asimetrični vrhovi gdje su elektronski modovi rascijepljeni. Zbog tih efekata npr. $A_g(\nu_3)$ i nekoliko simetričnih i asimetričnih vibracija CH_3 [206] na otprilike 1400 cm^{-1} pokazuju ne samo plavi pomak s vrpcom prijenosa naboja u srednjem infra-crvenom području, već i promjenu oblika u usku i asimetričnu vrpcu (Slika 8.14). I dok su modovi nižih frekvencijama slabo vidljivi u metalnoj fazi, u izolatorskoj fazi opažamo sve A_g vibracije koje predviđaju Meneghetti *et al.* [206] (Slika 8.15): npr. mod $\nu_{15}(A_g)$

na 260 cm^{-1} (vezan uz deformaciju vanjskih EDT prstenova), $\nu_{16}(A_g)$ na 124 cm^{-1} (deformacija unutarnjih TTF prstenova). Ove su vrce vrlo jako samo za $\mathbf{E} \parallel a$, a jedva vidljive duž b -osi, što se dobro slaže s prisutnim lomovima simetrije, tj. dimerizacijom duž nizova (a -osi) i pruga koje se formiraju duž b -osi u fazi uređenog naboja kao što prikazuje Slika 8.13(b).

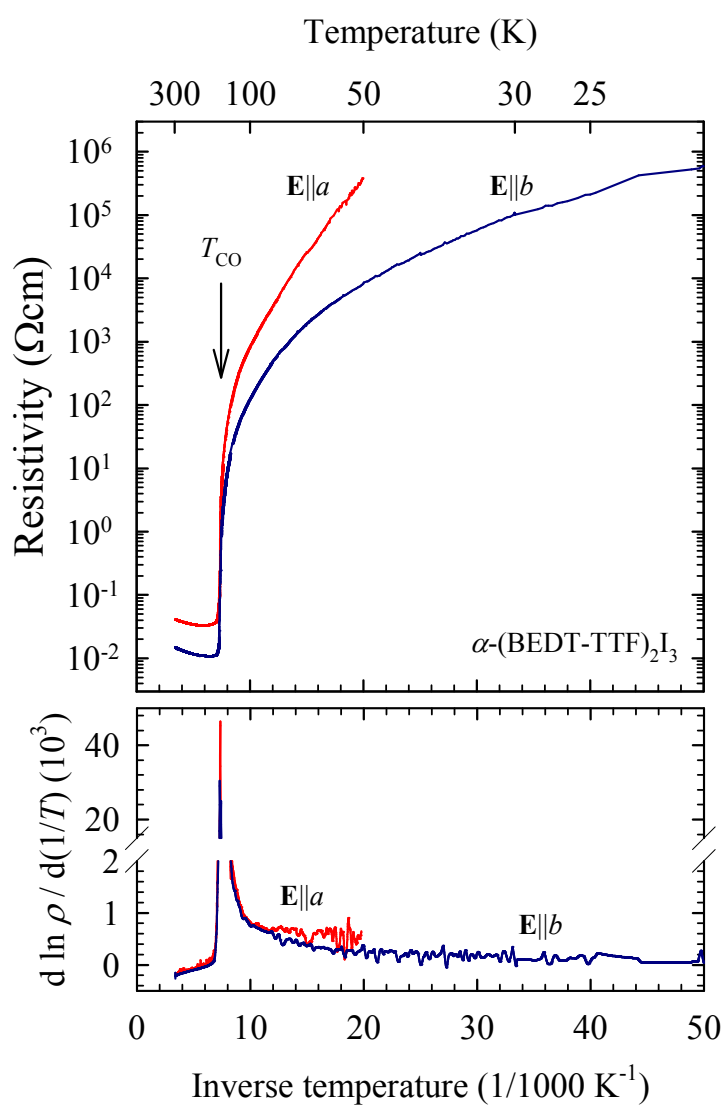
Zanimljivo je da se samo mod na 410 cm^{-1} (Slika 8.20) mijenja s hlađenjem u izolatorskoj fazi. Vrpca je mnogo šira nego ostale značajke na tim frekvencijama tik ispod prijelaza i nastavlja se sužavati s padom temperature. Prema Meneghettiju, *et al.* [206] ovaj mod dodjeljujemo $\nu_{14}(A_g)$ koji se uglavnom tiče deformacija vanjskih prstenova.

Konačno, jake vibracijske oblike oko 1300 cm^{-1} (nije prikazano) dodjeljujemo emv-vezanom $\nu_4(A_g)$ modu molekule BEDT-TTF. Oštiji je i naglašeniji za $\mathbf{E} \parallel a$, iako je ukupna vodljivost u srednjem infracrvenom području otprilike pola one za $\mathbf{E} \parallel b$. Ispod 1000 cm^{-1} javlja se velik broj molekulskih vibracija i vibracija rešetke čim se izgubi zasjenjenje elektronima.

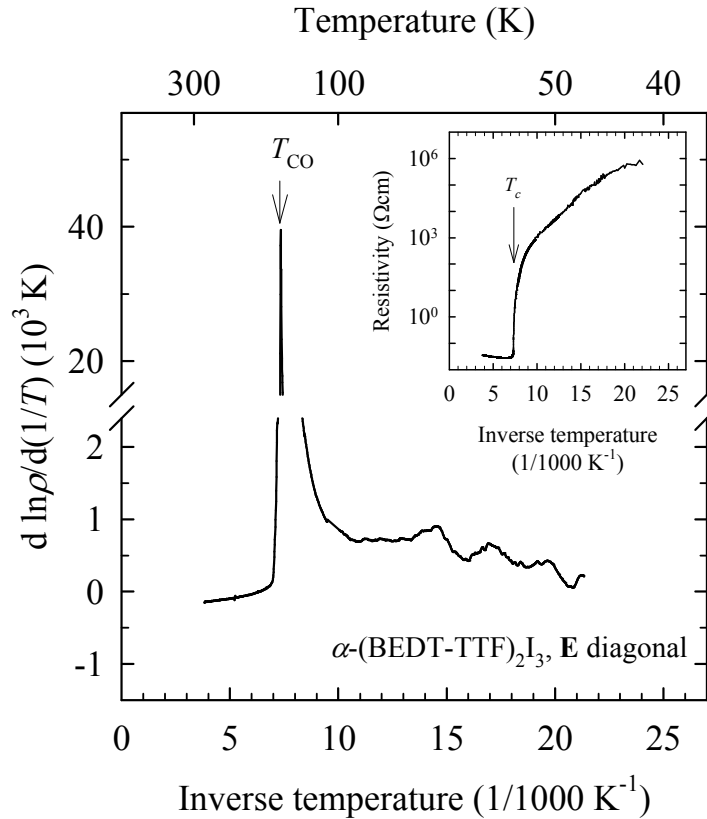
Transport

Mjerenja transporta otkrivaju da mala anizotropija dc otpornosti na sobnoj temperaturi, [114] $\rho_a/\rho_b \approx 2$, opstaje u cijelom metalnom režimu i približno je konstantna sve do T_{CO} . Kao novi rezultat dobili smo da anizotropija otpornosti tj. vodljivosti u izolatorskoj fazi značajno evoluirala s temperaturom budući da otpor duž a -osi raste bitno brže s hlađenjem nego duž b -osi: na 50 K anizotropija doseže vrijednost $\rho_a/\rho_b = 50$ (Slika 8.21). Slična anizotropija vodljivosti također je opažena u fazi uređenja naboja kvazi-jednodimenzionalnog (TMTTF) $_2$ AsF $_6$. [218] Za naše uzorke možemo unatoč temperaturno ovisnoj aktivaciji procijeniti anizotropni transportni procjep u fazi uređenog naboja za obje polarizacije, $2\Delta = 80\text{ meV}$ and 40 meV za redom $\mathbf{E} \parallel a$ i $\mathbf{E} \parallel b$. Na prvi pogled anizotropni transportni procjep ne slaže se s izotropnim optičkim procjepom (Slika 8.16). No, dobro je poznato da sustavi sa složenom strukturom vrpca kao npr. α -(BEDT-TTF) $_2$ I $_3$ mogu pokazivati vrlo različite optičke i transportne procjepe: optička mjerenja ispituju direktne prijelaze između valentne i vodljive vrpce dok transport gleda prijelaze s najmanjom energetsom razlikom između dvije vrpce.

Također smo karakterizirali dc otpornost u ab ravnini za tzv. dijagonalni smjer, $\mathbf{E} \parallel [1\bar{1}0]$, pod kutem od otprilike 45° na kristalografske osi. Metalno ponašanje otpora prisutno je od sobne temperature sve do 156 K . Oštar prijelaz u izolatorsku fazu [117] potvrđen je na $T_{CO} = 136.2\text{ K}$, vidljivo u vrhu $d(\ln \rho)/d(1/T)$ s punom širinom na



Slika 8.21 – Otpornost (gornji panel) i logaritamska derivacija otpora (donji panel) α -(BEDT-TTF) $_2$ I $_3$ u ovisnosti o inverznoj temperaturi za $\mathbf{E} || a$ (crvena linija) i $\mathbf{E} || b$ (plava linija).



Slika 8.22 – Logaritamska derivacija otpornosti (glavna slika) i otpornost (umetak) u ovisnosti o inverznoj temperaturi za α -(BEDT-TTF) $_2$ I $_3$ s s električnim poljem $\mathbf{E} \parallel [1\bar{1}0]$.

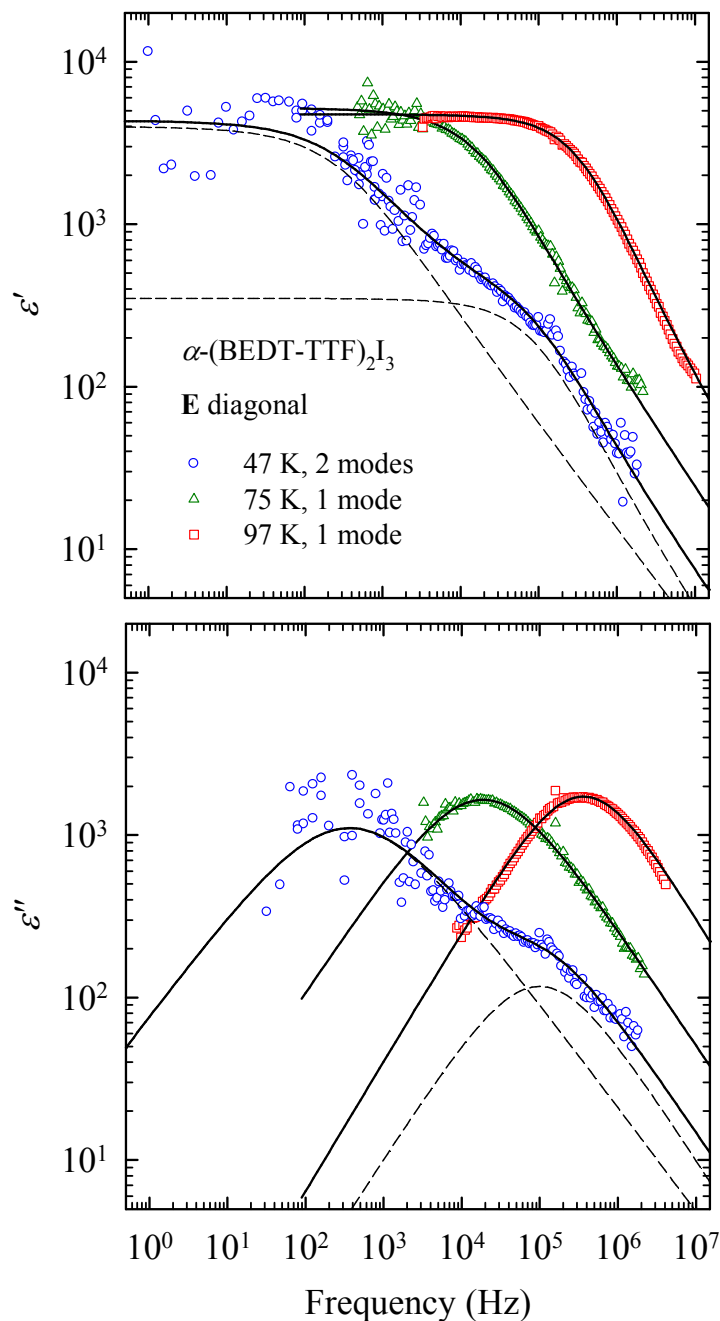
polovici visine $2\delta T_{CO} = 1.5 \text{ K}$; $2\delta T_{CO}/T_{CO} = 0.011$ (Slika 8.22). Ispod prijelaza otporna krivulja raste s temperaturno ovisnom aktivacijom od otprilike 80 meV . Nema značajne histereze u dc otpornosti blizu T_{CO} .

Dielektrični odgovor

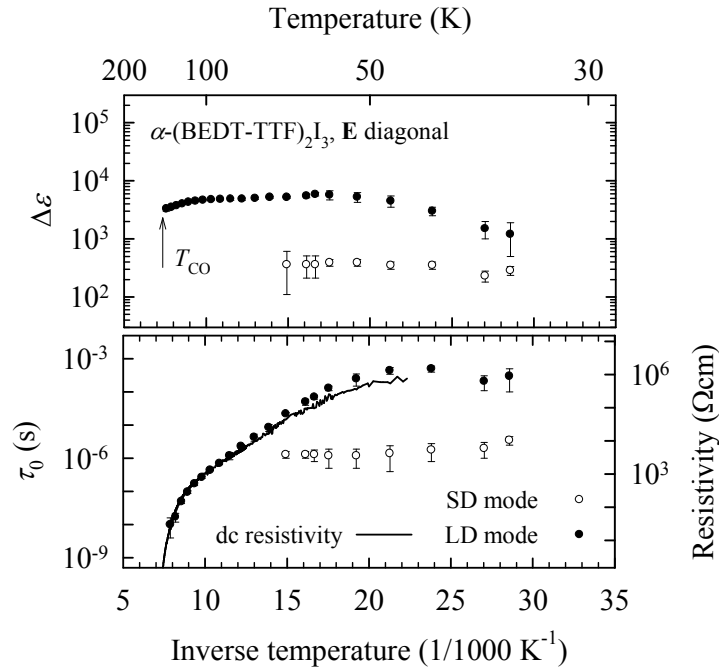
Mjerenja niskofrekventnih dielektričnih spektara obavljena su na čitavom rasponu od najnižih temperatura do faznog prijelaza. Reprezentativne spektre za $\mathbf{E} \parallel [1\bar{1}0]$ prikazuje Slika 8.23. Najvažnije, između 35 K sve do 75 K razlučujemo dva relaksacijska moda. Kompleksni dielektrični spektri $\varepsilon(\omega)$ mogu se opisati kao suma dvije generalizirane Debyeve funkcije

$$\varepsilon(\omega) - \varepsilon_\infty = \frac{\Delta\varepsilon_{LD}}{1 + (i\omega\tau_{0,LD})^{1-\alpha_{LD}}} + \frac{\Delta\varepsilon_{SD}}{1 + (i\omega\tau_{0,SD})^{1-\alpha_{SD}}} \quad (8.3)$$

gdje je ε_∞ visokofrekventna dielektrična konstanta, $\Delta\varepsilon$ dielektrični intenzitet relaksacije, τ_0 srednje relaksacijsko vrijeme i $1 - \alpha$ parametar simetričnog proširenja distribucije



Slika 8.23 – Dvostruki logaritamski prikaz frekventne ovisnosti realnog (ϵ') i imaginarnog (ϵ'') dijela dielektrične funkcije α -(BEDT-TTF) $_2$ I $_3$ na reprezentativnim temperaturama za $\mathbf{E} \parallel [1\bar{1}0]$. Ispod 75 K vide se dva relaksacijska moda – pune linije za 47 K prikazuju prilagodbu na sumu dvije generalizirane Debyeve funkcije; crtkana linija predstavlja doprinose dva moda. Iznad 75 K detektiramo samo jedan mod i puna linija predstavlja fit na jednu generaliziranu Debyeovu funkciju.

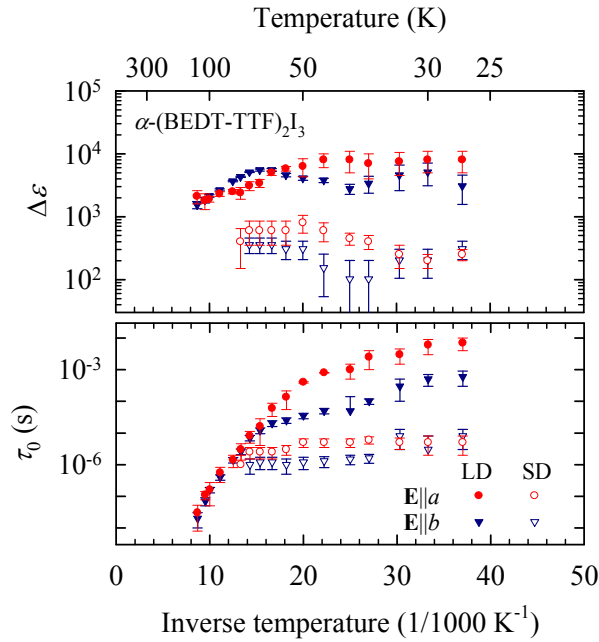


Slika 8.24 – Dielektrični intenzitet (gornji panel) i srednje relaksacijsko vrijeme s istosmjernom otpornošću (donji panel, točke i linija tim redom) u α -(BEDT-TTF) $_2$ I $_3$ kao funkcija inverzne temperature za $\mathbf{E} \parallel [1\bar{1}0]$.

relaksacijskih vremenaza mali (eng. large, LD) i mali (eng. small, SD) dielektrični mod. Parametar širenja $1 - \alpha$ oba moda je 0.70 ± 0.05 . Temperaturna ovisnost dielektričnog intenziteta i srednjih relaksacijskih vremena prikazuje Slika 8.24. Dielektrični intenzitet oba moda praktički ne ovisi o temperaturi ($\Delta\epsilon_{LD} \approx 5000$, $\Delta\epsilon_{SD} \approx 400$). Na približno 75 K veliki dielektrični mod preklapa mali mod. Nije jasno nestaje li mali mod na toj temperaturi ili je smao prekriven velikim. No, iznad 100 K, temperaturi na kojoj se veliki dielektrični mod miče na dovoljno visoke frekvencije, nema indikacija malog moda u rasponu 10^5 – 10^6 Hz. Zbog toga su iznad 75 K vršene prilagodbe samo na jednu Debyeovu funkciju koju povezujemo s velikim modom. Svi se parametri velikog moda mogu dobiti prilagodbom sve dok ne izađe van našeg frekventnog prozor na otprilike 130 K. Na temperaturama do 135 K (upravo ispod $T_{CO} = 136$ K) možemo razlučiti samo intenzitet dielektrične relaksacije velikog moda mjerenjem kapaciteta na 1 MHz.

Anizotropija

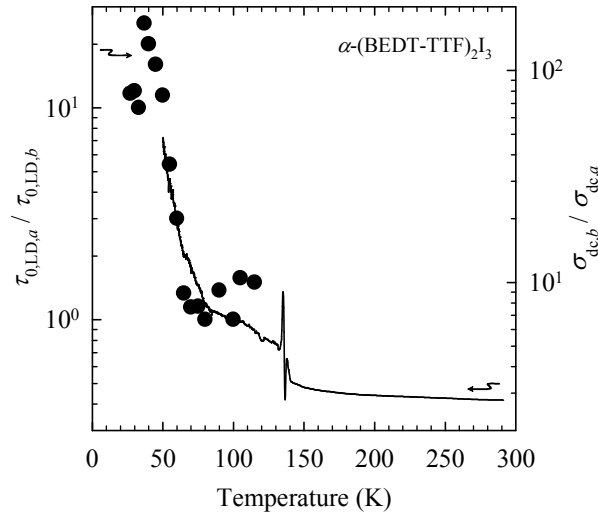
Jedan od najintragantnijih rezultata za električno polje u dijagonalnom smjeru je temperaturno ponašanje srednjeg relaksacijskog vremena koje se uvelike razlikuje među dva dielektrična moda. Veliki dielektrični mod slijedi termalno aktivirano ponašanje



Slika 8.25 – Dielektrični intenzitet (gornji panel) i srednje relaksacijsko vrijeme (donji panel) u α -(BEDT-TTF) $_2$ I $_3$ kao funkcija inverzne temperature; puni i prazni simboli redom označavaju parametre velikog i malog moda za \mathbf{E} duž a - (crveni krugovi) i b -osi (plavi trokuti). Uspoređeno sa Slikom 8.24, velika nepouzdanost podataka dolazi od nepovoljne geometrije uzoraka, koja je nužna za pravilnu orijentaciju električnog polja no donosi visoke otpore i veoma niski kapacitivni odziv.

proporcionalno dc otpornosti, dok je mali mod praktički neovisan o temperaturi. Ovo neočekivano i novo ponašanje faze uređenog naboja postavlja pitanje anizotropije dielektričnog odziva. S tim na umu obavljen je dodatan skup mjerenja na igličastim uzorcima orijentiranim duž a - i b -axis.

Niskofrekventna dielektrična spektroskopija za $\mathbf{E}||a$ i $\mathbf{E}||b$ daje rezultate koji su usporedivi s $\mathbf{E} || [1\bar{1}0]$: cveliki mod čije srednje relaksacijsko vrijeme slijedi istosmjernu otpornost, te mali temperaturno neovisni mod vidljiv ispod $T \approx 75$ K. Parametre prilagodbe na model (8.3) prikazuje Slika 8.25 u ovisnosti o inverznoj temperaturi. Nema naglašene anizotropije ili temperaturne ovisnosti intenziteta odziva, i očito vrijednosti $\Delta\epsilon$ velikog i malog moda odgovaraju onima za \mathbf{E} u dijagonalnoj orijentaciji. No, očit je jasni razvoj anizotropije u $\tau_{0,LD}$. Slika 8.26 pokazuje da ova novonađena anizotropija u $\tau_{0,LD}$ vrlo blisko slijedi anizotropiju istosmjerne vodljivosti.



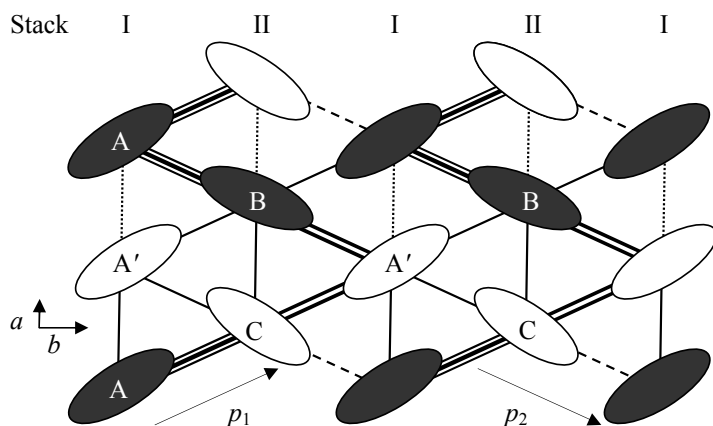
Slika 8.26 – Anizotropija srednjeg relaksacijskog vremena velikod dielektričnog moda α -(BEDT-TTF) $_2$ I $_3$ (točke) slijedi temperaturno ponašanje anizotropije istosmjerne vodljivosti (linija).

8.3.4 Diskusija

Optička ispitivanja u visokofrekventnom dijelu spektra pokazuju dvodimenzionalni sustav koji je dobro opisan proširenim Hubbardovim modelom. U fazi uređenja naboja opažamo nove procese an niskim frekvencijama, poglavito odziv koji podsjeća na VGN. Optički procjep je približno izotropan (kao što je rečeno gore, čini se da su za $\mathbf{E} \parallel b$ moguća pobuđenja i na nižim frekvencijama), u kontrastu s naglašenom anizotropijom u istosmjernom transportu in contrast to the pronounced anisotropy of the dc gap, što objašnjavamo time da optika i transport ispituju različite prijelaze. Vibracijski spektri otkrivaju da do statičkog uređenja naboja dolazi naglo odmah ispod faznog prijelaza (Slika 8.19) i da je popraćen odgovarajućim optičkim promjenama u vodljivoj ravnini. Iznenadujuće i zanimljivo je da optički procjep i neki od vibracijskih oblika vezanih za vanjski prsten BEDT-TTF pokazuju kontinuirani razvoj s hlađenjem kroz izolatorsku fazu, što bi značilo da ipak dolazi do postupnih promjena (no ne i preraspodjele naboja) u izolatorskoj fazi.

Opažena niskofrekventna anizotropija pokazuje složenu anizotropnu disperziju u fazi uređenog stanja. Prvo, slično Peierlsovom VGN, vidimo široku zasjenjenju relaksaciju (veliki dielektrični modovi) duž dijagonalnog smjera te a - i b -osi ravnina BEDT-TTF molekula. Ti se modovi mogu smatrati potpisom dugovalnih pobuđenja s anizotropnom disperzijom sličnom fazonu. Kao što je istaknuto u odjeljku o kvazijednodimenzionalnim kupratima, dvodimenzionalna disperzija nalik ovoj opažena je i u VGN fazi ljes-

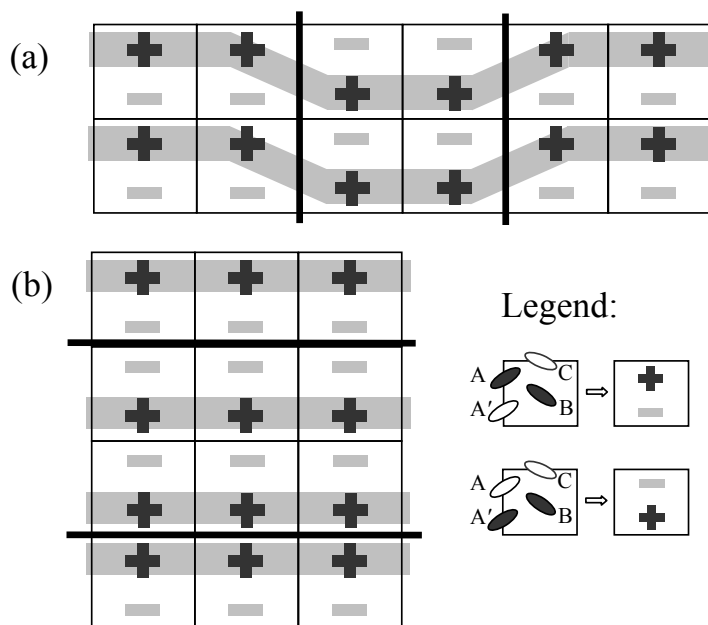
tvica Sr $_{14}$ Cu $_{24}$ O $_{41}$. [13, 17, 16] Kakiuchi *et al.* su prvi predložili postojanje $2k_F$ VGN u α -(BEDT-TTF) $_2$ I $_3$ koji se po njima formira duž cik-zak puteva CABA'C najvećeg integrala preklopa kojeg vide u svojim raspršenjima X-zraka. [27]. No, prisustvo $2k_F$ modulacije integrala preklopa duž dva p -smjera, ACA'BA i ABA'CA (Slika 8.27), upućuje na dodatnu složenost te prikazuje cik-cak puteve kao prilično proizvoljan odabir. Teorijski model za srodni četvrt-popunjen sustav θ -ET $_2$ X može pružiti dodatan uvid. [173] Clay *et al.* su pokazali da je faza uređenog naboja s horizontalnim prugama zapravo 1100 modulacija naboja na molekularnim mjestima duž dva neovisna p -smjera paralelna većim integralima preklopa, te 1010 modulacija duž a osi, okomito na pruge. Dodatno, to je konkretno uređenje naboja popraćeno $2k_F$ modulacijom, ili tetramerizacijom, integrala preklopa duž p -smjerova, gdje je teoretski najjači preklap između 1-1 a najslabiji 0-0. Dimerizacija veza je također prisutna duž molekularnih nizova. Drugim riječima, uređenje naboja s horizontalnim prugama odgovara konkretnoj modulaciji veza i naboja odn. kombiniranom $2k_F$ valu gustoće naboja i veza duž dva p -smjera BEDT-TTF ravnine s dimerizacijom veza u smjeru nizanja molekula. Kao što je gore spomenuto, analogna no donekle složenija tetramerizacija integrala veza razvija se u p -smjerovima α -(BEDT-TTF) $_2$ I $_3$. Podaci dobiveni difrakcijom X-zraka omogućila je Kakiuchiju *et al.* da izračunaju preklap među susjednim molekulama na osnovi aproksimacije čvrste veze i molekularnih orbitala dobivenih proširenom Hückelovom metodom. [27, 219] Kao što prikazuje Slika 8.27, duž jednog od p -smjerova, ABA'CA, najjači je integral preklopa među nabojem bogatim molekulama A i B, kao što se predviđa i za θ -materijal. Također, dimerizacija veza duž a -smjera i njegov uzorak u ab ravnini α -(BEDT-TTF) $_2$ I $_3$ odgovaraju modelu. No, u drugom p -smjeru, ACA'BA, red je pomaknut za jednu vezu: najveći integral preklopa je među nabojem bogatom molekulom A i siromašnom molekulom C. Dodatno, integrali preklopa nisu modulirani savršeno $2k_F$ sinusoidalno duž p -smjerova. Treba prepoznati ta odstupanja α -(BEDT-TTF) $_2$ I $_3$ od uređenja veza u θ -ET $_2$ X modelu, no ona nikako nisu iznenađujuća. Naime, α -(BEDT-TTF) $_2$ I $_3$ ima nižu simetriju od strukture θ -materijala, što naravno može uvesti suptilne razlike u uzorku veza. Također, integrali preklopa dobiveni difrakcijom X-zraka donekle ovise o korištenom računskom modelu. Uz to na umu glavni je fizikalni rezultat modela kojeg su razvili Clay *et al.*, formiranje vala gustoće naboja i veza u vodljivim molekulskim ravninama, potpuno primjenjiv i relevantan za α -(BEDT-TTF) $_2$ I $_3$. Objašnjenje porijekla fazonskog odziva u dielektričnim spektrima možemo potražiti u takvom $2k_F$ valu gustoće. Energetska skala barijera bi trebala biti bliska jednočestičnoj aktivacijskoj energiji kako bi nosioci aktivni u istosmjernoj vodljivosti bili odgovorni za opaženu zasjenjenu relaksaciju. Činjenica da temperaturno ponašanje anizotropije $\tau_{0,LD}$ blisko slijedi anizotropiju



Slika 8.27 – Shematski prikaz $2k_F$ vala gustoće naboja i veza u α -(BEDT-TTF) $_2$ I $_3$. Trostruke, dvostruke, jednostruke i crkane linije prikazuju relativne iznose integrala preklopa od najjačih prema najslabijima duž dva p -smjera. [27] Također su naznačene dimerizirane veze duž a -osi u nizovima molekula AA' i BC.

istosmjerne vodljivosti implicira da je gibanje VGN odgovorno za dielektrični odziv, dok je jednočestično elektronsko/šupljinsko gibanje duž p -smjerova, uz moguće prebacivanje među njima, odgovorno za dc transport.

Nadalje potrebno je komentirati i mali dielektrični relaksacijski mod čija svojstva su karakteristična za kratkovalna pobuđenja naboja. Porijeklo ovakve relaksacije može biti u *twiniranoj* prirodi faze uređenog naboja zbog loma simetrije na inverziju, gdje je omogućeno postojanje dva tipa ćelija: jedan tvori (A,B)-bogate domene, a drugi (A',B)-bogate domene. [27] Zaista, dimerizacija veza i naboja duž nizova molekula nagovještuje karakter uređenja naboja sličan feroelektričnom, zajedno sa stvaranjem optičkog drugog harmonika te fotoinduciranim taljenjem uređenja. [220, 221, 222] Naše se podatke može prirodno pripisati kretanju nabijenih defekata – solitona ili domenskih zidova u teksturi uređenog naboja. I domenski zidovi i solitoni su kratkovalna pobuđenja; međutim, soliton je obično jednodimenzionalni objekt dok domenski zidovi nemaju dimenzijskih ograničenja. Zahtjev neutralnosti uređenja naboja u α -(BEDT-TTF) $_2$ I $_3$ (zamjena pruga ekvivalentna je strogoj zamjeni jednog tipa ćelija drugim) također sugerira dva tipa solitonskih pobuđenja i/ili domenskih zidova. Prvi je par domenskih zidova (par soliton-antisoliton) između nabojem bogatih i siromašnih pruga duž b -osi, koje dobijemo postavimo li zahtjev neutralnosti duž te osi [Slika 8.28(a)]. Drugi tip parova domenskih zidova izlazi iz primjene zahtjeva neutralnosti duž a -osi [Slika 8.28(b)]. Gibanje takvih objekata inducira struju pomaka te se može smatrati mikroskopskim porijeklom polarizacije u fazi uređenog naboja. Naime, u prisustvu vanjskog polja okomitog na pruge naboja, $\mathbf{E} \parallel a$, vezanje na AA' dipolne momente svake jedinične ćelije razbija simetriju



Slika 8.28 – Dva različita tipa parova domenskih zidova u fazi uređenog naboja α -(BEDT-TTF) $_2$ I $_3$. (A,B)- i (A',B)-bogate jedinične ćelije simbolički su predstavljene kao +- i -+ ćelije koje tvore pruge uređenog naboja. Preglednosti radi izostavljamo molekule B i C. Sive debele linije označavaju pruge bogate nabojem. Tanke crne linije su parovi domenskih zidova.

između dvije moguće orijentacije tog dipola. Uslijed interakcija s prvim susjedima dipoli AA' molekula najlakše prebace orijentaciju na domenskom zidu, što uzrokuje gibanje parova zidova. Vezanje na polje $\mathbf{E} \parallel b$, paralelno s prugama tj. okomito na dipole AA', je donekle manje očito. Treba se podsjetiti da A i A' također interagiraju s B i C molekulama. Na energetski nepovoljnom domenskom zidu molekule B i C efektivno vežu AA' dipole na okomito vanjsko polje i dozvoljavaju tjerano solitonsko gibanje duž b -osi.

Teoretski, domenski bi zid trebao biti neovisan o položaju, no u stvarnom kristalu zapinje za defekte. [223] Takvo zapinjanje navodi domenski zid da sjedi u lokalnom energetskom minimumu. Široka raspodjela relaksacijskih vremena se stoga može pripisati raspodjeli aktivacijskih vremena vezanih uz mjesta zapinjanja. Slabo izmjenično električno polje inducira dielektrični odziv uslijed aktivacije među različitim metastabilnim stanjima. Ta stanja odgovaraju lokalnim promjenama raspodjele naboja na prostornoj skali debljine domenskog zida. Srednje relaksacijsko vrijeme gotovo neovisno o temperaturi ukazuje na to da otporna disipacija ne može biti bitna za domenske zidove te da je dielektrični odgovor dominiran niskim energetskim barijerama.

8.4 Zaključak

U ovom radu predstavljamo rezultate izučavanja nabojnog uređenja u tri strukture reducirane dimenzionalnosti: u lančastom perovskitu s degeneriranim orbitalama BaVS_3 , kompozitnom kupratu $(\text{La}, \text{Y}, \text{Sr}, \text{Ca})_{14}\text{Cu}_{24}\text{O}_{41}$ koji se sastoji od lanaca i ljestvica, te dvodimenzionalnom organskom vodiču $\alpha\text{-(BEDT-TTF)}_2\text{I}_3$.

BaVS_3 predstavlja interesantan primjer međugre orbitalne degeneracije s jedne strane, te spinskog i nabojnog sektora s druge, koju treba uzeti u obzir da bi se u potpunosti razumjelo porijeklo MI prijelaza i niskotemperaturnih faza u spojevima prijelaznih metala. Niskofrekventnom dielektričnom spektroskopijom je pokazano da se kod BaVS_3 javlja velika dielektrična konstanta koja je vezana uz prijelaz metal-izolator. Tokom hlađenja dielektrična konstanta opada sve do temperature magnetskog prijelaza, ispod koje se ustaljuje na konstantnoj vrijednosti. Moguće i najvjerojatnije objašnjenje takvog efekta je da kolektivna pobuđenja (čiju disperziju vidimo kao široki, zasjenjeni dielektrični mod) nisu fazonska pobuđenja vala gustoće naboja, već da predstavljaju kratkovalno pobuđenje orbitalnog uređenja koje se počinje uspostavljati na MI prijelazu i razvija dugodosežno uređenje ispod magnetskog prijelaza.

Kod kuprata, našli smo prelaženje s jednodimenzionalnog preskakivanja u lancima za $y \geq 3$ na dvodimenzionalno vođenje u ravninama ljestvica kod $y \lesssim 2$. Iz tih se rezultata iščitava da se šupljine raspodjeljuju među lancima i ljestvicama jednom kad im broj n_h pređe 4, dok su pri manjim dopiranjima sve u lancima. Nameće se da je raspodjela šupljina određena međusobno vezanim formiranjem antiferomagnetskog dimerskog i nabojnog uređenja lanaca, i vala gustoće vala u ljestvicama.

I na kraju, u $\alpha\text{-(BEDT-TTF)}_2\text{I}_3$ smo u metalnoj fazi opazili pregušeni Drudeov odziv i slabu optičku anizotropiju što je konzistentno s gotovo izotropnom i istosmjernom vodljivošću u molekulskim ravninama. Naišli smo na naglo formiranje statičkog uređenja naboja ispod $T_{\text{CO}} = 136 \text{ K}$ čemu je slijedio dramatičan pad optičke vodljivosti. Do disproporcijacije naboja dolazi oštro na $T_{\text{CO}} \text{ K}$ i ne mijenja se daljnjim hlađenjem. Opažene vrijednosti molekulskog naboja su $+0.8$ i $+0.85e$ na naboju bogatim molekulama, te $+0.2$ i $+0.15e$ za naboju siromašne molekule, što je u dobrom slaganju s procjenama difrakcije X-zraka. Ispod prijelaza uređenja naboja otkrivamo razvoj anizotropije istosmjerne vodljivosti tj. transportnog procjepa, za razliku od slabo anizotropne optičke vodljivosti koja je slična onoj u metalnoj fazi. Optički procjep iznosi otprilike 75 meV . Razvoj anizotropije dc vodljivosti u vodljivim slojevima popraćen je pojavom dva dielektrična relaksacijska moda u kHz–MHz području. Veliki dielektrični mod pokazuje

karakteristično fazonsko ponašanje dok je mali mod temperaturno neovisan i podsjeća na solitonski odziv. Svi ti rezultati ukazuju na to da je najkonzistentnija slika uređenja naboja u α -(BEDT-TTF)₂I₃ zapravo ona kooperativnog vala gustoće veza i naboja ferroelektrične prirode, za razliku od pretpostavljenog potpuno lokaliziranog Wignerovog kristala.

Sa svakim razjašnjenim detaljom u ova tri jako korelirana elektronska sustava ipak ostaju i otvorena pitanja. Kod BaVS₃ potrebno je direktno pokazati postojanje orbitalnog uređenja vezanog uz superstrukturu. Kod kvazijednodimenzionalnih kuprata (La,Y,Sr,Ca)₁₄Cu₂₄O₄₁ učvrstili smo sliku u kojoj lanci i ljestvice međudjeluju za razliku od stava da se radi samo o slabo vezanim rezervoarima šupljina. Posebne je težine pitanje α -(BEDT-TTF)₂I₃ budući da je teorijski rad za sad relativno ograničen na osnovno stanje jednostavnijeg θ -sustava, a računi otežani složenom mrežom interakcija u vodljivim ravninama. Nedavni eksperimentalni radovi ukazuju na emergentnu sličnost kvazijednodimenzionalnih valova gustoće i dvodimenzionalnih uređenja naboja, što naravno poziva za dodatni eksperimentalni i teorijski trud.

Appendix A

Dielectric spectroscopy: contact verification

As with any two-contact measurements, in dielectric spectroscopy one always needs to take care of possible contact influence and make certain that the observed effects come from the sample bulk only. Changing sample dimensions as well as varying different contact materials and preparation methods are reliable ways to check for possible contact influences, however they are often impractical: e.g., contacts cannot be easily removed, evaporated gold contacts destroy thin organic samples of α -(BEDT-TTF)₂I₃ due to heating, or, as is the case of BaVS₃, sample chemistry might be very sensitive and accept only a specific contact “recipe”.

First and foremost, a Maxwell-Wagner-type extrinsic effect at the sample-contact interface features a single dielectric relaxation mode with its mean relaxation time changing with temperature proportionally to sample resistivity. [229]. The small relaxation mode of α -(BEDT-TTF)₂I₃ can be safely identified as an intrinsic property because it does not change with temperature. On the other hand, in all the BaVS₃, Sr₁₄Cu₂₄O₄₁ and α -(BEDT-TTF)₂I₃ samples under scrutiny a relaxation mode does appear with a mean relaxation time proportional to dc resistivity of the sample. Even though this type of behavior can be caused by intrinsic, bulk screened relaxation processes, it might still be influenced by contact interfacial polarization which then requires a thorough verification.

The quality of contacts for dielectric spectroscopy measurements (produced as described in Section 3.5) were verified for each studied sample following the established procedure consistently used in our previous studies. [200] In short, we have routinely

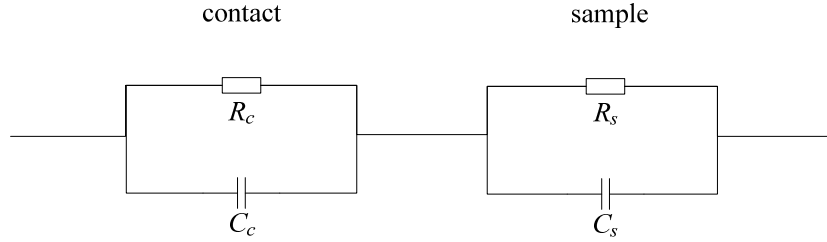


Figure A.1 – Two-contact measurements need to take into account the contribution of contacts (resistance R_c and capacitance C_c) together with bulk properties of the sample (resistance R_s and capacitance C_s).

ensured by performing open-circuit measurements that stray capacitances do not influence the real part of the conductivity in the frequency window 20 Hz - 10 MHz, inside the whole temperature range of our study. Further, we look for and stay inside the limits of linear response (this varies with different systems but is typically below 0.5 V/cm for the samples in this work). Lastly and most importantly, quality of contacts is verified by dc resistance measurements in the standard 4- and 2-contact configurations. Taking into account the difference in geometry between contacts in these two configurations, the 4-contact resistance can be scaled and subtracted from the 2-contact resistance in order to estimate contact resistance R_c *vs.* sample bulk resistance R_s .

Large contact resistances in an insulating phase could imply large capacitances at the contact depletion layers. Since contact capacitances cannot be measured directly, we use the following simple model. Sample circuit can be thought of as two parallel resistance-capacitance circuits, connected in series, one representing the contacts (R_c and C_c being the resistance and capacitance, respectively) and the other the bulk of the sample. For the sake of simplicity we assume frequency-independent capacitive and resistive components of the sample bulk, C_s and R_s . In other words the model pessimistically assumes any frequency-dependent response to be solely due to the sample and (bad) contacts being connected in series, and not due to bulk physics.

The conductivity Y of circuit shown in Fig. A is given by the following equations:

$$\frac{1}{Y} = \frac{1}{Y_s} + \frac{1}{Y_c} \quad (\text{A.1})$$

$$Y_s = \frac{1}{R_s} + i\omega C_s \quad (\text{A.2})$$

$$Y_c = \frac{1}{R_c} + i\omega C_c \quad (\text{A.3})$$

If we denote sample cross-section as S and length between current contacts (through

which the two-contact measurement is performed) as l_{II} , the resulting total complex dielectric function $\varepsilon(\omega) = \varepsilon'(\omega) + i\varepsilon''(\omega)$ of the circuit (sample and contacts) is given by

$$\begin{aligned}\varepsilon' &= \frac{l_{\text{II}}}{S} \frac{1}{\varepsilon_0} \frac{\Im Y}{\omega} \\ &= \frac{l}{S} \frac{1}{\varepsilon_0} \frac{C_c R_c^2 + C_s R_s^2 (1 + C_s (C_s + C_c) R_c^2 \omega^2)}{(R_s + R_c)^2 + (C_s + C_c)^2 R_s^2 R_c^2 \omega^2}\end{aligned}\quad (\text{A.4})$$

$$\begin{aligned}\varepsilon'' &= \frac{l_{\text{II}}}{S} \frac{1}{\varepsilon_0} \frac{\Re Y - \Re Y(\omega = 0)}{\omega} \\ &= \frac{l}{S} \frac{1}{\varepsilon_0} \frac{R_s R_c (C_s R_s - C_c R_c)^2 \omega}{(R_s + R_c) ((R_s + R_c)^2 + (C_s + C_c)^2 R_s^2 R_c^2 \omega^2)}\end{aligned}\quad (\text{A.5})$$

Obviously, these depend on the set of experimental values: R_c , C_c , R_s , C_s . Here the effective dc conductivity was taken out of the consideration by subtracting real part of $Y(\omega = 0)$.

In order to compare the predictions of this model with our experimental data obtained on particular samples, we take the limits $\omega \rightarrow 0$ and $\omega \rightarrow \infty$ for the real part of dielectric function. We obtain the following:

$$\varepsilon'_{\text{exp}}(0) = \frac{l}{S} \frac{1}{\varepsilon_0} \frac{C_c R_c^2 + C_s R_s^2}{(R_s + R_c)^2} \quad (\text{A.6})$$

$$\varepsilon''_{\text{exp}}(\infty) = \frac{l}{S} \frac{1}{\varepsilon_0} \frac{C_c C_s}{(C_c + C_s)^2} \quad (\text{A.7})$$

From these expressions it is possible to calculate how the effective dielectric strength $\Delta\varepsilon = \varepsilon'(0) - \varepsilon'(\infty)$ of the model circuit depends on its resistive and capacitive components' values. In order to retrieve contact and sample resistances R_c and R_s , we take into account our two-contact dc measurements of resistance, where contact resistance in series with sample bulk is obtained, and the four-contact measurements where the sample bulk resistance is found independently. In this manner we know contact, R_c , and sample, R_s resistances separately:

$$\rho_{\text{dc}} = R_{4\text{cont,dc}} \frac{S}{l_{\text{VV}}} \quad (\text{A.8})$$

$$R_s = \rho_{\text{dc}} \frac{l_{\text{II}}}{S} \quad (\text{A.9})$$

$$R_c = R_{2\text{cont,dc}} - R_s \quad (\text{A.10})$$

Table A.1 – Different regimes of contact/sample resistance relationships, with predictions for three different capacitance scenarios (see text).

Resistances	$C_s \approx C_c$			$C_s \ll C_c$			$C_s \gg C_c$		
	$\varepsilon'(0)$	$\varepsilon'(\infty)$	$\Delta\varepsilon$	$\varepsilon'(0)$	$\varepsilon'(\infty)$	$\Delta\varepsilon$	$\varepsilon'(0)$	$\varepsilon'(\infty)$	$\Delta\varepsilon$
$R_c = 0.1R_s$	C_s	$C_s/2$	$C_s/2$	$\ll C_c$	C_s	$\ll C_c$	C_s	C_c	C_s
$R_c \approx R_s$	$C_s/2$	$C_s/2$	0	$C_c/4$	C_s	$C_c/4$	$C_s/4$	C_c	$C_s/4$
$R_c = 10R_s$	C_s	$C_s/2$	$C_s/2$	C_c	C_s	C_c	$\ll C_s$	C_c	$\ll C_s$

where ρ_{dc} is sample resistivity, $R_{4\text{cont,dc}}$ and $R_{2\text{cont,dc}}$ are the measured four- and two-contact resistances, and l_{VV} and l_{II} distances between voltage and current contacts, respectively.

Typically there are three regimes of interest for contact/sample resistances relationships:

1. $R_c \ll R_s$ (in practice dc measurements are able to discern $R_c = 0.1R_s$),
2. $R_c \approx R_s$,
3. $R_c \geq R_s$.

The precise temperature position and width of these regimes depends on the specifics of sample-contact interface. Within these different resistance (temperature) regimes we evaluate effective values of $\varepsilon'(0)$, $\varepsilon'(\infty)$ and $\Delta\varepsilon$ for three possible capacitance scenarios: $C_c \approx C_s$, $C_s \ll C_c$ and $C_s \gg C_c$ (see Table A.1; the factor $\varepsilon_0 l_{\text{II}}/S$ has been left out for simplicity). The important result stemming from this calculation is that one can verify which capacitance scenario is relevant by checking how the dielectric strength $\Delta\varepsilon$ varies in the whole temperature range.

A.1 BaVS₃

The precise position and width of the three contact resistance regimes depends on the quality of contacts, which can be directly verified by R_c/R_s ratio in the vicinity of T_{MI} . Samples with good-quality contacts displayed R_c/R_s ratio between 1 and 5 in the metallic phase and in the vicinity of T_{MI} , while samples with poor contacts showed R_c/R_s ratio between 100 and 1000. As can be seen in Figs. A.2 – A.4, with cooling the contact resistance grows, reaches a maximum around T_{MI} and then drops to small values in the insulating phase.

In the $C_s \approx C_c$ scenario of comparable contact and sample bulk capacitances, $\Delta\varepsilon$ is expected to display a slight minimum at temperatures below and close to T_{MI} and to stay finite in the metallic phase of BaVS₃. Two samples with poor quality contacts ($R_c/R_s \approx 100 - 1000$ in the metallic phase) showed behavior expected in this scenario (see Fig. A.2).

In the scenario with dominant contact capacitances, $C_s \ll C_c$, $\Delta\varepsilon$ should rise steadily for several orders of magnitude starting from very low values at low temperatures, across T_{MI} and going into metallic phase where it stays finite. Two samples with poor contacts ($R_c/R_s \approx 100 - 1000$ in the metallic phase and in the vicinity of T_{MI}) behave as predicted in this scenario (see Fig. A.3). Moreover, note that in the case of these samples the mean relaxation time did not follow dc resistivity of the sample bulk in the entire temperature range of the insulating phase, reflecting the influence of $R_c C_c$ time constant.

The (desirable) small-contact capacitance scenario, $C_s \gg C_c$, should give us an almost temperature-independent $\Delta\varepsilon$ with a slight decrease close to T_{MI} . This decrease should become more pronounced above T_{MI} when R_c becomes larger than R_s (i.e., $1 < R_c/R_s \leq 5$). Keeping in mind that the temperature variation of $\Delta\varepsilon$ predicted by the model is uniquely due to the contact resistance influence, we can conclude that this scenario describes best the case of BaVS₃ samples with good contacts reported in this work and related publications (see Fig. A.4). This implies that the experimentally observed $\Delta\varepsilon$, a plateau up to 30 K followed by a rise of about 50-fold with a maximum at T_{MI} , reflects the intrinsic physical features of the BaVS₃ system. On the other hand, the observed sharp falloff in $\Delta\varepsilon$ just above T_{MI} might be partially caused by the contact resistance influence as expected by the model; however, an effect due to the vanishing collective response in the metallic state remains dominant.

In summary for BaVS₃ we can conclude that samples with good-quality contacts whose dielectric response reflects the intrinsic features of the sample bulk can easily be distinguished from bad samples by featuring the R_c/R_s ratio not larger than 5 in the metallic phase, and $R_c = 0.1R_s$ in the wide range of the insulating phase except close to T_{MI} . In contrast, the bad samples displayed an R_c/R_s ratio of the order of 100 – 1000 in the metallic phase and in the vicinity of T_{MI} , meaning very large contact resistances which also implies large contact capacitances. These large capacitances of the contact depletion layer remain unchanged in the whole temperature range of the insulating phase. The bad samples showed the desired $R_c = 0.1R_s$ in the insulating phase only at very low temperatures (below about 30 K). Therefore, the dielectric response registered

in bad samples was a result of sample bulk and contact capacitance influence, the latter becoming dominant with increasing temperature.

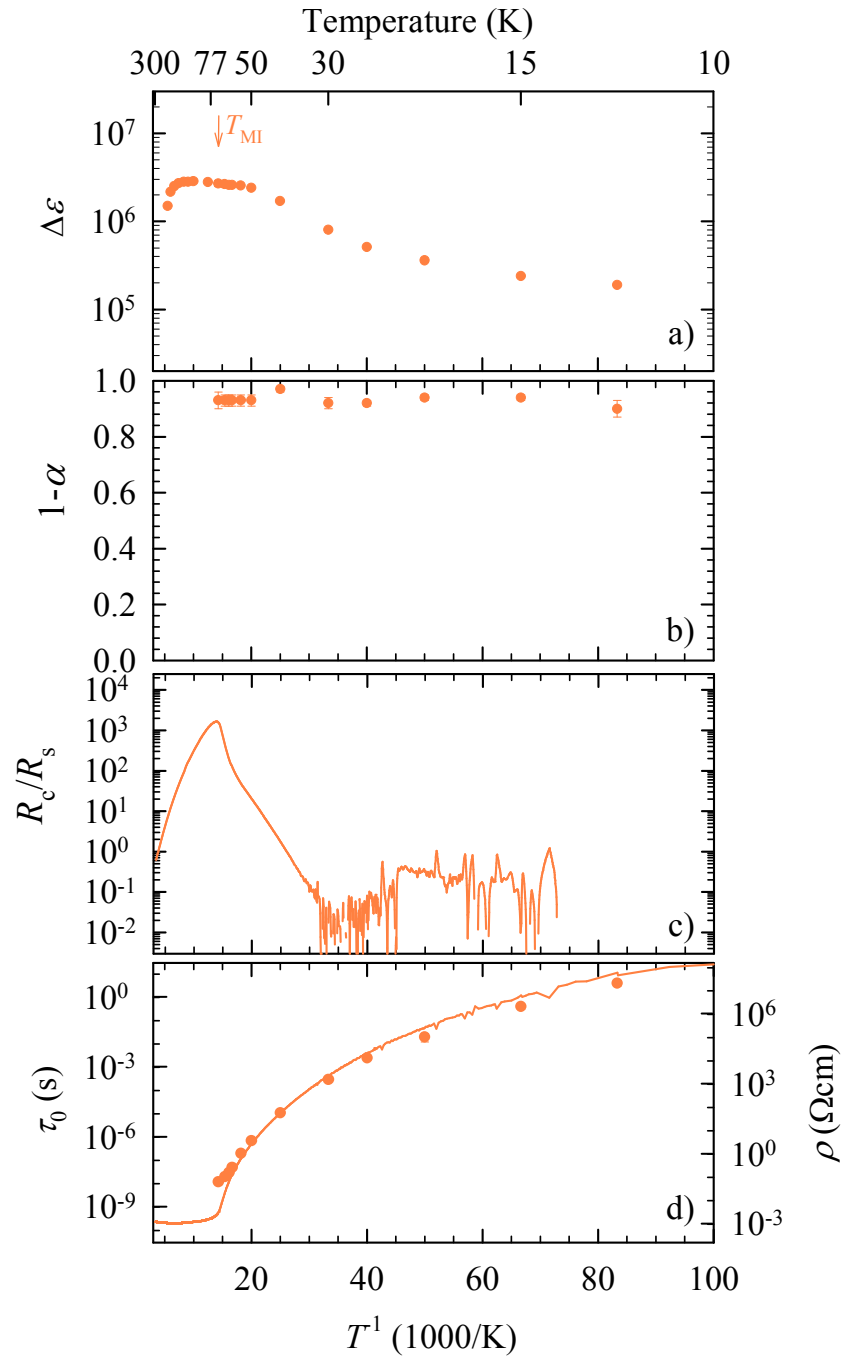


Figure A.2 – Dielectric fit parameters, bulk and contact resistances for a sample of BaVS₃. Dielectric response is under extrinsic influence of contacts, see text.

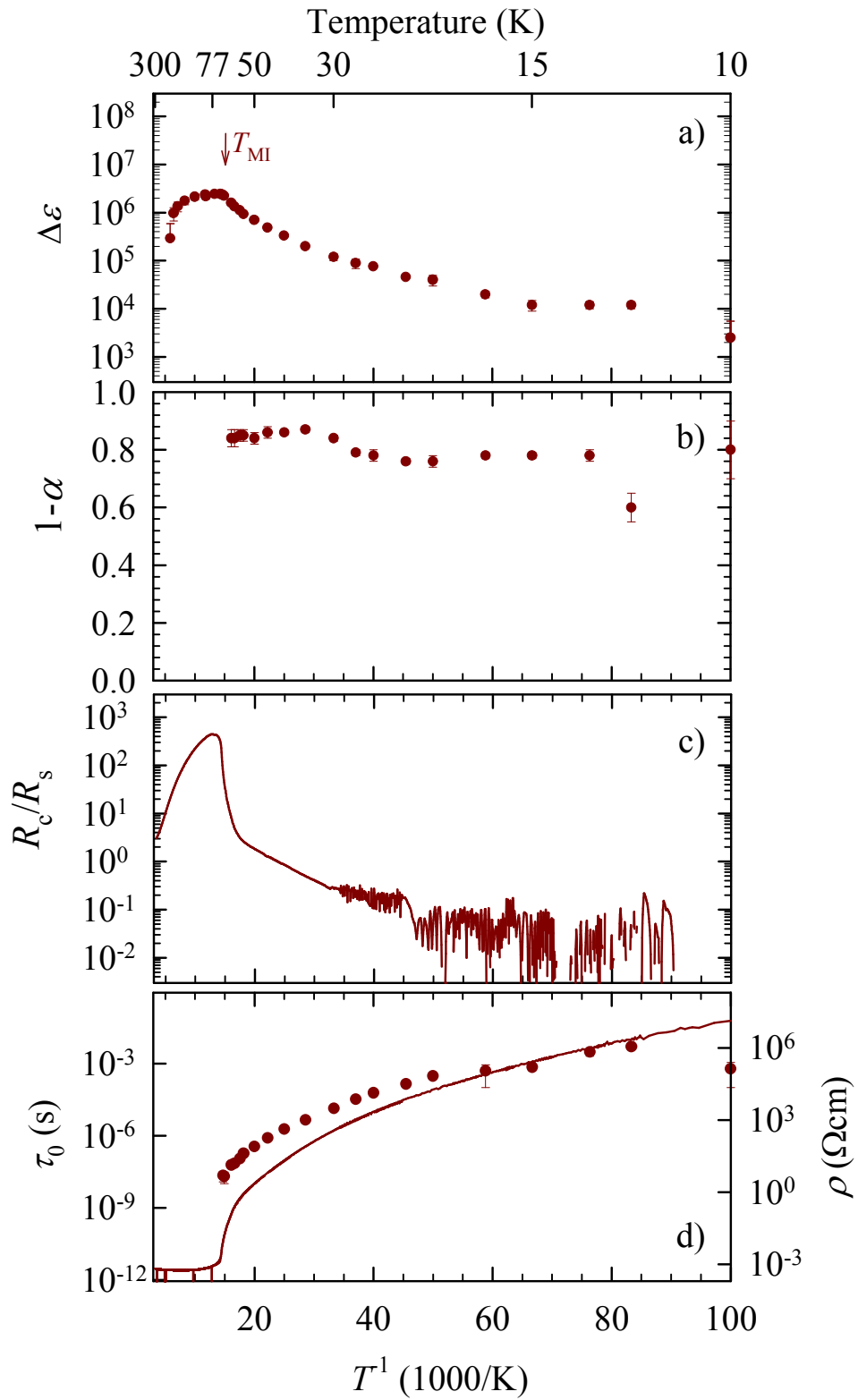


Figure A.3 – Dielectric fit parameters, bulk and contact resistances for a sample of BaVS₃. Dielectric response is under extrinsic influence of contacts, see text.

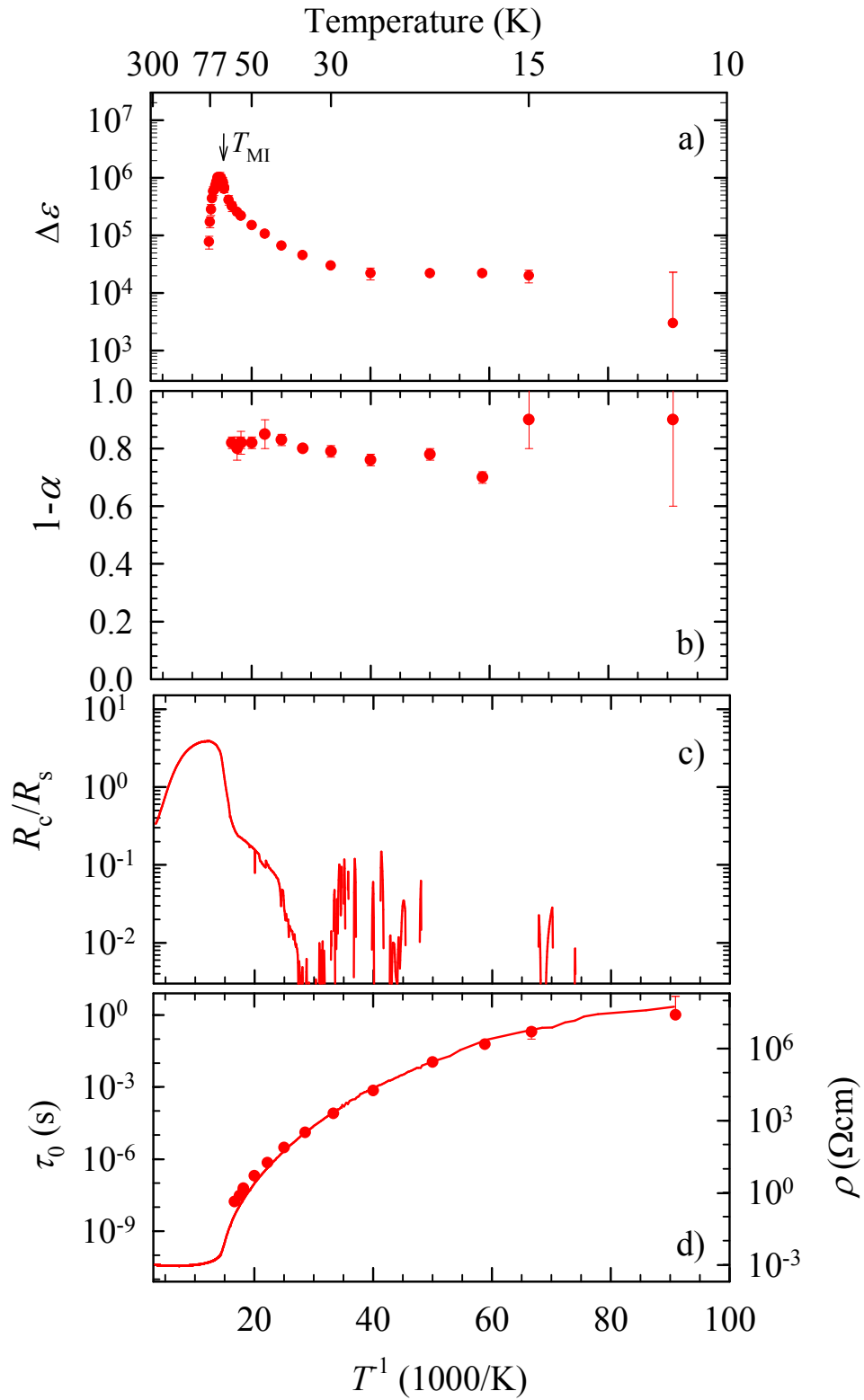


Figure A.4 – Dielectric fit parameters, bulk and contact resistances for a sample of BaVS₃. Contacts are of good quality and the dielectric response is intrinsic, see text.

A.2 α -(BEDT-TTF) $_2$ I $_3$

As demonstrated by Figs. A.5 and A.6, the α -(BEDT-TTF) $_2$ I $_3$ contact resistances are comparable to bulk in the metallic phase. Just below phase transition the ratio R_c/R_s drops to negligible values, but recovers back to approximately unity with cooling.

We again traverse three different capacitance scenarios. As mentioned above, the temperature-independent nature of the small dielectric mode identifies it as an intrinsic property of α -(BEDT-TTF) $_2$ I $_3$. That is why the screened, large dielectric mode is used here as the “suspicious relaxation”.

In the scenario with $C_s \approx C_c$, $\Delta\varepsilon$ is expected to display a minimum in the insulating phase around 50–70 K. None of our samples showed this behavior.

In the case of large contact capacitance $C_s \ll C_c$, $\Delta\varepsilon$ should fall steadily by several orders of magnitude starting from C_c at low temperatures and vanish before the phase transition at T_c . We do notice a drop in $\Delta\varepsilon$ while warming when R_c/R_s decreases from ~ 1 to ~ 0.1 , a finite dielectric relaxation strength is observed at all times. A dramatic drop in $\Delta\varepsilon$ near T_{CO} , which is predicted in this scenario, is absent in all of our samples.

In the scenario of negligible contact capacitance $C_s \gg C_c$, $\Delta\varepsilon$ is expected to steadily increase and show a plateau near T_{CO} . This increase should become more pronounced when R_c becomes larger than R_s (i.e., $1 < R_c/R_s \leq 5$). Keeping in mind that the temperature variation of $\Delta\varepsilon$ assumed by the bulk-contact model is solely due to the influence of contact resistance and capacitance, we can conclude that this scenario describes best the case of all presented α -(BEDT-TTF) $_2$ I $_3$ samples. This implies that the observed behavior of $\Delta\varepsilon$ below T_{CO} (approximately constant, with a slight maximum around 50 K) reflects intrinsic physical features of the α -(BEDT-TTF) $_2$ I $_3$ system. On the other hand, $\Delta\varepsilon$ falloff found experimentally below about 50 K might be partially caused by the contact influence; however, this decrease is smaller than modeled, and $\Delta\varepsilon$ still dominantly reflects sample bulk behavior.

In conclusion, contact resistances did not qualitatively influence the measured dielectric response of α -(BEDT-TTF) $_2$ I $_3$ which stayed approximately temperature-independent in the whole set of samples, through a range of contact-to-sample resistance ration from 0.1 to 10.

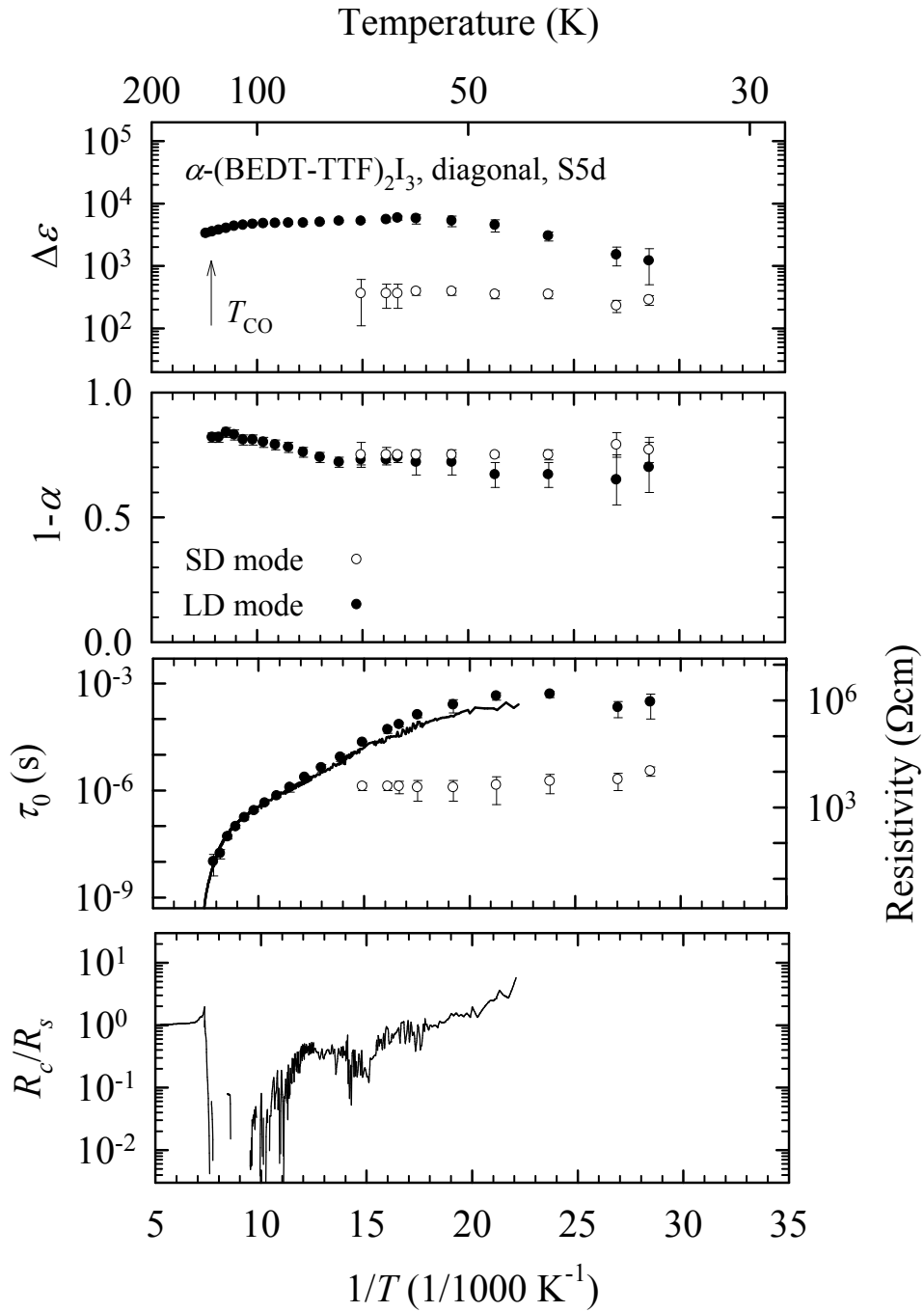


Figure A.5 – Dielectric fit parameters, bulk and contact resistances for a sample of α -(BEDT-TTF) $_2$ I $_3$, $\mathbf{E} \parallel [1\bar{1}0]$. Contacts are of good quality and the dielectric response is intrinsic, see text.

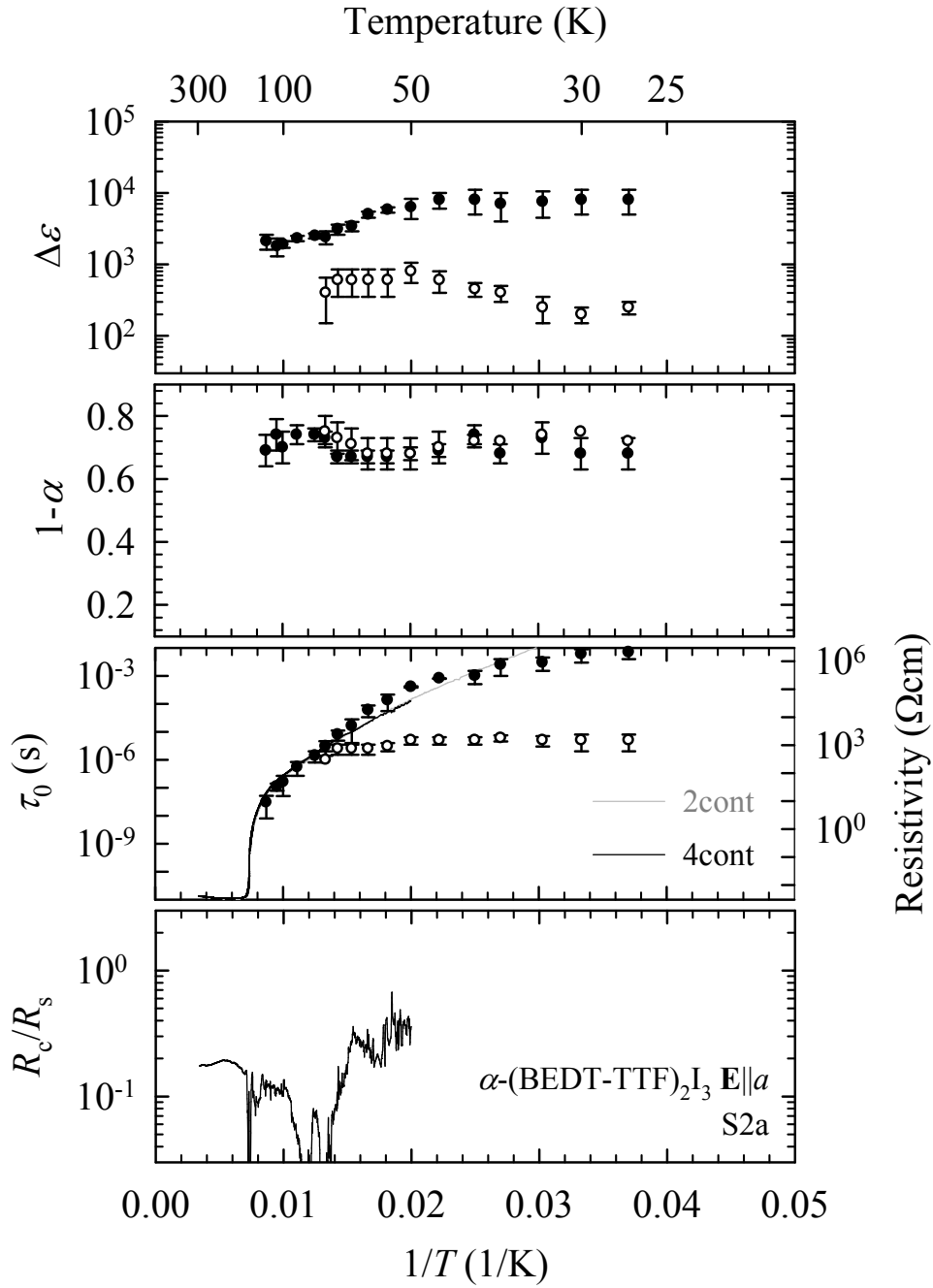


Figure A.6 – Dielectric fit parameters, bulk and contact resistances for a sample of α -(BEDT-TTF) $_2$ I $_3$, $\mathbf{E} \parallel b$. Contacts are of good quality and the dielectric response is intrinsic, see text.

A.3 (La,Y,Sr,Ca)₁₄Cu₂₄O₄₁

Of all the samples presented in this work, our group has had the most experience with contact preparation on quasi-1D cuprates. Different contacts have been tested on many fully-doped and underdoped samples, and we have settled on the method described in Section 3.5 as the one giving the most robust contacts (resistant to thermal cycling) with low resistances. As the most reliable way to test for contact influence, measurements on samples of Sr₁₄Cu₂₄O₄₁, Y_{0.55}Sr_{13.45}Cu₂₄O₄₁ and Y_{1.6}Sr_{12.4}Cu₂₄O₄₁ have been tested with differently spaced contacts, always with consistent dielectric response, meaning that the geometric scaling involved in converting admittances to dielectric response always operated on extensive, bulk values instead of scale-independent contact contributions.

Bibliography

- [1] D. Jérôme, Chem. Rev. **104**, 5565 (2004).
- [2] T. Vuletić, B. Korin-Hamzić, T. Ivek, S. Tomić, B. Gorshunov, M. Dressel, and J. Akimitsu, Phys. Rep. **428**, 169 (2006).
- [3] H. Seo, J. Merino, H. Yoshioka, and M. Ogata, J. Phys. Soc. Jpn. **75**, 051009 (2006).
- [4] Massenet O., J. J. Since, J. Mercier, M. Avignon, R. Buder, V. D. Nguyen, and J. Kelber., J. Phys. Chem. Solids, **40**, 573 (1979).
- [5] L. F. Mattheiss, Solid State Commun. **93**, 791 (1995).
- [6] R. A. Gardner, M. Vlasse, and A. Wold, Acta Crys. B, **25**, 781 (1969).
- [7] G. Mihály, I. Kézsmárki, F. Zamborszky, M. Miljak, K. Penc, P. Fazekas, H. Berger, and L. Forró, Phys. Rev. B **61**, R7831 (2000).
- [8] S. Fagot, P. Foury-Leylekian, S. Ravy, J. P. Pouget, and H. Berger, Phys. Rev. Lett. **90**, 196401 (2003).
- [9] S. Fagot, P. Foury-Leylekian, S. Ravy, J. P. Pouget, E. Lorenzo, Y. Joly, M. Greenblatt, M. V. Lobanov, and G. Popov, Phys. Rev. B **73**, 033102 (2006).
- [10] H. Nakamura, H. Imai, and M. Shiga, Phys. Rev. Lett. **79**, 3779 (1997).
- [11] M. Uehara, T. Nagata, J. Akimitsu, H. Takahashi, N. Mōri and K. Kinoshita, J. Phys. Soc. Jpn. **65**, 2764 (1996).
- [12] B. Gorshunov, P. Haas, T. R o om, M. Dressel, T. Vuletić, B. Korin-Hamzić, S. Tomić, J. Akimitsu and T. Nagata, Phys. Rev. B **66**, 060508(R) (2002).
- [13] T. Vuletić, B. Korin-Hamzić, S. Tomić, B. Gorshunov, P. Haas, T. R o om, M. Dressel, J. Akimitsu, T. Sasaki and T. Nagata, Phys. Rev. Lett. **90**, 257002 (2003).
- [14] N. Nücker, M. Merz, C. A. Kuntscher, S. Gerhold, S. Schuppler, R. Neudert, M. S. Golden, J. Fink, D. Schild, S. Stadler, V. Chakarian, J. Freeland, Y. U. Idzerda, K. Conder, M. Uehara, T. Nagata, J. Goto, J. Akimitsu, N. Motoyama, H. Eisaki, S. Uchida, U. Ammerahl and A. Revcolevschi, Phys. Rev. B **62**, 14384 (2000).

-
- [15] H. Kitano, R. Isobe, T. Hanaguri, A. Maeda, N. Motoyama, M. Takaba, K. Kojima, H. Eisaki, S. Uchida, *Europhys. Lett.* **56** 434 (2001).
- [16] P. Abbamonte, G. Blumberg, A. Rusydi, A. Gozar, P. G. Evans, T. Siegrist, L. Venema, H. Eisaki, E. D. Isaacs and G. A. Sawatzky, *Nature* **431**, 1078 (2004).
- [17] T. Vuletić, T. Ivek, B. Korin-Hamzić, S. Tomić, B. Gorshunov, P. Haas, M. Dressel, J. Akimitsu, T. Sasaki and T. Nagata, *Phys. Rev. B* **71**, 012508 (2005).
- [18] M. Matsuda and K. Katsumata, *Phys. Rev. B* **53**, 12201 (1996).
- [19] M. Matsuda, K. Katsumata, H. Eisaki, N. Motoyama, S. Uchida, S. M. Shapiro and G. Shirane, *Phys. Rev. B* **54**, 12199 (1996).
- [20] M. Takigawa, N. Motoyama, H. Eisaki and S. Uchida, *Phys. Rev. B* **57**, 1124 (1998).
- [21] L. P. Regnault, J. P. Boucher, H. Moudden, J. E. Lorenzo, A. Hiess, U. Ammerahl, G. Dhalenne and A. Revcolevschi, *Phys. Rev. B* **59**, 1055 (1999).
- [22] T. Vuletić, B. Korin-Hamzić, S. Tomić, B. Gorshunov, P. Haas, M. Dressel, J. Akimitsu, T. Sasaki and T. Nagata, *Phys. Rev. B* **67**, 184521 (2003).
- [23] T. Mori, A. Kobayashi, Y. Sasaki, H. Kobayashi, G. Saito, and H. Inokuchi, *Chem. Lett.* **1984**, 957 (1984).
- [24] K. Bender, K. Dietz, H. Endres, H. W. Helberg, I. Hennig, H. J. Keller, H. W. Schäfer, and D. Schweitzer, *Mol. Cryst. Liq. Cryst.* **107**, 45 (1984).
- [25] Y. Takano, K. Hiraki, H. M. Yamamoto, T. Nakamura, and T. Takahashi, *J. Phys. Chem. Solids* **62**, 393 (2001).
- [26] S. Moroto, K.-I. Hiraki, Y. Takano, Y. Kubo, T. Takahashi, H. M. Yamamoto, and T. Nakamura, *J. Phys. IV France* **114**, 339-340 (2004).
- [27] T. Kakiuchi, Y. Wakabayashi, H. Sawa, T. Takahashi, and T. Nakamura, *J. Phys. Soc. Jpn.* **76**, 113702 (2007).
- [28] J. Moldenhauer, C. Horn, K. I. Pokhodnia, D. Schweitzer, I. Heinen, and H. J. Keller, *Synth. Met.* **60**, 31 (1993).
- [29] R. Wojciechowski, K. Yamamoto, K. Yakushi, M. Inokuchi, and A. Kawamoto, *Phys. Rev. B* **67**, 224105 (2003).
- [30] R. A. Gardner, M. Vlasse, and A. Wold, *Am. Ceram. Soc. Bull.* **47**, 383 (1968).
- [31] F. Sayetat, M. Ghedira, J. Chenavas, and M. Marezio, *J. Phys. C: Solid State Phys.* **15**, 1627-1635 (1982).
- [32] M. Ghedira, M. Anne, J. Chenavas, M. Marezio, and F. Sayetat, *Phys. C: Solid State Phys.* **19**, 6489-6503 (1986).

-
- [33] S. Fagot, P. Foury-Leylekian, S. Ravy, J. P. Pouget, M. Anne, G. Popov, V. Lobanov, and M. Greenblatt, *Solid. State. Sci.* **7**, 718 (2005).
- [34] I. Kézsmárki, G. Mihály, R. Gaal, N. Barišić, A. Akrap, H. Berger, L. Forró, C. C. Homes, and L. Mihály, *Phys. Rev. Lett.* **96**, 186402 (2006).
- [35] I. Kézsmárki, Sz. Csonka, H. Berger, L. Forró, P. fazekas, and G. Mihály, *Phys. Rev. B* **63**, 081106(R) (2001).
- [36] T. Inami, K. Ohwada, H. Kimura, M. Watanabe, Y. Noda, H. Nakamura, T. Yamasaki, M. Shiga, N. Ikeda, and Y. Murakami, *Phys. Rev. B* **66**, 073108 (2002).
- [37] L. Forró, *Solid State Comm.* **73**, 265 (1990).
- [38] B. Horowitz, *Phys. Rev. B*, **16**, 3943 (1977).
- [39] L. P. Gorkov and A. G. Lebed, *Phys. Rev. B*, **51**, 3285 (1995).
- [40] A. Heidemann and M. Takano, *Phys. Stat. Solidi B* **100**, 343 (1980).
- [41] H. Nakamura, T. Yamasaki, S. Giri, H. Imai, M. Shiga, K. Kojima, M. Nishi, K. Kakurai, and N. Metoki, *J. Phys. Soc. Jpn.* **69**, 2763 (2000).
- [42] O. Massenet, M. Avignon, B. K. Chakraverty, and J. Marcus, *Ann. Condensed Matter Div. EPS Meeting 9 - 11 April 1980*.
- [43] M. H. Whangbo, H. J. Koo, D. Dai, and A. Villesuzanne, *J. Solid State Chem.* **165**, 345 (2002) and **175**, 384 (2003).
- [44] X. Jiang and G. Y. Guo, *Phys. Rev. B* **70**, 035110 (2004).
- [45] F. Lechermann, S. Biermann, and A. Georges, *Phys. Rev. B* **76**, 085101 (2007).
- [46] F. Lechermann, S. Biermann, and A. Georges, *Phys. Rev. Lett.* **94**, 166402 (2005).
- [47] P. Fazekas, K. Penc, K. Radnóczia, N. Barišić, H. Berger, L. Forró, S. Mitrović, A. Gauzzi, L. Demkó, I. Kézsmárki, and G. Mihály, *J. of Magn. and Magn. Materials* **310**, 928-934 (2007).
- [48] A. Tanaka, *J. of Magn. and Magn. Materials* **310**, 898 (2007).
- [49] S. Mitrovic, P. Fazekas, C. Søndergaard, D. Ariosa, N. Barišić, H. Berger, D. Cloëtta, L. Forró, H. Höchst, I. Kupčić, D. Pavuna, and G. Margaritondo, *Phys. Rev. B* **75**, 153102 (2007).
- [50] D. S. Dessau, T. Saitoh, C.-H. Park, Z.-X. Shen, P. Villeda, N. Hamada, Y. Moritomo, and Y. Tokura, *Phys. Rev. Lett.* **81**, 192 (1998).
- [51] J. G. Bednorz and K. A. Müller, *Z. Physik B* **64** 189-193 (1986).

- [52] T. Siegrist, L. F. Schneemeyer, S. A. Sunshine, J. V. Waszczak and R. S. Roth, *Mat. Res. Bull.* **23**, 1429 (1988).
- [53] E. M. McCarron, M. A. Subramanian, J. C. Calabrese, and R. L. Harlow, *Mat. Res. Bull.* **23**, 1355 (1988).
- [54] E. Dagotto, J. Rieira and D. Scalapino, *Phys. Rev. B* **45**, 5744 (1992).
- [55] T. M. Rice, S. Gopalan and M. Sigrist, *Europhys. Lett.* **23**, 445 (1993).
- [56] E. Dagotto and T. M. Rice, *Science* **271**, 618 (1996).
- [57] K. Ishida, K. Kitaoka, Y. Tokunaga, S. Matsumoto, K. Asayama, M. Azuma, Z. Hiroi, and M. Takano, *Phys. Rev. B* **53**, 2827 (1996).
- [58] T. Vuletić, T. Ivek, B. Korin-Hamzić, S. Tomić, B. Gorshunov, M. Dressel, C. Hess, B. Büchner, and J. Akimitsu, *J. Phys. IV France* **131**, 299 (2005).
- [59] O. Milat, G. Van Tendeloo, S. Amelinckx, M. Mehbod, and R. Deltour, *Acta Cryst. B* **48**, 618 (1992).
- [60] Z. Hiroi, S. Amelinckx, G. Van Tendeloo, and N. Kobayashi, *Phys. Rev. B* **54**, 15849 (1996).
- [61] S.-C. Zhang and T. M. Rice, *Phys. Rev. B* **37**, R3759 (1988).
- [62] M. Isobe, M. Onoda, T. Ohta, F. Izumi, K. Kimoto, E. Takayama-Muromachi, A. W. Hewat and K. Ohoyama, *Phys. Rev. B* **62**, 11667 (2000).
- [63] J. B. Goodenough, *Phys. Rev.* **100**, 564 (1955).
- [64] J. Kanamori, *J. Phys. Chem. Solids* **10**, 87 (1959).
- [65] P. W. Anderson, *Solid State Phys.* **14**, 99 (1963).
- [66] W. Geertsma and D. I. Khomskii, *Phys. Rev. B* **54**, 3011 (1996).
- [67] S. Gopalan, T. M. Rice and M. Sigrist, *Phys. Rev. B* **49**, 8901 (1994).
- [68] M. Arai and H. Tsunetsugu, *Phys. Rev. B* **56**, R4305 (1997).
- [69] T. Takahashi, T. Yokoya, A. Ashihara, O. Akaki, H. Fujisawa, A. Chainani, M. Uehara, T. Nagata, J. Akimitsu, and H. Tsunetsugu, *Phys. Rev. B* **56**, 7870 (1997).
- [70] T. F. A. Müller, V. Anisimov, T. M. Rice, I. Dasgupta and T. Saha-Dasgupta, *Phys. Rev. B* **57**, R12655 (1998).
- [71] T. Sato, T. Yokoya, T. Takahashi, M. Uehara, T. Nagata, J. Goto, and J. Akimitsu, *J. Phys. Chem. Solids* **59**, 1912 (1998).

-
- [72] T. Osafune, N. Motoyama, H. Eisaki and S. Uchida, *Phys. Rev. Lett.* **78**, 1980 (1997).
- [73] Y. Piskunov, D. Jérôme, P. Auban-Senzier, P. Wzietek, A. Yakubovsky, *Phys. Rev. B* **72**, 064512 (2005).
- [74] A. Rusydi, M. Berciu, P. Abbamonte, S. Smadici, H. Eisaki, Y. Fujimaki, S. Uchida, M. Rübhausen, and G. A. Sawatzky, *Phys. Rev. B* **75**, 104510 (2007).
- [75] E. Tafra, B. Korin-Hamzić, M. Basletić, A. Hamzić, M. Dressel, and J. Akimitsu, *Phys. Rev. B* **78**, 155122 (2008).
- [76] T. Nagata, M. Uehara, J. Goto, J. Akimitsu, N. Motoyama, H. Eisaki, S. Uchida, H. Takahashi, T. Nakanishi, and N. Mōri, *Phys. Rev. Lett.* **81**, 1090 (1998).
- [77] T. Vuletić, B. Korin-Hamzić, S. Tomić, B. Gorshunov, P. Haas, M. Dressel, J. Akimitsu, T. Sasaki, and T. Nagata, *Phys. Rev. B* **67**, 184521 (2003).
- [78] S. T. Carr and A. M. Tsvelik, *Phys. Rev. B* **65**, 195121 (2002).
- [79] M. Tsuchiizu and Y. Suzumura, *J. Phys. Soc. Jpn.* **73**, 804 (2004).
- [80] M. Tsuchiizu and Y. Suzumura, *Phys. Rev. B* **72**, 075121 (2005).
- [81] N. Fujiwara, N. Mori, Y. Uwatoko, T. Matsumoto, N. Motoyama and S. Uchida, *Phys. Rev. Lett.* **90**, 137001 (2003).
- [82] E. Orignac and T. Giamarchi, *Phys. Rev. B* **56**, 7167 (1997).
- [83] M. Kato, K. Shiota and Y. Koike, *Physica C* **258**, 284 (1996).
- [84] T. Vuletić, T. Ivek, B. Korin-Hamzić, S. Tomić, B. Gorshunov, M. Dressel, C. Hess, B. Büchner, and J. Akimitsu *J. Phys. IV France* **131**, 299-305 (2005).
- [85] H. Seo, C. Hotta and H. Fukuyama, *Chem. Rev.* **104**, 5005-5036 (2004).
- [86] H. Mori, S. Tanaka, T. Mori, and Y. Maruyama, *Bull. Chem. Soc. Jpn.* **68**, 1136 (1995).
- [87] H. Mori, S. Tanaka, T. Mori, A. Kobayashi, and H. Kobayashi, *Bull. Chem. Soc. Jpn.* **71**, 797 (1998).
- [88] T. Komatsu, H. Sato, T. Nakamura, N. Matsukawa, H. Yamochi, G. Saito, M. Kusunoki, K. Sakaguchi, and S. Kagoshima, *Bull. Chem. Soc. Jpn.* **68**, 2233 (1995).
- [89] K. Miyagawa, A. Kawamoto, and K. Kanoda, *Phys. Rev. B* **62**, R7679 (2000); H. Tajima, S. Kyoden, H. Mori, and S. Tanaka, *Phys. Rev. B* **62**, 9378 (2000); N. L. Wang, H. Mori, S. Tanaka, J. Dong, and B. P. Clayman, *J. Phys.: Condens. Matter* **13**, 5463 (2001).

-
- [90] T. Nakamura, W. Miyagawa, R. Kinami, Y. Konishi, and T. Takahashi, *Synth. Met.* **103**, 1898 (1999).
- [91] T. Nakamura, W. Minagawa, R. Kinami, and T. Takahashi, *J. Phys. Soc. Jpn.* **69**, 504 (2000).
- [92] C. Hotta, *J. Phys. Soc. Jpn.* **72**, 840 (2003).
- [93] E. B. Yagubskii, I. F. Shchegolev, V. N. Laukhin, P. A. Kononovich, M. V. Kartsovnic, A. V. Zvarykina, and L. I. Buravov, *Pis'ma Zh. Eksp. Teor. Fiz.* **39**, 12 (1984).
- [94] K. Murata, M. Tokumoto, H. Anzai, H. Bando, G. Saito, K. Kajimura, and T. Ishiguro, *J. Phys. Soc. Jpn.* **54**, 1236 (1985).
- [95] A. J. Schultz, M. A. Beno, H. H. Wang, and J. M. Williams, *Phys. Rev. B* **33**, 7823 (1986); S. Kagoshima, Y. Nogami, M. Hasumi, H. Anzai, M. Tokumoto, G. Saito, and N. Mori, *Solid State Commun.* **69**, 1177 (1989).
- [96] J. M. Williams, H. H. Wang, M. A. Beno, T. J. Emge, L. M. Sowa, P. T. Copps, F. Behroozi, L. N. Hall, K. D. Carlson, and G. W. Crabtree, *Inorg. Chem.* **23**, 3839 (1984).
- [97] H. H. Wang, M. A. Beno, U. Geiser, M. A. Firestone, K. S. Webb, J. M. Williams, L. J. Azevedo, J. F. Kwak, and J. E. Schirber, *Inorg. Chem.* **24**, 2465 (1985).
- [98] T. J. Emge, H. H. Wang, M. A. Beno, P. C. W. Leung, M. A. Firestone, H. C. Jenkins, J. D. Cook, K. D. Carlson, J. M. Williams, E. L. Venturini, L. J. Azevedo, and J. E. Schirber, *Inorg. Chem.* **24**, 1736 (1985).
- [99] K. Miyagawa, A. Kawamoto, Y. Nakamura, and K. Kanoda, *Phys. Rev. Lett.* **75**, 1174 (1995).
- [100] K. Kanoda, *Physica C* **282–287**, 299 (1997).
- [101] U. Welp, S. Fleshler, W. K. Kwok, G. W. Crabtree, K. D. Carlson, H. H. Wang, U. Geiser, J. M. Williams, and V. M. Hitsman, *Phys. Rev. Lett.* **69**, 840 (1992).
- [102] U. Geiser, H. H. Wang, K. D. Carlson, J. M. Williams, H. A. Charlier, J. E. Heindl, G. A. Yaconl, B. J. Love, M. W. Lathrop, J. E. Schirber, D. L. Overmyer, J. Ren, and M.-H. Whangbo, *Inorg. Chem.* **30**, 2586 (1991).
- [103] A. Kawamoto, H. Taniguchi, and K. Kanoda, *J. Am. Chem. Soc.* **120**, 10984 (1998).
- [104] H. Taniguchi, A. Kawamoto, and K. Kanoda, *Phys. Rev. B* **59**, 8424 (1999).
- [105] R. H. McKenzie, *Comments Condens. Matter Phys.* **18**, 309 (1998).

-
- [106] H. Mayaffre, P. Wzietek, C. Lenoir, D. Jerome and P. Batail, Europhys. Lett. **28**, 205 (1994); S. M. De Soto, C. P. Slichter, A. M. Kini, H. H. Wang, U. Geiser, and J. M. Williams, Phys. Rev. B **52**, 10364 (1995).
- [107] A. Kawamoto, K. Miyagawa, Y. Nakazawa, and K. Kanoda, Phys. Rev. Lett. **74**, 3455 (1995); *ibid.* **75**, 3586 (1995); A. Kawamoto, K. Miyagawa, Y. Nakazawa, and K. Kanoda, Phys. Rev. B **52**, 15522 (1995); A. Kawamoto, K. Miyagawa, and K. Kanoda, *ibid.* **55**, 14140 (1997).
- [108] J. Müller, M. Lang, F. Steglich, J. A. Schlueter, A. M. Kini, and T. Sasaki, Phys. Rev. B **65**, 144521 (2002); T. Sasaki, N. Yoneyama, A. Matsuyama and N. Kobayashi, *ibid.* **65**, 060505 (2002).
- [109] U. Geiser, H. H. Wang, J. A. Achlueter, S. L. Hallenbeck, T. J. Allen, M. Y. Chen, H.-C. I. Kao, K. D. Carlson, L. E. Gerdorn, and J. M. Williams, Acta Crystallogr. C **44**, 1544 (1984); M. A. Beno, D. D. Cox, J. M. Williams, and J. F. Kwak, *ibid.* **40**, 1334 (1984).
- [110] H. Tanaka, T. Adachi, E. Ojima, H. Fujiwara, K. Kato, H. Kobayashi, A. Kobayashi, and P. Cassoux, J. Am. Chem. Soc. **121**, 11243 (1999).
- [111] H. H. Wang, K. D. Carlson, U. Geiser, W. K. Kwok, M. D. Vashon, J. E. Thompson, N. F. Larsen, G. D. McCabe, R. S. Hulscher, and J. M. Williams, Physica C **166**, 57 (1990).
- [112] J. Singleton, J. Rep. Prog. Phys. **63**, 1111 (2000).
- [113] N. Tajima, A. Ebina-Tajima, M. Tamura, Y. Nishio, and K. Kajita, J. Phys. Soc. Jpn. **71**, 1832 (2002).
- [114] K. Bender, I. Hennig, D. Schweitzer, K. Dietz, H. Endres, and H. J. Keller, Mol. Cryst. Liq. Cryst. **108**, 359 (1984).
- [115] M. Przybylski, H. W. Helberg, D. Schweitzer, and H. J. Keller, Synth. Met. **19**, 191 (1987).
- [116] Y. Hasegawa and H. Fukuyama, Physica B **184**, 498 (1993).
- [117] M. Dressel, G. Grüner, J. P. Pouget, A. Breining, and D. Schweitzer, J. de Physique I (France) **4**, 579 (1994).
- [118] M. Dressel and N. Drichko, Chem. Rev. **104**, 5689 (2004).
- [119] N. Drichko, S. Kaiser, Y. Sun, C. Clauss, M. Dressel, H. Mori, J. Schlueter, E. I. Zhyliaeva, S. A. Torunova, and R. N. Lyubovskaya, Physica B **404**, 490 (2009).
- [120] H. H. Wang, R. Ferraro, J. M. Williams, U. Geiser, and A. Schlueter, J. Chem. Soc. Chem. Commun. **1994**, 1893 (1994).

-
- [121] H. H. Wang, A. M. Kini, and J. M. Williams, *Mol. Cryst. Liq. Cryst.* **284**, 211 (1996).
- [122] K. Yamamoto, K. Yakushi, K. Miyagawa, K. Kanoda, and A. Kawamoto, *Phys. Rev. B* **65**, 085110 (2002).
- [123] O. O. Drozdova, V. N. Semkin, R. M. Vlasova, N. D. Kushch, and E. B. Yagubskii, *Synth. Met.* **64**, 17 (1994).
- [124] T. Yamamoto, M. Uruichi, K. Yamamoto, K. Yakushi, A. Kawamoto, and H. Taniguchi, *J. Phys. Chem. B* **109**, 15226 (2005).
- [125] V. Železny, J. Petzelt, R. Swietlik, B. P. Gorshunov, A. A. Volkov, G. V. Kozlov, D. Schweitzer, and H. J. Keller, *J. Phys. France* **51** 869 (1990).
- [126] N. Tajima, M. Tamura, Y. Nishio, K. Kajita, and Y. Iye, *J. Phys. Soc. Jpn.* **69**, 543 (2000).
- [127] S. Katayama, A. Kobayashi and Y. Suzumura, *J. Phys. Soc. Jpn.* **75**, 054705 (2006).
- [128] A. Kobayashi, S. Katayama, Y. Suzumura, and H. Fukuyama, *J. Phys. Soc. Jpn.* **76**, 034711 (2007).
- [129] H. Kino and T. Miyazaki, *J. Phys. Soc. Jpn.* **78**, 105001 (2009).
- [130] R. E. Peierls, *Quantum Theory of Solids*, (Oxford University, New York/London, 1955).
- [131] G. Grüner, *Rev. Mod. Phys.* **60**, 1129 (1988).
- [132] J. Sólyom, *Adv. Phys.* **28**, 201 (1979).
- [133] S. Barišić, *Mol. Cryst. Liq. Cryst.* **119**, 413 (1985); S. Barišić, *Electronic properties of inorganic materials with quasi-one-dimensional structures*, Part 1, page 1, ed. P. Monceau (Reidel, Dordrecht/Boston/Lancaster, 1986).
- [134] P. A. Lee, T. M. Rice, and P. W. Anderson, *Phys. Rev. B* **14**, 703 (1974).
- [135] S. Tomić, J. R. Cooper, W. Kang, D. Jérôme, and K. Maki, *J. Phys. France* **1**, **1603** (1991).
- [136] A. Bjeliš, in *Applications of Statistical and Field Theory Methods to Condensed Matter*, ed. D. Baeriswyl *et al.* (Plenum Press, New York, 1990).
- [137] H. Fukuyama, P. A. Lee, *Phys. Rev. B* **17**, 535 (1978); P. A. Lee and T. M. Rice, *Phys. Rev. B* **19**, 3970 (1979).
- [138] E. Wigner, *Phys. Rev.* **46**, 1002 (1934).
- [139] D. M. Ceperley, *Phys. Rev. Lett.* **45**, 566 (1980).

- [140] N. D. Drummond, Z. Radnai, J. R. Trail, M. D. Towler, and R. J. Needs, *Phys. Rev. B* **69**, 085116 (2004).
- [141] K. Haraki and K. Kanoda, *Phys. Rev. Lett.* **80**, 4737 (1998).
- [142] J. Bylander, T. Duty and P. Delsing, *Nature* **434**, 361 (2005).
- [143] V. J. Goldman, M. Santos, M. Shayegan, and J. E. Cunningham, *Phys. Rev. Lett.* **65**, 2189 (1990).
- [144] J. Hubbard, *Proc. R. Soc. A* **276**, 238 (1963).
- [145] J. R. Waldram, *Superconductivity of metals and cuprates* (IOP Publishing, Bristol & Philadelphia, 1996).
- [146] *The Hubbard Model: Its Physics and Mathematical Physics*, eds. D. Baeriswyl, D. K. Campbell, J. M. P. Carmelo, F. Guinea, and E. Louis (NATO ASI Series B, Vol. 343, Plenum Press, New York, 1995).
- [147] F. H. L. Essler, H. Frahm, F. Göhmann, A. Klümper, and V. E. Korepin, *The One-Dimensional Hubbard Model* (Cambridge Univ. Press, Cambridge, 2005).
- [148] *The Hubbard model*, ed. M. Rasetti (World Scientific, Singapore, 1991).
- [149] M. Imada, A. Fujimori, and Y. Tokura, *Rev. Mod. Phys.* **70**, 1039 (1998).
- [150] V. J. Emery, *Phys. Rev. B* **14**, 2989 (1976).
- [151] K. V. Efetov and K. I. Larkin, *Soviet Phys. JETP* **42**, 390 (1975).
- [152] V. J. Emery in *Highly Conducting One-Dimensional Solids*, eds. J. Devreese, R. Evrard and V. van Doren, page 247 (Plenum, New York, 1979).
- [153] P. W. Anderson, *Phys. Rev.* **115**, 2 (1959).
- [154] K. C. Ung, S. Mazumdar, and D. Toussaint, *Phys. Rev. Lett.* **73**, 2603 (1994).
- [155] S. Mazumdar, R. T. Clay, and D. K. Campbell, *Phys. Rev. B* **62**, 13400 (2000).
- [156] J. P. Pouget in *Highly Conducting Quasi-One-Dimensional Organic Crystals, Semiconductors and Semimetals*, ed. E. M. Conwell, Vol.27, page 87 (Academic Press, New York, 1988).
- [157] J. P. Pouget in *Physics and Chemistry of Low Dimensional Inorganic Conductors*, eds. C. Schlenker, J. Dumas, M. Greenblatt and S. van Smaalen, (NATO ASI Series B, Vol. 354, Plenum Press, New York, 1996).
- [158] D. J. Scalapino and J. E. Hirsch, *J. Phys. Colloq.* **44**, C3-1507 (1983).
- [159] J. Riera and D. Poilblanc, *Phys. Rev. B* **59**, 2667 (1999).

- [160] S.-C. Zhang and T. M. Rice, Phys. Rev. B **37**, R3759 (1988).
- [161] D. Adler in *Solid State Physics*, eds. F. Seitz, D. Turnbull and H. Ehrenreich, Vol.21 (Academic Press, New York, 1968).
- [162] E. Dagotto, Rep. Prog. Phys. **62**, 1525 (1999).
- [163] R. S. Eccleston, M. Uehara, J. Akimitsu, H. Eisaki, N. Motoyama, and S. Uchida, Phys. Rev. Lett. **81**, 1702 (1998).
- [164] M. Matsuda, K. Katsumata, R. S. Eccleston, S. Brehmer, and H. J. Mikeska, Phys. Rev. B **62**, 8903 (2000).
- [165] R. M. Noack, S. R. White, and D. J. Scalapino, Physica C **270**, 281 (1996).
- [166] H. Kino, H. Fukuyama, J. Phys. Soc. Jpn. **65**, 2158 (1996).
- [167] H. Kino and H. Fukuyama, J. Phys. Soc. Jpn. **64**, 1877 (1995).
- [168] H. Seo and H. Fukuyama, J. Phys. Soc. Jpn. **67**, 1848 (1998).
- [169] H. Seo, J. Phys. Soc. Jpn. **69**, 805 (2000).
- [170] T. Mori, Bull. Chem. Soc. Jpn. **73**, 2243 (2000).
- [171] R. H. McKenzie, J. Merino, J. B. Marston, and O. P. Sushkov, Phys. Rev. B **64**, 085109 (2001).
- [172] M. Calandra, J. Merino, and R. H. McKenzie, Phys. Rev. B **66**, 195102 (2002).
- [173] R. T. Clay, S. Mazumdar, and D. K. Campbell, J. Phys. Soc. Jpn. **71**, 1816 (2002).
- [174] A. Girlando, M. Masino, A. Brillante, R. G. Della Valle, and E. Venuti, Phys. Rev. B **66**, 100507 (2002).
- [175] S. Mazumdar, S. Ramasesha, R. T. Clay, and D. K. Campbell, Phys. Rev. Lett. **82**, 1522 (1999).
- [176] Z. N. C. Ha, Phys. Rev. B **59**, 1559 (1999).
- [177] C. Hotta and F. Pollmann, Phys. Rev. Lett. **100**, 186404 (2008).
- [178] Y. Takahide, T. Konoike, K. Enomoto, M. Nishimura, T. Terashima, S. Uji, and H. M. Yamamoto, Phys. Rev. Lett. **96**, 136602 (2006).
- [179] Y. Takahide, M. Kimata, K. Hazama, T. Terashima, S. Uji, T. Konoike, and H. M. Yamamoto, Phys. Rev. B **81**, 235110 (2010).
- [180] M. Pinterić, T. Vuletić, S. Tomić, and J. U. von Schütz, Eur. Phys. J. B **22**, 335 (2001).

- [181] S. Havriliak and S. Negami, *J. Polym. Sci. C* **14**, 99 (1966).
- [182] H. C. Montgomery, *J. Appl. Phys.* **42**, 2471 (1971).
- [183] N. Barišić, Doctoral Thesis, Faculte des Sciences de Base, Institut de Physique de la Matiere Complexe, Ecole Polytechnique Federale de Lausanne, Lausanne (2004).
- [184] H. Kuriyaki, H. Berger, S. Hishioka, H. Kawakami, K. Hirakawa, and F. A. Levy, *Synth. Metals* **71**, 2049 (1995).
- [185] I. Tanaka and H. Kojima, *Nature* **337**, 21 (1989).
- [186] T. Vuletić, Doctoral Thesis, University of Zagreb, Faculty of Science, Zagreb (2004).
- [187] P. B. Littlewood, *Phys. Rev. B* **36**, 3108 (1987).
- [188] J. C. Dyre and T. B. Schrøder, *Rev. Mod. Phys.* **72**, 873 (2000).
- [189] P. Lunkenheimer, T. Rudolf, J. Hemberger, A. Pimenov, S. Tachos, F. Lichtenberg, and A. Loidl, *Phys. Rev. B* **68**, 245108 (2003).
- [190] N. F. Mott and E. A. Davis, *Electronic Processes in Noncrystalline Solids* (Oxford University, London, 1971).
- [191] P. Foury-Leylekian, Habilitation Thesis, Université Paris-Sud, Paris (2007).
- [192] I. Kézsmarki, Doctoral Thesis, Ecole Polytechnique Federale de Lausanne, Lausanne (2004).
- [193] S. Tomić, N. Biškup and A. Omerzu, *Synth. Met.* **85**, 1597 (1997).
- [194] T. Vuletić, D. Herman, N. Biškup, M. Pinterić, A. Omerzu, S. Tomić, and M. Nasagawa, *J. Phys. IV France* **9**, Pr10-275 (1999).
- [195] V. Ilakovac, Habilitation Thesis, Université Pierre et Marie Curie (Paris 6), France (2010).
- [196] M. Miljak, private communication.
- [197] W. Higemoto, A. Koda, G. Maruta, K. Nishiyama, H. Nakamura, S. Giri, and M. Shiga, *J. Phys. Soc. Jpn.* **71**, 2361 (2002).
- [198] G. Allodi, A. Prodi, R. De Renzi, F. Licci, F. Bolzoni, G. Guidi, E. Gilioli, A. Gauzzi, M. Marezio, and R. Scheuermann, *Physica B* **374–375**, 44 (2006).
- [199] H. Okamoto, T. Mitani, Y. Tokura, S. Koshihara, T. Komatsu, Y. Iwasa, T. Koda, and G. Saito, *Phys. Rev. B* **43**, 8224 (1991).

-
- [200] M. Pinteric, M. Miljak, N. Biskup, O. Milat, I. Aviani, S. Tomic, D. Schweitzer, W. Strunz, and I. Heinen, *Eur. Phys. J. B* **11**, 217 (1999).
- [201] M. Matsuda, K. Katsumata, T. Osafune, N. Motoyama, H. Eisaki, S. Uchida, T. Yokoo, S. M. Shapiro, G. Shirane, J. L. Zarestky, *Phys. Rev. B* **56**, 14499 (1997).
- [202] M. Herak, M. Miljak, unpublished.
- [203] K. I. Kumagai, S. Tsuji, M. Kato, and Y. Koike, *Phys. Rev. Lett.* **78**, 1992 (1997).
- [204] V. Kataev, K. Y. Choi, M. Grüninger, U. Ammerahl, B. Büchner, A. Freimuth, A. Revcolevschi, *Phys. Rev. B* **64**, 104422 (2001).
- [205] T. Sugano, K. Yamada, G. Saito, and M. Kinoshita, *Solid State Commun.* **55**, 137 (1985).
- [206] M. Meneghetti, R. Bozio, and C. Pecile, *J. Physique* **47**, 1377 (1986); *Synth. Met.* **19**, 143 (1987).
- [207] K. Yakushi, H. Kanbara, H. Tajima, H. Kuroda, G. Saito, and T. Mori, *J. Phys. Soc. Jpn* **60**, 4251 (1987).
- [208] Y. Yue, K. Yamamoto, M. Uruichi, C. Nakano, K. Yakushi, S. Yamada, T. Hiejima, and A. Kawamoto, *Phys. Rev. B* **82**, 075134 (2010).
- [209] R. Zamboni, D. Schweitzer, H. J. Keller, and C. Taliani, *Z. Naturforsch.* **44a**, 295 (1989).
- [210] V. Želzný, J. Petzelt, R. Swietlik, B. P. Gorshunov, A. A. Volkov, G. V. Kozlov, D. Schweitzer, and H. J. Keller, *J. Phys. I (France)* **51**, 869 (1990).
- [211] S. Gärtner, D. Schweitzer, and H. J. Keller, *Synth. Met.* **44**, 227 (1991).
- [212] C. Clauss, N. Drichko, D. Schweitzer, and M. Dressel, *Physica B* (2009), doi:10.1016/j.physb.2009.11.036.
- [213] U. Fano, *Phys. Rev.* **124**, 1866 (1961).
- [214] N. L. Wang, H. Mori, S. Tanaka, J. Dong, and B. P. Clayman, *J. Phys.: Cond. Matter* **13**, 5463 (2001).
- [215] N. Drichko, M. Dressel, C. A. Kuntscher, A. Pashkin, A. Greco, J. Merino, and J. Schlueter, *Phys. Rev. B* **74**, 235121 (2006); M. Dressel, N. Drichko, J. Schlueter, and J. Merino, *Phys. Rev. Lett.* **90**, 167002 (2003).
- [216] J. Merino, A. Greco, R. H. McKenzie, and M. Calandra, *Phys. Rev. B* **68** 245121 (2003).
- [217] T. Takahashi, Y. Nogami, and K. Yakushi, *J. Phys. Soc. Jpn.* **75**, 051008 (2006).

-
- [218] B. Korin-Hamzić, E. Tafra, M. Basletić, A. Hamzić, and M. Dressel, *Phys. Rev. B* **73**, 115102 (2006).
- [219] T. Mori, A. Kobayashi, Y. Sasaki, H. Kobayashi, G. Saito, and H. Inokuchi, *Bull. Chem. Soc. Jpn.* **57**, 627 (1984).
- [220] K. Yamamoto, S. Iwai, S. Boyko, A. Kashiwazaki, F. Hiramatsu, C. Okabe, N. Nishi, and K. Yakushi, *J. Phys. Soc. Jpn.* **77**, 074709 (2008).
- [221] Y. Tanaka and K. Yonemitsu, *J. Phys. Soc. Jpn.* **79**, 024712 (2010).
- [222] H. Nakaya, K. Itoh, Y. Takahashi, H. Itoh, S. Iwai, S. Saito, K. Yamamoto, and K. Yakushi, *Phys. Rev. B* **81**, 155111 (2010).
- [223] P. M. Chaikin and T. C. Lubensky, *Principles of Condensed Matter Physics* (Cambridge University Press, Cambridge, 1995), Sec. 10.
- [224] S. R. White, I. Affleck, and D. J. Scalapino, *Phys. Rev. B* **65**, 165122 (2002).
- [225] K. Tamura, T. Ozawa, Y. Bando, T. Kawamoto, and T. Mori, *J. Appl. Phys.* **107**, 103716 (2010).
- [226] J. Bardeen, E. Ben-Jacob, A. Zettl, and G. Grüner, *Phys. Rev. Lett.* **49**, 493 (1982).
- [227] P. Monceau, J. Richard, and M. Renard, *Phys. Rev. B* **25**, 931 (1982).
- [228] T. Ivek, I. Kovačević, M. Pinterić, S. Tomić, and M. Dressel, unpublished.
- [229] P. Lunkenheimer, V. Bobnar, A. V. Pronin, A. I. Ritus, A. A. Volkov, and A. Loidl, *Phys. Rev. B* **66**, 052105 (2002).
- [230] P. Fulde, *Electron Correlations in Molecules and Solids*, 3rd edition, Springer-Verlag, Berlin (1995).
- [231] S. Maekawa, T. Tohyama, S. E. Barnes, S. Ishihara, W. Koshibae, and G. Khalullin, *Physics of Transition Metal Oxides*, Springer, Berlin (2004).
- [232] D. I. Khomskii, *Physica Scripta* **72**, CC8-14 (2005).
- [233] L. Paolasini, C. Vettier, F. de Bergevin, F. Yakhou, D. Mannix, A. Stunault, W. Neubeck, M. Altarelli, M. Fabrizio, P. A. Metcalf, and J. M. Honig, *Phys. Rev. Lett.* **82**, 4719 (1999).
- [234] H. F. Pen, J. van den Brink, D. I. Khomskii, and G. A. Sawatsky, *Phys. Rev. Lett.* **78**, 1323 (1997).
- [235] G. Blumberg, P. Littlewood, A. Gozar, B. S. Dennis, N. Motoyama, H. Eisaki, and S. Uchida, *Science* **297**, 584 (2002).

- [236] A. Rusydi, P. Abbamonte, H. Eisaki, Y. Fujimaki, G. Blumberg, S. Uchida, and G. A. Sawatzky, *Phys. Rev. Lett.* **97**, 016403 (2006).
- [237] Y. Piskunov, D. Jérôme, P. Auban-Senzier, P. Wzietek, C. Bourbonnais, U. Ammerahl, G. Dhalenne and A. Revcolevschi, *Eur. Phys. J. B* **24**, 443 (2001).
- [238] Y. Piskunov, D. Jérôme, P. Auban-Senzier, P. Wzietek and A. Yakubovsky, *Phys. Rev. B* **69**, 014510 (2004).
- [239] <http://www.ccp14.ac.uk/tutorial/lmgp/orientexpress.htm>
- [240] B. Gorshunov, A. Volkov, I. Spektor, A. Prokhorov, A. Mukhin, M. Dressel, S. Uchida, and A. Loidl, *Int. J. Infrared and Millimeter Waves* **26**, 1217 (2005).
- [241] P. Monceau, F. Y. Nad, S. Brazovskii, *Phys. Rev. Lett.* **86**, 4080 (2001).
- [242] K. Kanoda, *J. Phys. Soc. Jpn.* **75**, 051007 (2006).
- [243] N. Tajima, J. Fujisawa, N. Naka, T. Ishihara, R. Kato, Y. Nishio, and K. Kajita, *J. Phys. Soc. Jpn.* **74**, 511 (2005).
- [244] S. Iwai, K. Yamamoto, A. Kashiwazaki, F. Hiramatsu, H. Nakaya, Y. Kawakami, K. Yakushi, H. Okamoto, H. Mori, and Y. Nishio, *Phys. Rev. Lett.* **98**, 097402 (2007).
- [245] T. Mori, *J. Phys. Soc. Jpn.* **79**, 014703 (2010).
- [246] N. Tajima, S. Sugawara, M. Tamura, R. Kato, Y. Nishio, and K. Kajita, *Eur. Phys. Lett.* **80**, 47002 (2007).
- [247] N. Tajima, S. Sugawara, R. Kato, Y. Nishio, and K. Kajita, *Phys. Rev. Lett.* **102**, 176403 (2009).
- [248] N. Tajima, S. Sugawara, M. Tamura, Y. Nishio, and K. Kajita, *J. Phys. Soc. Jpn.*, **75**, 051010 (2006).

Curriculum vitae

Tomislav Ivek was born on 12. September 1980 in Varaždin, Croatia.

Education:

- **Primary school:** Varaždin (1987–1995)
- **High school:** Gimnazija Varaždin (1995–1999)
- **Undergraduate study:** University of Zagreb, Faculty of Science - Physics Department (1999-2004)
- **Diploma thesis:** *Charge-density wave in quasi-one-dimensional cuprates*, mentor: Silvia Tomić, Institut za fiziku; University of Zagreb, Faculty of Science - Physics Department, Zagreb (2004)
- **Graduate study:** University of Zagreb, Faculty of Science - Physics Department (2005-2010)

Work experience: From 1. February 2005 employed as a research assistant at the Institut za fiziku, Zagreb, Croatia, in the group of S. Tomić.

List of publications

1. T. Vuletić, **T. Ivek**, B. Korin-Hamzić, S. Tomić, B. Gorshunov, P. Haas, M. Dressel, J. Akimitsu, T. Sasaki, and T. Nagata, *Anisotropic Charge Modulation in the Ladder Planes of $Sr_{14-x}Ca_xCu_{24}O_{41}$* , Phys. Rev. B **71**, 012508 (2005).
2. T. Vuletić, **T. Ivek**, B. Korin-Hamzić, S. Tomić, B. Gorshunov, M. Dressel, C. Hess, B. Büchner, and J. Akimitsu, *Phase diagrams of $(La, Y, Sr, Ca)_{14}Cu_{24}O_{41}$: switching between the ladders and the chains*, J. Phys. IV France **131**, 299-305 (2005).
3. T. Vuletić, B. Korin-Hamzić, **T. Ivek**, S. Tomić, B. Gorshunov, M. Dressel, and J. Akimitsu, *The Spin-Ladder and Spin-Chain System $(La, Y, Sr, Ca)_{14}Cu_{24}O_{41}$: Electronic Phases, Charge and Spin Dynamics*, Phys. Rep. **428**, 169-258 (2006).
4. **T. Ivek**, T. Vuletić, S. Tomić, A. Akrap, H. Berger, and L. Forró, *Collective Charge Excitations below the Metal-to-Insulator Transition in $BaVS_3$* , Phys. Rev. B **78**, 035110 (2008).
5. S. Tomić, S. Dolanski Babić, **T. Ivek**, T. Vuletić, S. Krča, F. Livolant, and R. Podgornik, *Short-fragment Na-DNA dilute aqueous solutions: fundamental length scales and screening*, Europhys. Lett. **81**, 68003 (2008).
6. **T. Ivek**, T. Vuletić, B. Korin-Hamzić, O. Milat, S. Tomić, B. Gorshunov, M. Dressel, J. Akimitsu, Y. Sugiyama, C. Hess, and B. Büchner, *Crossover in charge transport from one-dimensional copper-oxygen chains to two-dimensional ladders in $(La, Y)_y(Sr, Ca)_{14-y}Cu_{24}O_{41}$* , Phys. Rev. B **78**, 205105 (2008).
7. T. Vuletić, S. Dolanski Babić, **T. Ivek**, D. Grgičin, S. Tomić, and R. Podgornik, *Structure and dynamics of hyaluronic acid semidilute solutions: a dielectric spectroscopy study*, Phys. Rev. E **82**, 011922 (2010).
8. **T. Ivek**, B. Korin-Hamzić, O. Milat, S. Tomić, C. Clauss, N. Drichko, D. Schweitzer, and M. Dressel, *Collective Excitations in the Charge-Ordered Phase of α - $(BEDT-TTF)_2I_3$* , Phys. Rev. Lett. **104**, 206406 (2010).
9. S. Tomić, D. Grgičin, **T. Ivek**, S. Dolanski Babić, T. Vuletić, G. Pabst, and R. Podgornik, *Dynamics and Structure of Biopolyelectrolytes characterized by Dielectric Spectroscopy*, accepted in Macromolecular Symposia (2011).

10. **T. Ivek**, B. Korin-Hamzić, O. Milat, S. Tomić, C. Clauss, N. Drichko, D. Schweitzer, and M. Dressel, *Electrodynamical Response of the Charge Ordering Phase: Dielectric and Optical Studies of α -(BEDT-TTF) $_2$ I $_3$* , Phys. Rev. B **83**, 165128 (2011).